Integrated Extracellular Matrix Mimetic Biomaterials and Microfabricated Platforms for Studying Mechanobiology in Cardiomyocyte Maturation and Cardiac Disease

by

Samuel J. DePalma

A dissertation submitted in partial fulfillment
of the requirements for the degree of
Doctor of Philosophy
(Biomedical Engineering)
in the University of Michigan
2024

Doctoral Committee:

Associate Professor Brendon M. Baker, Chair
Professor Christopher S. Chen
Assistant Professor Adam S. Helms
Associate Professor David A. Nordsletten
Assistant Professor Abdon Pena-Francesch

Sameul J. DePalma

samdep@umich.edu

ORCID iD: 0000-0001-6708-5019

Dedication

To Kennedy, for being a beacon of joy and love in my life. None of this would have been possible without your unwavering support.

To my family, thank you for always being my biggest supporters and instilling in me a lifelong passion for learning.

To my friends, old and new, near and far, who have cheered me on through thick and thin, and always remind me to not take myself too seriously.

Acknowledgements

The work presented in this thesis would not have been possible without the incredible support from my advisor, lab mates, collaborators, and thesis committee members. First, I would like to thank my advisor, Brendon. Your thoughtful guidance constantly challenged me to be a better scientist and I truly would not be where I am today without your support. Your passion and dedication to mentorship is evident, and I am extremely privileged to have had the opportunity to learn from you and am proud to be able to call you a great friend.

This work also contains key contributions from many lab mates and close collaborators. To Harrison: from staring in the lab on the same day to defending two days apart, I am so lucky to have experienced all the highs and lows of graduate school with you working side-by-side with you. You are a phenomenal scientist and an even better friend. To Chris, Willy, and Dan: thank you so much for taking me and Harrison under your wing when we joined the lab and for being such great role models for us to look up to. To Bobby, Raha, Maggie, Jingyi, Firaol, Michael, and Elizabeth: your constant input and feedback helped shape important parts of this work and your friendship made coming to lab everyday so much fun. To all the undergraduate researchers who helped me along the way: your hard work and dedication was critical to all aspects of this work. Thank you for being patient and attentive learners and for helping me to grow as a mentor and scientist.

Lastly, to my committee members Dr. Adam Helms, Dr. David Nordsletten, Dr, Christopher Chen, and Dr. Abdon Pena-Francesch: thank you for being such great mentors and collaborators and for challenging me to think more deeply. Your curiosity and passion for research is inspiring and has helped shape this work in profound ways.

Table of Contents

List of Figures

List of Tables

List of Movies

Abstract

The mechanical function of the myocardium is dictated by contractile cardiomyocytes (CMs) and the fibrous extracellular matrix (ECM) that surrounds, organizes, and supports bundles of CMs. Previous studies have implicated ECM mechanics in driving cardiac tissue assembly and overall contractile function through mechanosensitive CM-ECM adhesion complexes called costameres. However, due to limitations in existing engineered models of myocardium which require the inclusion of stromal cells or lack orthogonal mechanical control over matrix properties, how CMs sense and respond to specific mechanical microenvironmental cues has not been established. Therefore, the focus of this dissertation is to develop improved *in vitro* models of the cardiac ECM to advance our understanding of how microenvironmental mechanics impact cardiac tissue assembly and function in both healthy and diseased contexts.

First, this thesis reviews the vast array of engineered heart tissue platforms that have been previously developed to study the maturation of induced pluripotent stem cell-derived cardiomyocytes (iPSC-CMs) and the utility of these platforms for studying CM maturation, modeling disease processes, or screening drugs for cardiotoxicity. Through an in-depth meta-analysis of >300 manuscripts, we highlight the vast array of iPSC-CM differentiation protocols, iPSC-CM maturation techniques, and analysis methods used to generate and assess previously established *in vitro* cardiac model systems and note significant progress in the field over time. Additionally, we discuss opportunities to unify and compare these various techniques by using common controls and tunable engineered heart tissue platforms, enabling continued

comprehensive benchmarking of progress in developing physiological relevant models of the adult myocardium.

Next, we describe the development and characterization of two biomaterial platforms composed of electrospun dextran vinyl sulfone (DVS) fiber matrices that recapitulate the architecture and mechanics of collagen fiber networks that scaffold CMs. Taking inspiration from previously established engineered heart tissue models, these cardiac microtissues systems enable orthogonal tuning of various biophysical and biochemical properties of the cardiac microenvironment. Using these platforms, we define a set of scaffold parameters that drive the efficient assembly of functional myocardial syncytia and promote both structural and functional maturation of iPSC-CMs. In particular, we demonstrate that iPSC-CM mechanosensing of changes in matrix stiffness underlies the formation of costameres which corresponds to greater structural, electrical, and contractile maturity of engineered cardiac tissues.

Finally, this thesis describes a platform using the same fibrous DVS matrices that enables co-culture of cardiac fibroblasts and iPSC-CMs to explore how biophysical and biochemical microenvironmental cues impact heterocellular signaling in the heart. As fibroblasts sit within the collagen networks between CMs in the native myocardium, bilayer tissues composed of CMs and cardiac fibroblasts separated by synthetic ECM-mimetic matrices were utilized for two major objectives: 1) examining how cardiac fibroblasts sense and respond to mechanical changes of fibrous matrices, and 2) dissecting how physical and paracrine signaling between CMs and fibroblasts regulates fibroblast quiescence versus fibrogenic activation.

Overall, the work presented in this dissertation integrates stem cells, biomaterials, tissue engineering, and microfabrication approaches to develop highly tunable cardiac microtissue platforms to study how microenvironmental cues influence fundamental biological processes

involved in cardiac tissue assembly, healthy function, or disease. The results presented here help inform the design of biomaterial scaffolds for use in engineered tissue replacement therapies and provide new insights into how cellular mechanosensing in the heart regulates tissue development and disease processes.

Chapter 1: Introduction

The overall goal of this thesis is to investigate how biophysical cues in the cardiac microenvironment drive fundamental biological processes such as cardiac development, maturation, and disease. By integrating synthetic fibrous biomaterials that mimic the architecture of the myocardial extracellular matrix (ECM) with microfabrication techniques, confocal microscopy, and live imaging, this work employs three cardiac microtissue platforms that enable orthogonal tuning of physiologically relevant biophysical properties to identify key biological regulators of myofibril maturation, homeostatic cellular communication, and pathogenic signaling.

Chapter 2 provides a broad overview of the structure of the myocardial extracellular matrix and how dynamic changes throughout tissue development and fibrosis dictate cellular signaling and overall tissue function. Next, this chapter examines the types of *in vitro* models utilized to generate mature induced pluripotent stem cell-derived cardiomyocytes (iPSC-CM) by highlighting both the strengths and weaknesses of each of these platforms. Lastly, Chapter 2 outlines our current knowledge of mechanosensing in the myocardium and explores how we might leverage our synthetic biomaterial platforms to further interrogate these complex signaling pathways.

Chapter 3 then dives deeper into some of these concepts via a comprehensive review of engineered heart tissue platforms used in the past for evaluating iPSC-CM maturation, disease modeling, and drug screening. Through a meta-analysis spanning more than 300 papers, this work sheds light on the variety of strategies used for iPSC-CM differentiation, maturation, and tissue assessment, recognizing significant advancements over the past decade. This work also emphasizes standardization opportunities in the field by suggesting the adoption of universally

accepted controls and tunable engineered heart tissue models to facilitate continued advancements toward engineering mature, translatable iPSC-CM *in vitro* platforms. To further advance our knowledge in this space, the remaining chapters focus on utilizing synthetic biomaterial platforms to study iPSC-CM mechanosening in tissue maturation and disease.

Chapter 4 outlines the application of highly tunable synthetic fibrous scaffolds composed of dextran vinyl sulfone (DVS) to investigate biophysical and biochemical regulators of iPSC-CM tissue assembly and function. Using these scaffolds whose architecture mimics collagen networks found in the native heart, this work identified optimal cell adhesive motifs, cellular density, and matrix alignment needed to form functional iPSC-CM tissues. Unlike simple cardiac microtissue platforms, these synthetic fibers also promote long term stability of iPSC-CM tissues, enabling in-depth investigation into various tissue maturation and disease related processes.

Chapter 5 subsequently describes the creation of a more complex DVS-based cardiac microtissue platform designed to enable additional mechanical tunability of ECM and boundary stiffness, in addition to supporting real-time contractile force measurements. These platforms helped identify key scaffold characteristics that facilitate the formation of functional myocardial tissue and promote iPSC-CM maturation. In contrast to previous findings on non-fibrous hydrogel substrates, iPSC-CMs in soft environments that mimic the stiffness of the fetal heart were the most contractile and mature. Furthermore, matrix stiffness, matrix alignment, and tissue constraints had distinct effects on iPSC-CM function and structure, potentially due to differential influence on costamere formation, cell-cell junctions, and myofibrillar assembly. Lastly, optimal mechanical conditions were critical for the formation of costameres, specialized cell-ECM adhesions that are associated with myofibril maturation.

Chapter 6 focuses on a platform that again leverages DVS fibrous matrices and microfabrication techniques, this time to investigate the influence of microenvironmental cues on intercellular communication in the heart between CMs and cardiac fibroblasts. To recapitulate the organization of fibroblasts in the heart's native endomoysial collagen networks, bilayer structures comprising CMs and fibroblasts, separated by synthetic ECM analogs were generated. While fibroblasts differentiated to myofibroblasts when cultured alone on aligned fiber matrices, in a coculture setting paracrine signaling between CMs and fibroblasts mitigates this response. Overall, this work posits the presence of homeostatic communication networks between CMs and fibroblasts that could be potential targets for anti-fibrotic therapeutics.

Finally, Chapter 7 provides a summary of the major findings from this thesis work and future directions towards investigating cardiac mechanobiology in fundamental tissue processes, iPSC-CM maturation, and translating the finding presented herein toward translatable regenerative therapies. In conjunction with in-depth study of mechanosensing pathways and intercellular communication using imaging and high-dimensional analysis techniques, advances in iPSC-CM maturation and assessment will enable the generation of more functionally mature translatable cardiac tissue models.

Chapter 2: Background

2.1 The extracellular matrix of the myocardium

The extracellular matrix (ECM) is defined as the non-cellular components present in all tissues that provides structural support, organizes constituent cells, and provides mechanical and biochemical cues to cells that regulate their behavior and fate (Cruz Walma and Yamada 2020; Frantz, Stewart, and Weaver 2010). Both physical and biochemical cues encoded by the ECM are critically important in fundamental biological processes intrinsic to tissue morphogenesis, homeostasis, and disease progression (Bonnans, Chou, and Werb 2014). The ECM in each tissue or organ is composed of unique combinations of fibrous proteins, such as collagen, fibronectin, and elastin, and charged polysaccharides that act to retain water and fill interstitial spaces (Järveläinen et al. 2009). The composition and distribution of each of these components is produced and maintained by various cellular components (e.g. fibroblasts, endothelial cells, parenchymal cells, etc.) and collectively as a composite material defines overall tissue physical properties such as tensile strength and elasticity, allowing for proper tissue function (Goldsmith et al. 2004, 2014). Additionally, the organization of these components and how resident cells interact with various ECM components can initiate a wide array of biological signaling pathways critical to development, tissue homeostasis, and disease progression (Bonnans, Chou, and Werb 2014).

2.1.1 Structure and function of the myocardial extracellular matrix

The mechanical function of the healthy myocardium is dictated by contractile cardiomyocytes (CMs) and the fibrous ECM that surrounds, orients, and groups them (Karl T. Weber 1989). The major components of the cardiac ECM include collagen I, elastin, fibronectin, and laminin, in addition to various glycoproteins and proteoglycans, whose exact composition throughout the tissue changes drastically throughout heart development, maturation in the adult, and the course of cardiac disease (Derrick and Noel 2021; Frangogiannis 2017, 2019; Rienks et al. 2014). Collagen I is the most abundant ECM protein in the adult heart and forms a hierarchical, multi-scale fibrillar mesh in which resident cells, such as CMs, fibroblasts, and endothelial cells, reside (C. Williams et al. 2014). This complex collagen network organizes myocardium at multiple length scales spanning tissue down to individual cells: 1) large epimysial collagen fibers surround large groups of muscle bundles to provide mechanical stability, thereby preventing excessive stretching of the tissue; 2) micron-scale perimysial fibers wrap around and organize individual bundles of CMs; and 3) nano-scale endomysial fibers found within each bundle connect to the cytoskeleton of each CM via costameres (**Figure 2.1**) (Fleischer and Dvir 2013; Karl T. Weber 1989; Karl T. Weber et al. 1994). In particular, perimysial collagen fibers are approximately 1 μm in diameter and are co-aligned along the long axis of each CM bundle (**Figure 2.1c**) (Pope et al. 2008). The alignment of individual CMs composing each bundle as well as contractile myofibrils within each cell mirror the orientation of perimysial collagen networks. Together, highly aligned CMs and surrounding ECM enable mechanically anisotropic contractions critical to healthy cardiac function. In addition to being highly organized at the cellular scale, bundles of myocytes are locally aligned with a change in overall alignment at different locations throughout the myocardial wall. The transmural helical orientation from the epicardium to the endocardium

results in simultaneous longitudinal shortening, radial thickening, and torsion that gives rise to optimal pumping function of the ventricle (Costa et al. 1999; LeGrice et al. 1995; Pope et al. 2008; Poveda et al. 2013).

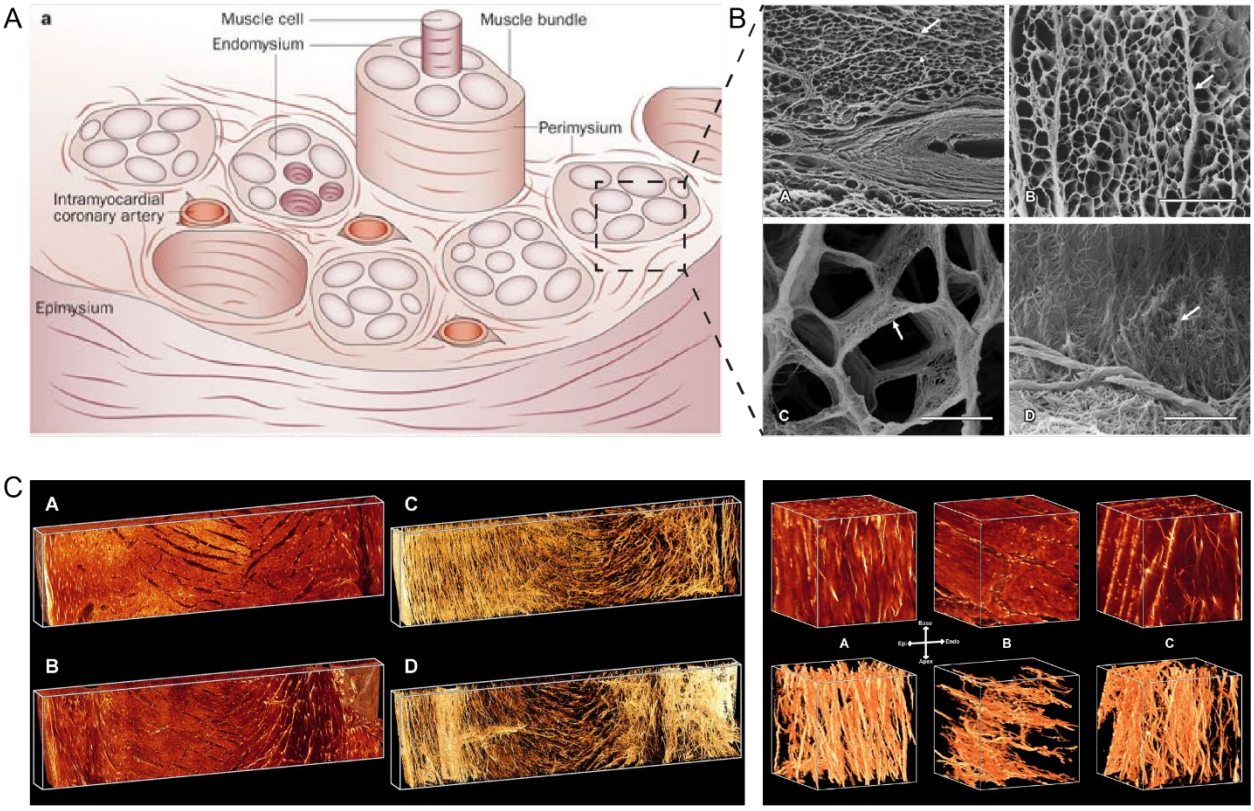

Figure 2.1: Hierarchical organization of the myocardial ECM. A) Schematic showing organization of myocardial tissue. Image reproduced from (Karl T. Weber et al. 2012). B) SEM images of the hierarchical organization of the cardiac ECM around the cardiomyocytes. Top left: scale bar = 200 µm, thick arrow, perimysium; thin arrow, endomysium. Top right: The multiscale myocardial ECM consists of the perimysium (thick arrow) which surrounds groups of cardiomyocytes and the endomysium (thin arrow) which surrounds each cardiomyocyte (scale bar = 100 µm). Bottom left: shows a closer view of the endomysial supports (scale bar = 10 µm). Botton right: displays collagen interconnections on the surface of cardiomyocytes (scale bar = 3 µm). Multiscale myocardial ECM figure inset. Image reproduced from (Kanzaki et al. 2010). C) 3-dimensional volume renderings of the perimysial collagen networks in the myocardium. Images reproduced from (Pope et al. 2008).

As is the case in many other tissues, the ECM in the myocardium is highly dynamic as cells continually remodel the tissue (Bowers, Meng, and Molkentin 2022; Rienks et al. 2014). Cardiac fibroblasts sitting within the endomysial fibers between myocytes and perimysial matrices between bundles of myocytes are believed to be primarily cell type responsible for the production, maintenance, and remodeling of the cardiac ECM in both homeostatic and pathological conditions (Goldsmith et al. 2004; Hall et al. 2021). Physical and biochemical changes to the ECM mediated by fibroblasts, and to a lesser extent smooth muscle cells, endothelial cells, and cardiomyocytes, facilitate significant changes in myocardial function during tissue development and disease progression (Frangogiannis 2019; Shinde and Frangogiannis 2014).

2.1.2 Myocardial ECM in tissue development

Biomechanical and biochemical changes to the myocardial ECM have been associated with heart morphogenesis and increases in contractile function over time (Derrick and Noel 2021; Rienks et al. 2014; Silva et al. 2021). As the heart is beginning to form, endoderm-derived ECM composed mainly of hyaluronic acid, fibronectin, fibrillin, and laminin along with collagen I and IV, orchestrates the differentiation and positioning of cardiac progenitors (Little and Rongish 1995; Lockhart et al. 2011a; Silva et al. 2021). Disrupting fibronectin production results in improper heart morphogenesis (e.g. cardiac bifida) and ultimately leads to embryonic lethality (George et al. 1993). Throughout fetal heart development, cardiac fibroblasts continue to secrete fibronectin, promoting CM proliferation (Ieda et al. 2009; C. Williams et al. 2014). The presence of agrin within the ECM has also been linked to proliferation of CMs at these early stages of development (Bassat et al. 2017). Polarized proliferation of CMs is important for morphogenic processes such as trabeculation and is dependent on the composition and organziation of the ECM (del Monte-Nieto et al. 2018; Passer et al. 2016). Subsequently, ECM remodeling via various ECM

proteases (e.g. ADMTS1, MMP2) plays an important role in myocardial compaction, as disruptions in these processes can lead to congenital cardiomyopathies (W. Lin et al. 2018; del Monte-Nieto et al. 2018).

In the neonatal and postnatal heart, the amount of fibronectin and hyaluronic acid decreases as collagen, I, collagen III, and laminin increase (Silva et al. 2021; C. Williams et al. 2014). This increase in more fibrous, structural ECM components corresponds to increases in both tissue contractility and stiffness. Studies examining heart tissue in developing chick embryos report an increase in tissue elastic modulus from < 1 kPa at embryonic day 1 to approximately 10 kPa at day 14 (Majkut et al. 2013; Young and Engler 2011). Majkut et al. showed that this increase in tissue stiffness corresponds with increases in collagen I expression and other cardiomyocyte contractility related proteins (Majkut et al. 2013). Changes in tissue stiffness directly impact both the mechanical and biological function of the heart. Inhibition of the ECM crosslinker lysyl oxidase in P3 mice, decreased tissue stiffness and reduced the regenerative capacity of the tissue (Notari et al. 2018). Taken together, carefully orchestrated changes in ECM composition and mechanical properties of the myocardium regulate various aspects of heart development.

2.1.3 Myocardial ECM in fibrotic disease

The importance of the structure of the myocardium in supporting proper contractile function of the heart is particularly evident in cardiac fibrosis (M. D. Davidson, Burdick, and Wells 2020; Kong, Christia, and Frangogiannis 2014; Karl T. Weber 1989). Most cardiac pathologies involve fibrotic changes to the myocardium that are driven by the recruitment and proliferation of MFs, believed largely to arise from resident cardiac fibroblasts (Kanisicak et al. 2016; Tallquist and Molkentin 2017; Travers et al. 2016). MFs activated by cues from the tissue microenvironment deposit excessive amounts of pathologic ECM in the perimysial space (Y. Sun et al. 2000; K T

Weber 2000), leading to progressive structural and mechanical changes that impair cardiac function and culminate with heart failure (Fan et al. 2012; Hinz 2006; Kong, Christia, and Frangogiannis 2014). This disruption in the architecture and mechanics of the ECM is believed to establish a positive feedback loop that drives further fibrotic remodeling and diminished cardiac function.

2.1.3.1 Cardiac fibrosis resulting from myocardial infarction

Fibrosis of the heart can be classified into two main categories: replacement fibrosis and interstitial fibrosis (**Figure 2.2**). Replacement fibrosis occurs after a myocardial infarction, where tissue ischemia results in significant loss of myocytes (> 1 billion) (Laflamme and Murry 2005). In response, resident fibroblasts and potentially other cell types (such as endothelial cells) respond by differentiating into activated myofibroblasts that deposit significant amounts of scar tissue as part of a wound healing response aimed at maintaining the mechanical integrity of the myocardial wall. During the initial inflammatory response after injury, tissue necrosis signals promote an innate immune response, where infiltrating leukocytes remove dead cells and matrix debris (Shinde and Frangogiannis 2014). Myofibroblasts additionally begin to break down the existing matrix and replace it with a transient reparative matrix consisting of mainly fibrin and fibronectin (Frangogiannis 2014; Talman and Ruskoaho 2016). As pro-fibrogenic signaling takes hold, fibroblasts and myofibroblasts continue to proliferate within the scar region and synthesize structural proteins including collagen I and laminin which act to increase the tensile strength of the heart wall and preventing rupture (Talman and Ruskoaho 2016). Scar maturation is characterized by the continued synthesis of collagen I and increased lysyl oxidase (LOX)-catalyzed collagen crosslinking (Van Den Borne et al. 2009; Shinde and Frangogiannis 2014). The replacement of healthy contractile tissue with non-contractile, stiff scar tissue results in abnormal

mechanics of the surrounding uninjured tissue as well. In the border region surrounding the scar tissue, contractile CMs and the surrounding fibroblasts experience heightened mechanical strain that has been shown to drive further activation of myofibroblasts (Herum et al. 2017). The heightened mechanical strains present in these regions also correspond with aligned collagen fibrils that may promote myofibroblast activation (**Fig. 2b**) (Bugg et al. 2020). In fact, it has been suggested that myofibroblasts originate from the border region and migrate towards the center of the scar along newly synthesized matrix during the proliferative phase of scar formation post-infarct (Van Den Borne et al. 2009).

In more distant regions of the myocardium, interstitial fibrosis and ECM remodeling often persists, accompanied by CM hypertrophy to compensate for decreased ventricular function caused by the significant areas of non-contractile and stiff scar tissue (Heineke and Molkentin 2006). The resulting increase in heart wall thickness and stiffness from increased collagen deposition and crosslinking eventually leads to diastolic dysfunction (Karl T. Weber et al. 2012). Specific mechanisms describing how fibrosis in regions distant from the infarct scar persists are the subject of current investigation. Initial studies suggest that activated myofibroblasts and hypertrophic CMs may secrete pro-fibrotic factors that can signal to distant regions in the myocardium (Karl T. Weber et al. 2012). Further, increased mechanical stress-induced activation of latent TGF-β1 may occur as the mechanics of the myocardium change throughout disease (Wipff et al. 2007).

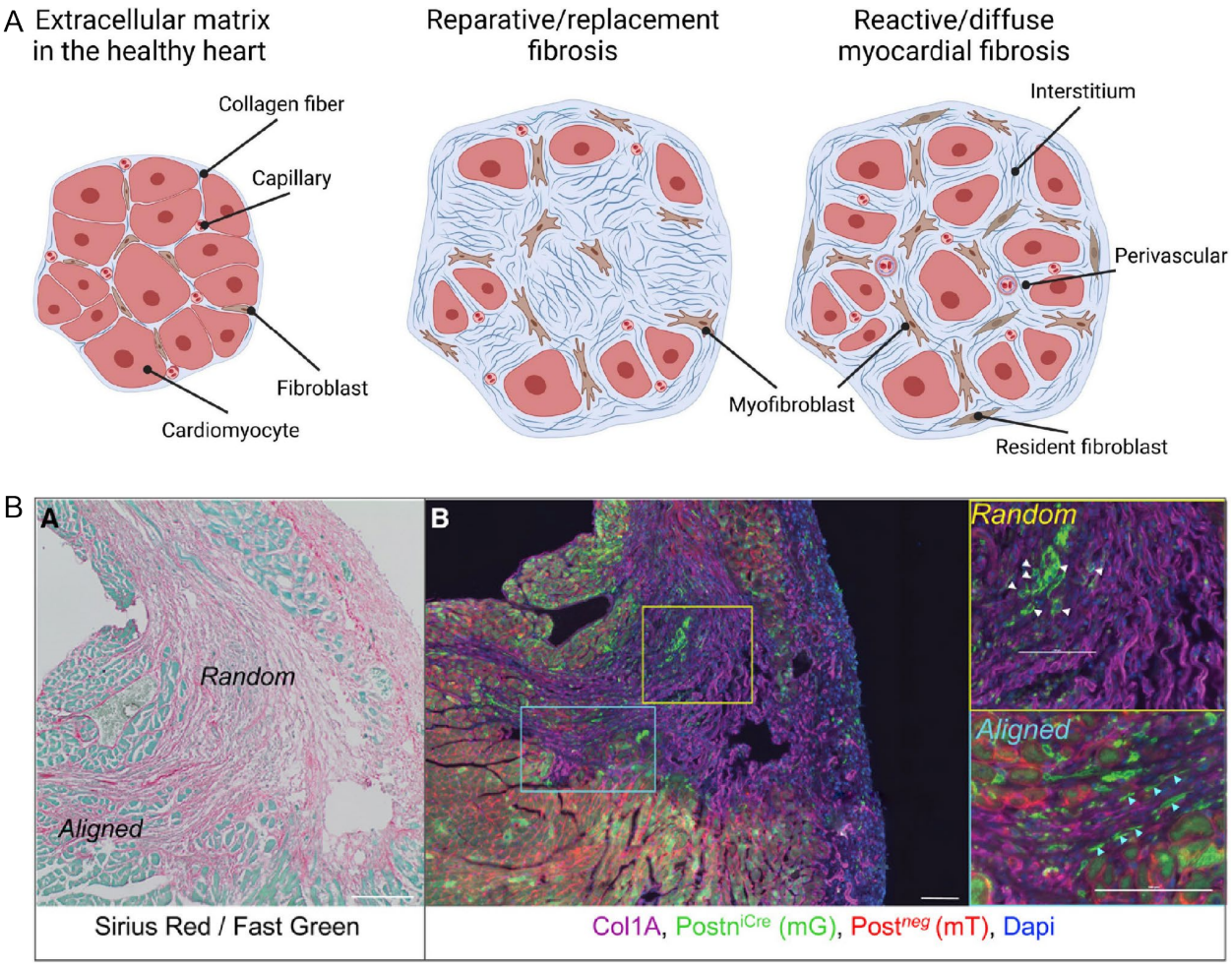

Figure 2.2: Alterations to the myocardial ECM in fibrotic disease. A) Schematic showing the changes that occur in myocardial tissues containing replacement fibrosis or reactive or interstitial fibrosis. Image reproduced from (Schimmel et al. 2022). B) Immunofluorescent images of infarcted mouse heart sections. Image reproduced from (Bugg et al. 2020).

2.1.3.2 Interstitial fibrosis in chronic cardiac disease

Fibrosis throughout the myocardium is also a hallmark of various forms of cardiomyopathy, including hypertrophic and dilated cardiomyopathies (Nakamura and Sadoshima 2018; Schultheiss et al. 2019). However, the precise causes of such fibrosis are still debated and may vary in etiology across different forms of cardiomyopathy. In hypertrophic cardiomyopathies (HCM), it is suggested that first, premature CM death caused by increased mechanical stresses

induced by genetic mutations and then later, microvessel obstruction and tissue ischemia may trigger fibrotic signaling pathways. Similarly, in dilated cardiomyopathies (DCM), increased cardiac workload and stress caused by overall tissue dysfunction and volume overload leads to tissue damage and fibrotic signaling. In both cases, increases in collagen I are typical at early stages of disease progression in the form of both replacement fibrosis filling in regions where CM death is prominent and interstitial fibrosis throughout other regions of the tissue (Ho et al. 2010; Marijianowski et al. 1995; Karl T. Weber et al. 2012; Yoshikane et al. 1992).

More specifically, interstitial fibrosis manifests as collagen networks become thicker and stiffer in both the endomysium between individual CMs and the perimysium around bundles of CMs (González et al. 2024). The response of fibroblasts, myofibroblasts and cardiomyocytes to these significant change in tissue mechanics caused by increased collagen accumulation likely contributes in various ways to continued pro-fibrotic signaling in HCM, DCM, and other forms of cardiomyopathy (González et al. 2024; Maesen et al. 2022). In this thesis, we utilize engineered biomaterial platforms to recapitulate changes in architecture and mechanics that occur throughout various disease states to further elucidate how cells respond to these aberrant biophysical signals.

2.2 Engineered in vitro systems to model the cardiac microenvironment

2.2.1 In vitro platforms for studying cardiomyocyte interactions with their mechanical environment

Recent advances in induced pluripotent stem cell (iPSC) technology have made it possible to develop patient-specific *in vitro* models of myocardial tissue for studying tissue development, regeneration, and pathogenesis (Campostrini et al. 2021; Tenreiro et al. 2021). These engineered

heart tissues (EHTs) typically consist of iPSC-derived CMs (iPSC-CMs) integrated with engineered biomaterial substrates or scaffolds. Given the high degree of organization to the myocardium, a number of established engineered platforms seek to drive the anisotropic assembly of CM syncytia *in vitro* by recapitulating various aspects of the myocardial ECM.

While traditional plastic or glass substrates are the simplest and most widely used platforms for studying cardiac regeneration and disease *in vitro*, these platforms lack an anisotropic organizational cues and are orders of magnitude stiffer that the endomysial and perymisal collagen fibers that CMs adhere to in the native myocardium. As such, improved 2D culture platforms have been developed with the hopes of generating high throughput, accessible models of cardiac tissue that generate iPSC-CMs that are mature enough to accurately capture the biology of the native adult myocardium (Campostrini et al. 2021; Cho et al. 2022). First, a number of studies have examined the effect of matrix stiffness on CM behavior and cardiac fibroblast differentiation using 2D elastic hydrogel or elastomer surfaces such as polyacrylamide, hyaluronic acid, and polydimethylsiloxane (Herron et al. 2016; Herum et al. 2017; A. Kumar et al. 2019; A. J. S. Ribeiro et al. 2015; Tsan et al. 2021; Young et al. 2014; Young and Engler 2011). While these studies have helped to highlight the importance of ECM mechanics in iPSC-CM maturation and disease progression, these platforms lack fibrous topography and are mechanically isotropic, thus failing to mimic an important aspect of the cardiac ECM (Spinale et al. 2016). Other material platforms have been developed to recapitulate these cell-instructive fibrous and mechanical cues to drive structural and functional maturation of engineered cardiac tissue. ECM proteins can be micropatterned into anisotropic geometries (e.g. lines or rectangles) to organize attached CMs and improve tissue functionality, but these models still lack fibrous topography and control over matrix architecture (McCain et al. 2012; M. C. Ribeiro et al. 2015; Sheehy et al. 2017). Attempts to better

recapitulate cardiac ECM topography have included culturing CMs on nano-grooved substrates and electrospun scaffolds. While these methods promote robust structural alignment and higher tissue maturity, they lack mechanical tunability, preventing the study of how CMs might respond to changes in matrix stiffness during disease progression (Allen et al. 2019; Carson et al. 2016; Fleischer et al. 2015; Khan et al. 2015; Kharaziha et al. 2013; Luna et al. 2011; Wanjare et al. 2017; Yu et al. 2014).

Three dimensional EHTs have also been widely used to study cardiac disease and are often composed of CMs encapsulated in natural materials (eg. collagen and/or fibrin) suspended between two deformable cantilevers (Bliley et al. 2021; Boudou et al. 2012; Legant et al. 2009; Leonard et al. 2018; Ronaldson-Bouchard et al. 2018; E. Y. Wang et al. 2019) or self-assembled spheroids (Beauchamp et al. 2020; Figtree et al. 2017; Giacomelli et al. 2020; Polonchuk et al. 2017). In comparison to established 2D models, these systems have the advantage of better recapitulating the 3D organization of native tissue. Additionally, systems incorporating two flexible cantilevers afford control of tissue boundary constraints not possible in many 2D culture systems. However, in addition to a lack of orthogonal control over ECM architecture and mechanics, many of these systems require the inclusion of stromal cells to compact and form properly which hinders our ability to directly connect the impact of microenvironment cues on CM function and structure. Recent work from multiple groups has explored how to incorporate alignment cues into 3D EHTs by bioprinting anisotropic tissue building blocks (J. Ahrens et al. 2022). By extruding these tissue microbundles through a small print head, the tissues align in the direction of printing enabling precise control of tissue scale anisotropy. Similarly, other groups have explored the impact of including prefabricated 5-10 μm diameter gelatin fibers into a bulk hydrogel to provide controlled contact guidance cues for CMs to spread along (S. Choi et al. 2023). Shear-induced alignment of

these fibers during bioprinting was shown to facilitate anisotropic assembly of CMs. Taken together, each engineered platform has advantages and disadvantages; as the model becomes more complicated, tissue becomes harder to fabricate, potentially limiting their translatability (**Figure 2.3**). Therefore, it is important to choose the model system that is best suited for the specific question you would like to answer. Further discussion on how each of these platforms can be leveraged to mature engineered heart tissues is included in Chapter 3 of this thesis.

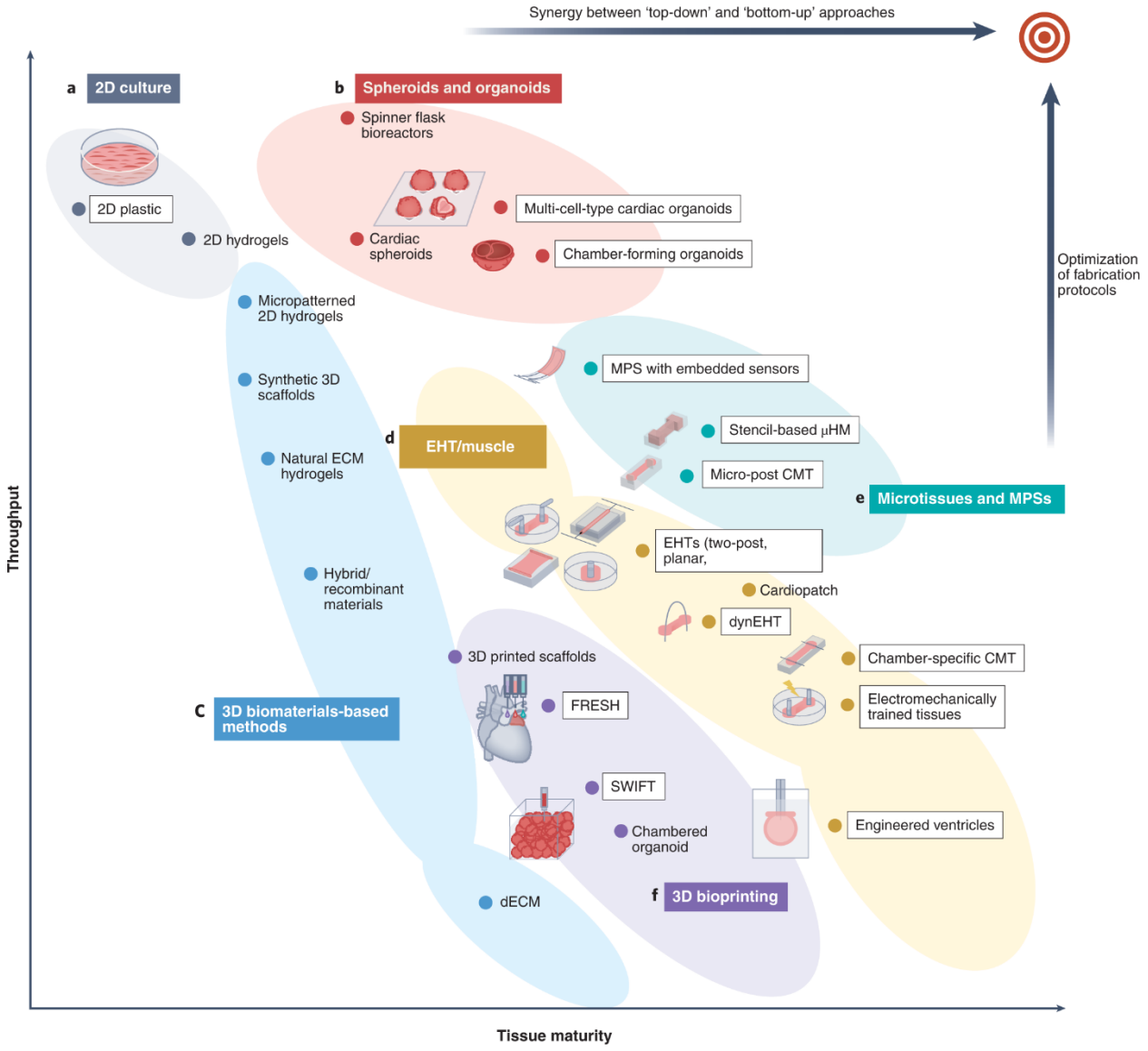

Figure 2.3: Types of in vitro models organized to show the tradeoffs between tissue maturity and throughput. Generally, more simple tissues are higher throughput but less mature while more complex tissues are more mature but harder to manufacture. Image reproduced from (Cho et al. 2022).

2.2.2 Techniques to promote the maturation of iPSC-CM models

Despite various techniques to generate functional *in vitro* myocardial tissue models, iPSC-CMs remain immature compared to the adult CMs, limiting the utility of these platforms for

disease models, drug screening, and engineered tissue replacement therapies (Y. Guo and Pu 2020; Karbassi et al. 2020). To induce maturation, extensive work has examined how exposing iPSC-CMs respond to biophysical stimuli such as electrical stimulation or metabolic maturation media supplements (**Figure 2.4**) (Karbassi et al. 2020). As these maturation techniques are described in depth in Chapter 3 of this dissertation, the most prominent iPSC-CM maturation strategies are summarized here.

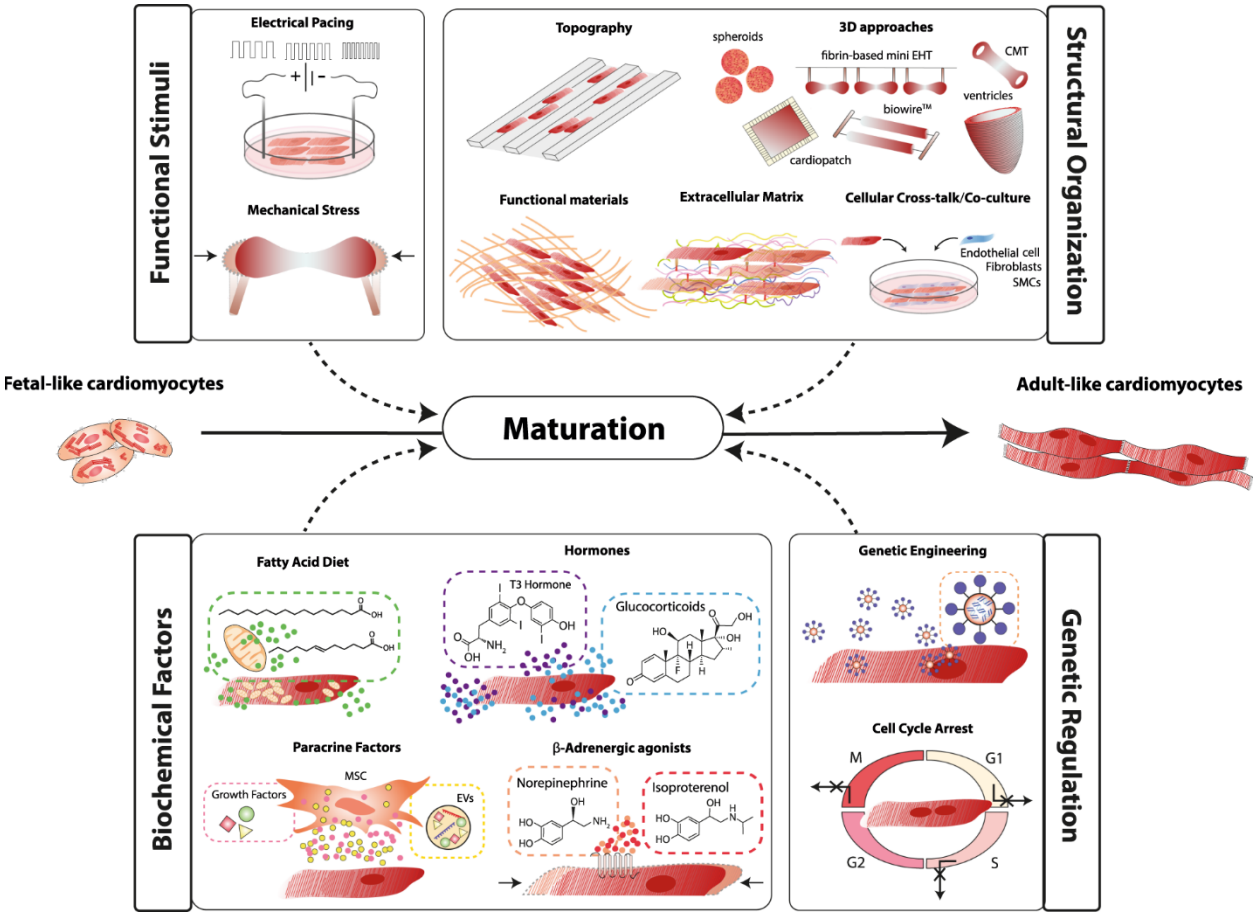

Figure 2.4: Engineering strategies for maturing iPSC-CMs. Application of maturation techniques can induce more mature phenotypes in iPSC-CM *in vitro* cultures. Image reproduced from (Tenreiro et al. 2021).

The most common strategies for maturing iPSC-CMs typically involve recapitulating the biophysical properties of the cardiac microenvironment. In 2D cultures, a number of studies have explored how culturing iPSC-CMs on hydrogels of varying stiffness, with moduli mimicking fetal cardiac tissue (~1 kPa), adult healthy tissue (8-10 kPa) and diseased tissue (>15 kPa) (McCain et al. 2012; A. J. S. Ribeiro et al. 2015; Tsan et al. 2021). Taken together, these studies support the claim that iPSC-CMs cultured on hydrogels with a stiffness closest to the elastic modulus of adult myocardial tissue results in the most contractile and functionally mature iPSC-CMs (Corbin et al. 2019; McCain et al. 2012; A. J. S. Ribeiro et al. 2015; Tsan et al. 2021). In contrast, iPSC-CMs plated on hydrogels with stiffnesses reflecting diseased tissue can lead to aberrant mechanical function and arrythmias (A. J. S. Ribeiro et al. 2015). Mechanical properties of the tissue can also be modulated in 3D tissue systems where tissues are suspended between two elastic cantilevers (Boudou et al. 2012; Leonard et al. 2018; Ronaldson-Bouchard et al. 2018). As tissues assemble and mature, they will adapt to contract against stiffer cantilevers until the stiffness of the boundary approaches the mechanics of diseased tissue (Leonard et al. 2018). Further, dynamic mechanical stimulation has also been applied to these systems to induced mechanical maturation of iPSC-CMs (Bliley et al. 2021; Ruan et al. 2015, 2016). Alignment of iPSC-CMs can also be controlled on 2D culture substrates by either micropatterning ECM proteins, creating surfaces with nanogrooves, or collecting electrospun fibers on glass slides (Allen et al. 2019; Carson et al. 2016). Anisotropic assembly of single iPSC-CMs and multicellular tissues gives rise to more mature and contractile iPSC-CMs compared to disorganized iPSC-CMs (Carson et al. 2016; A. J. S. Ribeiro et al. 2015; Tsan et al. 2021). As mentioned previously, translating tunable mechanical and topographical cues to 3D settings remains a challenge, as most 3D EHTs are formed using natural biomaterials such as collagen or fibrin (Boudou et al. 2012; Ronaldson-Bouchard et al. 2018). These materials are

rapidly remodeled by constituent cells and furthermore have limited orthogonal tunability in terms of key properties including ECM mechanics, porosity, and adhesive ligand density.

Electrical pacing has been applied to 2D and 3D EHT models and has shown great promise for maturing iPSC-CMs (Ronaldson-Bouchard et al. 2018; Shen et al. 2022; Y. Zhao et al. 2019). By starting electrical pacing early in the differentiation process and gradually ramping up the frequency of pacing, Ronaldson-Bouchard and colleagues show high levels of structural and functional maturation, including the formation or T-tubules (Ronaldson-Bouchard et al. 2018). Metabolic maturation has also shown promise as a versatile maturation technique, as various media formulations have been developed aimed at encouraging fatty acid metabolism (Correia et al. 2017; Feyen et al. 2020; X. Yang et al. 2019). Compared to traditionally used EHT culture media better mimics the metabolic state of the fetal heart, culturing tissues in metabolic medias that promote adult-like cardiac metabolism have demonstrated improvements in CM energy handling as well as structural maturation (Campostrini et al. 2021).

Finally, there have been many studies exploring how co-culture of iPSC-CMs with other cell types in EHTs impacts CM maturation (Campostrini et al. 2021; Karbassi et al. 2020). Work from Giacomelli and colleagues explored how the presence of endothelial cells and fibroblast of various origin impacted iPSC-CM in scaffold-free organoid models (Giacomelli et al. 2020). They found that the presence of endothelial cells and primary cardiac fibroblasts resulted in the most structurally, functionally, and metabolically mature tissues. Additionally, the inclusion of other cell types such as epicardial cells have also been shown to induce more mature tissue phenotypes and improve engraftment of iPSC-CMs *in vivo* (Bargehr et al. 2019).

2.2.3 Applications of in vitro iPSC-CM engineered heart tissues

In part due to many recent advances in iPSC-CM maturation described above, *in vitro* models of myocardial tissues have shown great utility in several applications. First, EHTs can be used to model various types of cardiac diseases *in vitro*, enabling gene- and patient-specific investigation of disease mechanisms and assessing the efficacy of gene editing strategies for correcting HCMs (Cho et al. 2022; Tenreiro et al. 2021). Tissues generated from iPSC-CMs derived from patients with genetic cardiomyopathies have been utilized to explore how specific genetic mutations impact tissue function. For example, iPSC-CM models harboring mutations in a number of cardiac myosins have helped elucidate how these mutations can drive aspects of HCM (Roest et al. 2021). Other studies have examined the impact of junctional protein mutations such as in plakophilin or desmoplakin on the manifestation of arrhythmogenic cardiomyopathies or DCM as a function of iPSC-CM maturation (Bliley et al. 2021; Simmons et al. 2024; K. Zhang et al. 2021). For example, Bliley and colleagues generated tissues from iPSC-CMs containing a mutation in desmoplakin, which has been associated with dilated and arrhythmogenic cardiomyopathies (Bliley, Vermeer, et al. 2021). They showed that pathological phenotypes associated with mutations in this protein were only present in more mature 3D tissues under dynamic mechanical loads, whereas unloaded 3D tissues and iPSC-CMs plated on 2D substrates did not reveal phenotypic differences compared to healthy control CMs (Bliley, Vermeer, et al. 2021). Additionally, *in vitro* models can be exposed to other pathological signals such as ischemia by removing oxygen and nutrients from the culture media to examine the iPSC-CM response (Davis et al. 2021; Yadid et al. 2020). There have also been models established to better understand fibrotic progression, including 3D models incorporating fibroblasts at supraphysiologic ratios in 3D cardiac microtissues as well as simpler, 2D co-culture platforms for studying fibroblast and CM communication (Herum et al. 2017; E. Y. Wang et al. 2019).

EHT platforms also have also shown significant potential to be used as platforms to efficiently screen the efficacy of cardiac targeting drugs or alternatively, potential cardiotoxicity. As many drug candidates fail late in clinical trials due to previously unidentified cardiotoxic effects, many regulatory groups including the FDA have taken great interest in *in vitro* assays that can more accurately identify these potential side effects earlier on in the drug discovery process (Colatsky et al. 2016). Various types of *in vitro* cardiac models have been utilized for these purposes including simpler 2D, high throughput assays and more complex 3D tissue culture systems (Block et al. 2020; Conant et al. 2017; Correia et al. 2017; Richards et al. 2020; Tenreiro et al. 2021). Continued work in this space is needed however to generate tissue that are mature enough to accurately recapitulate the response of adult CMs to therapeutics (Correia et al. 2017; Karbassi et al. 2020).

Finally, EHT constructs are also being developed for use as regenerative therapies. The myocardium lacks the ability to self-regenerate after traumatic injury such as a myocardial infarction and current therapeutic interventions are only effective at slowing further progression of the injury and cardiac fibrosis . Thus, many groups have explored methods to engineer myocardial tissue implants that could effectively integrate with the host to replace scarred tissue and restore muscle function (Jianyi Zhang et al. 2018). Early attempts at injecting suspended iPSC-CMs or small aggregates of iPSC-CMs into injured hearts demonstrated limited success, as they failed to integrate properly and lead to arrythmias (Liu et al. 2018). This has led many groups to postulate that iPSC-CMs may require some scaffolding that guides tissue assembly and maturation prior to implantation (Eschenhagen and Weinberger 2024; Hashimoto, Olson, and Bassel-Duby 2018). Such studies have shown promising results, restoring to some degree the functionality of

myocardial tissue after injury in small animal models and even non-human primates (Kobayashi et al. 2024; Liu et al. 2018; Querdel et al. 2021; Stüdemann et al. 2022).

Despite significant progress in developing mature EHTs that can be applied in the various applications described above, iPSC-CMs remain closer to fetal CMs than adult CMs by many structural, contractile, metabolic, and electrophysiological measures (Karbassi et al. 2020). Additionally, we still lack a precise understanding of how to best assemble iPSC-CMs into multicellular syncytial structures in a way that accurately mimics the structure of the native myocardium. Thus, in this thesis we focus on developing controlled biomaterial systems that can be used to understand how iPSC-CM mechanobiology impacts tissue assembly and maturation processes towards informing the more intelligent design of EHTs for both *in vitro* tissue models and regenerative therapies.

2.3 Mechanosensing in the myocardium

2.3.1 Cellular mechanosensing mechanisms

Cellular mechanosensing is a critical biological process through which cells detect and respond to mechanical stimuli from their environment. This allows cells to adapt to physical changes, such as alterations in tissue stiffness, shear stress from fluid flow, and mechanical loading (Kim et al. 2021). Mechanosensing mechanisms are essential for a variety of cellular functions, including proliferation, differentiation, and tissue morphogenesis (Ahmed et al. 2023; Kim et al. 2021; Lutolf and Hubbell 2005; L. R. Smith, Cho, and Discher 2018). In the heart, cellular mechanosensing plays a vital role in both healthy tissue function and adaptation to pathophysiological conditions (Gaetani et al. 2020). Various cell types in the myocardium

including CMs, fibroblasts, and endothelial cells are continuously subjected to mechanical forces due to the cyclic contraction and relaxation of the heart and must therefore sense and respond appropriately to these dynamic forces to maintain cardiac homeostasis and support effective pumping action (Gaetani et al. 2020; Jacot, Martin, and Hunt 2010; Lyon et al. 2015; Schroer and Merryman 2015).

Focal adhesions and cell-cell junctions are principal sites of mechanosensing in the heart, allowing resident cells such as CMs to interpret and respond to the mechanical properties of their environment (Danowski et al. 1992; Delmar and McKenna 2010; Nielsen et al. 2023; Samarel 2005). Focal adhesions are multi-protein complexes that serve as the physical link between the ECM and the cellular cytoskeleton (Bershadsky, Balaban, and Geiger 2003; Kanchanawong and Calderwood 2022; Parsons, Horwitz, and Schwartz 2010). At these sites, cells sense physical cues such as stiffness, strain, and pressure, which are integral for modulating cell behavior. In cardiac tissue, specialized focal adhesion known as costameres link the myofibril directly to the ECM, facilitating efficient force transfer to the surrounding tissue (Pardo, D'Angelo Siliciano, and Craig 1983b, 1983a; Samarel 2005).

In addition to directly interacting with the ECM, CMs are mechanically linked through specialized cell-cell junctions complexes known as intercalated discs, which contain gap junctions, desmosomes, and adherens junctions (Nielsen et al. 2023; Rampazzo et al. 2014). Adherens junctions, mediated by cadherin proteins, particularly N-cadherin, are crucial for transmitting contractile forces across the myocardium by anchoring the actin cytoskeleton of one cell to its neighbor (Zuppinger, Eppenberger-Eberhardt, and Eppenberger 2000). Together, mechanosensing at focal adhesions and cell-cell junctions is crucial for maintaining tissue integrity, orchestrating

collective tissue function, and enabling the conversion of mechanical information into biological signals in both cardiac development and disease.

2.3.2 Cardiomyocyte mechanosensing in myofibril assembly and tissue development

Mechanosensing in cardiac development is a fundamental aspect of how the heart forms and matures (Haack and Abdelilah-Seyfried 2016; Jacot, Martin, and Hunt 2010; J. Wang et al. 2018). During embryogenesis, the heart is one of the first organs to begin functioning, and its development is closely tied to both external and internally generated mechanical forces (Granados-Riveron and Brook 2012; Mandrycky et al. 2020). As the heart begins to beat, the cells within the developing heart muscle tissue are exposed to hemodynamic forces, including shear stress and cyclic mechanical stretch (Bornhorst et al. 2019; Fukuda et al. 2019; Hove et al. 2003; Y. F. Lin, Swinburne, and Yelon 2012). These mechanical cues are crucial for the proper alignment and organization of cardiac cells and their eventual differentiation into mature cardiomyocytes.

At the cellular level, mechanosensing is critical to myofibril assembly within these developing cardiomyocytes (Sparrow and Schöck 2009). The assembly of myofibrils is a highly orchestrated event where premyofibrils form initially, emanating from nascent cell-ECM adhesion site termed protocostameres (Chopra et al. 2018; Fenix et al. 2018; Taneja, Neininger, and Burnette 2020). These myofibrils subsequently will mature into fully functional myofibrils capable of generating contractile force. This maturation process is influenced by the mechanical load encountered by the cells (Fukuda et al. 2019; Y. Guo et al. 2021). Mechanosensitive proteins, such as titin and talin, are thought to act as molecular rulers that maintain sarcomere integrity and contribute to the spatial organization of myofilaments (Chopra et al. 2018; Pandey et al. 2018).

Changes in the mechanical environment during tissue development and morphogenesis can lead to abnormal heart development (Bornhorst et al. 2019; Y. F. Lin, Swinburne, and Yelon 2012).

Disruptions in mechanosensing mechanisms can impede myofibril assembly and lead to congenital heart defects and cardiomyopathies. For example, disruptions in vinculin expression during early development results in significant heart defects (Hawley et al. 2020; W. Xu, Baribault, and Adamson 1998). Precise mechanosensitive signaling pathways orchestrate a multitude of gene expression changes and cellular behaviors in response to these mechanical forces, ensuring that emerging cardiomyocytes align, elongate, and organize into a functional syncytium capable of coordinated contraction (Fukuda et al. 2019; Kidokoro et al. 2018; Priya et al. 2020). Thus, understanding the molecular mechanics of myofibril assembly has critical implications for congenital heart disease diagnosis and therapy, in addition to the design of *in vitro* models of for studying CM maturation (Hofbauer, Jahnel, and Mendjan 2021; Ottaviani et al. 2023).

2.3.3 Cardiomyocyte mechanosensing in disease

Mechanosensing in cardiac disease is a critical area of investigation, as the heart's ability to respond to mechanical stresses is fundamental to its adaptation during various pathologies (Gaetani et al. 2020; Knöll, Hoshijima, and Chien 2003). In diseases such as hypertension, myocardial infarction, and cardiomyopathy, changes in the mechanical environment of the heart, such as increased pressure, volume overload, or injury to the myocardial tissue, can lead to maladaptive cardiac remodeling (Frangogiannis 2017; González et al. 2018; Nakamura and Sadoshima 2018). This remodeling often results in altered cell signaling and excessive synthesis of ECM proteins, contributing to detrimental changes in myocardial structure and function.

In hypertrophic cardiomyopathy, for example, disrupted mechanical function of the tissue resulting from genetic mutations results in altered mechanosensing that initiates CM growth in response to the increased strain (Heineke and Molkentin 2006; Nakamura and Sadoshima 2018). Chronically elevated mechanical stress can ultimately lead to fibrosis and heart failure due to

stiffening of the cardiac tissue, disturbance in electrical signaling, and impaired contractility (Kong, Christia, and Frangogiannis 2014; Nakamura and Sadoshima 2018). Mechanosensitive pathways, including those involving the angiotensin II type 1 receptor, the Hippo pathway, and various integrin-linked signaling cascades are implicated in these disease processes (J. Wang et al. 2018). Activation of these pathways can lead to changes in CM function and survival, as well as stimulation of cardiac fibroblasts to produce extracellular matrix proteins, contributing to the fibrotic response (Frangogiannis 2014, 2017; K T Weber 2000).

Mechanosensing also plays a crucial role in the heart's response to myocardial infarction (Talman and Ruskoaho 2016). Post-injury, the necrotic loss of CMs and the subsequent scarring leads to a mechanical mismatch in the myocardium, disturbing the normal distribution of forces across the heart (Herum et al. 2017; Yamada et al. 2022). In trying to compensate for the lost contractile function, the mechanosensitive pathways in the surviving myocardium become overactive, often leading to further pathological changes rather than restoration of normal cardiac function (Talman and Ruskoaho 2016). Targeting the dysregulated mechanotransduction that underlies these adaptations holds therapeutic potential. For example, therapies aimed at reducing mechanical stress on the heart, such as with the use of ventricular assist devices or pharmacological interventions like beta-blockers, have been shown to mitigate some of these maladaptive responses and improve clinical outcomes for heart disease patients (Goldsmith et al. 2014; S. Park et al. 2019). Understanding the mechanisms of cardiac mechanosensing could therefore lead to more refined strategies to prevent the progression of heart disease and promote cardiac repair and regeneration.

As mechanosensing pathways and ECM remodeling play a critical role in the cardiac function from development to disease, developing model systems that facilitate careful

examination of these mechanosensing pathway is critical for understanding cardiac function engineering tissues that accurately recapitulate native myocardial function. The following thesis chapters focus on utilizing fibrous biomaterial systems that support the study of CM maturation (Chapters 4-5) and fibrotic disease progression (Chapter 6). Prior to those discussions, we dig deeper into the many *in vitro* model systems previously developed in the field to study CM maturation and model disease (Chapter 3). Lastly, Chapter 7 will provide a summary of the main findings of the work presented and future directions of how to leverage mechanically tunable biomaterial systems towards improved iPSC-CM maturation, disease models, and translatable therapies.

Chapter 3: Induced Pluripotent Stem Cell-Derived Cardiomyocyte *in vitro* Models: Benchmarking Progress and Ongoing Challenges

3.1 Authors

Samuel J. DePalma[‡], Jourdan K. Ewoldt[‡], Maggie E. Jewett, M. Cağatay Karakan, Yih-Mei Lin, Paria Mir Hashemian, Xining Gao, Lihua Lou, Micheal McLellan, Jonathan Tabares, Marshall Ma, Adriana C. Salazar Coariti[1], Jin He, Kimani C. Toussaint, Jr., Thomas G. Bifano, Sharan Ramaswamy, Alice E. White, Arvind Agarwal, Emma Lejeune, Brendon M. Baker[*], Christopher S. Chen[*]

3.2 Abstract

The advent of human induced pluripotent stem cells (hiPSCs) and techniques to differentiate cardiomyocytes from these cells has unlocked a viable path to creating *in vitro* models of normal and diseased heart, accelerating more predictive drug screening and therapeutic strategies for cardiac pathologies. Currently, hiPSC-derived cardiomyocytes (hiPSC-CMs) are more similar to fetal than adult cardiomyocytes, leading many in the field to explore approaches to enhance cell and tissue maturation. There are over 2,000 studies utilizing hiPSC-CMs in models composed of various combinations of cell and extracellular matrix components, using a plethora of differentiation protocols, culture formats, and methods for quantifying cardiomyocyte function.

To assess the current state of this rapidly growing area, we systematically analyzed 300 studies using hiPSC-CM models for their selection of hiPSC lines, hiPSC-CM differentiation protocols, types of in vitro models, maturation techniques, and metrics used to assess cardiomyocyte functionality and maturity, and compiled the data into an open access database. Based on this analysis, here we present the diversity of, and current trends in, in vitro model designs and highlight the most common and promising practices for functional assessments. We further analyzed outputs spanning structural maturity, contractile function, electrophysiology, and gene expression and note field-wide improvements over time. Finally, we observe that a persistent lack of coordination amongst investigators is limiting the field's ability to benchmark and advance hiPSC-CM function against previous studies. We discuss opportunities to collectively pursue the common goal of hiPSC-CM model development, maturation, and assessment that we believe are critical to drive the entire community forward in engineering mature cardiac tissue.

3.3 Introduction

3.3.1 Utility of hiPSC-cardiomyocyte models

The average cost to bring a new pharmaceutical to the market in the United States is estimated at more than one billion dollars, with many drugs costing greater than two billion dollars to develop (Wouters, McKee, and Luyten 2020). About 11% of pharmaceuticals worldwide have been withdrawn due to adverse cardiovascular side effects, wasting significant resources (Kocadal 2018; Varga et al. 2015). This high failure rate is in part due to the relative difficulty in predicting which drugs will have adverse cardiac effects: primary human cardiomyocytes (CMs) are difficult to obtain and rapidly dedifferentiate *in vitro*, rendering them incapable of faithfully detecting anything but the most acute effects of candidate pharmaceuticals on the heart (Bird et al. 2003).

On the other hand, while animal studies can reveal cardiotoxic and arrhythmogenic activity of pharmaceuticals, there are key differences in cardiac biology between animal models and humans that limit their ability to fully predict the potential for adverse cardiovascular effects in humans (Lelovas, Kostomitsopoulos, and Xanthos 2014; Milani-Nejad and Janssen 2014).

The advent of the first differentiation protocol of human embryonic stem cells (hESCs) into cardiomyocytes in 1993 enabled researchers to study human cardiomyocytes *in vitro* in ways not possible with primary CMs[7]. In 2007, the first human induced pluripotent stem cells (hiPSCs) were generated. Derived from skin or blood cells and reprogrammed into a pluripotent state, these cells can be patient-derived and of any genetic background, and similarly can be differentiated into cardiomyocytes without the ethical challenges associated with sourcing hESCs (Takahashi et al. 2007). This approach, which enables patient-specific *in vitro* models of cardiac tissue and allows for the testing of cardiovascular effects of pharmaceuticals in a more physiologically relevant model, has thus been adopted by regulatory safety committees (Colatsky et al. 2016).

The use of hiPSC technology to generate human cardiomyocytes has also dramatically increased opportunities to study the physiology and pathobiology of the human heart. Inherited cardiomyopathies, such as hypertrophic, dilated, and arrhythmogenic cardiomyopathies, affect 1/500, 1/250, and 1/2,000-5,000 of the population, respectively (McKenna and Judge 2021). There are over 100 genes housing mutations that have been implicated in various cardiomyopathies (McNally, Barefield, and Puckelwartz 2015), with over 1,000 possible mutations across these genes known to cause disease (Haas et al. 2015; Ho et al. 2018; Lippi et al. 2022). Patient-derived hiPSC-CM models of genetic cardiomyopathies and CRISPR/Cas9 edited hiPSC-CMs have thus been used to recapitulate disease *in vitro*, to shed light on new disease mechanisms, and to establish the promise for gene-editing strategies to correct these diseases (Bhagwan et al. 2019; Briganti et

al. 2020; Cohn et al. 2019; Hinson et al. 2015; Knight et al. 2021; Loiben et al. 2023; Mosqueira et al. 2018; Nishiga et al. 2022; Prondzynski et al. 2019; Toepfer et al. 2020; K. Zhang et al. 2021). Additionally, hiPSC-CMs show promise as regenerative therapies for patients with heart failure (Karbassi et al. 2020; Liu et al. 2018; Querdel et al. 2021).

However, despite all the promise associated with hiPSC-CMs, the overall immaturity of hiPSC-CMs leads to significant limitations in their utility. Fetal-like gene expression patterns, immature structure and function of tissues created from these cells, and non- or sub-physiologic electromechanical activity are all significant caveats to the conclusions drawn from studies using these cells to test pharmaceuticals or model disease states and are major hurdles for using these cells in regenerative or reparative therapies.

3.3.2 Immaturity of hiPSC-cardiomyocyte models

While the use of hiPSC-CMs has been widely adopted in recent years, hiPSC-CMs remain immature relative to adult human cardiomyocytes, possessing a more fetal-like phenotype[25]. Immature hiPSC-CMs typically contain disorganized myofibrils, fewer mitochondria, and poor co-localization of calcium channels and ryanodine receptors that ultimately impair the functionality of hiPSC-CMs as compared to adult cardiomyocytes (**Table 3.1**) (Karbassi et al. 2020). Additionally, engineered cardiomyocytes mainly rely on glycolysis for energy, rather than more efficient energy production from oxidative phosphorylation utilized by adult cardiomyocytes.

Benchmarking parameters and corresponding values of adult cardiomyocyte/tissue	
Structural Organization	• Rod-shaped with aligned, developed myofibrils • Binucleated (Olivetti et al. 1996) • Sarcomere length: ~ 2.0 – 2.2 μm (Martin Gerdes et al. 1992; Squire 1997) • Cardiomyocyte surface area: ~ 10,000-14,000 μm^2 (Feric and Radisic 2016) • T-tubules present • Mitochondria localized near sarcomere (Porter et al. 2011) • Expression of adult ventricular CM-specific structural genes (i.e. *MYH7*, *MYL2*, *TNNI3*, etc.)
Mechanical Properties	• Tissue elastic modulus ~10 – 50 kPa (Nagueh et al. 2004)
Force	• Contractile stress: ~ 30 – 60 mN/mm^2 (Hasenfuss et al. 1990; Van Der Velden et al. 1999) • Positive force-frequency ratio
Electrophysiology	• Low to zero spontaneous contractions (Karbassi et al. 2020; Tenreiro et al. 2021) • Characteristic notch at peak (Feric and Radisic 2016) • Resting membrane potential: ~ -90 mV (Drouin et al. 1995) • Action potential amplitude: ~ 100-110 mV (Koncz et al. 2011) • Action potential duration: ~ 230-300 ms (Dangman et al. 1982) • Depolarization velocity: ~ 250- 300 V/s (Koncz et al. 2011) • Conduction velocity: ~ 30-100 cm/s (X. Yang, Pabon, and Murry 2014)

Calcium Conduction	• Cytosolic Ca^{2+} concentration (Carafoli et al. 2001):
	  ○ Resting ~100 nM
	  ○ Post SR calcium release ~1 μM
	• Mature sarcoplasmic reticulum function
	• Increased gene expression of calcium handling machinery *CACNA1C*, *SCN5A*, *KCND3*, *KCNJ2*, *SLC8A*, *ATP2A2*, *CASQ2*, *RYR2*, *GJA1*, *PLN*
	• Robust organization of calcium handling machinery

Metabolic Maturity	• Reliant mainly on fatty acid oxidation

Table 3.1: Adult cardiomyocyte benchmarking parameters and values.

Functionally, human adult cardiomyocytes exhibit a resting membrane potential and conduction velocity of approximately -90 mV and 30-100 cm/s (X. Yang, Pabon, and Murry 2014), respectively, while very few hiPSC-CM models have shown a resting membrane potential below -80 mV (Feyen et al. 2020; Herron et al. 2016; B. Lin et al. 2017; Querdel et al. 2021; Tsan et al. 2021) or a conduction velocity above 40 cm/s (Herron et al. 2016; Miki et al. 2021; Querdel et al. 2021). Additionally, the twitch force of adult human cardiomyocytes is 25-44 mN/mm^2 (Mulieri et al. 1992), and only a few recent hiPSC-CM engineered constructs have reached this level of contractility (Knight et al. 2021; Melby et al. 2021).

In the past decade, there have been great strides made toward understanding how to further mature hiPSC-CMs by combining knowledge from diverse fields including developmental biology, materials science, and biomedical engineering (Cho et al. 2022). In achieving these advances, researchers have used a vast array of cell lines, differentiation protocols, maturation techniques, and functional tissue assessments, making it challenging for the field to make head-to-head comparisons between studies and laboratories. Consequently, there is no consensus on which differentiation protocols or culture formats are most promising and should be employed going forward. As the field of cardiac tissue engineering itself matures, standardized benchmarking across the field will be essential to extracting key findings and applying them toward future advances.

To assess the current state of the art, we sought to systematically analyze a breadth of studies utilizing hiPSC-CMs by extracting information such as differentiation protocols, culture platforms, maturation techniques, and functional assessment metrics. In synthesizing the key findings from these analyses, here we provide guidance on best practices for generating and

assessing the maturity of hiPSC-CMs with the goal of fostering a transparent discussion toward convergence amongst the community as we progress toward engineering functional, adult-like hiPSC-CMs.

3.4 Methodology

Across over 2,000 studies utilizing hiPSC-CMs from 2016-2022, there exists high variability in differentiation protocols, maturation strategies, and assessment of cell or tissue functionality. To understand the nature of this variability, we systematically analyzed 300 studies using hiPSC-CM models and compiled data on hiPSC lines, hiPSC-CM differentiation protocols, types of 2D and 3D *in vitro* models, maturation techniques, and metrics used to assess hiPSC-CM functionality and maturity. Using a PubMed search for "(((induced pluripotent stem cells) OR (iPSC)) AND ((cardiomyocyte) OR (cardiomyocytes) OR (iPSC-CM) OR (iPSC-CMs) OR (induced pluripotent stem cell-cardiomyocytes) OR (induced pluripotent stem cell-CMs))) AND ((engineered heart tissue) OR (cardiac microtissue) OR (maturation) OR (mature))" we identified 846 potential publications for analysis. We eliminated publications focusing on atrial differentiation due to relatively limited published work in this space, and focused our benchmarking on ventricular cardiomyocytes, which are of particular interest in the development of cardiac regenerative therapies (Cyganek et al. 2018; J. H. Lee et al. 2017). We also eliminated publications that were solely focused on disease modeling and/or mechanistic studies but included disease modeling publications in which maturation techniques (the primary focus of our analysis) were utilized in model development. To capture overall trends in the field, we focused on 300 publications. This included the top 100 cited publications from the 846 potential publications based on citation numbers reported by the Web of Science database as of 2022, 100 publications from

the PubMed 846 potential publications (that were not the 100 top-cited publications) selected randomly, and 100 additional hiPSC-CM publications that were manually selected from references in recent high impact reviews on cardiac tissue engineering or top search results for "iPSC-cardiomyocytes" on Google Scholar that utilized unique culture platforms, maturation techniques, and/or assessments.

After accumulating and analyzing data reported from these publications, we analyzed functional outputs in structural, contractile, calcium handling, electrophysiology, gene expression, and metabolic assessments to identify patterns in the effects of model parameters on cardiac maturation. Graphs depicting functional outputs show mean ± standard error of the mean (SEM) unless otherwise noted. Data were assessed with a one-way ANOVA that was corrected for multiple comparisons using a Tukey test with a 95% confidence level. All data used for these analyses can be found in Supplementary Table 3 (J. K. Ewoldt et al. 2023).

3.5 Current approaches to engineer hiPSC-CM *in vitro* models

3.5.1 hiPSC culture and differentiation

With the widespread adoption of hiPSC-CMs in the field of cardiac tissue engineering, more hiPSC lines are being generated and used in studies to capture global diversity and generate patient-specific models of cardiac diseases. The protocols for differentiating these cells into cardiomyocytes have also been continuously adapted and improved. Here, we compiled information on the most commonly used hiPSC lines and hiPSC-CM differentiation protocols within the field.

3.5.1.1 hiPSC lines

A major source of variability across studies is the choice of hiPSC lines and the number of lines employed in a given study. Over 200 different hiPSC-lines were used across the analyzed studies. Over two-thirds of these studies used only one healthy control hiPSC line, thus failing to assess how different hiPSC lines may influence study findings (**Figure 3.1a**). Less than 15% of analyzed studies used more than two hiPSC healthy control lines, while a single study examined 43 hiPSC lines (Burnett et al. 2019). Of the 15 most used hiPSC lines (**Figure 3.1b**), two-thirds have a female genetic background and only six have ancestral information available (**Table 3.2**). Four of these 15 lines are hiPSC lines that are commercially differentiated into cardiomyocytes by companies including FUJIFILM Cellular Dynamics, Inc., Axiogenesis, and Ncardia (**Figure 3.1b**). Of note, Cor.4U cardiomyocytes that are used in 5% of studies we analyzed were found to be derived from hESCs, rather than hiPSCs, which are the focus of this review (Lapp et al. 2021). The most frequently reported lines that are not commercially differentiated include WTC11, IMR-90, DF19-9-11T.H, PGP1, 253G1, Gibco episomal line, 201B7, BJ1, SCVI-273, C25, and ATCC, ordered by the number of publications in which they appear (**Figure 3.1b**).

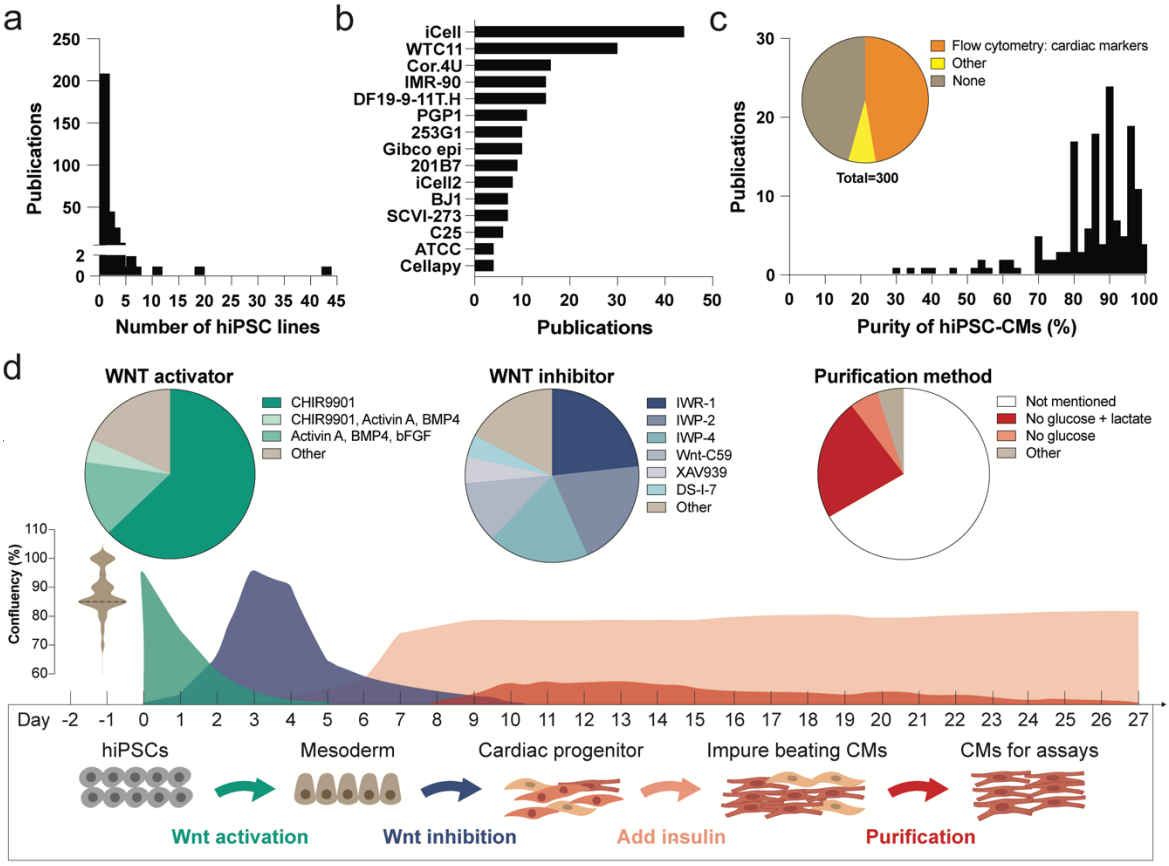

Figure 3.1: hiPSC culture and differentiation. a. Histogram of the number of control hiPSC lines publications reported using for hiPSC-CM differentiation. b. Top 15 reported hiPSC lines in the analyzed publications. c. Histogram of the reported purity of cardiomyocytes after hiPSC-CM differentiation. Inset: The reported methods of assessing the purity of cardiomyocytes after hiPSC-CM differentiation. d. Schematic of the variability in hiPSC-CM differentiation protocols. Confluency of hiPSCs is typically at ~80-90% at the start of differentiation (Day 0) (n = 108). There is variability in the time course of Wnt pathway activation (green) and inhibition (blue) in hiPSC-CM differentiation, along with when insulin is added to the media (pink) and the hiPSC-CM purification method (red). Pie charts represent the top reported Wnt pathway activators (n = 229), Wnt pathway inhibitors (n = 219), and purification methods (n = 300). n values represent the number of publications that utilized and reported on each differentiation component.

Cell Line	Biological Sex	Reported Ancestry
iCell	Female	Caucasian
WTC11	Male	Asian
Cor.4U	Female	Not listed
IMR-90	Female	Not listed
DF19-9-11T.H	Male	Not listed
PGP1	Male	Not listed
253G1	Female	Caucasian
Gibco epi	Female	Not listed
201B7	Female	Caucasian
BJ1	Male	Not listed
iCell2	Female	Caucasian
SCVI-273	Female	Asian
C25	Female	Not listed
ATCC	Male	Not listed
Cellapy	Female	Not listed

Table 3.2: Top 15 reported hiPSC lines and their biological sex and ancestry. Information was obtained from publication, references, or Cellosaurus.org.

It has been shown that the genetic background of hiPSC lines impacts the maintenance of hiPSC pluripotency (Schnabel et al. 2012) and influences transcriptional variation (Rouhani et al. 2014) that could ultimately impact the differentiation and function of derived hiPSC-CMs

(Mannhardt et al. 2020). The utilization of hiPSCs from diverse genetic backgrounds is crucial to the creation of hiPSC-CM *in vitro* models that accurately represent the global population.

3.5.1.2 hiPSC differentiation to cardiomyocytes

The hiPSC culture medium can also influence the maintenance of hiPSC pluripotency and self-renewal (Marinho, Chailangkarn, and Muotri 2015). Over 55% of publications utilized one of two commercially available hiPSC culture media as backbone medium: mTeSR-1 (STEMCELL Technologies) or Essential 8 Medium (E8) (Gibco) (**Supplementary Table 3.1**). During and after differentiation, the backbone culture medium was typically changed to RPMI-1640 (>50%), StemPro-34 (Gibco) (~5%), or commercially available differentiation kits or hiPSC-CM maintenance media, such as STEMdiff (STEMCELL Technologies), iCell Maintenance Medium (FUJIFILM Cellular Dynamics, Inc.), and Cor.4U Complete Medium (Axiogenesis) (**Supplementary Table 3.1**). Supplements and additives such as B-27 Supplement with or without insulin (Gibco) (>50% of publications), L-ascorbic acid, albumin, L-glutamine, HEPES, and more were added to some cultures (**Supplementary Table 3.1**). Additionally, the matrix (if any) that hiPSCs are seeded on during and after differentiation into hiPSC-CMs has been found to impact hiPSC-CM purity and maturation (Barnes et al. 2022; Block et al. 2020; Jianhua Zhang et al. 2022). Of the publications that listed the matrix (including no matrix) utilized for hiPSC culture, Matrigel (~30%), gelatin (~20%), and fibronectin (~15%) were the most commonly reported (**Supplementary Table 3.1**).

While most protocols used to generate cardiomyocytes are based on temporal modulation of the Wnt signaling pathway (Lian et al. 2012), adjustments to differentiation parameters are often required for successful CM differentiation of different hiPSC lines (Mummery et al. 2012). Moreover, empirically observed variations in the purity and function of resulting hiPSC-CMs are

common (**Figure 3.1d**) (Branco et al. 2019; Nijak et al. 2022). In the analyzed studies, CHIR9901 was the most commonly employed Wnt agonist used to initiate the differentiation process (used in >60% of studies analyzed). CHIR9901 was typically added to hiPSCs at ~80-90% confluency for 24 hours from Day 0 to about Day 1. Subsequent inactivation of the Wnt pathway via IWR-1, IWP-2, or IWP-4 was conducted from approximately Day 3 to Day 4 of differentiation. Insulin was typically added on Day 7 of differentiation. The use of metabolic selection to improve the purity of hiPSC-CMs (Tohyama et al. 2013, 2016) is only reported in one-third of the publications. Of these publications, about 70% removed glucose from the media and supplemented the media with lactate in order to starve non-myocytes.

While many studies failed to quantify hiPSC-CM purity following differentiation, over half of the studies reported using either flow cytometry or immunohistochemistry for cardiac-specific markers, such as cardiac troponin T (cTnT) or α-actinin, to quantify the percentage of hiPSCs that were successfully differentiated into cardiomyocytes (**Figure 3.1c**). The average reported purity of cardiomyocytes was 84%. Of the studies that reported hiPSC-CM purity, almost 50% used differentiated hiPSCs that were >90% cardiomyocytes.

Overall, similar differentiation protocols are used across the field; however, variations in the factors, their timing, and concentrations appear to be necessary for successful CM differentiation of different hiPSC lines (Mummery et al. 2012). Additional variability arises from differences in culture techniques across research groups. While we acknowledge the challenges associated with controlling for these variables, it would be advantageous for the field if the variability in differentiation protocols were decreased to the greatest extent possible. As a start, more studies should adopt a common differentiation protocol at least as a comparator to their group's traditional protocol, as well as measure and report the purity of their hiPSC-CMs to allow

for comparisons. Purity is important not only to interpret studies but also to provide additional assurances that non-cardiomyocytes are not unknowingly impacting downstream functional outputs and resulting interpretations. Identifying and reporting the common non-cardiomyocyte cell populations that arise during differentiation could also aid in optimizing differentiation protocols to improve differentiation efficiency (Grancharova et al. 2021).

3.5.2 Platforms used to study hiPSC-CMs

Following the differentiation of hiPSCs into cardiomyocytes, these cells are typically incorporated into a variety of culture platforms to study their function, ranging from simple, high-throughput platforms to more complex bioreactor-like systems, many of which require engineering expertise to create and/or the inclusion of other cell types in addition to hiPSC-CMs. Given the evident diversity of approaches, we quantitatively assessed the range of hiPSC-CM culture platforms used across the field towards identifying field-level trends.

3.5.2.1 2D platforms

A variety of platforms have been used to generate hiPSC-CM models for studying hiPSC-CM maturation, disease progression, and drug toxicity. These models can broadly be divided into 2D vs. 3D tissue platforms. 2D platforms are more commonly used than 3D tissue platforms due to their accessibility and higher throughput readouts. Additionally, 2D platforms facilitate the use of imaging and higher resolution analysis techniques to study cardiomyocyte structure and function, such as patch clamping, the standard for electrophysiology recordings.

Across both 2D and 3D tissues, the most used culture platform for hiPSC-CMs was extracellular matrix (ECM)-coated glass or plastic substrates. About 60% of studies in our analysis utilized simple 2D platforms such as ECM-coated glass or plastic (**Figure 3.2a**). While fibronectin or Matrigel are typically coated onto culture surfaces to facilitate cell adhesion, stromal cell-

derived ECM has recently been reported to improve the maturation of hiPSC-CMs (Block et al. 2020).

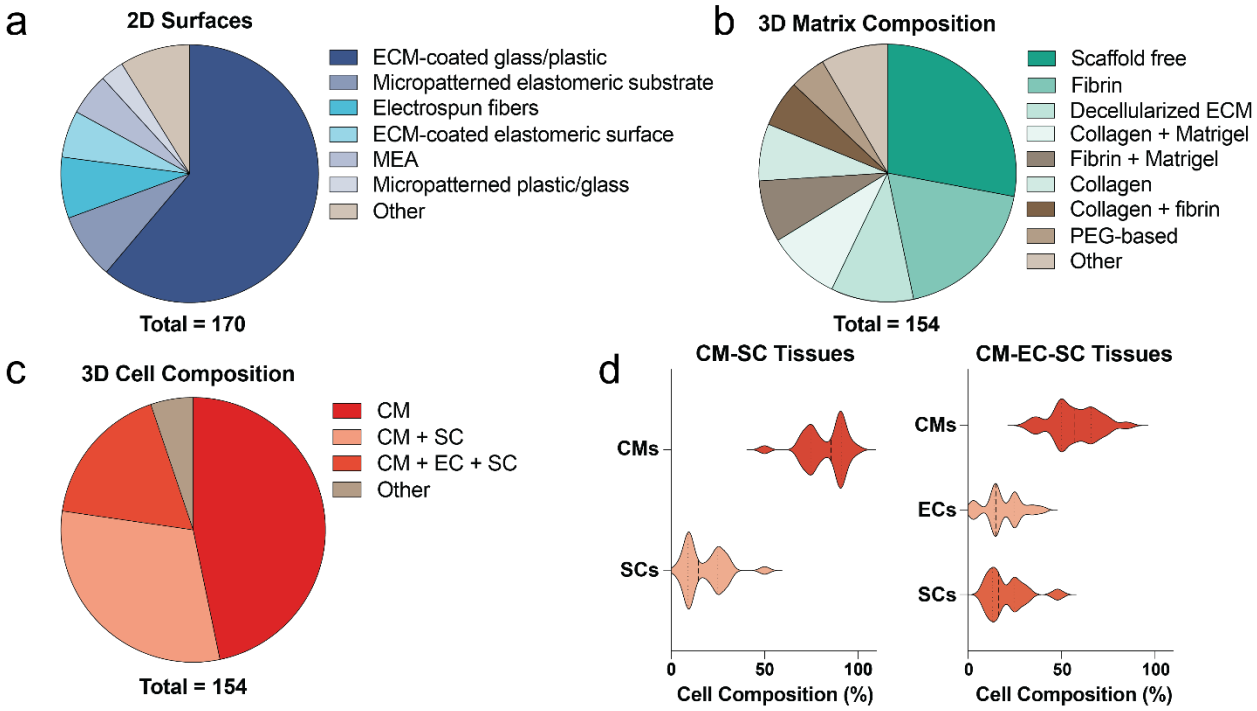

Figure 3.2: Variability in hiPSC-CM platforms. a. Top types of substrate platforms that hiPSC-CMs are seeded on in 2D. Multielectrode array (MEA). b. Top extracellular matrix (ECM) or biomaterial platform used to engineer cardiac microtissues. Polyethylene glycol (PEG). c. Fraction of cardiac microtissues that are composed of hiPSC-CMs alone (CM), hiPSC-CMs with mesenchymal stromal cells (CM + SC), or hiPSC-CMs with endothelial cells and mesenchymal stromal cells (CM + EC + SC). d. Left: Distribution of CM and SC composition in CM-SC cardiac microtissues (n = 50). Right: Distribution of CM, EC, and SC composition in CM-EC-SC cardiac microtissues (n = 26). Dashed and dotted lines represent medians and quartiles, respectively.

Recent improvements to 2D platforms have focused on providing topographical cues to hiPSC-CMs to drive CM alignment, mimicking the organization of the native myocardium. This alignment has been achieved by culturing CMs on micropatterned rectangles or lines (Hart et al. 2018; Kit-Anan et al. 2021; Knight et al. 2021; Kujala et al. 2016; Z. Ma et al. 2015; Martewicz et

al. 2019; Pioner et al. 2016; Schulze et al. 2019; Strimaityte et al. 2022; S. Sun et al. 2020; Tsan et al. 2021; Wheelwright et al. 2018; C. Xu et al. 2017), electrospun scaffolds composed of aligned polymeric fibers (Chen et al. 2022; DePalma et al. 2021; Khan et al. 2015; N. Kumar et al. 2020; J. Li et al. 2016; Pushp et al. 2020; Tang et al. 2016; Wanjare et al. 2017), grooved substrates (Afzal et al. 2022; Carson et al. 2016; Huethorst et al. 2020; Pioner et al. 2019; A. S. T. Smith et al. 2020; Takada et al. 2022), and 3D-printed anisotropic scaffolds (H. Cui et al. 2020; Gao et al. 2017; Y. S. Zhang et al. 2016). Additionally, several studies have cultured hiPSC-CMs on elastomeric surfaces that better recapitulate the mechanics of the native myocardium (Feaster et al. 2015; Garbern et al. 2020; Jia et al. 2016; Lind et al. 2017; Parikh et al. 2017; Park et al. 2019). These substrates are typically made from hydrogels or elastomers, including polyacrylamide (Buikema et al. 2020; Kit-Anan et al. 2021; Pasqualini et al. 2015; Strimaityte et al. 2022; Wheelwright et al. 2018) or polydimethylsiloxane (PDMS), respectively (Dou et al. 2021; J. Guo et al. 2021; Herron et al. 2016; Kroll et al. 2017). While 2D platforms can provide insights into the effect of specific parameters (i.e. substrate stiffness and ligand type/density) on cardiomyocytes, they are difficult to maintain in long-term culture and do not accurately recapitulate the complex structure and dimensionality of native tissue. Thus, they are limited in their ability to mimic specific aspects of development, physiology, and disease.

3.5.2.2 3D platforms

3D hiPSC-CM tissues have increased in popularity as they more accurately recapitulate the 3D architecture of the cardiac microenvironment in which CMs normally function. The majority of 3D-cardiac microtissues studied are considered scaffold-free (**Figure 3.2b**). Examples of scaffold-free microtissues include spheroid cultures, which have been used as a high-throughput assay to test the effects of non-cardiomyocytes on tissue stability and maturation and as disease

models (Giacomelli et al. 2017). Other 3D hiPSC-CM tissues require the addition of ECM proteins to facilitate proper compaction and assembly of the tissue. The most common ECM proteins used include fibrin, collagen, Matrigel, or some combination of these materials. Additionally, a handful of groups have explored the use of decellularized ECM (Blazeski et al. 2019; Goldfracht et al. 2019; Noor et al. 2019; Schwan et al. 2016) and synthetic hydrogels made of materials such as polyethylene glycol (H. Cui et al. 2020; Vannozzi et al. 2018) to generate cardiac microtissues. Further, the media used in culture has a significant impact on the system, and over 80 combinations of media components were utilized. Despite the use of serum in culture media, which limits the translational potential of cardiac microtissues given the variability in serum composition, more than one-third of the 3D hiPSC-CM models included serum in culture media. 3D hiPSC-CMs are more physiologically relevant overall, but complex fabrication processes and increased sources of variability limit both the accessibility and throughput of these models.

Another layer of complexity to some 3D cardiac microtissues is the incorporation of supporting cell types that facilitate the assembly of tissues containing hiPSC-CMs. While some 2D hiPSC-CM tissues contained admixed cell types (Abecasis et al. 2019; Floy et al. 2022; Peters et al. 2022), over 90% of 2D studies used pure hiPSC-CM cultures. In contrast, about half of the 3D hiPSC-CM tissues contained cell types such as mesenchymal stromal cells (SCs), endothelial cells (ECs), or other cell types due to either their ability to facilitate tissue compaction or the potential to study the impact of these additional cell types on cardiac microtissue maturation and function. (**Figure 3.2c**). Mesenchymal stromal cells used in these studies include primary human cardiac fibroblasts, human mesenchymal stem cells, hiPSC-derived cardiac fibroblasts, human lung fibroblasts, human mural cells, human dermal fibroblasts, human foreskin fibroblasts, hiPSC-derived stromal cells, hiPSC-derived mural cells, human adipose-derived stem cells, human

pericytes, and hiPSC-derived smooth muscle cells. Additional stromal cell populations used include primary dermal, foreskin, and lung fibroblasts. This variability is consequential, as it has been shown that the stromal cell source can impact tissue assembly and functionality (Hookway et al. 2019). Additionally, the number of stromal cells added to the hiPSC-CM microtissues varies, but many groups either used them in a 1:9 or 1:3 ratio with hiPSC-CMs (**Figure 3.2d**). This ratio of stromal cells can also impact the functionality and maturation of hiPSC-CMs and has been leveraged to model cardiac fibrosis (Rupert et al. 2020; E. Y. Wang et al. 2019).

Lastly, many groups have also explored the incorporation of ECs to vascularize and further mature *in vitro* cardiac microtissues (**Figure 3.2c**). Not only does vascularization of cardiac microtissues enable the generation of thicker tissues, but the addition of ECs has also been found to mature cardiac microtissues via paracrine signaling (Giacomelli et al. 2017). Prominent EC sources include hiPSC-derived ECs and primary human umbilical vein ECs. In CM-EC-SC tissues, ECs and stromal cells were most often used in a 1:1 ratio, with over 50% of the tissue being composed of hiPSC-CMs (**Figure 3.2d**).

Overall, the composition of each platform is influenced by the intended use and resource accessibility. This variability in model design can impact the techniques used to assess resulting tissues and their maturation. Dissemination of detailed protocols is critical to making complex cardiac microtissue platforms widely accessible, allowing others in the field to apply new techniques to improve the maturation and physiological relevance of their established hiPSC-CM models.

3.5.3 Strategies used to mature hiPSC-CMs

Numerous strategies have been developed to simulate developmental cues found in the native cardiac microenvironment to direct hiPSC-CM maturation toward a more adult-like

phenotype (**Figure 3.3**). In this analysis, we grouped these cues into five categories (alignment, mechanical, electrical, co-culture, and metabolic maturation techniques) to identify trends in how these techniques are being implemented across the field.

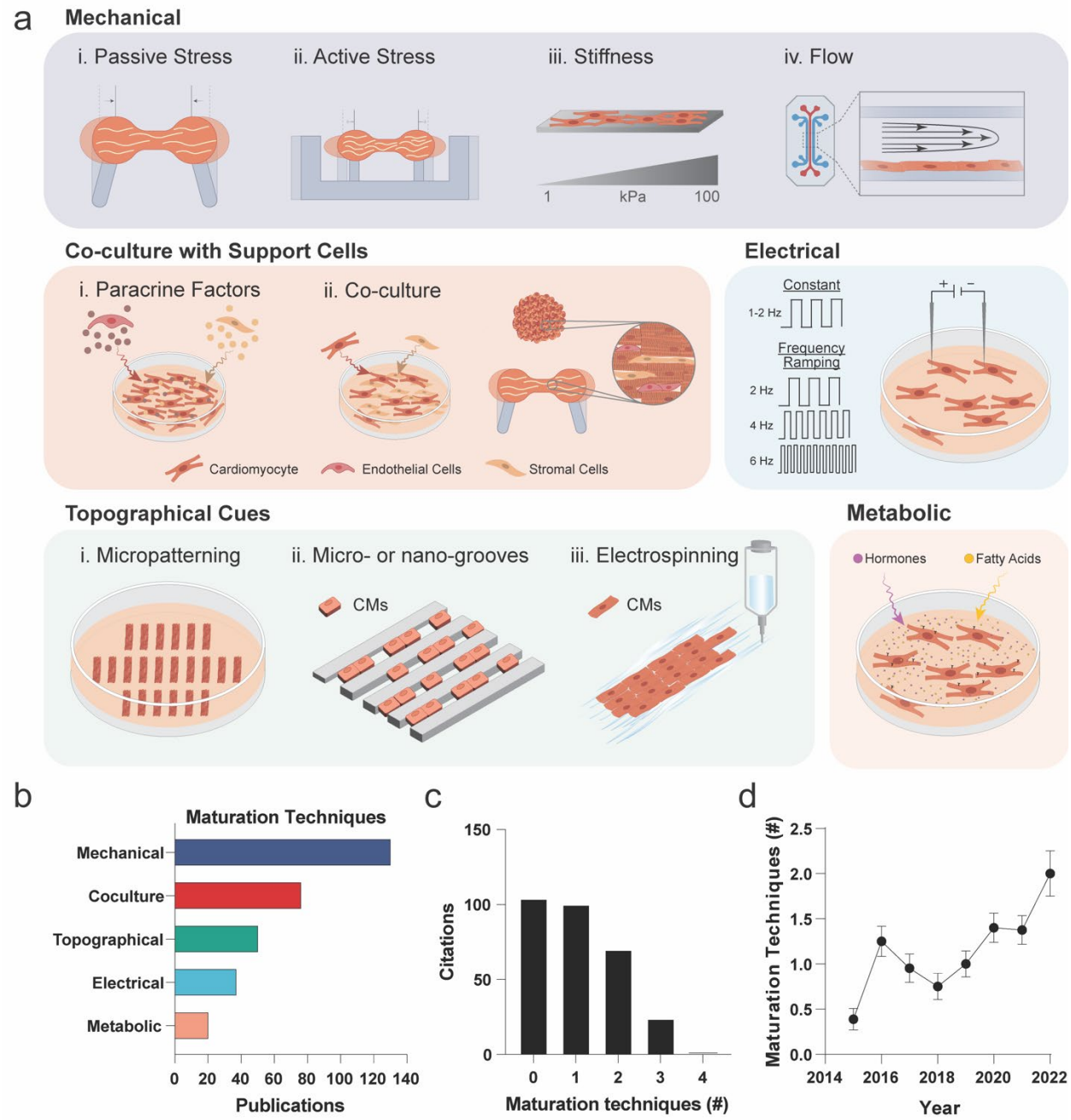

Figure 3.3: Maturation techniques used in hiPSC-CM culture. a. Schematic of types of maturation techniques, including mechanical, metabolic, co-culture, electrical stimulation, and

alignment cues. b. Number of publications that reported using the listed maturation techniques. c. Histogram of the number of maturation techniques that the analyzed publications reported. d. Average number of maturation techniques reported over time (n = 18-34). Error bars are standard error of the mean (SEM).

3.5.3.1 Alignment cues

Given the high degree of alignment of native cardiomyocytes, alignment cues are common maturation techniques in 2D hiPSC-CM platforms and include micropatterning, aligned electrospun fibrous scaffolds, and grooved surfaces (**Figure 3.3a**). Both alignment cues at the microscale (Strimaityte et al. 2022; Takada et al. 2022; Tsan et al. 2021; Wanjare et al. 2017) and the nanoscale (Afzal et al. 2022; DePalma et al. 2021; Khan et al. 2015) have been shown to improve the structure and function of hiPSC-CMs, and in particular induce myofibril alignment as compared to surfaces lacking topographical instruction. Other variables that may contribute to the success of alignment cues in 2D platforms include adhesive ligand and substrate stiffness, which impact tissue assembly and function on aligned electrospun fibers (DePalma et al. 2021). Recent work extended these observations to 3D tissues by bioprinting anisotropic microtissues into larger-scale organized tissue patches (J. H. Ahrens et al. 2022). This work highlights the challenges associated with scaling well-established 2D alignment cues into 3D tissue platforms to drive proper assembly and structural maturation of 3D tissues.

3.5.3.2 Mechanical stimulation

Mechanical maturation techniques include the use of passive tension (J. Ahrens et al. 2022; Boudou et al. 2012; Feric et al. 2019; Tamargo et al. 2021; Ulmer et al. 2018), hydrogel or elastomeric substrates in 2D platforms (Feaster et al. 2015; S. Lee et al. 2017; Pioner et al. 2019), dynamic mechanical stimulation of tissue (Dou et al. 2021; Jackman, Carlson, and Bursac 2016;

Jayne et al. 2021; X. Ma et al. 2019; Ng et al. 2020; Rogers, Fast, and Sethu 2016; Ruan et al. 2015), and the application of scear forces (Gao et al. 2018; Kolanowski et al. 2020; Marsano et al. 2016) (**Figure 3.3**). Across all studies analyzed, mechanical cues were the most used maturation technique (**Figure 3.3b**), likely due to the widespread adoption of 2D hydrogel culture platforms as well as 3D engineered heart tissue (EHT) platforms where tissues are tethered between two elastomeric pillars (**Figure 3.2a-b**). Modulating the stiffness of deformable substrates has been used to improve the maturation of hiPSC-CMs in 2D. Elastic hydrogels of physiologically relevant elastic moduli between 3 to 10 kPa can improve the maturation and function of hiPSC-CMs compared to supraphysiologically stiff tissue culture plastic or glass (Feaster et al. 2015; A. J. S. Ribeiro et al. 2015; Tsan et al. 2021; Wheelwright et al. 2018). In EHT platforms, the passive tension, or afterload, modulated by pillar stiffness has been shown to impact tissue formation, CM alignment, and functional maturation, with increased afterload generally improving structural and functional outputs of EHTs (Abilez et al. 2018; J. H. Ahrens et al. 2022). However, too high of an afterload can lead to pathological responses (Bliley et al. 2021; Leonard et al. 2018).

Lastly, cyclic mechanical stimulation to mimic the contractile behavior of the heart and pace hiPSC-CMs in 2D or 3D has been achieved using pressure changes (Jayne et al. 2021; Rogers, Fast, and Sethu 2016) and cyclic stretching (X. Ma et al. 2019; Ng et al. 2020; Ruan et al. 2016). However, this technique was used sparingly, in less than 7% of the studies we analyzed.

3.5.3.3 Electrical stimulation

Electrical pacing has shown great improvements in the maturation (Ronaldson-Bouchard et al. 2018) and vascularization (Lu et al. 2023) of engineered heart tissue, leading >12% of studies to utilize this technique (**Figure 3.3b**). Previous work showed that initiating electrical stimulation earlier in hiPSC-CM differentiation and gradually increasing stimulation frequency over time

(**Figure 3.3a**) can greatly improve the maturation of EHTs compared to the commonly used constant stimulation of 1 Hz initiated later after EHT assembly (Ronaldson-Bouchard et al. 2018). These electrically paced tissues had adult-like gene expression profiles, increased mitochondrial density, presence of transverse tubules (t-tubules), and a positive force-frequency relationship.

3.5.3.4 Co-culture of hiPSC-CMs with other cell types

As heterocellular signaling plays an important role in native tissue development (Karbassi et al. 2020), there have been significant efforts to characterize the impact of other cell types on hiPSC-CM maturation and overall tissue function. Over 50% of publications incorporated mesenchymal stromal cells and/or endothelial cells when generating cardiac microtissues (**Figure 3.2c**, **Figure 3.3b**). Tri-cultures including mesenchymal and endothelial cells have been shown to improve the maturation of hiPSC-CM engineered constructs, contributing to the formation of t-tubules, increased tissue contractility, and improved electrophysical function (Giacomelli et al. 2020). Other studies have also shown improvements in the electrophysical function of cardiac microtissues with just the addition of stromal cells (Beauchamp et al. 2020) [beau] or endothelial cells (Z. Lin et al. 2023). Soluble factors from stromal cells alone, without physical co-culture, can also improve the maturation of hiPSC-CMs (Yoshida et al. 2018).

3.5.3.5 Metabolic maturation

Strategies focusing on metabolic maturation typically employ media formulations and small molecules that drive a shift from glycolysis to oxidative phosphorylation as the primary source of adenosine triphosphate (ATP) production in hiPSC-CMs. Studies have shown that the use of triiodothyronine (X. Yang et al. 2014) and dexamethasone (Parikh et al. 2017) increases mitochondrial activity and improves contractile performance and calcium handling of hiPSC-CMs. Other studies have shown that the switch from media containing glucose to those containing

galactose and fatty acids promotes maturation (Correia et al. 2017; Feyen et al. 2020), and that adjusting the levels of glucose and calcium concurrent with fatty acid supplementation improves the maturation of hiPSC-CMs (Feyen et al. 2020). These studies highlight the importance of utilizing physiologically relevant media with hiPSC-CMs to promote their maturation. Although metabolic maturation is a more nascent technique, adopted in under 10% of studies, its ease of implementation makes it likely to be more widely integrated into workflows across many labs.

3.5.3.6 Utilization of maturation techniques

Despite maturation techniques generally leading to improvements in the function, robustness, and utility of hiPSC-CM models, more than a third of the studies we analyzed did not use any of the listed maturation techniques (**Figure 3.3c**). In contrast, many studies combined multiple maturation techniques toward enhancing hiPSC-CM maturation, with about one-third of studies analyzed exploring at least two maturation techniques (**Figure 3.3c**). We note a steady increase in the number of maturation techniques implemented per study, since 2016, with the average number of maturation techniques used being 1.3 in 2016 and 2.0 in 2022 (**Figure 3.3d**). More systematic studies are needed to understand which of these techniques are most successful in driving specific phenotype changes in hiPSC-CMs and how combinations of techniques may act synergistically to improve maturation.

3.5.4 Metrics to assess hiPSC-CM maturity and function

Identifying techniques that are most effective in driving hiPSC-CM maturation requires robust methods to assess hiPSC-CM and EHT function. To quantify which assessment metrics are most commonly used and might best inform overall tissue maturity, we examined commonly reported approaches used to obtain qualitative and quantitative data on the structure and functionality of hiPSC-CMs and derivative cardiac tissues.

3.5.4.1 Structural analysis

Structural organization is the primary measure used to assess differences in cardiomyocyte maturation. Over 85% of studies reported data on the morphology and organization of sarcomeres in hiPSC-CMs or cardiac microtissues, given the critical role of myofibrils in cell contractile function (**Figure 3.4a**). To obtain these metrics, over 60% of studies performed immunostaining (either immunofluorescence or immunohistochemistry (IHC)), while over 20% of studies utilized transmission electron microscopy (TEM) or scanning electron microscopy (SEM) to assess the structure of hiPSC-CMs (**Figure 3.4b**). Proteins that were commonly labeled by immunostaining to visualize hiPSC-CM subcellular structure include cardiac troponin T, α-actinin, cardiac troponin I, β myosin heavy chain, and connexin-43. While some studies showed qualitative differences in the images that they present, many used immunostaining of sarcomeric proteins to assess myofibril morphometrics, such as sarcomere length, and orientation of cardiomyocytes and constituent myofibrils. There are dozens of published image analysis scripts used to analyze sarcomere alignment (Morrill et al. 2016; Pasqualini et al. 2015; Stein et al. 2022; Sutcliffe et al. 2018; Toepfer et al. 2019; B. Zhao et al. 2021). More specifically, there are multiple ways in which sarcomere direction is identified, such as explicit sarcomere segmentation, computing gradients within an image, or analyzing other image features. These differing methods lead to many forms of how alignment is reported, including orientation order parameter (Morrill et al. 2016; Toepfer et al. 2019), dispersion parameter (Sutcliffe et al. 2018), and Haralick correlation score (Stein et al. 2022), thereby obfuscating direct comparisons across studies.

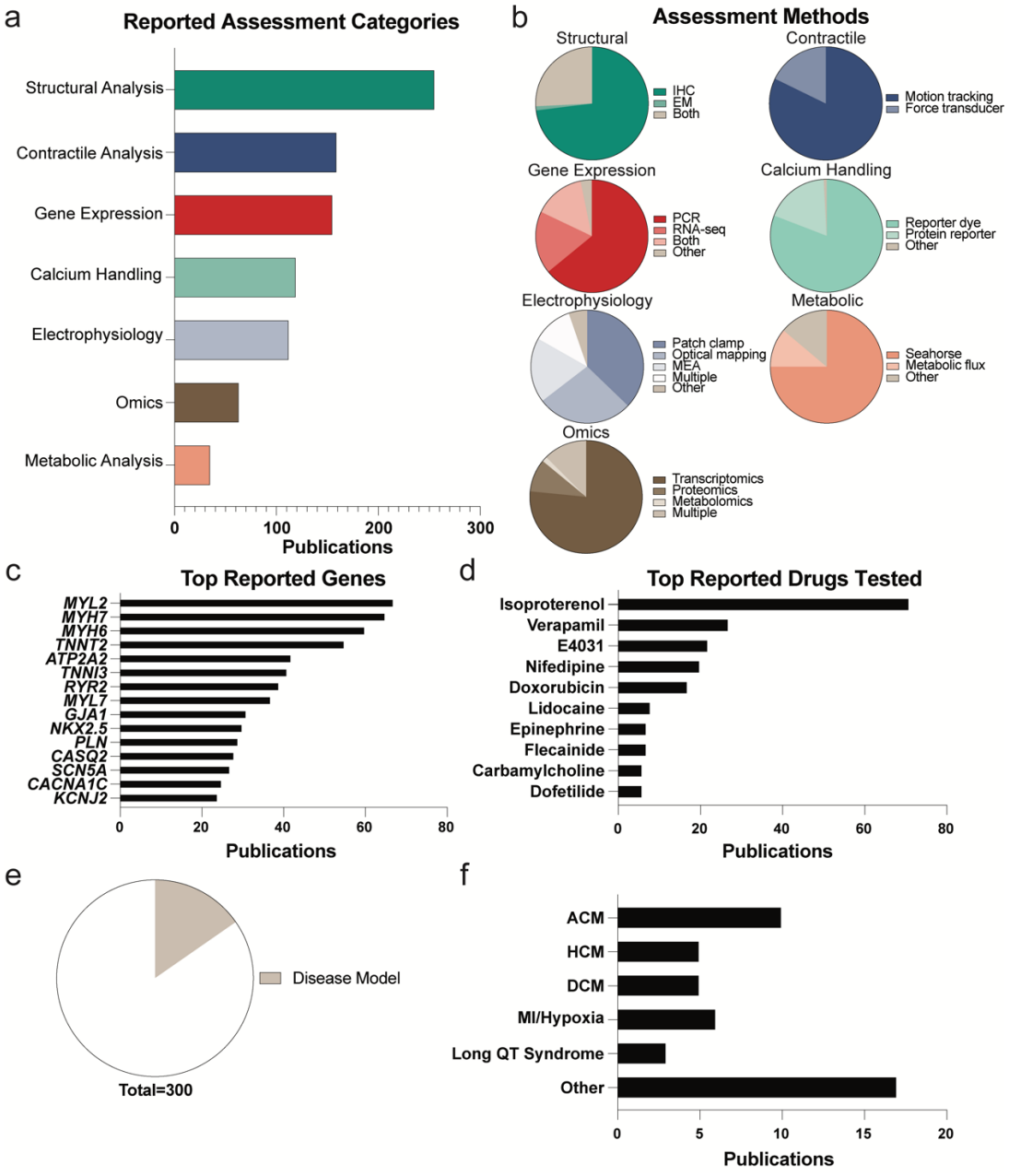

Figure 3.4: Methods of assessing hiPSC-CM functionality and maturation. a. Number of publications that reported analysis of the structure, contraction, gene expression, calcium handling, electrophysiology, and metabolism of hiPSC-CMs. b. Top methods of obtaining each of the reported metrics in a. c. Top genes that were reported in the assessment of hiPSC-CM maturation. d. Top pharmaceutical drugs used to test the ability of hiPSC-CMs to respond as known clinically. e. Proportion of publications that used hiPSC-CM platforms to model disease. f. Top diseases modeled by hiPSC-CM platforms including arrhythmogenic cardiomyopathy (ACM), hypertrophic cardiomyopathy (HCM), dilated cardiomyopathy (DCM), myocardial infarction (MI), and long QT syndrome (LQT). g. Graphs show the fraction of instances in which specific

maturation techniques were implemented when generating hiPSC-CM models to study each cardiac disease.

Methods of imaging the ultrastructure of hiPSC-CMs, such as TEM, mainly focus on identifying key subcellular structural components and their positioning. These features include the relative organization of Z-lines, I-band, H-zones, and M-lines in sarcomeres, the morphology and density of mitochondria, and the presence of caveolae. A structural feature that is associated with high levels of maturation of hiPSC-CMs is the presence and orientation of t-tubules, which has been confirmed in numerous recent studies (Y. Cui et al. 2019; Ergir et al. 2022; Fukushima et al. 2020; Garay et al. 2022; Giacomelli et al. 2020; Hatani et al. 2018; Huang et al. 2020; Jabbour et al. 2021; Kerscher et al. 2016; Miki et al. 2021; Parikh et al. 2017; Pioner et al. 2016; Ronaldson-Bouchard et al. 2018; Strimaityte et al. 2022).

3.5.4.2 Contractility measurements

The organization of myofibrils and constituent sarcomeres in hiPSC-CM can greatly impact contractility, the primary function of CMs. Contractility measurements were the second most reported metric of analysis, with over half of the studies reporting a cell- or tissue-level contractility measurement (**Figure 3.4a**).

In 2D, the most high-throughput and accessible method of obtaining a contractility metric was using video-based analysis to quantify the displacement of hiPSC-CMs during contraction (Huebsch et al. 2015; Tsan et al. 2021). While this method provides valuable data on contractility kinetics and allows for insight into relative changes in contractility, it does not provide a quantitative value of contractile force or stress that can be compared to results from other studies. A more quantitative contractility metric that is used in 2D is sarcomere shortening, or the fraction

that sarcomeres displace relative to their spacing in a relaxed state (Toepfer et al. 2019). While this quantification method can be more readily compared across studies and has physiological relevance, it still does not directly quantify the contractile force or stress of the cells, and it requires high-magnification imaging and live-cell fluorescent labeling of sarcomeres (Sharma, Toepfer, Schmid, et al. 2018). Traction force microscopy (TFM), in which the displacement of fluorescent beads embedded in an elastic hydrogel of known stiffness is tracked over time, can be used to quantify the contractile force and stress of unpatterned or patterned hiPSC-CMs, both at the single-cell (A. J. S. Ribeiro et al. 2015) and multicellular level (K. Zhang et al. 2021).

Similarly, contractile force and stress of hiPSC-CMs in 3D platforms can be quantified using video-motion analysis of the displacement of tissue constraints of known stiffness such as elastomeric pillars (Boudou et al. 2012; Legant et al. 2009). 3D hiPSC-CM tissues also produce enough force to be captured by force transducers that convert mechanical tension to an electrical output signal. Among the studies we analyzed that reported contraction metrics, over 15% of studies used force transducers (**Figure 3.4b**). Interestingly, we found that reported contractile force was significantly higher in studies that used force transducers compared to the studies that quantified contractile force from pillar displacement (2.5 mN vs 0.6 mN, $p = 0.01$), which could be due to differences in tissue size. To address the variable size of 3D microtissues across and within platforms, contractile stress factoring in tissue geometry should be calculated in addition to force to enable benchmarking of contractility between various platforms. Additionally, we have noted that in traditional EHT systems composed of two elastic pillars that both deflect inwards upon tissue contraction, some groups calculate the EHT contractile force by measuring the displacement of one of the pillars while others other groups sum the deflection of the two pillars to obtain a “total” tissue displacement. While the latter method is valid when calculating total

tissue fractional shortening, only one post displacement should be considered when quantifying the contractile force of EHTs. Tension within the suspended tissue is applied equally on each post and thus, the tension in the tissue equals the tension applied at each post, not the sum of the tension at both posts. These observations and suggestions highlight the importance of the quantification method in comparing metrics across studies.

3.5.4.3 Genetic analyses

The next most reported metric was gene expression of hiPSC-CM models. Most studies that report metrics of gene expression used reverse transcription-quantitative polymerase chain reaction (RT-qPCR) to report relative changes in expression of genes pre-determined from their study design. A more thorough look at changes in gene expression is now accessible due to the advent of RNA-sequencing, in which the average relative changes in expression of all detected genes can be reported. This allows assessment of expression levels of many genes and enables pathway-level analyses to determine changes in cellular signaling underlying cardiomyocyte maturation.

Genes that were most reported include *MYL2*, *MYH7*, *MYH6*, *TNNT2*, *ATP2A2*, *TNNI3*, *RYR2*, *MYL7*, *GJA1*, *NKX2.5*, *PLN*, *CASQ2*, *SCN5A*, *CACNA1C*, and *KCNJ2* (**Figure 3.4c**). These genes are associated with pathways and proteins involved in cardiac contraction, electrical conduction, and ion channels. As the composition of cardiomyocytes evolves during maturation, their gene expression of different protein isoforms does as well. Oftentimes, the relative expressions of genes encoding these isoform transitions are reported to assess improvements in maturation. For example, ratios of *MYH7*/*MYH6*, *MYL2*/*MYL7*, and *TNNI3*/*TNNI1* are commonly utilized maturation metrics.

In addition to gene expression analyses of hiPSC-CM models, other omics analyses have been used to obtain a more complete understanding of changes within hiPSC-CMs and cardiac microtissues, with over 20% of studies performing omics on their samples. While transcriptomics providing gene expression analyses were the most common, proteomics and metabolomics have also been used recently, often in combination with transcriptomics to better understand transcriptional and translational changes as well as their interrelationship during hiPSC-CM maturation.

3.5.4.4 Calcium handling and electrophysiological measurements

Calcium handling and electrophysiological measurements were also common measures of cardiomyocyte function (**Figure 3.4a**), as they are directly related to both the structural and functional maturity of hiPSC-CMs. Calcium handling is most often quantified with calcium sensitive dyes, such as Rhod-2, Fura-2AM, or Fluo-4AM, which enable imaging of calcium dynamics via high-speed microscopy (**Figure 3.4b**). Some studies have also implemented genetically encoded calcium indicators, such as GCaMP (Maddah et al. 2015; Shinnawi et al. 2015) to observe calcium transients without the addition of dyes to culture. Several algorithms have been developed to quantify calcium fluxes (Huebsch et al. 2015; Psaras et al. 2021; H. Yang et al. 2022), and cell screening systems such as FLIPR and IonOptix have implemented software for the high-throughput analysis of calcium fluxes.

Similarly, electrophysiology can also be quantified by adding voltage sensitive dyes, such as FluoVolt, Di-4-ANEPPS, Di-8-ANEPPS, or BeRST to CMs, imaging genetically encoded voltage sensors (eg. Archon1 (Shroff et al. 2020)), or by directly measuring the electrical properties of cell populations and single cells using multielectrode arrays (MEA) or patch clamping, respectively (**Figure 3.4b**). Patch clamping is the gold standard for electrophysical recordings of

cells, providing specific electrophysical properties such as resting membrane potential (RMP), that allow for benchmarking of hiPSC-CMs against adult cardiomyocytes. However, it can be difficult to obtain patch clamp measurements from 3D cultures, leading many groups to opt for optical mapping via voltage-sensitive dyes to obtain tissue-scale measurements.

One of the most reported metrics from both calcium handling and electrophysiological measurements was conduction velocity, or the speed at which the electrical signal travels across heart tissue. Conduction velocity assesses the maturity of the calcium handling machinery across an entire tissue and the electrical coupling of hiPSC-CMs within the tissue, both of which are critical to the function of myocardial tissue.

3.5.4.5 Metabolic measurements

A final commonly used metric to report on the maturation of hiPSC-CMs was metabolic activity. As metabolic changes in cardiomyocytes are observed throughout the development of the myocardium, increasing efforts have been made to quantify metabolic activity of hiPSC-CMs to capture the shift from glycolysis to oxidative phosphorylation for ATP production. Quantifying metabolic activity has become more common in recent years to assess hiPSC-CM maturity, although was still only used by <15% of studies (**Figure 3.4a**).

The most common assay used to quantify metabolic activity was the Agilent Seahorse assay, which monitors ATP production from glycolytic and oxidative pathways in cultures due to changes in free protons and dissolved oxygen in culture medium (**Figure 3.4b**). Some groups also used live cell fluorescent trackers to visualize and quantify mitochondria, as more mature cardiomyocytes possess greater mitochondrial density and organization.

Many of the publications that used this assessment metric are also focused on developing methods to specifically mature hiPSC-CMs by directly shifting their metabolic activity (Correia et

al. 2017; Feyen et al. 2020; Horikoshi et al. 2019; X. Yang et al. 2019). However, studies focused on developing other maturation techniques have also used metabolic analysis to assess hiPSC-CM maturation more holistically (Giacomelli et al. 2020; Ronaldson-Bouchard et al. 2018; J. Z. Zhang et al. 2019).

3.5.4.6 Pharmaceutical drug screening

A final method for assessing hiPSC-CM maturation was treating cultures with small molecules that are known to impact cardiomyocyte function and quantifying the ability of hiPSC-CMs to respond in a manner reflecting the response of adult cardiomyocytes (**Figure 3.4d**). Most commonly, the beta-adrenergic agonist isoproterenol was added to culture media to quantify the chronotropic and inotropic responses, with a greater contractile force or frequency response indicating increased adrenergic receptors and greater maturity. hiPSC-CMs have also been treated with many other drugs to assess maturation. For example, whether hiPSC-CM contractility is impaired upon inhibition of specific ion channels found in adult cardiomyocytes provides insight into the maturity of the calcium handling machinery present (Da Rocha et al. 2017).

In addition to using drug challenges to assess the maturity of hiPSC-CM tissues, many of the systems described in the analyzed papers show great potential as mid- to high-throughput drug screening platforms. As such, many groups, including regulatory agencies such as the FDA, have begun exploring how patient-specific hiPSC-CM tissues could be used to more accurately identify cardiotoxic effects of therapeutics and ultimately replace expensive and time-consuming *in vivo* cardiotoxicity assays (Colatsky et al. 2016). However, hiPSC-CMs used for cardiotoxicity testing must be sufficiently mature to ensure that the drug-induced phenotype faithfully represents the cardiac response to the drug in human patients.

For example, one study examined how the addition of metabolic maturation medium impacts hiPSC-CM response to treatment with the anti-arrhythmia drug mexiletine (Feyen et al. 2020). Specifically, they found that hiPSC-CMs carrying a gain-of-function mutation in *SCN5A* only responded to mexiletine treatment after being first treated with metabolic maturation media, likely due to increased sodium channel activity observed in hiPSC-CMs cultured in these conditions. Another study asked whether culturing 3D hiPSC-CM microtissues in fatty-acid-enriched maturation media could improve the accuracy of hiPSC-CM models in predicting drug toxicity (Huebsch et al. 2022). Specifically, verapamil can exhibit false positives in commonly used 2D monolayer toxicity assays, prolonging action potential duration at low doses (Huebsch et al. 2022). By treating hiPSC-CMs in 3D culture with maturation media, these effects were no longer observed at relevant doses, likely due to changes in ion channel expression in more mature tissues. The results described in these two studies and others that implemented various other maturation techniques such as electrical pacing before conducting drug challenges (Goldfracht et al. 2019; Kofron et al. 2021; N. Kumar et al. 2020; Lemme et al. 2020; Qu et al. 2020; Ronaldson-Bouchard et al. 2018) highlight the necessity to generate mature hiPSC-CMs to accurately assess the potential effectiveness or toxicity of a drug *in vitro*.

However, in many of the analyzed studies that explored the utility of hiPSC-CM models in drug testing applications, maturation techniques were not employed. This indicates that less mature hiPSC-CMs may be sufficient for testing the efficacy and toxicity of certain drugs but not all, depending on their mechanisms of action (**Supplementary Table 3.1**). Additional work should be done to investigate how various combinations of maturation techniques might alter cardiotoxic responses to drug treatments to encourage further development of reproducible and efficient screening assays.

3.5.4.7 Disease modeling

The increased maturation of hiPSC-CM models has also enabled *in vitro* studies of a multitude of cardiac pathologies. Over 15% of the studies analyzed utilized hiPSC-CM platforms to model various cardiac pathologies, including arrhythmogenic cardiomyopathy (ACM), hypertrophic cardiomyopathy (HCM), dilated cardiomyopathy (DCM), myocardial infarction, and long QT syndrome (**Figure 3.4e,f**). By utilizing patient-derived or genetically edited hiPSC-CMs or stress-inducing culture conditions, such as hypoxia, studies have been able to model changes in cardiomyocyte structure, contractility, and electrophysiology associated with disease(Bliley et al. 2021; Knight et al. 2021; Martewicz et al. 2019; Strimaityte et al. 2022; K. Zhang et al. 2021). Further, implementing maturation techniques, such as metabolic conditioning, has enabled the recapitulation of key disease phenotypes that were not otherwise prominent in hiPSC-CMs derived from patients with long QT syndrome (Knight et al. 2021) (**Figure 3.4g**). Other maturation techniques including mechanical conditioning, topographical cues, and coculture with other cell types were also used when generating models of ACM, HCM, and DCM (**Figure 3.4g**). With increasing maturation of hiPSC-CMs, there is growing potential to utilize these models to shed light on disease mechanisms and potential therapeutic approaches.

3.6 Performance of hiPSC-CM models

3.6.1 Improvements to the maturation of hiPSC-CMs

Despite high variability amongst maturation techniques and assessment metrics, there were noticeable improvements in frequently assessed metrics (**Figure 3.5a-d**). Sarcomere length, contractile stress, and conduction velocity all trended upwards over time, suggesting that the field is engineering more mature hiPSC-CMs. Improved measurement tools and techniques such as

open-source code for assessing structural organization, contractile function, and electrophysiological activity could also be contributing to these improvements by enabling more accessible and standardized assessment metrics.

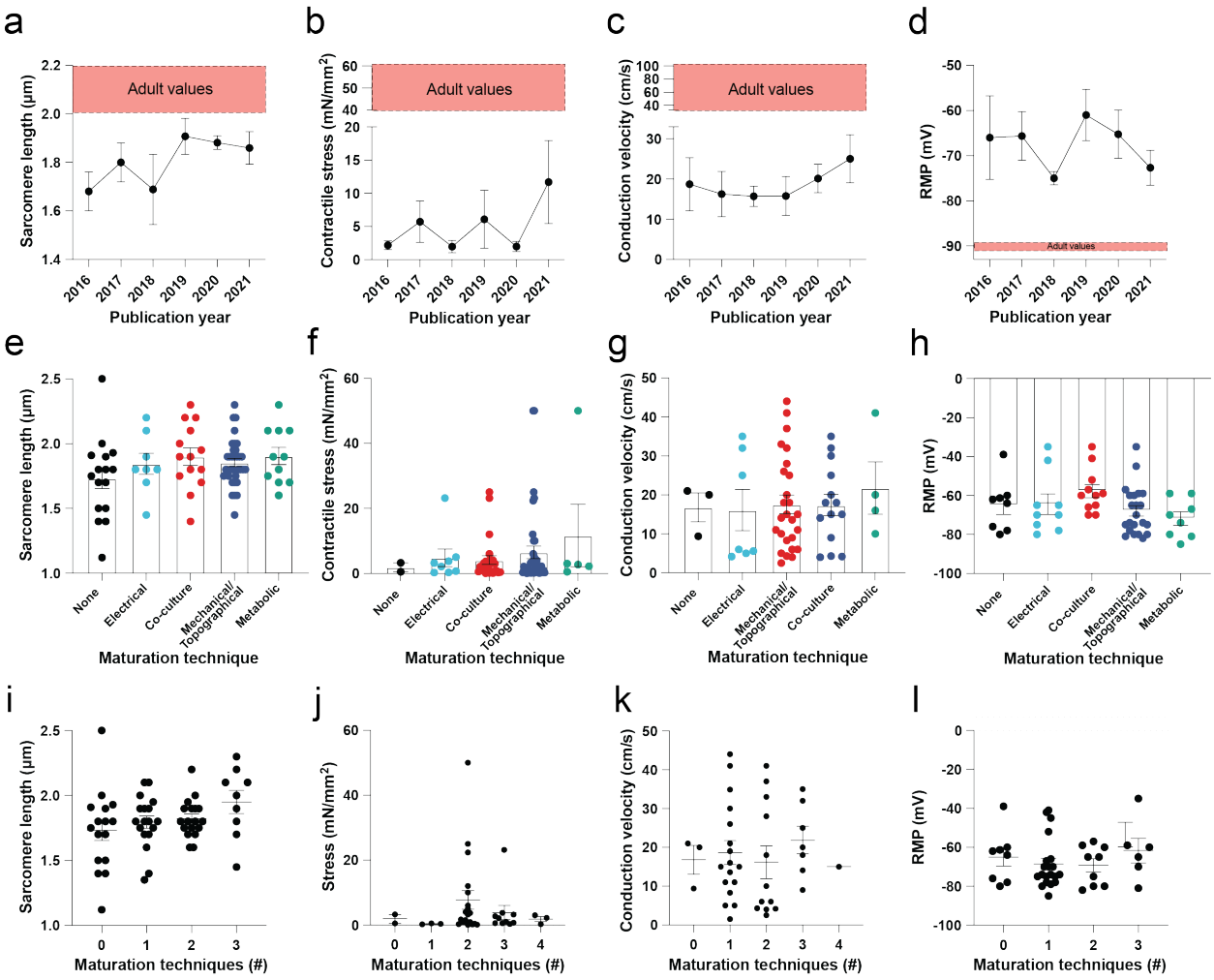

Figure 3.5: Quantification of hiPSC-CM functionality and maturation. a-d. Average reported sarcomere length, contractile stress, conduction velocity (CV), and resting membrane potential (RMP) in hiPSC-CMs each year from 2016-2021 (n = 4-11). 2015 and 2022 were excluded from these graphs due to limited data availability (analysis was performed mid-2022). Red regions represent values benchmarked in adult human CMs. e-h. Average reported metrics based on types of maturation techniques that were used from all analyzed publications (n = 2-34). i-l. Average reported metrics based on the number of maturation techniques that were used from all analyzed publications (n = 2-20). Maturation techniques were classified as described in Figure 2. Error bars are standard error of the mean (SEM).

The average reported sarcomere length of hiPSC-CM models increased from ~1.7 μm in 2016-2018 to 1.8-1.9 μm in 2020-2021, approaching the sarcomere length of adult cardiomyocytes, ~2 μm (Lemcke et al. 2020) (**Figure 3.5a**). Sarcomere length measurements have been obtained with many different approaches, including the use of different protein markers, imaging techniques, and image analyses. Thus, while maturation strategies should lead to improvements in this value, reported values may also be influenced by the employed measurement methods, each of which may have limitations. While some of the highest reported sarcomere lengths are from hiPSC-CM models from studies exploring maturation techniques such as intensity-ramped electrical stimulation (Ronaldson-Bouchard et al. 2018), tri-cultures (B. Yang et al. 2019), or patterned elastomeric substrates (Tsan et al. 2021), the highest reported average sarcomere length is from a study that did not use any of the maturation techniques assessed here, but instead simply cultured hiPSC-CMs for extended periods of time (N. Cui et al. 2019). Extended culture as a technique for hiPSC-CM maturation has also been explored by other groups, but the use of simplistic, 2D culture platforms employed in these studies appears to limit the development of other features of maturation such as t-tubules (Kamakura et al. 2013; Lundy et al. 2013; Piccini et al. 2015).

Contractile stress, on the other hand, has seen more marked improvements in recent years (**Figure 3.5b**). While the average contractile stress of hiPSC-CM models was 12 mN/mm^2 (or 12 kPa) in 2021, more recent models have shown contractile stress performance approaching that of adult cardiomyocytes (25-44 mN/mm^2 or 25-44 kPa). These models include a micropillar system with passive tension and co-culture (Melby et al. 2021) and metabolic maturation on micropatterned substrates (Knight et al. 2021). While it appears that the use of maturation

techniques is important to the improved contractility of hiPSC-CMs, a variety of maturation techniques appear to yield similar enhancements in contractile function.

Numerous maturation strategies have targeted calcium handling and electrophysiology of hiPSC-CMs. As a result, conduction velocity trended upward in recently published work (**Figure 3.5c**). Multiple models achieved average conduction velocities greater than 30 cm/s (**Table 3.1**), including models with dynamic mechanical culture (Querdel et al. 2021), small molecules targeting signaling pathways (Miki et al. 2021), conductive biomaterials (Lind et al. 2017), decellularized ECM (Guyette et al. 2016; Tsui et al. 2021), human perinatal stem cell-derived ECM (Block et al. 2020), ventricular-specific tissues (Y. Zhao et al. 2019), and 3D printed tri-cultures (Pretorius et al. 2021).

Of the main metrics we assessed, resting membrane potential (RMP) remained stagnant over time at ~-65 mV with recent decreases towards more adult-like levels (Fig 5d). This could be, at least in part, because many recent advances have been focused on the development of 3D tissues, in which patch-clamp electrophysiology measurements are difficult to obtain directly. 3D tissues must be dissociated into single cells to conduct this measurement, potentially altering hiPSC-CM electrophysiology in the process (Ronaldson-Bouchard et al. 2018). While other electrophysiological assays such as imaging with voltage sensitive dyes have been implemented, these techniques do not enable quantitative measurements of resting membrane potential. Models that have obtained adult-like RMP, below -80 mV, utilized dynamical mechanical stretch (Bliley et al. 2021; Querdel et al. 2021), ECM-coated elastomeric surfaces (Herron et al. 2016; Tsan et al. 2021), and modifications to culture media (Feyen et al. 2020; B. Lin et al. 2017), all in 2D culture systems. Overall, there is a clear need for improved measurement techniques that accurately assess electrophysiology in 3D tissues.

3.6.2 Variability at all levels of hiPSC-CM tissue formation affects maturation outcomes

A major limitation in the field is that it is difficult to parse the individual impacts of each maturation technique due to numerous variables present at all levels of engineering hiPSC-CM tissues, including choices of hiPSC line(s) and differentiation protocols. While the use of numerous hiPSC lines is critical towards inclusive research, such as lines from donors of varying ancestorial backgrounds, biological sexes, and ages, for example, comparing outputs from studies using different lines is difficult given the underlying genetic differences inherent to each individual and their hiPSCs. Variations in culture technique and differentiation protocols may also contribute to functional differences observed between studies. Overall, we found no statistically significant differences in sarcomere length, contractile stress, conduction velocity, and RMP due to the type of maturation technique (**Figure 3.5f-h**). Additionally, utilizing a greater number of maturation techniques did not improve hiPSC-CM performance (**Figure 3.5i-l**). For this analysis, maturation techniques were grouped as described in Figure 2. For instance, tissues formed between elastomeric pillars with stromal cells to aid in compaction would be considered to have utilized two maturation techniques. Thus, while individual studies have shown improvements in hiPSC-CM maturation compared to internal study controls as a function of employed maturation techniques or culture platforms, field-level findings do not reflect this.

Surprisingly, hiPSC-CMs matured with electrical stimulation did not perform as well as hiPSC-CMs matured with other approaches. There are many variables that contribute to differences in electrical stimulation protocols across studies, including the time between differentiation initiation and the beginning of stimulation, stimulation duration, and electrical pulse voltage, width, and frequency. For example, the frequency of stimulation can greatly impact the effect of electrical stimulation on hiPSC-CMs. One study showed that constant high-frequency

stimulation at 3 Hz leads to mitochondrial dysfunction and increased apoptosis in hiPSC-CMs, while low-frequency stimulation at 1 Hz did not (Geng et al. 2018). Another study showed that intensity-ramped frequencies improved the maturation of hiPSC-CMs, likely due to beneficial effects of mimicking the changes in electromechanical loading that occur during the fetal-postnatal transition of cardiomyocytes (Ronaldson-Bouchard et al. 2018).

Taken together, it is difficult to parse the individual impacts of each maturation technique because of the numerous variables involved including the choice of hiPSC line, differentiation protocols, culture platforms, and functional output measurement methods. It is clear from experimental controls that these maturation techniques exert a positive effect within a specific study. However, numerous variables at multiple levels prevent comparisons of outcomes across studies towards and therefore also limit convergence on the most promising maturation strategies.

3.7 Collective outlook for improved hiPSC-CM maturation

Comprehensive studies that directly compare current maturation techniques are essential to improving the function and reproducibility of hiPSC-CM models. One way to bypass the influence of protocol variability in determining which maturation techniques are most effective is through a series of studies directly comparing maturation techniques using the same few hiPSC lines within the same platform, culture conditions, measurement techniques, and assessment metrics. If research groups with expertise in specific maturation techniques, such as cyclic stretch, electrical stimulation, specific patterning techniques, and maturation media, for example, worked together to implement these techniques in the same setting, then the field could gain a better understanding of which components of the cardiomyocyte are most responsive to a given stimulation, and further, how changes in particular components impact different aspects of cell or

cardiac tissue function. Furthermore, measuring the same metrics with the same techniques and software is necessary for direct comparisons of hiPSC-CM functionality. The measurements should also be taken at the same time point, as time post-differentiation can affect the performance of hiPSC-CMs (Fukushima et al. 2020; de Lange et al. 2021). These incremental comparisons, exemplified in a study testing parameter effect on tissue engraftment *in vivo*, will allow the field to address the experimental "replication crisis" in the cardiac engineering space (Brady et al. 2023).

In addition to existing maturation techniques being examined, there are many other parameters that have been understudied as potentially important factors to systematically investigate. For example, the field still lacks consensus on what extracellular matrix composition best impact hiPSC-CM maturity or promote stable tissue formation. There exists high variability in ECM and ECM-like components used in hiPSC-CM models(Dickerson 2022), but there are very few studies investigating the effects of this variable on hiPSC-CM functionality (Kaiser et al. 2019; Tani et al. 2023). Not only does ECM composition impact maturation, but the ECM concentration and how it's presented to cells does as well (de Lange et al. 2021). An in-depth study on the effects of commonly used ECM compositions on hiPSC-CM maturation is desperately needed. This example highlights a common issue within the field of underpowered statistics needed to determine which variables have the largest impact on hiPSC-CM function. Many protocols across the field are developed and used by one or a handful of groups and are not systematically compared to other existing protocols. As such, we do not have sufficient data to identify which variables presented yield the best results, which in turn hampers the field from progressing.

To benchmark new approaches against prior literature and future studies, researchers should utilize the same control to report on a predetermined set of metrics. One study directly

compared hiPSC-CMs derived from ten different lines and showed wide variability in functional outputs within the same EHT platform (Mannhardt et al. 2020). To address this variability, each new study could compare functional properties of hiPSC-CM models to that of the same cell line, perhaps commercially available hiPSC-CMs such as already commonly used lines like iCell (Cellular Dynamics International) and Pluricyte (Ncardia) that come as pre-differentiated CMs, minimizing variability that arises from different differentiation protocols. The experimental techniques, such as maturation media or electrical stimulation, should be tested on hiPSC-CMs in a dish as well as in the engineered platform to separate the effects of experimental techniques from that of the platform on hiPSC-CM maturation. In addition to a shared control line, studies focused on improving hiPSC-CM maturity or platform development should utilize at least five hiPSC-CM lines to test the consistency of their protocols. Far more lines should be included when reporting pharmaceutical and therapeutic effects, including a representative number of lines from different sexes and ancestorial backgrounds to account for the variability in potential hiPSC-CM responses. There are increasing efforts to establish and share hiPSCs lines from different sexes and ancestorial backgrounds (Lv et al. 2024) that should then further be utilized in hiPSC-CM maturation platforms.

While we have highlighted the plethora of metrics used to assess hiPSC-CM structure and function, we propose converging on a few essential metrics that are widely accessible using the same methodology to enable direct comparisons across studies and labs. Some of the most reported metrics that provide important insight into hiPSC-CM maturation include sarcomere/myofibril morphometrics, contractile stress, conduction velocity, and gene expression. Some metrics, for example those related to sarcomere alignment highlighted above, are highly sensitive to the specific image analysis pipeline utilized. Thus, it would be critical to develop and jointly adopt

open-source analysis pipelines (Mohammadzadeh and Lejeune 2023; Pasqualini et al. 2015; Stein et al. 2022; Sutcliffe et al. 2018) that robustly handle data generated from a range of different platforms to enable direct comparison of data across experiments and labs. The need for open-source analysis pipelines is also important when quantifying contractile stress of hiPSC-CM platforms. Though we acknowledge that many pipelines are platform specific, including post-tracking algorithms (Tamargo et al. 2021), motion tracking analysis (Sala et al. 2018; Toepfer et al. 2019; B. Zhao et al. 2021), or traction force microscopy (A. J. S. Ribeiro et al. 2017), the ability to analyze datasets with common algorithms enables comparison and eventual convergence on optimal analysis pipelines. Further, we encourage the use of voltage-sensitive dyes, such as FluoVolt or Di-4-ANEPPS, or calcium-sensitive dyes, such as Fluo-4AM, to report conduction velocity (Soepriatna et al. 2023). Lastly, gene expression ratios of key maturation-related genes, such as *MYH7*/*MYH6*, *MYL2*/*MYL7*, and *TNNI3*/*TNNI1*, should be reported.

To begin to rigorously assess our progress as a field, we have created an accessible database with the protocol parameters and functional outputs of the 300 studies reported here. These data will allow researchers to determine current trends more easily within the field, directly compare studies, and extract the information needed to replicate a study (J. K. Ewoldt et al. 2023). We urge researchers to continue to add to this starting dataset with existing and upcoming publications not yet included, as well as to make their ongoing and new data available to be incorporated into this database moving forward so that it can stay current and provide a forum for coordinating progress.

Implementing common analysis software and experimental controls in future experiments, and subsequently updating this database with these new results will facilitate the growth of a resource that can be mined using machine learning techniques and high-dimensional data analysis techniques. Analyzing a more comprehensive dataset using such techniques could glean valuable

insights into the effects of specific maturation techniques or combinations thereof on maturation outcomes. While the current dataset presented here is currently the most comprehensive analysis in this space, the lack of consistency among studies and limited number of comparable datapoints makes such analyses quite challenging. For instance, multiple regression analysis on the impact of maturation techniques on reported tissue contractile stress did not yield useful information due to the limited number of papers that report contractile stress (33 out of 300 analyzed studies). Within these 33 studies, only a select few use the same maturation techniques, resulting in weak correlations quantified between said maturation techniques and key outputs such as contractile stress. As such, once a more comprehensive and consistent dataset can be compiled, these techniques and others could be leveraged to extract information that can guide continued progress of the field toward generating mature hiPSC-CMs and derivative cardiac tissue.

The multidisciplinary nature of the cardiac tissue engineering field brings together clinicians, biologists, and engineers. Clinicians provide insights into clinically relevant research questions for hiPSC-CM models; biologists have expertise in analyzing and assessing the maturation in addition to a deep understanding of biological processes occurring throughout cardiac development and hiPSC differentiation; and engineers design creative platforms to interrogate these clinical questions and develop algorithms to quantify the biological responses of hiPSC-CMs. Providing researchers from diverse perspectives with a standardized venue to report their findings will allow them to learn from each other and move forward more efficiently. These types of analyses will allow the field to streamline advances in developing models for drug discovery and therapies for cardiac pathologies.

3.8 Conclusion

In recent years, there has been significant progress in the field of cardiac tissue engineering toward generating mature tissues composed of hiPSC-CMs for use as disease models and drug screening platforms. However, quantitatively benchmarking progress across the field has proved challenging due to variability in many aspects of tissue formation, culture, and subsequent assessment, including the choice of hiPSC lines, differentiation protocols for generating CMs, platforms for forming tissues, maturation techniques, and various measurements used to assess cell or tissue function. Given the many sources of variability at multiple levels, it is difficult to ascertain which techniques are most effective in improving the maturation of hiPSC-CMs or derivative tissues formed from these cells. Here, we highlight the need for convergence on controls and quantitative analysis methods that will enable more efficient progress toward generating hiPSC-CM tissues that recapitulate adult cardiac physiology with utility for numerous applications. Further, we have made all data used in this analysis freely accessible and encourage others in the field to contribute to and utilize this database to better inform their ongoing research and support the collective advancement of the field as a whole (J. K. Ewoldt et al. 2023).

Supplemental Tables

Supplementary Table 3.1: We have provided the data compiled from our analysis described above so others in the field can utilize it to inform their research. This data is published on Dryad and will be updated as new data is compiled. Additionally, we hope to encourage other researchers to contribute to these benchmarking efforts and support the collective advancement of the field. If you would like to contribute new data to be included in the database, please fill out the form linked here, and a group of researchers within the CELL-MET Engineering Research Center will periodically review each new entry and update the database.

https://doi.org/10.5061/dryad.ksn02v7bh

Chapter 4: Microenvironmental Determinants of Organized iPSC-Cardiomyocyte Tissues in Synthetic Fibrous Matrices

4.1 Authors

Samuel J. DePalma, Christopher D. Davidson, Austin E. Stis, Adam S. Helms, Brendon M. Baker

4.2 Abstract

Cardiomyocytes derived from induced pluripotent stem cells (iPSC-CMs) show great potential for engineering myocardium to study cardiac disease and create regenerative therapies. However, iPSC-CMs typically possess a late embryonic stage phenotype, with cells failing to exhibit markers of mature adult tissue. This is due in part to insufficient knowledge and control of microenvironmental cues required to facilitate the organization and maturation of iPSC-CMs. Here, we employed a cell-adhesive, mechanically tunable synthetic fibrous extracellular matrix (ECM) consisting of electrospun dextran vinyl sulfone (DVS) fibers and examined how biochemical, architectural, and mechanical properties of the ECM impact iPSC-CM tissue assembly and subsequent function. Exploring a multidimensional parameter space spanning cell-adhesive ligand, seeding density, fiber alignment, and stiffness, we found that fibronectin-functionalized DVS matrices composed of highly aligned fibers with low stiffness optimally promoted the organization of functional iPSC-CM tissues. Tissues generated on these matrices

demonstrated improved calcium handling and increased end-to-end localization of N-cadherin as compared to micropatterned fibronectin lines or fibronectin-coated glass. Furthermore, DVS matrices supported long-term culture (45 days) of iPSC-CMs; N-cadherin end-to-end localization and connexin43 expression both increased as a function of time in culture. In sum, these findings demonstrate the importance of recapitulating the fibrous myocardial ECM in engineering structurally organized and functional iPSC-CM tissues.

4.3 Introduction

Heart disease is the leading cause of death worldwide (Virani et al. 2020). This is in part due to the fact that many cardiomyopathies lead to permanent damage to the myocardium, which has limited potential to regenerate. Existing therapies fail to restore cardiac function after damage arising from chronic conditions or traumatic injury from myocardial infarction (Funakoshi et al. 2016). Thus, there is a pressing need to develop engineered myocardial tissue that can be used in replacement or regenerative therapies. Additionally, physiologically representative *in vitro* models of cardiac tissue can aid in the advancement of our understanding of cardiac disease progression and the identification and subsequent development of effective pharmacologic interventions.

Cardiomyocytes derived from induced pluripotent stem cells (iPSC-CMs) show promise for engineering myocardium for regenerative therapies and for disease modeling (Karbassi et al. 2020). In recent years, there have been many advances in culture protocols to improve the efficiency of stem cell differentiation towards a myocardial lineage (Allen et al. 2019; Garbern et al. 2020; Ronaldson-Bouchard et al. 2018; X. Yang et al. 2019). However, in most cases, iPSC-CM maturation stops at the late embryonic stage, with cells failing to exhibit hallmarks of maturity such as myofibril alignment, end-to-end polarization of gap junctions, and enhanced calcium

handling (Karbassi et al. 2020; Uosaki et al. 2015). More recent studies have demonstrated the ability to achieve higher levels of engineered cardiac tissue maturation through the use of naturally derived biomaterials (e.g. collagen, fibrin, and Matrigel) combined with iPSC-CMs and stromal cells, such as fibroblasts or mesenchymal stem cells (Giacomelli et al. 2020; Ronaldson-Bouchard et al. 2018; Shadrin et al. 2017). Despite their success in improving the function of engineered cardiac tissues, the incorporation of stromal cell populations can confound study interpretation due to uncontrolled and uncharacterized crosstalk between these stromal support cells and cardiomyocytes (CMs). Therefore, there remains a need to engineer materials that can accurately present the appropriate physical and mechanical cues present in the native ECM to promote myocyte tissue formation in the absence of supporting cells.

The mechanical function of the myocardium is dictated by contractile CMs and the fibrous ECM that surrounds, orients, and groups them (Karl T. Weber 1989). This complex, hierarchical collagen network organizes myocardium at multiple length scales: 1) epimysial collagen fibers surround large groups of muscle bundles to provide mechanical stability preventing excessive stretching of the tissue; 2) perimysial fibers wrap around and organize individual bundles of CMs; 3) small endomysial fibers found within each bundle connect to the cytoskeleton of each CM via costameres (Fleischer and Dvir 2013; Karl T. Weber 1989; Karl T. Weber et al. 1994). In particular, perimysial collagen fibers are approximately 1 μm in diameter and are co-aligned along the long axis of each CM bundle (Pope et al. 2008). The structural organization of surrounding perimysial fiber networks parallel that of the myofibers within each muscle bundle. Together, highly aligned CMs and surrounding ECM enable mechanically anisotropic contractions critical to healthy cardiac function. The importance of this structure-function relationship is particularly evident in disease states such as fibrosis where fibroblasts deposit excessive amounts of

disorganized matrix in the perimysial space, impairing overall tissue function (M. D. Davidson, Burdick, and Wells 2020; Kong, Christia, and Frangogiannis 2014; Karl T. Weber 1989).

As it is evident that organized fibrous ECM plays a critical role in facilitating myofibrillar alignment, a number of material platforms have been developed to recapitulate these cell-instructive cues to drive structural and functional maturation of engineered cardiac tissue. ECM proteins can be micropatterned into anisotropic geometries (e.g. lines or rectangles) to organize attached CMs and improve tissue functionality (McCain et al. 2012; A. J. S. Ribeiro et al. 2015; Sheehy et al. 2017). However, these substrates lack cell-scale topographical cues reminiscent of perimysial matrix which may be required for myocardial tissue assembly and function. Attempts to better recapitulate cardiac ECM topography have included culturing iPSC-CMs on nanogrooved substrates (Carson et al. 2016; Luna et al. 2011). While these methods promote robust structural alignment and higher tissue maturity, they lack mechanical tunability and fail to accurately mimic the complex fibrous topography cells experience *in vivo*. Electrospun scaffolds come closest to recapitulating perimysial network architecture, but commonly used electrospun biomaterials (e.g. polycaprolactone, polylactide-co-glycolide, or polyvinyl alcohol) are typically orders of magnitude stiffer than CMs or cardiac ECM (Allen et al. 2019; Fleischer et al. 2015; Khan et al. 2015; Kharaziha et al. 2013; J. Li et al. 2017; Yu et al. 2014). This is particularly important given recent evidence that culture substrates with elastic moduli approximating that of native myocardium can enhance myofibril formation and overall tissue maturity (Engler et al. 2008; Herum et al. 2017; Jacot, McCulloch, and Omens 2008; Young and Engler 2011). Despite the success of these and other culture platforms in improving iPSC-CM tissue function, each of these approaches only mimic certain aspects of the cardiac ECM. As such, a comprehensive, multiparameter understanding of the physical environmental cues necessary to form high-

functioning CM tissues is currently lacking. Thus, new biomaterial approaches are needed that can accurately and orthogonally recapitulate fibrous, biochemical, and mechanical attributes of the cardiac ECM to promote further maturation.

We previously developed a synthetic fibrous ECM-like material composed of polymeric fibers with comparable geometry to perimysial collagen fibers (C.D. Davidson et al. 2020). These fibers have a highly tunable elasticity over a range reflecting measurements of type I collagen fibers and enable user-defined control over presented adhesive ligands and overall architectural organization. In this work, we alter biochemical, architectural, and mechanical properties of these synthetic fibrous matrices to identify critical ECM determinants to iPSC-CM attachment and subsequent tissue assembly, structure, and function. Systematically exploring a multidimensional biomaterial parameter space, we find that soft, aligned DVS networks presenting fibronectin (FN) promote the highest levels of structural organization and function as assessed by calcium flux imaging. Additionally, we compare iPSC-CMs cultured in our material system to commonly used CM culture platforms that lack anisotropic adhesive cues or topography and find that compliant and aligned fibrous ECM yields the highest degree of iPSC-CM tissue organization and function. Lastly, we demonstrate the ability of DVS fiber matrices to facilitate long-term culture of iPSC-CMs that enables further structural organization as evidenced by end-to-end localization of cell-cell adhesions. Taken together, these studies highlight the importance of recapitulating key physical attributes of the cardiac extracellular microenvironment and isolating their respective influences on iPSC-CM tissues formation and maturation.

4.4 Results and Discussion

4.4.1 Synthetic extracellular matrix fabrication and iPSC-CM seeding parameters

To mimic perimysial collagen networks of native myocardium, we fabricated fibrous matrices composed of electrospun DVS fibers following methods established in our lab (C.D. Davidson et al. 2020). We previously used this material system to investigate the effects of physical matrix properties on cell behaviors including fibroblast spreading and myofibroblast differentiation (C.D. Davidson et al. 2020; Matera et al. 2019). These studies demonstrated the mechanical tunability, biocompatibility, and stability of this material over long-term culture thus motivating its use as suitable platform for studying iPSC-CM engineered tissue formation. Here, we altered biochemical, architectural, and mechanical parameters to examine how each feature impacts the structure and function of iPSC-CM tissues. Controlling the speed of a rotating, hexagonal mandrel with affixed glass coverslips reproducibly defined the degree of fiber alignment within each matrix (**Figure 4.1a-c)**. Control over subsequent photoinitiated free radical polymerization via LAP photoinitiator concentration defined the degree of crosslinking within each fiber and resulting stiffness of bulk matrices (**Figure 4.1e**). To facilitate cell attachment, fibers were functionalized with short cell-adhesive peptides cRGD or GFOGER directly coupled to remaining VS groups via Michael type addition. Alternatively, HepMA was covalently coupled to remaining VS groups to enable functionalization with full length heparin sulfate proteoglycan (HSPG)-binding ECM proteins, including collagen and fibronectin (**Figure 4.1d**). iPSC-derived CMs were differentiated and purified as previously described (Lian et al. 2012; Tohyama et al. 2013, 2016), then seeded on substrates of varying material parameters and subsequently characterized by immunostaining and calcium imaging (**Figure 4.1f**). Differentiation of iPSC-CMs was further confirmed by immunofluorescent staining of α-actinin and cardiac troponin T (**Supplementary Figure 4.3**). In contrast to electrospun materials that have been previously used to induce cardiac tissue organization and function, DVS matrices provide concurrent architectural,

mechanical, and biochemical control, enabling careful dissection of how iPSC-CMs respond to critical ECM features known to vary with the age and disease status of cardiac tissue (Jacot, Martin, and Hunt 2010; Kong, Christia, and Frangogiannis 2014; Mccormick and Thomas 1998; Corin Williams and Black 2015).

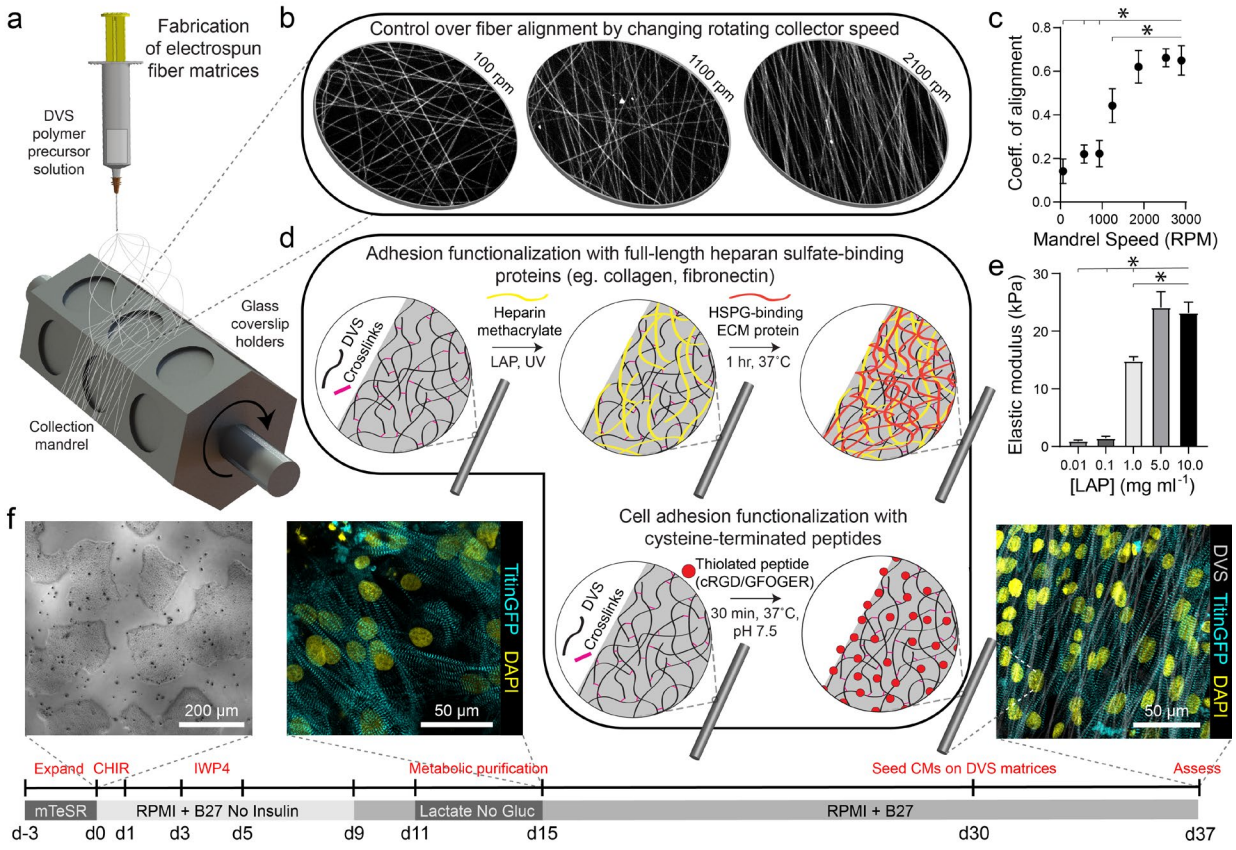

Figure 4.1: Tunable DVS fibrous matrices for culturing iPSC-CMs. (a) Schematic of fabrication setup used to generate DVS matrices. A photocrosslinkable DVS polymer solution was electrospun and collected on glass coverslips affixed to a rotating hexagonal mandrel. (b,c) Mandrel rotation speed was varied to define fiber alignment. (d) To facilitate cell adhesion, fibers were functionalized with full length proteins fibronectin or collagen via a heparin sulfate conjugation scheme, or short adhesive peptides cRGD or GFOGER via Michael-type addition chemistry. (e) Fiber stiffness was tuned by altering the amount of photoinitiated crosslinking. (f) iPSCs were differentiated through temporal modulation of the Wnt signaling pathway as previously described (Lian et al. 2012), purified via metabolic selection for at least 4 days, and seeded on DVS fibrous substrates 30 days post initiation of differentiation. Progression of the differentiation process can be seen from brightfield images of iPSCs taken before differentiating,

immunofluorescent images of iPSC-CMs just after metabolic selection, and iPSC-CMs seeded on aligned DVS matrices. All data presented as mean ± std; $n \geq 5$ matrices; * $p < 0.05$.

Having defined parameters to control biochemical and biophysical attributes of DVS matrices, we next sought to identify adhesive ligands that facilitate robust iPSC-CM attachment to aligned DVS fiber matrices, given previous observations that anisotropic substrates promote the formation of organized cardiac tissues (Allen et al. 2019; Carson et al. 2016; Sheehy et al. 2017; Wanjare et al. 2017). Matrices were functionalized for cell adhesion with full length ECM proteins type I collagen or fibronectin, or shorter peptides containing their integrin-binding domains, GFOGER or cRGD, respectively. Fiber diameter remained consistant regardless of functionalization scheme (**Supplementary Figure 4.4a**). Overall, there was less robust iPSC-CM adhesion on substrates modified with GFOGER or full length type I collagen as compared to cRGD or fibronectin (**Figure 4.2a,b**). In general, engineered healthy myocardium exhibits regular and synchronous patterns of calcium flux as well as highly aligned contractile machinery, as aberrations to these characteristics have been implicated in a number of disease states, including cardiac fibrosis (Kong, Christia, and Frangogiannis 2014; A. Kumar et al. 2019). Therefore, the overall functionality of iPSC-CM tissues was assessed by live imaging with a calcium sensitive dye after an additional 7 days of culture on engineered substrates. The spontaneous beat rate of tissues was found to be consistent across adhesive moieties (**Figure 4.2c**). We found that tissues cultured on matrices presenting cRGD or fibronectin contract with a more regular frequency and more synchronously across the tissue surface (**Figure 4.2d,e; Supplementary Figure 4.1; Supplementary Movie 4.1**). These findings are in line with the critical role of fibronectin in myocardial development and in facilitating CM integrin engagement to the ECM *in vivo* (Farhadian et al. 1995; Lockhart et al. 2011). Inhibition o10af the integrin α5 subunit, a receptor

that predominately binds fibronectin, during cardiac development has demonstrated a critical role for this specific binding moiety in cardiac morphogenesis (Israeli-Rosenberg et al. 2014; Mittal et al. 2013). More recently, Neiman et al. highlighted the importance of the α5 subunit in iPSC differentiation to CMs *in vitro*, as knockdown of this integrin resulted in less efficient differentiation, implying that integrin binding could also dictate CM maturation (Neiman et al. 2019). These results indicate that fibronectin or its cRGD derivative exhibit superior capacity for *in vitro* cardiac tissue generation on our fibrous matrices as compared to collagen. Although no functional differences in tissues created on fibronectin and cRGD functionalized matrices were noted, full-length fibronectin was utilized in all subsequent studies described below, given its importance in the cardiac ECM and widespread use in other iPSC-CM studies (Chopra et al. 2018; Farhadian et al. 1995; S. Sengupta et al. 2019; Sheehy et al. 2017). Previous work has also demonstrated the potential utility of functionalizing ECM mimetic scaffolds with developmentally informed bioactive ligands to direct stem cell differentiation (Bian et al. 2013; R. Li et al. 2019; Padin-Iruega et al. 2009). For example, Li et al. showed that coupling a Wnt5a mimetic ligand, Foxy5, to hyaluronic acid scaffolds increased noncanonical Wnt signaling, enhanced mechanotransduction through RhoA-ROCK signaling, and drove osteogenic differentiation of human mesenchymal stem cells (R. Li et al. 2019). In separate studies, cardiac tissue regeneration was improved post-infarction after the introduction of nanofibers functionalized with insulin-like growth factor 1 (Padin-Iruega et al. 2009). Thus, the effect of presenting other bioactive ligands in addition to integrin-binding proteins or peptides is worth exploring in future work.

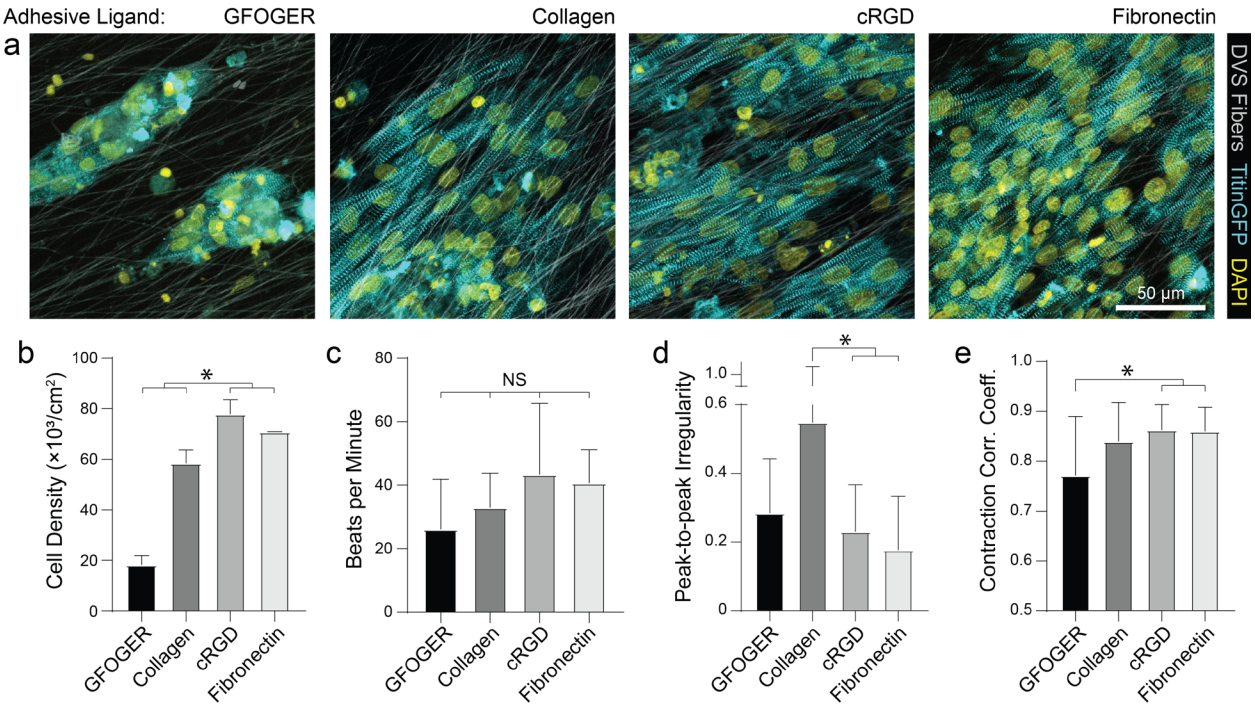

Figure 4.2: DVS functionalization with FN and cRGD increase cell attachment and enable formation of contractile tissues. (a) Confocal fluorescent images of iPSC-CMs cultured on aligned DVS matrices functionalized with different cell-adhesive proteins or peptides. (b) Density of resultant iPSC-CM tissues on fibers functionalized with different cell adhesion functionalization schemes. Calcium flux dynamics were analyzed to determine (c) contraction rate, (d) peak-to-peak irregularity, as quantified by the standard deviation of time interval between peaks, and (e) contraction correlation coefficient for formed tissues, as calculated by Pearson's correlation coefficient between fluorescent profiles of subdivided regions within a field of view. All data presented as mean ± std; $n \geq 8$ fields of view across 3 tissues; * $p < 0.05$.

As different adhesive ligands resulted in variations in attachment and subsequent CM density that correlated with calcium transient synchronicity, we next sought to determine the optimal density of CMs required to create an organized and functional layer of tissue on DVS matrices (**Figure 4.3a**). At low seeding densities (50 and 100 k/cm^2), myofibrils were highly aligned, as quantified by image analysis of titinGFP-demarcated sarcomeres (**Supplementary Figure 4.2**), however confluent monolayers did not form across the matrix (**Figure 4.3a-c**). Disconnections across the monolayer resulted in greater beat irregularity and lower synchronicity across the tissue (**Figure 4.3e-f; Supplementary Movie 4.2**). At higher seeding densities (200

and 250 k/cm^2), beat rates were more consistent and synchronous, but an increase in the angular deviation of myofibrils was noted (**Figure 4.3a-f; Supplementary Movie 4.2**). Optical sectioning through the thickness of tissues by confocal microscopy revealed that cells directly in contact with the underlying matrix possessed highly aligned myofibrils (**Figure 4.3g-h**). iPSC-CMs farther away from the matrix surface were increasingly disorganized as evidenced by an increase in myofibril angular deviation (**Figure 4.3g-h**). These results highlight the significant role that ECM architecture plays in iPSC-CM organization (Pope et al. 2008; Karl T. Weber 1989). Given these findings, an intermediate seeding density (150k/cm^2) that yields a confluent layer of iPSC-CMs where all cells receive alignment cues from the underlying matrix was selected for subsequent studies. CM density has also been shown to affect overall tissue function in other previously established *in vitro* models (Shadrin et al. 2017). Shadrin et al. found that iPSC-CMs in a 3D hydrogel at high densities had reduced force output per cell and increased conduction velocity, most likely due to restricted space for CMs to grow in these dense tissues (Shadrin et al. 2017). These findings further motivate the use of intermediate seeding densities on DVS where iPSC-CMs are given adequate space to spread as they sense the fibrous matrix below.

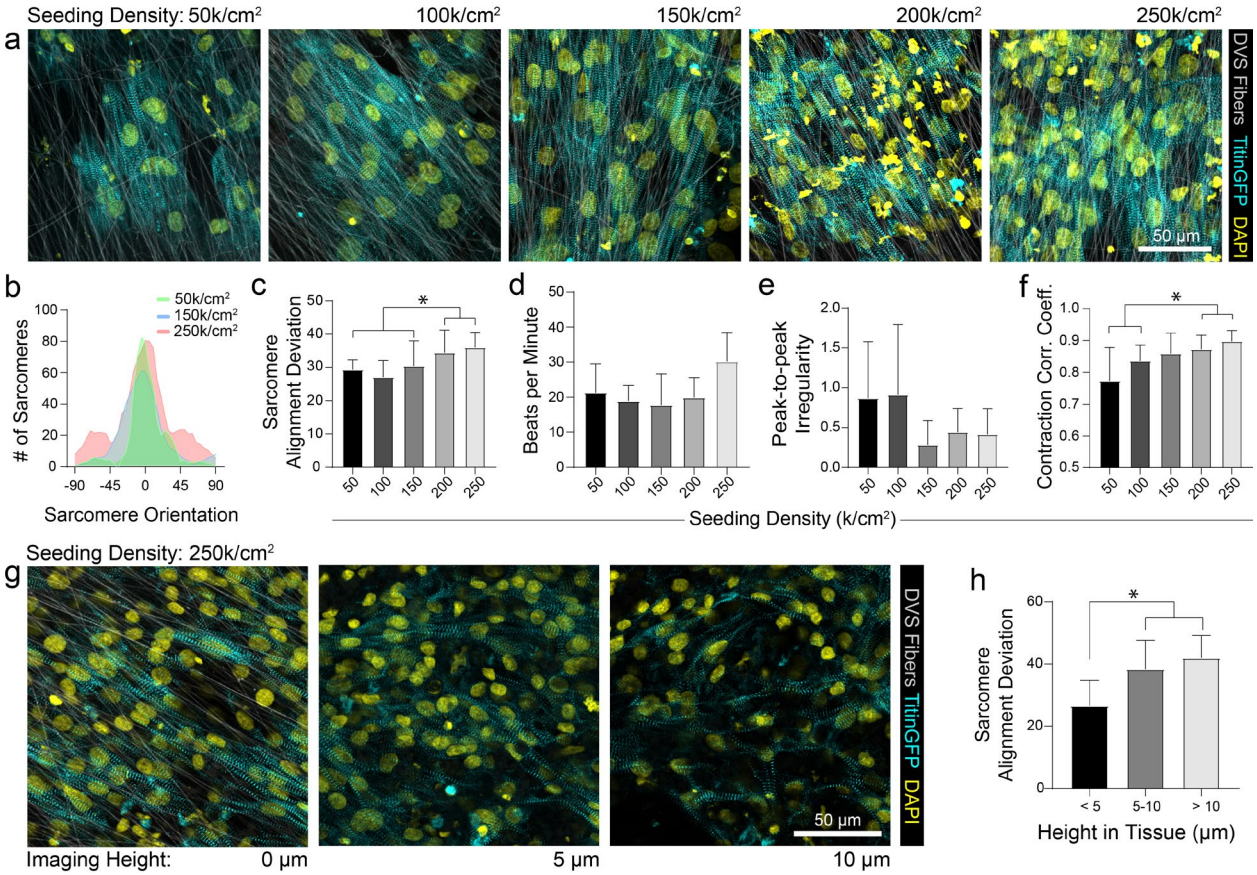

Figure 4.3: iPSC-CMs at intermediate seeding density form highly organized and functional tissues. (a) Confocal fluorescent images of iPSC-CMs on aligned DVS matrices functionalized with fibronectin seeded at different densities ranging from 50 to 250 k/cm^2. (b) Histogram of distribution of sarcomere angle in representative tissues seeded at 50, 150, and 250 k/cm^2. (c) Quantification of overall sarcomere alignment of tissues seeded at densities ranging from 50 to 250 k/cm^2. (d) Beat rate, (e) peak-to-peak irregularity and (f) contraction correlation coefficient for formed tissues obtained via analysis of calcium fluxes. (g) Image slices at 0, 5, and 10 µm from substrate surface taken via confocal microscopy within a dense (250 k/cm^2) tissue. (h) Sarcomere alignment deviation of slices within specified height ranges for tissues seeded at 250 k/cm^2. All data presented as mean ± std; n ≥ 8 fields of view across 3 tissues; * $p < 0.05$.

4.4.2 Effect of altered matrix alignment and mechanics on iPSC-CMs

The preceding studies imply that contact with aligned fibrous matrices is critical for creating iPSC-CM tissues with organized myofibrils. To confirm that matrix architecture dictates tissue organization, we next examined how alterations to the alignment of the fibrous matrices

affect iPSC-CM tissue organization and function. As previously described, fiber alignment can be easily defined by changing the speed of the rotating collector (**Figure 4.1c**). Seeding iPSC-CMs on nonaligned (100 RPM; 0.916 m s^{-1}), intermediate (1100 RPM; 10.1 m s^{-1}), and aligned (2100 RPM; 19.3 m s^{-1}) matrices resulted in increasing levels of myofibril organization (**Figure 4.4a,b**). Matrix alignment also resulted in increased synchronicity across the tissue but no change in peak-to-peak irregularity (**Figure 4.4c,d; Supplementary Movie 4.3**). Furthermore, tissues formed on nonaligned matrices exhibited longer calcium flux rise and decay times (**Figure 4.4e**), both of which are established indicators of immaturity in tissues (Ronaldson-Bouchard et al. 2018; Shadrin et al. 2017). This finding is consistent with other studies indicating the importance of matrix anisotropy in generating cardiac tissues with enhanced organization and calcium handling (Allen et al. 2019; Carson et al. 2016; Sheehy et al. 2017; Wanjare et al. 2017). Interestingly, the data presented here suggests that while the highest degree of fiber alignment induced greater myofibril alignment (**Figure 4.4b**), an intermediate degree of fiber alignment was sufficient for rapid calcium handling (**Figure 4.4c-e**). Previous studies have shown that integrin organization and overall structural anisotropy directly influences the organization and expression of calcium handling machinery within cardiomyocytes, leading to changes in overall tissue function (Karbassi et al. 2020; A. J. S. Ribeiro et al. 2015; S. Sengupta et al. 2019). These data suggest however that only an intermediate degree of adhesive or topographical anisotropy is necessary to elicit functional improvements. As fine control over matrix alignment is straightforward with this platform, future studies could explore how matrix alignment guides subcellular organization in the contexts of cardiac development, during which the ECM transitions from disorganized to highly ordered between gestation days 100 and 143 (Corin Williams and Black 2015), or disease

progression, characterized by increasing deposition of disorganized matrix (Kong, Christia, and Frangogiannis 2014; Karl T. Weber 1989).

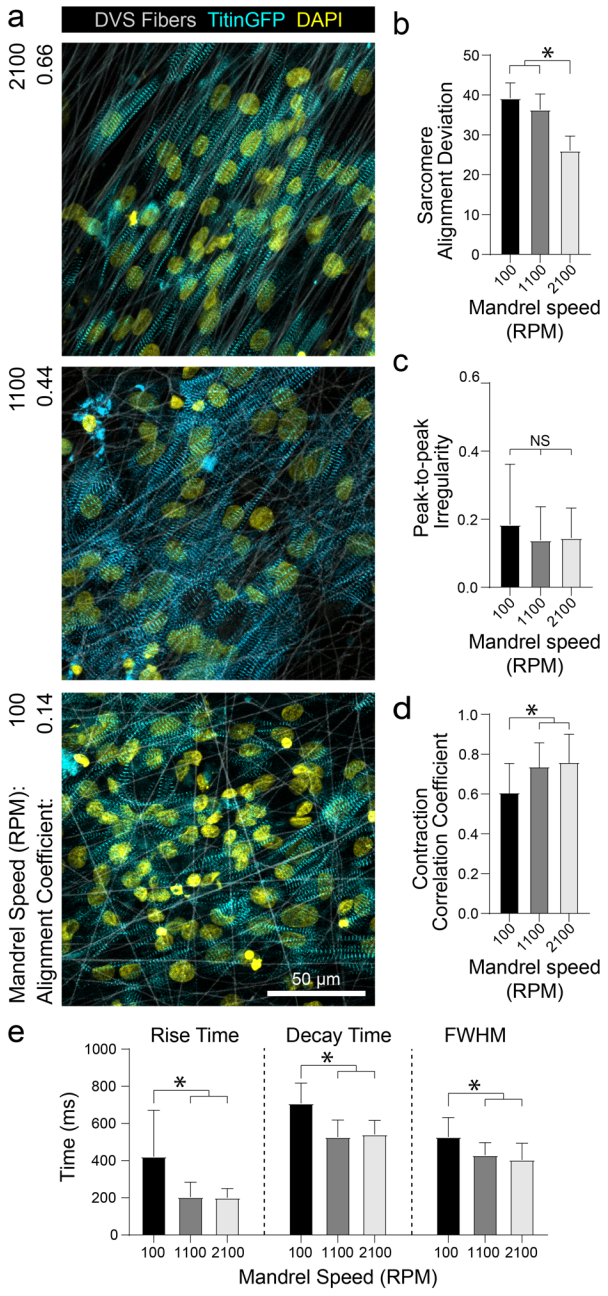

Figure 4.4: Aligned matrices promote myofibril organization and improve tissue function. (a) Confocal fluorescent images of iPSC-CMs seeded on aligned (2100 RPM), intermediate (1100 RPM), and random (100 RPM). (b) Quantification of sarcomere alignment deviation. (c) Peak-to-peak and (d) correlation coefficient irregularity, as calculated from calcium flux data. (e)

Individual calcium fluxes were analyzed to determine flux rise time, decay time, and peak full width half max. All data presented as mean ± std; $n \geq 12$ fields of view across 3 tissues; * $p < 0.05$.

In conjunction with organizational cues, substrate stiffness close to that of healthy cardiac tissues has also been shown to promote further functional maturation of CMs compared to culture on tissue culture plastic or glass (Herron et al. 2016; Jacot, McCulloch, and Omens 2008; A. J. S. Ribeiro et al. 2015; Young and Engler 2011). For example, Riberio et al. showed that culturing CMs on non-fibrous hydrogel substrates approximating the stiffness of myocardium (~10 kPa) resulted in higher functioning CMs, whereas stiffer substrates hindered structural, functional, and transcriptional development of iPSC-CMs (A. J. S. Ribeiro et al. 2015). These findings have been corroborated by studies using other hydrogel systems (Engler et al. 2008; Jacot, McCulloch, and Omens 2008; Young and Engler 2011), but these settings fail to recapitulate the fibrous architecture of native cardiac ECM. Additionally, electrospun fibrous materials used to induce greater iPSC-CM function are typically supraphysiologic in stiffness and lack mechanical tunability (Allen et al. 2019; Fleischer et al. 2015; Wanjare et al. 2017). After defining matrix architecture, DVS matrix stiffness can be tuned over the range of Young's moduli reported for developmental (< 6 kPa), physiologic (9-14 kPa), and pathophysiologic myocardial tissues (> 20 kPa) (Engler et al. 2008) via tuning photocrosslinking (**Figure 4.1d**) (C.D. Davidson et al. 2020).

To examine if iPSC-CMs sense changes to the stiffness of fibrous matrices, we controlled the amount of photoinitiated crosslinking of the DVS fibers while keeping matrix fiber density and alignment constant (C.D. Davidson et al. 2020). Altering the stiffness of the underlying fibers had no effect on myofibril alignment or beat synchronicity (**Figure 4.5a-b,d**). However, iPSC-CMs cultured on low stiffness fibers (~1 kPa) resulted in greater calcium flux regularity with faster calcium fluxes in contrast to tissues generated on stiffer fibers (>20 kPa) (**Figure 4.5c,e;**

Supplementary Movie 4.4). These findings indicate that CMs can sense the stiffness of the matrix despite the fact that fibers were tethered to an underlying rigid glass surface that did not support fractional shortening of contracting tissues. This mechanoresponse may potentially be modulated by non-muscle myosin activity at costameres or integrin clustering, both of which have been previously shown to activate structural and functional changes in CMs (Chan and Odde 2008; Pandey et al. 2018; S. Sengupta et al. 2019). There was also evidence of cell force-mediated matrix deformations and permanent reorganization on soft fiber matrices, as indicated by lateral translocations of fibers; in contrast, no deformations were evident in matrices of stiffer fibers (**Supplementary Figure 4.5**). Additionally, as it has been suggested that CM proliferation can increase on stiffer substrates (Bajaj et al. 2010), we examined iPSC-CM proliferation after 7 days of culture by immunostaining for Ki67, a proliferation marker. We find that iPSC-CMs on DVS matrices exhibited low proliferation rates with no differences noted across the range of stiffnesses explored here (**Supplementary Figure 4.6**).

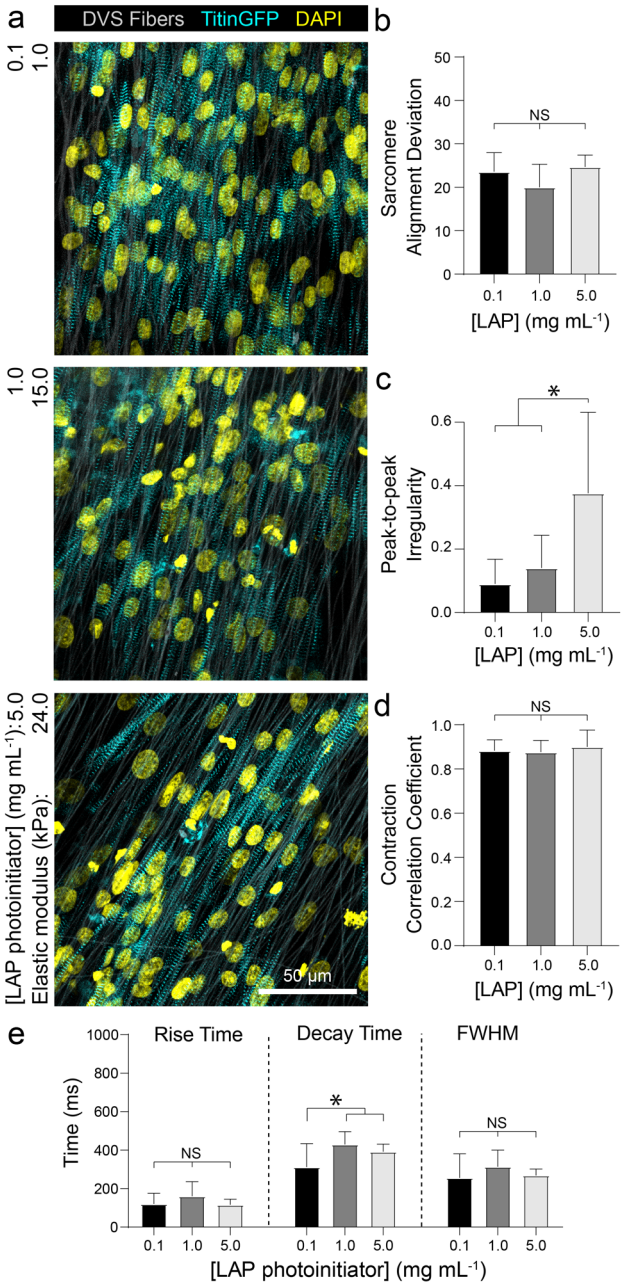

Figure 4.5: iPSC-CMs on soft, DVS fibers exhibit improved calcium handling. (a) Confocal fluorescent images of iPSC-CMs seeded on aligned matrices composed of DVS fibers of differing stiffnesses by tuning photoinitiated crosslinking via photoinitiator (LAP) concentration. (b) Quantification of sarcomere alignment deviation. (c) Correlation coefficient and (d) peak-to-peak irregularity, as calculated from calcium flux data. (e) Individual calcium fluxes were analyzed to determine flux rise time, decay time, and peak full width half max. All data presented as mean ± std; n ≥ 12 fields of view across 3 tissues; * $p < 0.05$.

After examining how matrix architecture and mechanics independently alter iPSC-CM organization and function, we next explored how simultaneously altering these two physical properties influence iPSC-CM-matrix interactions. iPSC-CMs were seeded on DVS matrices with orthogonally varied alignment and stiffness and immunostained for the focal adhesion (FA) protein, vinculin. Custom image analysis was used to segment and quantify the total FA area per cell, the average size of individual FAs within each cell, and the aspect ratio of adhesions (**Supplementary Figure 4.7a**). While the alignment of matrix fibers increased the aspect ratio and size of individual FAs (**Supplementary Figure 4.7c,d**), total FA area per cell appeared to be affected by both fiber organization and stiffness, with soft/non-aligned fibers expressing similar overall FA area to both soft/aligned and stiff/aligned matrices (**Supplementary Figure 4.7b**). Softer matrices may lead to increased FA adhesion formation via the increased nanoscale flexibility of adhesive ligands, thereby enabling integrin clustering required for focal adhesion formation (Arnold et al. 2004; C.D. Davidson et al. 2020; Houseman and Mrksich 2001; Trappmann et al. 2012). Additionally, we qualitatively noted an impact on the organization of FAs which aligned with their long axis in the direction of myofibrils and underlying DVS fibers. On aligned matrices, FAs appeared to co-localize with sarcomeres, potentially to optimally mechanically support the more organized contractile myofibrils within aligned iPSC-CMs. The influence of fiber alignment on iPSC-CM myofibril assembly and organization may explain the equivalent total FAs area per cell of stiff/aligned matrices as compared to soft/aligned or soft/nonaligned matrices (McCain et al. 2012). This potential additive effect is reiterated by the marked increase in FA aspect ratio on soft aligned matrices as compared to all other matrix conditions (**Supplementary Figure 4.7**). These results highlight the importance of orthogonally

controlling fiber organization and mechanics when studying how CMs respond to changes in their microenvironment.

4.4.3 DVS matrices afford improved tissue organization and function over other platforms

While ECM-coated tissue culture plastic or glass remain a typical setting for studies of iPSC-CMs, the use of micropatterned or topographical substrates to promote tissue organization and improve overall function has become increasingly common (Allen et al. 2019; Carson et al. 2016; Fleischer et al. 2015; A. J. S. Ribeiro et al. 2015; Sheehy et al. 2017; Wanjare et al. 2017). To explore the relative importance of anisotropic adhesive patterning vs. topographical cues, we compared tissue organization and calcium handling characteristics of iPSC-CMs cultured on fibronectin-functionalized DVS matrices, microcontact-printed fibronectin lines, and fibronectin adsorbed to glass substrates (**Figure 4.6**). Soft aligned DexVS matrices were selected for this comparison, as they guided the formation of the highest functioning tissues in the studies above. Microcontact-printed arrays of fibronectin lines (3 μm width with 3 μm spacing) on glass were chosen to approximate the adhesive surface area and alignment of DVS fibers and non-patterned fibronectin-coated glass served as a control. Functionally, iPSC-CMs seeded on DVS matrices exhibited more regular and synchronous calcium transients compared to tissues on micropatterned and non-patterned fibronectin (**Figure 4.6b,c; Supplementary Movie 4.5**). Furthermore, DVS induced faster rise and decay times in calcium fluxes (**Figure 4.6d**). Structurally, iPSC-CMs on DVS matrices exhibited the highest levels of myofibrillar organization (**Figure 4.6a,b**). As the native myocardium matures, proteins such as N-cadherin and connexin43 localize end-to-end at intercalated discs to enable directional propagation of action potentials (Vreeker et al. 2014). Immunostaining for N-cadherin, we noted more frequent end-to-end localization of N-cadherin on DVS matrices than on glass controls or micropatterned lines where such localization was not

observed (**Figure 4.6a**). Although the mechanism mediating this localization requires further study, this observation suggests a critical requirement for both topography and anisotropic adhesive cues afforded by fibers. Taken together, these studies highlight the importance of recapitulating the geometry and organization of perimysial fibers for promoting maturation of engineered iPSC-CM tissues (**Figure 4.6a**).

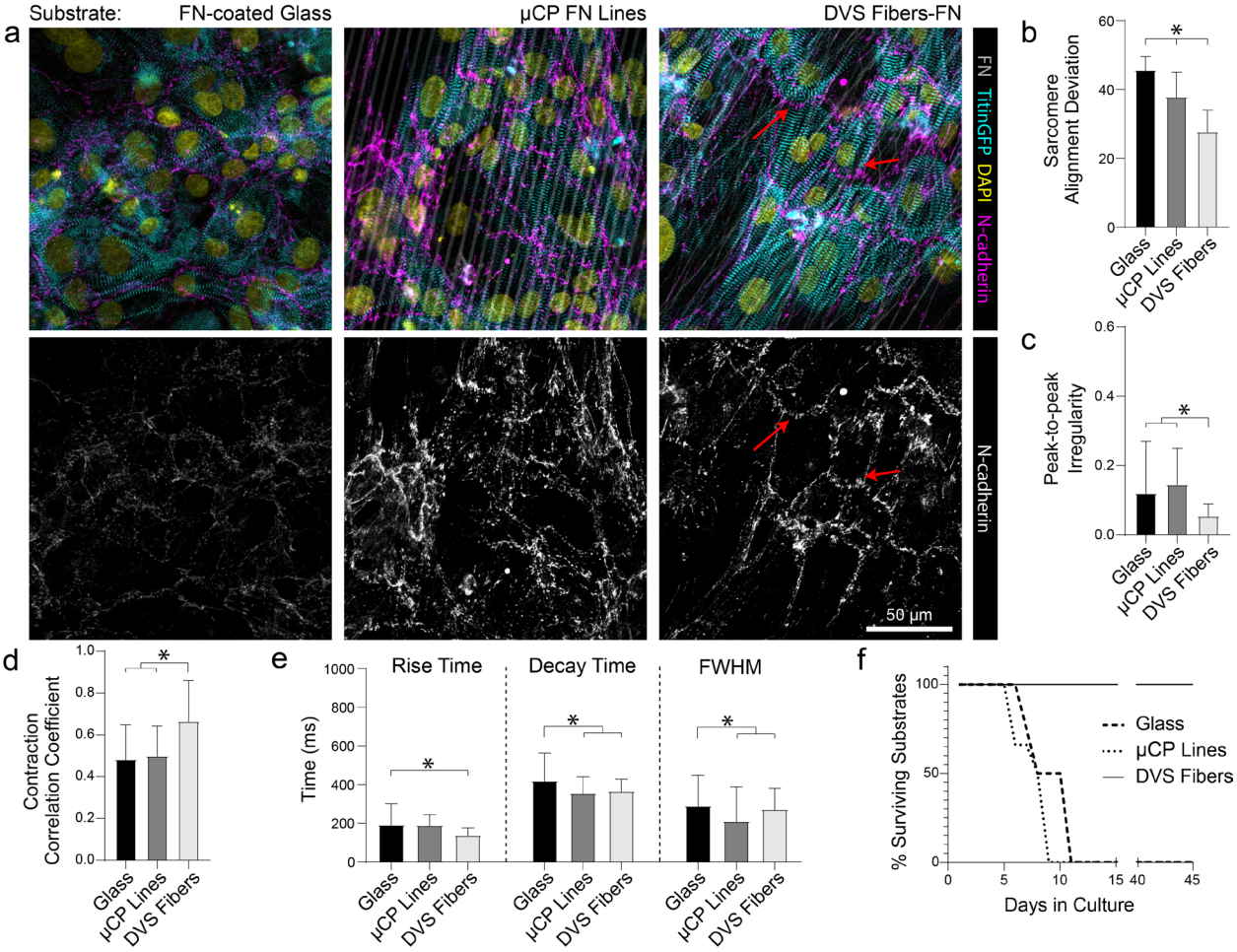

Figure 4.6: Fibrous DVS matrices promote increased tissue function and organization and allow for long-term culture of confluent iPSC-CMs. (a) Confocal fluorescent images of iPSC-CMs seeded on fibronectin-coated glass, microcontact printed fibronectin lines, and aligned DVS fibers modified with adhesive fibronectin after 7 days in culture. Red arrows indicate areas of N-cadherin localization at end-end cell junctions. (b) Quantification of sarcomere angle deviation across all substrates. (c) Calcium handling quantifications of peak-to-peak irregularity, (d) contraction correlation coefficient, and (e) flux rise time, decay time, and full width half max. (f)

Survival of cultures over time on various substrates. All data presented as mean ± std; n ≥ 12 fields of view across 3 tissues; * $p < 0.05$.

4.4.4 Long term culture of iPSC-CMs on DVS matrices

In addition to these improvements in subcellular organization quantified after 7 days in culture, DVS matrices also supported long-term culture of iPSC-CMs. Whereas confluent iPSC-CMs seeded on both micropatterned and non-patterned fibronectin detached from underlying substrates after 8-10 days of culture due to their innate contractile forces, DVS matrices enabled culture of purified confluent iPSC-CMs to at least 45 days post-seeding (**Figure 4.6f**). High magnification imaging of tissues immunostained for vinculin demonstrated increased numbers of costameres distributed at greater density across multiple imaging planes in DVS matrices compared to standard substrates (**Supplementary Figure 4.8**). This suggests that the three-dimensional nature of DVS fibers promotes increased cell-ECM adhesion to stabilize tissues. Long-term culture of iPSC-CM on fibrous matrices could facilitate time-dependent maturation processes required for intercalated disc assembly or T-tubule formation (Karbassi et al. 2020). A number of other studies have also applied external mechanical or electrical stimuli to drive maturation of tissues (Mihic et al. 2014; Ronaldson-Bouchard et al. 2018; Ruan et al. 2015, 2016). Given the long-term stability of these tissues and the facile deposition of DVS fibers on elastomer or electrically conductive substrates, future studies will explore these important maturation signals.

Previous work has shown that long-term culture (up to 45 days) of non-confluent iPSC-CM facilitates further maturation, as characterized by improved sarcomere organization, hypertrophy, reduced proliferation, and enhanced calcium handling (Karbassi et al. 2020; Lundy et al. 2013). As we observed improved iPSC-CM subcellular organization and function after 7 days on DVS matrices, we hypothesized that prolonged culture of pure, confluent iPSC-CMs could

facilitate further maturation. Culturing iPSC-CMs on soft, aligned DexVS matrices for up to 28 days, we observed no changes in calcium handling outputs including rise and decay time as a function of culture duration (**Figure 4.7e-g**). End-to-end localization of N-cadherin to intercellular junctions was evident at all time points while myofibril alignment remained constant (**Figure 4.7a,b**). Since connexin43 accumulates in developing gap junctions during development, we also stained for this protein in tissues on aligned DVS matrices (Fishman et al. 1991; Vreeker et al. 2014). Immunostaining for connexin43 revealed increased production as a function of culture duration, further indicating that anisotropic fibrous cues drive the assembly of key subcellular structures (**Figure 4.7c,d; Supplementary Figure 4.9**). Changes in connexin43 localization and other maturation markers over time warrants further study, and in sum we conclude that while structural cues guide tissue organization and function, they alone are not sufficient for driving significant iPSC-CM tissue maturity.

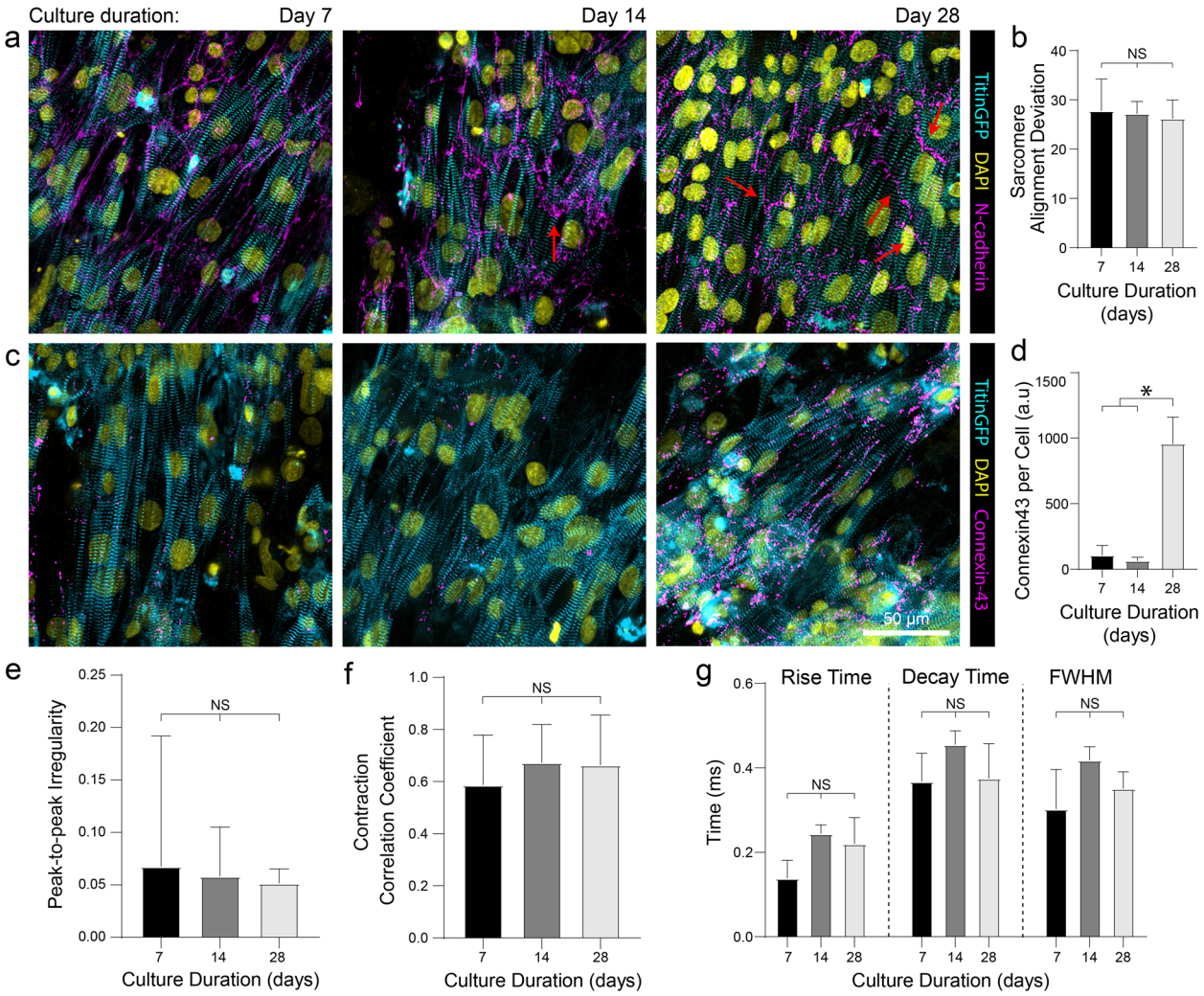

Figure 4.7: Aligned fibrous matrices induce myofibril organization and improve tissue function. Confocal fluorescent images of iPSC-CMs seeded on DVS cultured for 7, 14, and 28 days with immunostaining for (a) N-cadherin and (c) connexin43. Red arrows indicate localization of N-cadherin at end-to-end cell-cell junctions. (b) Quantification of sarcomere angle deviation over time. (d) Quantification of connexin43 expression over time. (e) Calcium handling quantifications of peak-to-peak irregularity, (f) contraction correlation coefficient, and (g) flux rise time, decay time, and full width half max. All data presented as mean ± std; n ≥ 12 fields of view across 3 tissues; * $p < 0.05$.

Previous studies have also suggested limitations to long-term culture on substrates that solely define tissue anisotropy, indicating that while alignment cues induce the expression of some maturation markers, further maturation requires the addition of other stimuli such as mechanical loading, electrical pacing, soluble factors or even other heterotypic cell communication with

supporting cell types (Garbern et al. 2020; Giacomelli et al. 2020; Han et al. 2016; Karbassi et al. 2020; Ronaldson-Bouchard et al. 2018; Ruan et al. 2016; X. Yang et al. 2019). Nevertheless, organizational cues provided by DVS matrices that mimic aspects of the native perimysial ECM appear to drive cardiac tissue assembly and function by controlling adhesive signaling between iPSC-CMs and the ECM. Despite this, DVS matrices fail to recapitulate the more complex hierarchical organization of the cardiac ECM, limiting the study of how cues from other ECM layers, and interactions between them, impact overall tissue function (Karl T. Weber 1989). By altering electrospinning parameters, fibrous matrices could be fabricated with fiber diameters and mechanics similar to epimysial and endomysial networks (Fleischer et al. 2015). The future development of scalable technologies to generate tissues from multiple layers of iPSC-CM-laden fibrous matrices could provide a route to regenerative or tissue replacement therapies (Fleischer et al. 2017).

In addition, mechanosensing of ECM properties by CMs has been shown to be vital during cardiac tissue development and in supporting healthy tissue function, but many studies, including the ones described here, indicate that this relationship requires further investigation (Jacot, Martin, and Hunt 2010; Karbassi et al. 2020; Parker and Ingber 2007). Other work in our lab has explored the influence of fiber mechanics on cell spreading, migration, and multicellular network assembly by suspending matrices over microfabricated wells in contrast to the studies described above depositing fibers on rigid coverslips (Baker et al. 2015; C.D. Davidson et al. 2020; Christopher D. Davidson et al. 2019). As both passive and active mechanical properties of the ECM have been shown to foster tissue maturation (Leonard et al. 2018; A. J. S. Ribeiro et al. 2015; Ruan et al. 2015; Young et al. 2014; Young and Engler 2011), exploration of the iPSC-CMs response to ECM settings that enable fractional shortening of tissues is a focus of ongoing investigations. Studies

such as these could provide further insights into how CMs respond to dynamic mechanical changes of the ECM and could be integrated with previously established pacing protocols to promote iPSC-CM maturation.

4.5 Conclusion

In summary, we established synthetic, tunable DVS fibrous matrices that model perimysial collagen networks of native myocardium. Varying adhesive ligand, architecture, and mechanics of these matrices, we found that soft, aligned DVS fibers functionalized with fibronectin or cRGD best facilitate the formation of organized and contractile iPSC-CM tissue layers. Fibrous topographical cues and anisotropic distribution of adhesive ligand improved calcium handling, enhanced structural organization, including N-cadherin end-to-end localization, and enabled long-term culture of iPSC-CM tissues. While our results support the notion that fibrous ECM cues are not sufficient in generating iPSC-CM tissues with adult-like phenotypes, prolonged culture on DVS matrices promoted N-cadherin end-to-end localization and increased connexin43 expression. Taken together, these studies motivate the inclusion of fibrous cues in biomaterial culture platforms towards generating mature iPSC-CM tissues for applications in replacement/regenerative therapies, disease modeling, and drug screening.

4.6 Materials and Methods

4.6.1 Reagents

All reagents were purchased from Sigma Aldrich and used as received, unless otherwise stated.

4.6.2 DVS fibrous matrix fabrication

DVS polymer was synthesized as previously described by our lab(C.D. Davidson et al. 2020). Briefly, dextran was reacted with divinyl sulfone and the product was dialyzed and lyophilized. For electrospinning, DVS was dissolved at 0.7 g mL^{-1} in a 1:1 mixture of milli-Q water and dimethylformamide with 0.6% (w/v) lithium phenyl-2,4,6-trimethylbenzoylphosphinate (LAP; Colorado Photopolymer Solutions) photoinitiator, 2.5% (v/v) methacrylated rhodamine (25 mM; Polysciences, Inc., Warrington, PA), and 5.0% (v/v) glycidyl methacrylate. This solution was electrospun on coverslips affixed to a custom-built rotating mandrel with a hexagonal geometry (**Figure 4.1a**) driven by an AC motor with controllable speed. Electrospinning was conducted in an environmental chamber at 35% humidity with a flow rate of 0.2 ml h^{-1}, voltage of 7.0 kV, and a gap distance of ~5 cm to the grounded mandrel. After collection, fibers were stabilized by primary crosslinking under UV (100 mW cm^{-2}) for 20 s, then hydrated in varying concentrations of LAP photoinitiator solution and exposed again to UV for 20 s to tune fiber stiffness. To functionalize matrices with FN or collagen (Corning International), 2.5% (w/v) heparin methacrylate (HepMA) was dissolved in LAP solution during secondary UV exposure. ECM proteins were diluted at a concentration of 50 μg mL^{-1} and adsorbed to fibers at RT for 1 hour. Alternatively, matrices were functionalized with cell adhesive peptides cyclized [Arg-Gly-Asp-D-Phe-Lys(Cys)] (cRGD; Peptides International) or Gly-Phe-Hyp-Gly-Glu-Arg (GFOGER; CPC

Scientific) via Michael-Type addition to available vinyl sulfone groups. Peptides were dissolved at 200 μM in milli-Q water containing HEPES (50 mM), phenol red (10 μg mL^{-1}), and 1 M NaOH to bring the pH to 8.0. A volume of 150 μL was added to each substrate and incubated at room temperature for 30 min. Substrates were sterilized in 70% ethanol prior to cell seeding.

4.6.3 DVS matrix mechanical testing

Mechanical properties of DVS matrices were determined using previously developed methods.(Baker et al. 2015; C.D. Davidson et al. 2020) Briefly, suspended networks of DVS were indented with a rigid SU8 cylinder affixed to a pure tungsten filament using a commercial CellScale Microsquisher (CellScale). Young's modulus was approximated assuming the material behaves as an elastic membrane as previously described.(Baker et al. 2015; C.D. Davidson et al. 2020)

4.6.4 Microcontact printing

To create substrates to compare with DVS matrices, 3 μm wide FN parallel lines spaced 3 μm apart were created via traditional microcontact printing approaches. Using photolithography techniques, patterns were transferred to a silicon wafer spincoated with 1 μm thickness Microposit S1813 photoresist (MicroChem). Following development, polydimethylsiloxane (PDMS) (Sylgard 184, Dow Corning) was cast on to wafers and cured at 80 ℃ for 2 h to generate micropatterned stamps. To visualize patterns, FN was fluorescently tagged with AlexaFluor555 succidinyl ester following the manufacturer's protocol. Briefly, a 1 mg mL^{-1} solution of FN was reacted with AlexFluor55 succidinyl ester at a 9-fold molar excess for 2 h at RT with agitation in a 1 M sodium bicarbonate solution and purified by dialysis (6.5 kDa cutoff). For microcontact printing, fluorescent FN was diluted to 50 μg mL^{-1} in sterile milli-Q water and adsorbed to the

micropatterned stamps for 30 min at RT. The fibronectin pattern was transferred to UV ozone activated, PDMS coated coverslips (via spin coating, 5000 RPM). After sitting overnight to allow for the recovery of hydrophobicity, susbtrates were sterilized in 70% ethanol and then incubated in Pluronics F-127 (0.2% w/v in milli-Q water) for 30 min at RT to prevent protein and cell adhesion to non-printed regions of the substrate. To create control non-micropatterned substrates, FN (50 μg mL^{-1}) was adsorbed to UV ozone treated glass coverslips for > 30 min at RT.

4.6.5 iPSC culture and CM differentiation

Induced pluripotent stem cells containing a GFP-titin reporter (Sharma, Toepfer, Ward, et al. 2018) (gift from the Seidman Lab) were cultured in mTeSR1 media (StemCell Technologies) and differentiated in RPMI 1640 media supplemented with B27 minus insulin (ThermoFisher). Differentiation was initiated on day 0 with the addition of 12 μM CHIR99021 for 24 hours and then 5 uM IWP4 on day 3 for 48 hours. On day 9, media insulin was introduced and cells began to contract on day 10. For CM purification, cultures were transferred to RPMI lacking glucose and glutamine (Biological Industries) supplemented with 4 mM DL-lactate on day 11 for 4-6 days. Following purification, CMs were maintained in CM maintenance media (RPMI 1640 supplemented with 2% (v/v) B27 (Thermo Fischer)). On day 30, CMs were dissociated using accutase (Corning) and seeded on fibrous matrices or control substrates. Cultures were maintained in CM maintenance media replenished every other day for the duration of studies. All studies were carried out for 7 days unless otherwise specified.

4.6.6 Calcium imaging

Calcium handling analysis was performed by incubating cells for 1 hour at 37 ℃ with 5 μM Cal520, AM (AAT Bioquest). Cells were then returned to conditioned media preserved prior

to adding the calcium sensitive dye and allowed to equilibrate for >30 minutes at 37 ℃ and 5% CO_2. Following equilibration, tissues were imaged under epifluorescence at 96 Hz while maintaining temperature and CO_2.

4.6.7 Immunofluorescence staining

Samples were fixed in 2% paraformaldehyde for 15 min at RT. Autoflourescence quenching was performed by incubating samples in 0.1 M NH_4Cl (pH 8.0) for 10 min at RT, and then in a fresh NH_4Cl solution for an additional 5 min. This was followed by antigen retreival via incubation in pre-warmed 10 mM trisodium citrate dihydrate (pH 6.0) for 15 minutes. Samples were then permeablized in PBS solution containing Triton X-100 (0.2% v/v), sucrose (10% w/v), and magnesium chloride (0.6% w/v) for 10 min and blocked in 1% (w/v) bovine serum albumin. Tissues were incubated with mouse monoclonal anti-N-cadherin (1:200; BD Bioscience 610921) overnight at 4°C, rabbit monoclonal anti-connexin43 (1:1000; Millipore Sigma AB1728) antibodies overnight at 4°C, mouse monoclonal anti-α-actinin (1:500; Abcam ab9465) for 1 hour at RT, mouse monoclonal anti-cardiac troponin T (1:500; ThermoFisher MA5-12960) for 1 hour at RT, mouse monoclonal or rabbit monoclonal anti-Ki67 (1:1000; Sigma-Aldrich PIMA514520) for 1 hour at RT, followed by goat anti-mouse Alex Fluor 647 (1:1000; Life Technologies A21236), and goat anti-rabbit Alexa Fluor 647 secondary antibodies (1:1000; Life Technologies A21245) and DAPI for 1 hour at RT.

4.6.8 Image analysis

Time-lapse movies of calcium flux were analyzed with custom MATLAB scripts (**Supplementary Figure 4.1**). Briefly, average fluorescent profiles over time were determined from select areas of each tissue and parameters such as beats per minute, peak-to-peak irregularity,

flux rise time, flux decay time, and peak full width half max were calculated. Contraction correlation coefficient was determined by dividing the entire field of view into 16 regions of equal area and calculating the average Pearson's correlation coefficient between the flux profiles of each of these regions (A. Kumar et al. 2019). Sarcomere alignment was also quantified via custom MATLAB scripts (**Supplementary Figure 4.2**). Briefly, images of titin-GFP reporter were thresholded and individual z-discs segmented. Z-discs were subsequently grouped with neighboring z-discs based on proximity and orientation to identify myofibrils within the image. The orientation of all identified myofibrils within a field of view was fit to a Gaussian distribution. Sarcomere alignment deviation was defined at the standard deviation of this distribution using circular/angular statistics.(Berens 2009)

4.6.9 Statistical analysis

Statistical significance was determined by one-way analysis of variance (ANOVA) with post-hoc analysis (Tukey test), with significance indicated by $p < 0.05$. Studies were conducted a minimum of 3 times with at least $n = 3$ tissues per condition and the data presented are representative data sets from one these replicate studies. Specific sample size is indicated within corresponding figure legends and all data are presented as mean ± standard deviation.

4.7 Supplementary Figures

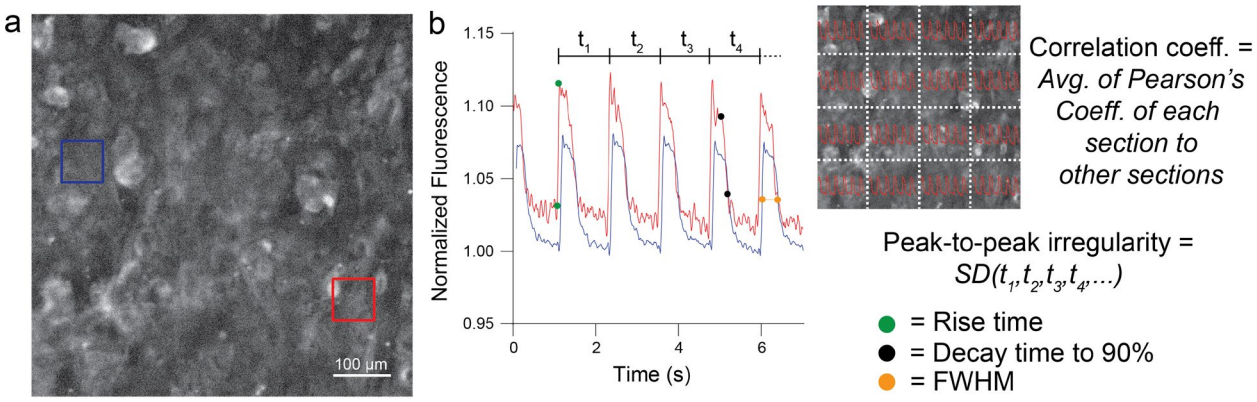

Supplementary Figure 4.1: Calcium imaging quantification methodology. Quantification of calcium transients were conducted by capturing time lapse movies at ~100 Hz after the introduction of a calcium sensitive dye. (a) Still frame of sample calcium transient time lapse with two regions indicated that are plotted in (b). (b) Contraction correlation coefficient was determined by calculating the Pearson's correlation coefficient between the flux profiles of multiple regions across the entire tissue. Peak-to-peak irregularity was calculated by finding the standard deviation in the times between subsequent peaks throughout a single time lapse. Flux rise time, decay time, and full width half max are indicated on the flux plots.

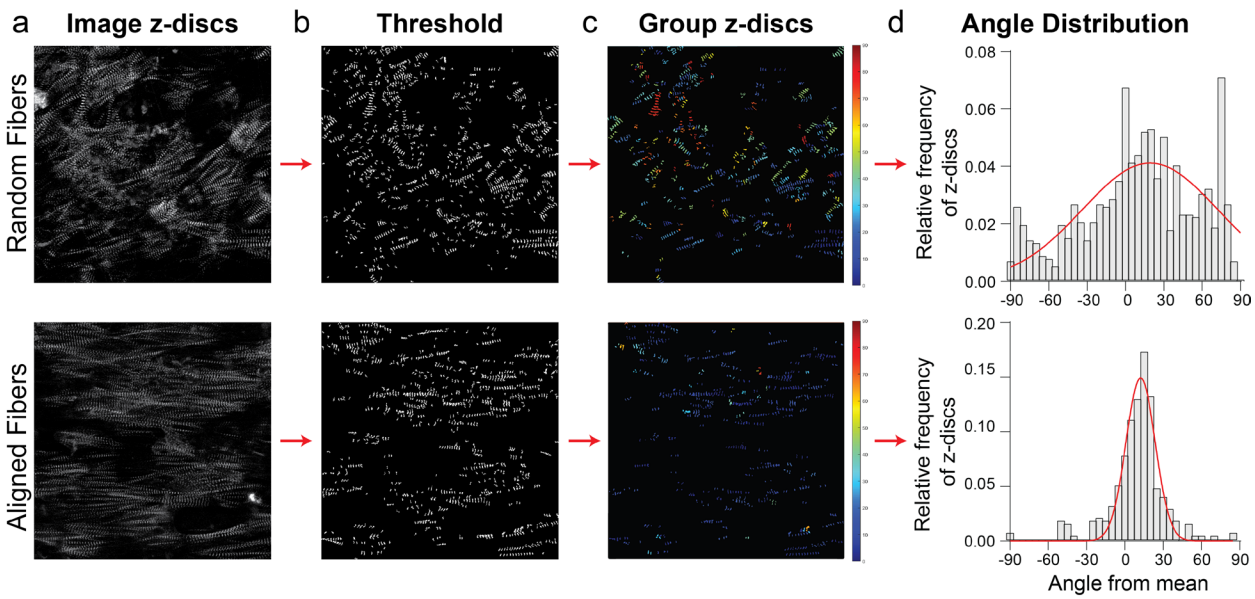

Supplementary Figure 4.2: Sarcomere alignment quantification. (a) Myofibril alignment was quantified by processing confocal fluorescent images of titinGFP with a custom Matlab script. (b) Images were thresholded and individual z-discs were identified and (c) grouped based on their orientation and proximity to other z-discs with similar orientation. (d) The distribution of the orientations of groups of z-discs were then plotted and fit to a Gaussian distribution. The standard deviation of this distribution was defined as the sarcomere alignment deviation.

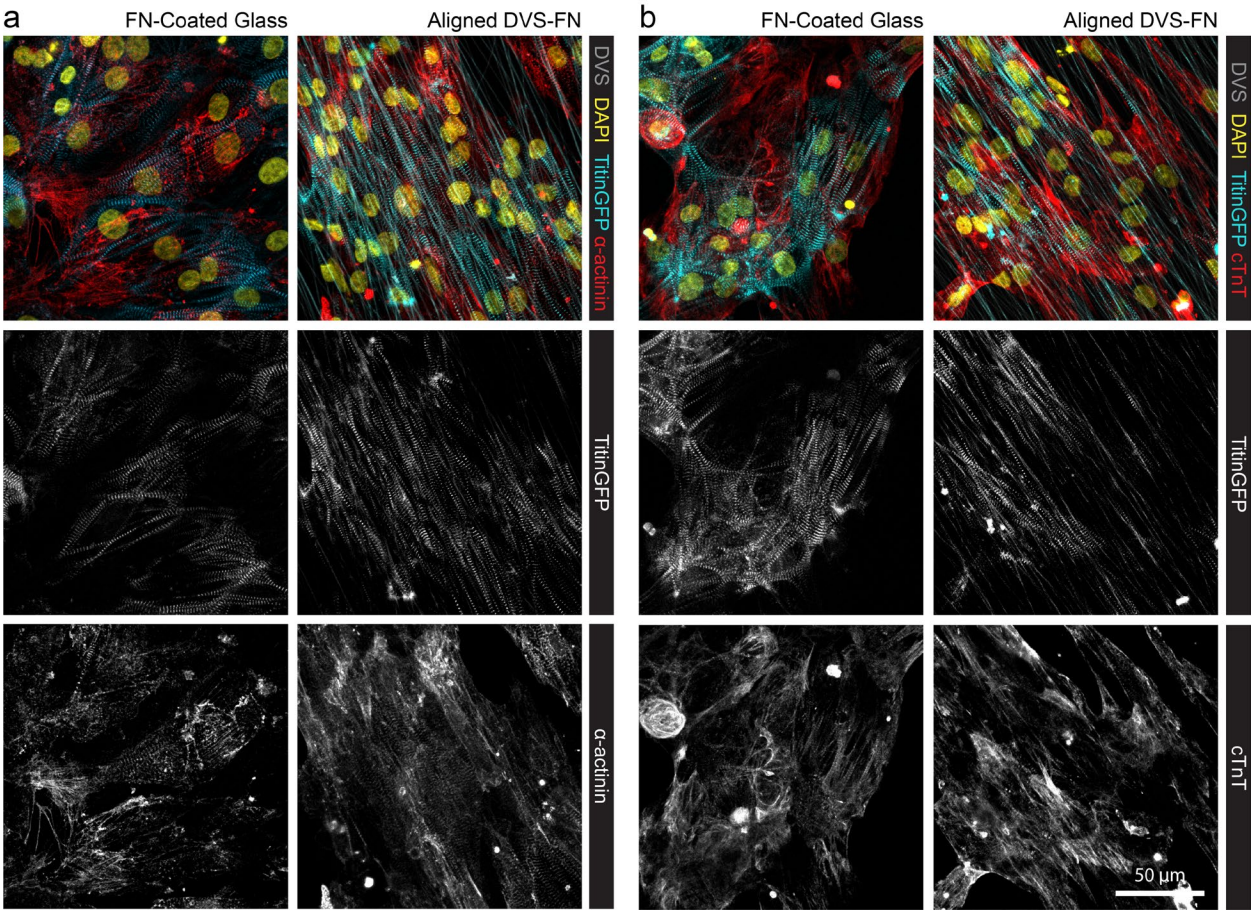

Supplementary Figure 4.3: iPSC-CMs express numerous cardiac specific myofibrilar proteins. Confocal fluorescent images of iPSC-CMs containing a titinGFP reporter seeded on FN-coated glass and aligned DVS matrices functionalized with fibronectin stained for (a) α-actinin or (b) cardiac troponin (cTnT).

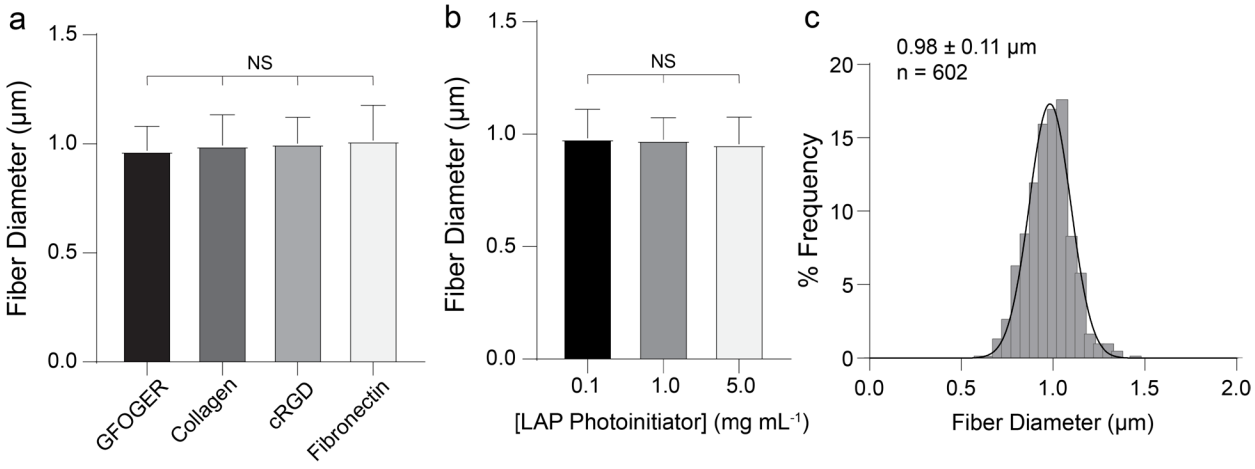

Supplementary Figure 4.4: DVS fiber diameter remains constant regardless functionalization scheme or photoinitiated crosslinking. (a) Fiber diameter of DVS fibers crosslinked in 1.0 mg mL^{-1} LAP solution modified with different adhesive moieties. (b) Fiber diameter of DVS fibers crosslinked in the LAP solutions of varied concentration, functionalized with HepMA/FN. All data presented as mean ± std; $n \geq 100$ fibers across 10 fields of view; * $p < 0.05$. (c) Histogram of all DVS fiber diameters. Fiber diameters were quantified using ImageJ.

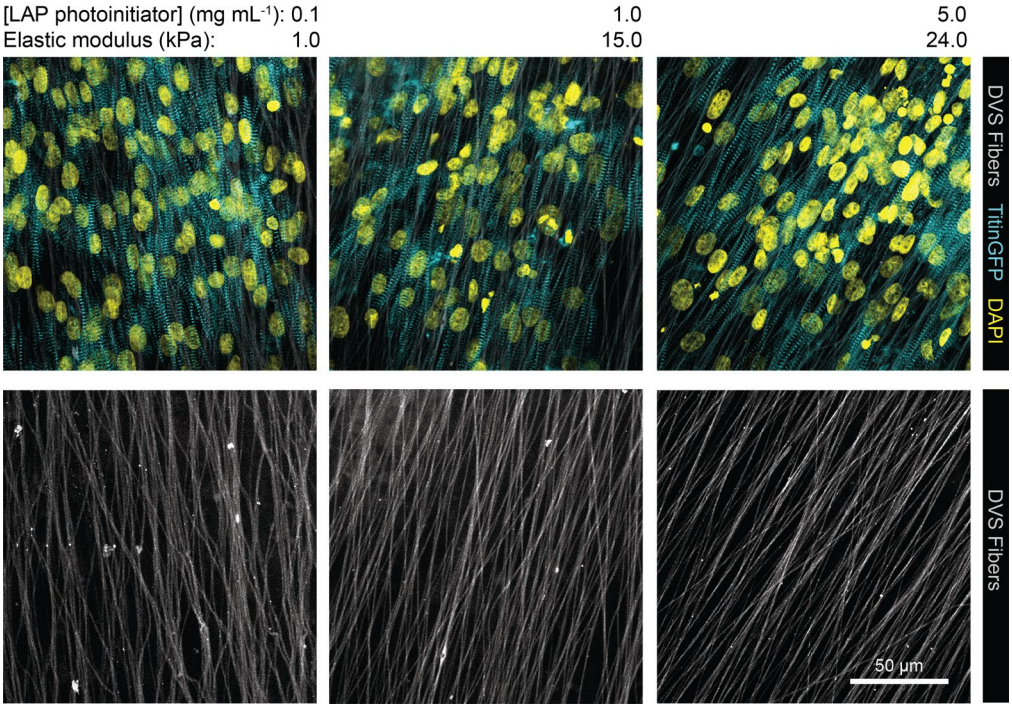

Supplementary Figure 4.5: iPSC-CMs deform soft DVS fibers matrices. Confocal fluorescent images of iPSC-CMs cultured on DVS fibers of increasing stiffness. Increased waviness in soft fibers indicate cell-force mediated deformations in soft matrices but not stiffer matrices.

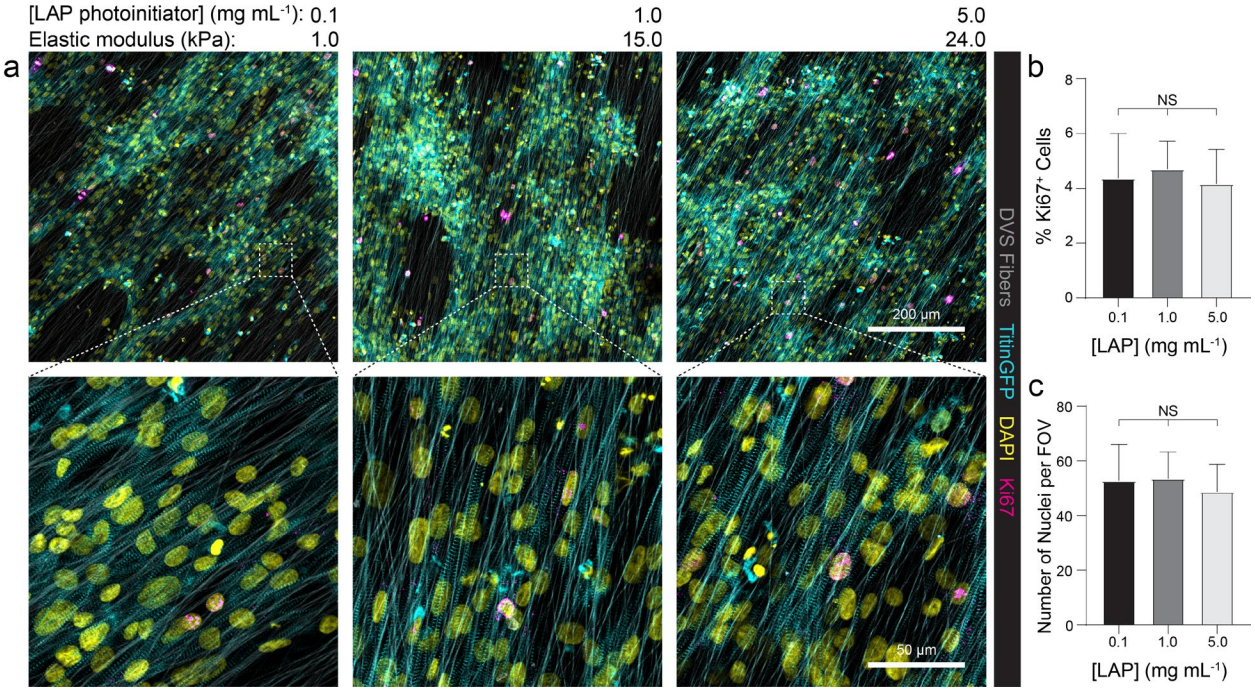

Supplementary Figure 4.6: iPSC-CMs remain largely non-proliferative on DVS matrices of different stiffnesses. (a) Confocal fluorescent images at 10x and 40x magnification of iPSC-CMs on aligned matrices composed of DVS fibers of differing stiffness by tuning photoinitiated crosslinking. Immunostaining was performed to visualize Ki67. (b) Quantification of the percentage of total cells expressing nuclear Ki67 across matrices if varied stiffness. (c) Quantification of the number of cells per field of view across matrices of varied stiffness. All data presented as mean ± std; $n \geq 17$ fields of view across 3 tissues; * $p < 0.05$.

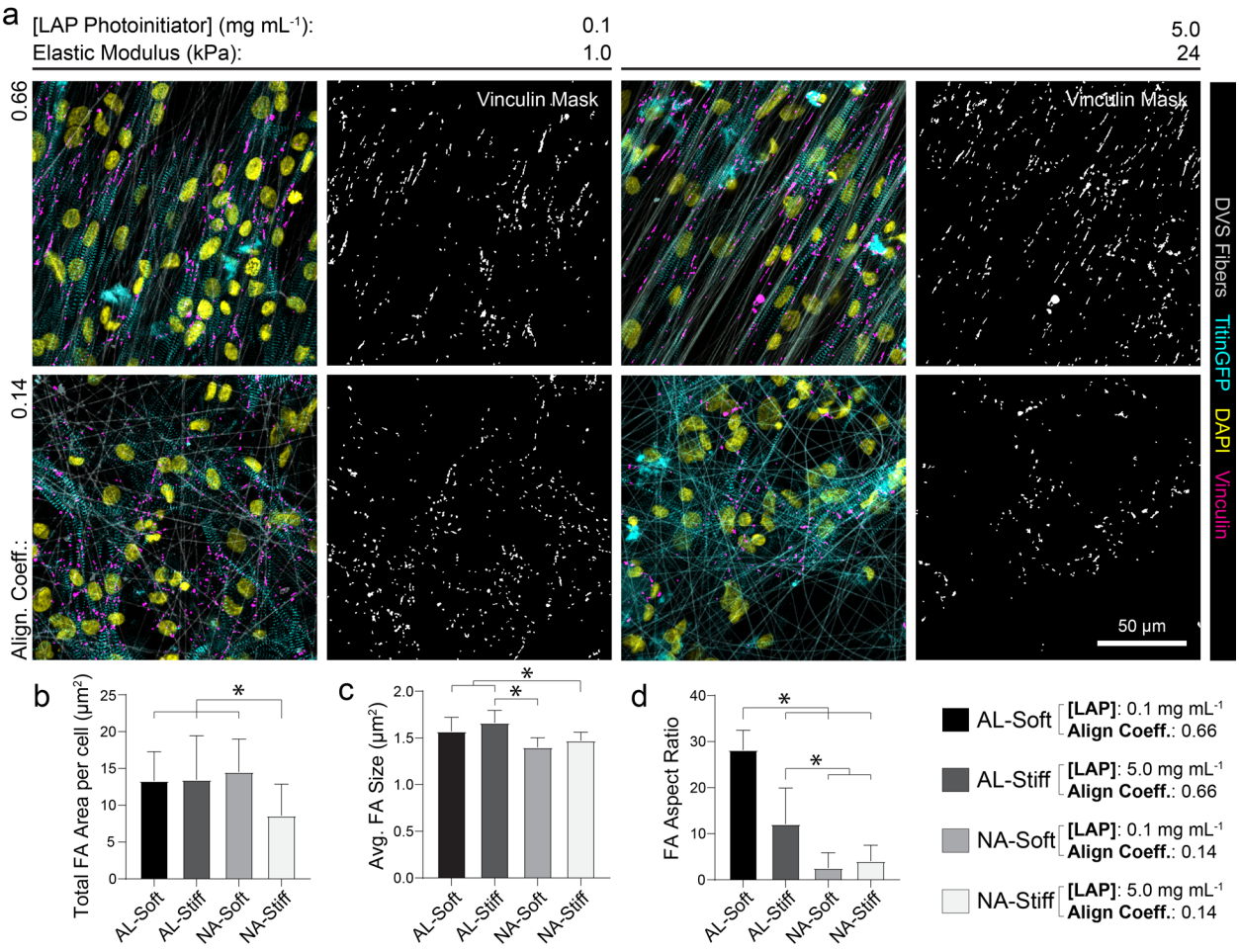

Supplementary Figure 4.7: DVS fiber alignment and stiffness synergistically affect iPSC-CM focal adhesion formation. (a) Confocal fluorescent images of iPSC-CMs stained for vinculin on matrices of varied alignment and stiffness. Quantification of (b) total vinculin positive area per cell, (c) average segmented focal adhesion size per cell, (d) and average focal adhesion aspect ratio per cell. All data presented as mean ± std; n ≥ 18 fields of view across 3 tissues; * $p < 0.05$.

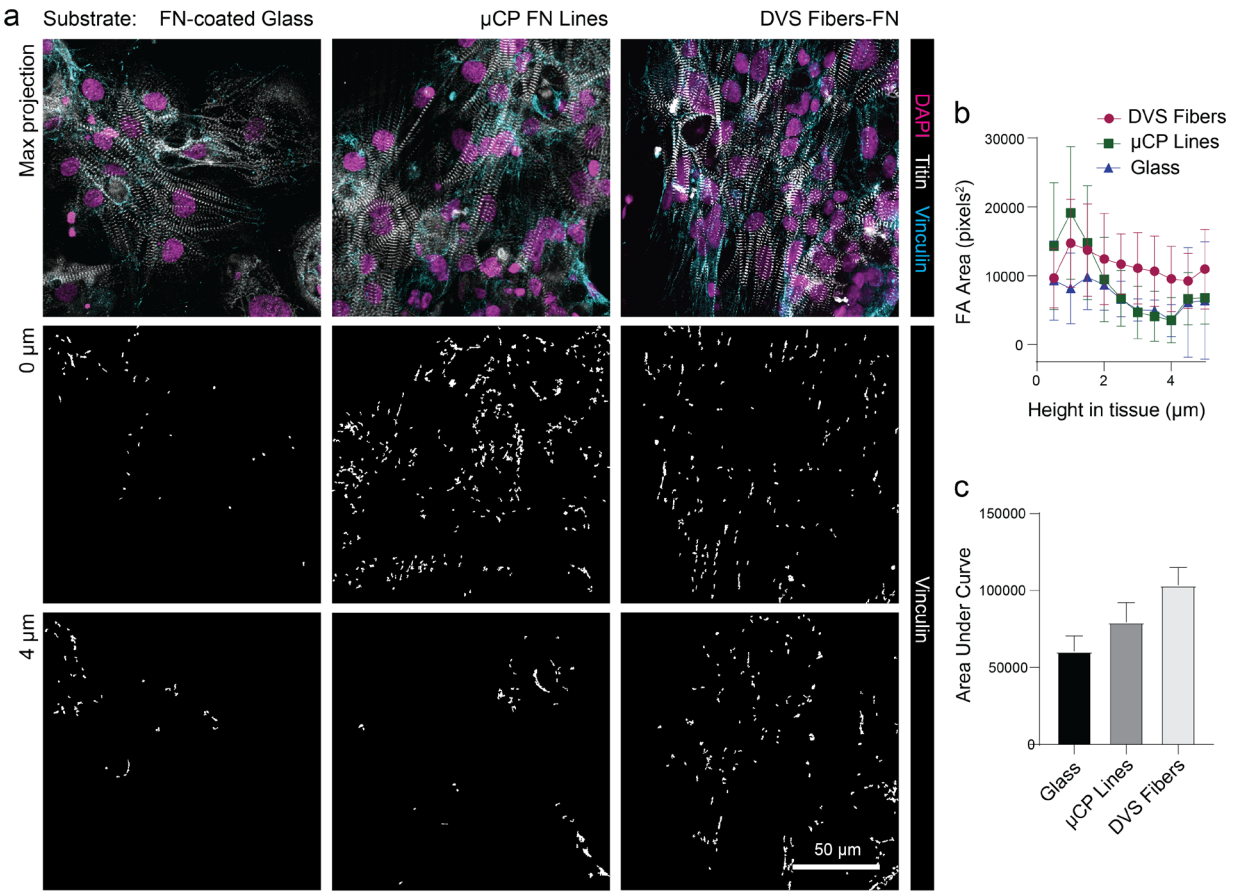

Supplementary Figure 4.8: Increased costameres results in more stable culture of iPSC-CMs on DVS fibers. (a) Confocal fluorescent images of iPSC-CMs seeded on fibronectin-coated glass, microcontact printed fibronectin lines, and aligned DexVS fibers modified with adhesive fibronectin. Bottom two rows of images show vinculin at two heights within the tissue. (b) Quantification of vinculin area as a function of height in the tissue. (c) Calculation of area under the curves plotted in (b). All data presented as mean ± std; $n \geq 12$ fibers fields of view; * $p < 0.05$.

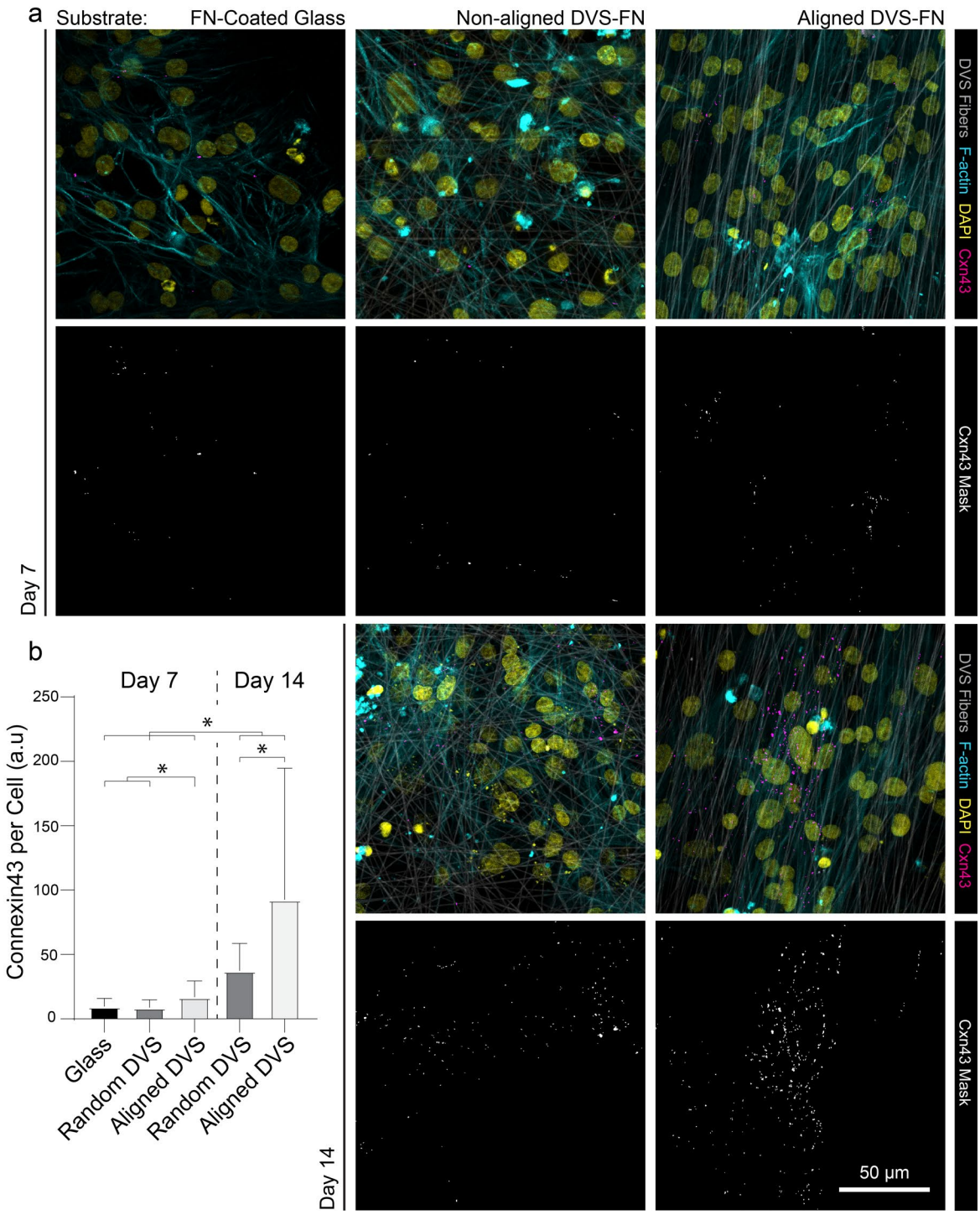

Supplementary Figure 4.9: Aligned fibrous matrices enhance iPSC-CM Connexin43 expression. (a) Confocal fluorescent images of iPSC-CM endogenously modified to express connexin43-GFP (Allen Institute; line ID = AICS-0053 cl.16) seeded on FN-coated glass, random DVS matrices, and aligned DVS matrices. Fibrous tissues were imaged on both day 7 and day 14 while iPSC-CMs were imaged only on day 7 due to detachment from the substrate shortly after

this time point. (b) Quantification of connexin43 expression per cell. Data presented as mean ± std; $n \geq 18$ fields of view across 2 tissues; * $p < 0.05$.

4.8 Supplementary Movies

Supplementary Movie 4.1: Calcium transients of iPSC-CMs on DVS matrices presenting varying adhesive moieties. (https://doi.org/10.1039/D0BM01247E)

Supplementary Movie 4.2: Calcium transients of iPSC-CMs seeded a varying densities on aligned DVS matrices. (https://doi.org/10.1039/D0BM01247E)

Supplementary Movie 4.3: Calcium transients of iPSC-CMs on DVS matrices of varying alignment. (https://doi.org/10.1039/D0BM01247E)

Supplementary Movie 4.4: Calcium transients of iPSC-CMs on DVS matrices of varying stiffness. (https://doi.org/10.1039/D0BM01247E)

Supplementary Movie 4.5: Calcium transients of iPSC-CMs seeded on FN-coated glass, microcontact printed FN lines, and aligned DVS matrices. (https://doi.org/10.1039/D0BM01247E)

Chapter 5: Matrix Architecture and Mechanics Regulate Myofibril Organization, Costamere Assembly, and Contractility in Engineered Myocardial Microtissues

5.1 Authors

Samuel J. DePalma, Javiera Jilberto, Austin E. Stis, Darcy D. Huang, Jason Lo, Christopher D. Davidson, Aamilah Chowdhury, Robert N. Kent III, Maggie E. Jewett, Hiba Kobeissi, Christopher S. Chen, Emma Lejeune, Adam S. Helms, David A. Nordsletten, Brendon M. Baker

5.2 Abstract

The mechanical function of the myocardium is defined by cardiomyocyte contractility and the biomechanics of the extracellular matrix (ECM). Understanding this relationship remains an important unmet challenge due to limitations in existing approaches for engineering myocardial tissue. Here, we established arrays of cardiac microtissues with tunable mechanics and architecture by integrating ECM-mimetic synthetic, fiber matrices and induced pluripotent stem cell-derived cardiomyocytes (iPSC-CMs), enabling real-time contractility readouts, in-depth structural assessment, and tissue-specific computational modeling. We find that the stiffness and alignment of matrix fibers distinctly affect the structural development and contractile function of pure iPSC-CM tissues. Further examination into the impact of fibrous matrix stiffness enabled by computational models and quantitative immunofluorescence implicates cell-ECM interactions in

myofibril assembly, myofibril maturation, and notably costamere assembly, which correlates with improved contractile function of tissues. These results highlight how iPSC-CM tissue models with controllable architecture and mechanics can elucidate mechanisms of tissue maturation and disease.

5.3 Introduction

Heart disease remains the leading cause of death worldwide (Tsao et al. 2023). Despite recent advances in treatment, existing therapies for treating heart disease fail to restore normal function of the heart following chronic or acute injury, due in part to the limited regenerative potential of the myocardium (Bergmann et al. 2009; Murry and MacLellan 2020). Thus, there is a critical need for regenerative or tissue-replacement therapies that restore normal cardiac architecture and mechanical function. In recent years, advances in induced pluripotent stem cell (iPSC) technologies have made the creation of engineered heart tissues (EHTs) feasible for use as regenerative therapies, *in vitro* models to study cardiac regeneration, or screening platforms to test the effectiveness and/or toxicity of new therapeutics (Burridge et al. 2014; Lian et al. 2012; Thomas et al. 2022).

Among the many techniques explored to generate mature iPSC-derived cardiomyocyte (iPSC-CM) tissues, significant efforts have focused on developing scaffolds that recapitulate physiologic tissue organization to improve overall tissue function and potentially maturity (Cho et al. 2022; Karbassi et al. 2020; Tenreiro et al. 2021). The mechanical function of the myocardium is dictated by contractile CMs and the surrounding fibrous extracellular matrix (ECM) that organizes and supports CMs (Fleischer and Dvir 2013; Pope et al. 2008; Karl T. Weber 1989). Individual layers of muscle tissue throughout the myocardium are highly anisotropic, driving

coordinated uniaxial contractions (Costa et al. 1999). These muscle fibers and their accompanying ECM twist transmurally, thus generating the torsional contractile behavior critical to proper systolic function of the ventricle (P. P. Sengupta et al. 2008). As such, scaffolds that recapitulate biochemical and mechanical features of native cardiac ECM and direct cellular orientation hold promise for improving the function and maturation of cardiac tissue constructs (Allen et al. 2019; Carson et al. 2016; DePalma et al. 2021; Gao et al. 2017; A. J. S. Ribeiro et al. 2015; Tsan et al. 2021). Scaffolding is often integrated into EHTs by combining naturally derived biomaterials materials such as purified collagen or fibrin with iPSC-CMs (Boudou et al. 2012; Gao et al. 2017; J. Guo et al. 2021; Ronaldson-Bouchard et al. 2018; Tenreiro et al. 2021; Tiburcy et al. 2017). However, these materials provide limited control over mechanical properties which is critical to providing insight into how iPSC-CMs sense and respond to matrix stiffness. Moreover, the addition of admixed stromal cells is often required to drive proper tissue assembly in these systems, precluding the direct study of CM behavior. Prior studies have explored the use of polymeric hydrogels providing improved mechanical control or electrospun polymeric scaffolds with fibrous topography that better recapitulates the native ECM; however, these materials either lack fibrous topography or sufficient tunability, respectively, both of which are needed for identifying critical mechanobiological mechanisms that drive cardiac tissue assembly or maturation (Allen et al. 2019; Carson et al. 2016; McCain et al. 2012; A. J. S. Ribeiro et al. 2015; Wanjare et al. 2017). Thus, EHTs formed from iPSC-CMs and highly tunable, fibrous matrices providing orthogonal control over architecture and mechanics could provide new and important insights into how iPSC-CMs respond to physical microenvironment inputs. Furthermore, a deeper understanding of how CMs interact with their physical microenvironment could in turn establish key design attributes of scaffolds that support stem cell-derived cardiac tissue formation and maturation.

The interactions between cardiomyocytes and their surrounding native ECM or a biomaterial scaffold are regulated by cellular mechanosensing and ultimately the transduction of mechanical forces into cell signaling cascades. CM mechanosensing has been shown to be critical in cardiac development, disease progression, and the assembly of *in vitro* engineered heart tissues, highlighting the necessity for the informed design of scaffolds used to engineer mature iPSC-CM tissues (Chopra et al. 2018; Fukuda et al. 2019; Kaushik et al. 2015; A. J. S. Ribeiro et al. 2015; Samarel 2005; Saucerman et al. 2019). As CMs have extremely dynamic mechanical functions, they use multiple mechanosensing mechanisms to sense and respond to changes in their mechanical environment (Saucerman et al. 2019). Forces generated by the myofibrils in CMs are transmitted to neighboring cells through specialized cell-cell adhesions termed intercalated discs (ICDs) and to the surrounding matrix through cell-matrix linkages(Ahmed et al. 2023; Gaetani et al. 2020; Lyon et al. 2015; Samarel 2005). Composed of adherens junctions and desmosomes, ICDs enable mechanical and electrical coupling of neighboring CMs and help to regulatethe mechanical function of the heart (Lyon et al. 2015). For the myocardium to contract uniformly, CMs not only must connect to one another but also to the surrounding matrix via integrins and associated complexes of cell-matrix adhesion proteins. In striated muscle cells such as cardiomyocytes, cell-matrix adhesions can be grouped into two categories: peripheral FAs, which link the myofibrillar cytoskeleton to the ECM and are generally found at the edges of cultured CMs, and costameres, specialized adhesion complexes that directly link the myofibril to the surrounding or underlying matrix through connections at the z-disc (Samarel 2005). During myofibril formation, peripheral FAs become load-bearing protocostameres, followed by α-actinin accumulation corresponding to the assembly of myofibrils (Chopra et al. 2018; Sparrow and Schöck 2009; Taneja, Neininger, and Burnette 2020). As myofibrils begin to assemble and mature,

costameres replace these adhesions and tether z-discs to the matrix (Shi, Wang, et al. 2022; Sparrow and Schöck 2009). Since they were first described as vinculin-containing structures proximal to z-discs, numerous other proteins commonly associated with FA complexes such as talin, paxillin, and FAK have been identified at costameres (Chopra et al. 2018; Pandey et al. 2018; Pardo, D'Angelo Siliciano, and Craig 1983a, 1983b; Shi, Wu, et al. 2022). Many of these proteins have also been implicated in fundamental cell processes such as myofibril assembly and tissue mechanosensing. However, how ECM and tissue mechanics impact the formation of these structures is not well understood.

Genetic variants that impact the function of mechanosensing proteins can render cardiomyocytes abnormally susceptible to mechanical stresses, leading to ventricular hypertrophy or dilation and ultimately heart failure (Harvey and Leinwand 2011; Jordan et al. 2021; Nakamura and Sadoshima 2018). In particular, the mechanosensitive protein vinculin is known to play a critical role at both costameres and intercalated discs during cardiac development and disease (Chopra et al. 2011; Fukuda et al. 2019; Merkel et al. 2019; Taneja, Neininger, and Burnette 2020; Xu, Baribault, and Adamson 1998; Zemljic-Harpf et al. 2007). Genetic variants of vinculin contribute to cardiomyopathies (Jordan et al. 2021) and cardiomyocyte-specific knock-out of vinculin leads to early cardiac failure or dilated cardiomyopathies (Xu, Baribault, and Adamson 1998; Zemljic-Harpf et al. 2007). Conversely, overexpression of vinculin in drosophila hearts leads to myocardial remodeling and improved cardiac function in aging hearts, resulting in extended organismal lifespan (Kaushik et al. 2015). Moreover, the mechanosensitivity of vinculin in CMs has been described both *in vitro* and *in vivo,* suggesting that vinculin localization to costameres and intercalated discs regulates myofibril maturation and is influenced by mechanical signals (Fukuda et al. 2019; McCain et al. 2012; Merkel et al. 2019; Shakp et al. 1997; Simpson et al.

1993). Despite these advances in our knowledge of vinculin's role in CM mechanosensing, it is unknown how fibrous matrix mechanics impact vinculin's localization to cell-cell or cell-ECM adhesions and the resulting implications on EHT function and maturation.

To study how specific and tissue-relevant structural and mechanical cues impact engineered cardiac tissue assembly, maturation, and function, we established a biomaterials-based platform for creating arrays of cardiac microtissues composed of tunable, synthetic, fibrous ECM and purified iPSC-CMs. Through carefully controlled studies varying ECM organization and mechanics, we found that microtissues formed on soft (< 1 kPa), aligned fibrous matrices tethered between soft elastic posts demonstrate improved CM adhesion, organization, and contractile function. Tissue-specific computational modeling revealed that altered cellular mechanical behavior, in conjunction with the passive mechanics of the tissue, drive the observed changes in tissue contractility. Associated with these effects, we found that vinculin localization to costameres during tissue formation was dependent on fibrous matrix stiffness. Moreover, robust vinculin localization to costameres was strongly associated with tissue maturation and increases in contractile function. These findings highlight the importance of highly controlled bioengineered platforms for studying CM mechanosensing and provide several key insights that inform the design of biomaterial scaffolds for engineered cardiac tissue replacement therapies.

5.4 Results

5.4.1 Development and characterization of mechanically tunable engineered heart tissue platform

As the myocardial microenvironment plays a vital role in both cardiac development and disease progression, constructing EHTs with biomaterials that recapitulate relevant architecture and mechanics of the fibrous cardiac ECM is critical for studying these processes *in vitro* (Cho et al. 2022). We previously developed matrices composed of synthetic dextran vinyl sulfone (DVS) polymeric fibers that possess comparable geometry to perimysial collagen fibers, which are ~1 μm in diameter and surround CM bundles to confer tissue mechanical anisotropy and enable mechanical function of cardiac tissue (DePalma et al. 2021; Fleischer and Dvir 2013; Pope et al. 2008; Karl T. Weber 1989). Using this biomaterial platform, we showed that matrix fiber alignment is critical to driving proper tissue organization and calcium handling dynamics (DePalma et al. 2021). Additionally, we found that these fibrous scaffolds facilitate long-term culture of iPSC-CMs (>28 days) enabled by robust cell-matrix interactions (DePalma et al. 2021). However, this culture platform did not allow for tissue fractional shortening, thereby preventing the assessment of contractile function of formed EHTs. Predicated on this previous work, here we advanced this model by generating a platform enabling fractional shortening and orthogonal mechanical tunability to explore the impact of an expanded array of architectural and mechanical cues on iPSC-CM function.

To examine how variations in the architecture and mechanics of the cardiac microenvironment influence iPSC-CM tissue formation, we established a new approach to generating arrays of cardiac microtissues (termed fibroTUGs or fibrous tissue μ-gauges) composed of tunable electrospun, synthetic fiber matrices suspended between two elastomeric posts seeded with pure populations of iPSC-CMs using a microfabrication-based cell patterning strategy. Microfabricated PDMS post arrays consisting of 98 pairs of rectangular posts were fabricated with standard soft lithography techniques (**Figure 5.1a,b**). Based on previous literature (Boudou et al.

2012; Leonard et al. 2018) and as confirmed via custom mechanical characterization methods (**Supplementary Figure 5.1a-c**), post heights were defined to generate soft (0.41 N/m) and stiff (1.2 N/m) mechanical boundary conditions (**Figure 5.1a,h**). Subsequently, electrospun DVS fibers were deposited upon post arrays affixed to a collecting mandrel rotating at various speeds to control fiber alignment, as previously described(DePalma et al. 2021) (**Figure 5.1a,f,g**). Next, fiber matrices spanning two posts were stabilized via photoinitiated free radical crosslinking by exposing substrates to UV light through a photopatterning mask in the presence of lithium phenyl-2,4,6-trimethylbenzoylphosphinate (LAP) photoinitiator. Upon hydration, uncrosslinked fibers were dissolved, resulting in fibrous matrices spanning only between pairs of posts. Stabilized fibrous matrices spanning posts could then be stiffened further via exposure to UV light in the presence of LAP to define a final matrix stiffness(C.D. Davidson et al. 2020; DePalma et al. 2021). Crosslinking parameters were identified to generate matrices with stiffnesses corresponding to developing (0.1 mg/mL LAP; 0.68 kPa), adult (1.0 mg/mL LAP; 10.1 kPa), or diseased (5.0 mg/mL LAP; 17.4 kPa) myocardium, as characterized by microindentation measurements (**Figure 5.1i, Supplementary Figure 5.1d-f**) (Engler et al. 2008; A. J. S. Ribeiro et al. 2015; Young and Engler 2011). To generate pure cardiomyocyte tissues without the requirement of admixed stromal cells, purified cultures of iPSC-CMs (≥95% TTN+ CMs; **Supplementary Figure 5.2**) were seeded upon photopatterned matrices using a physically registered, microfabricated seeding mask that funneled iPSC-CMs to the suspended matrices, limiting seeded cells from settling and adhering to the glass surface below suspended fiber matrices (**Figure 5.1a**). The resulting tissues contained ~100 iPSC-CMs regardless of the pre-defined mechanics of the posts or matrices (**Figure 5.1j**).

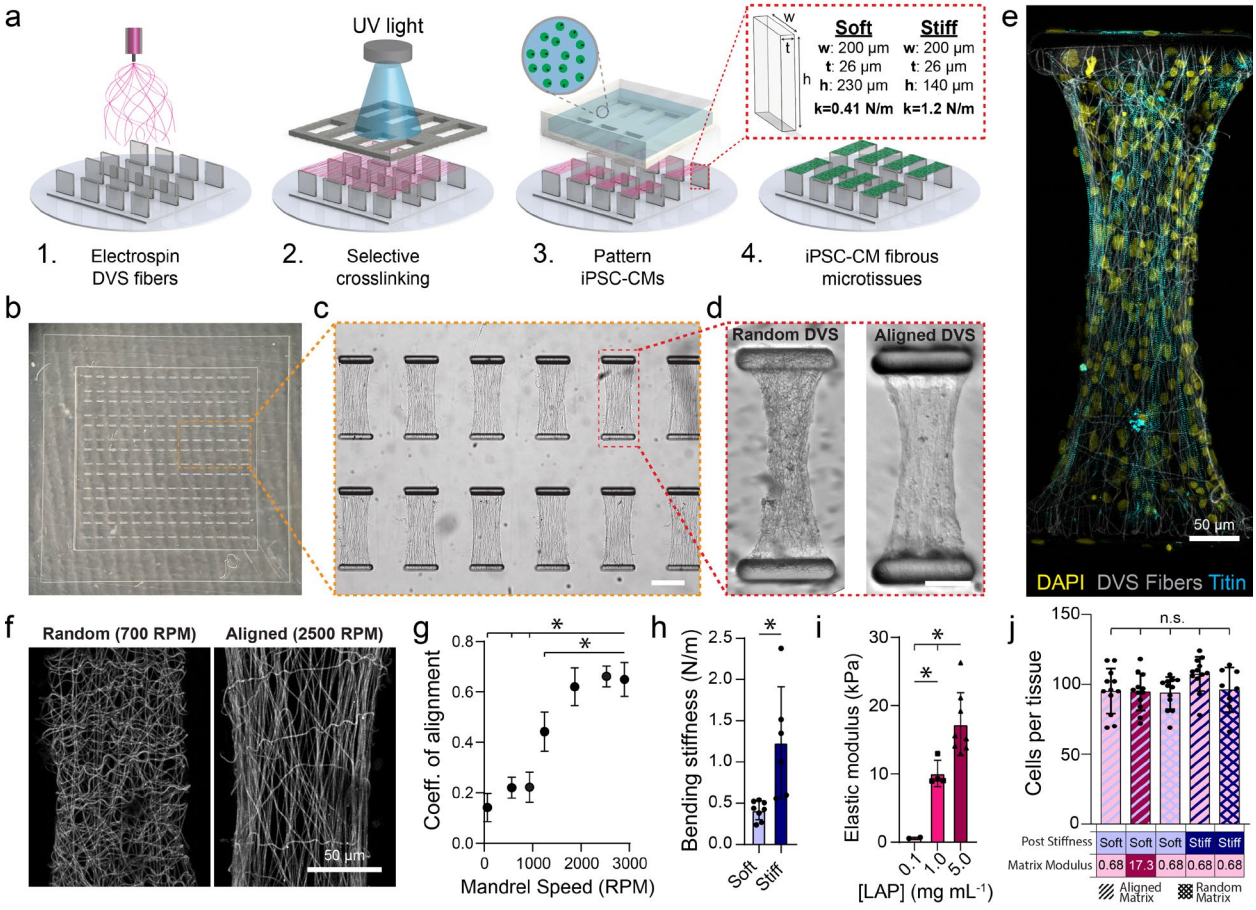

Figure 5.1: Fabrication of pure iPSC-CM microtissues with high mechanical tunability. (a) Schematic of fibroTUG fabrication and seeding. (**b**) Full array of microfabricated PDMS posts before DVS fiber electrospinning. (**c**) Brightfield image of photopatterned suspended matrices (scale bar: 200 µm). (**d**) Representative brightfield images of pure populations of iPSC-CMs seeded on random and aligned DVS matrices 7 days after seeding (scale bar: 100 µm). (**e**) Confocal fluorescent image of fibroTUG tissue formed on 0.68 kPa, aligned matrices suspended between soft posts. (**f**) Confocal fluorescent images of random and aligned fiber matrices functionalized with methacrylated rhodamine. (**g**) Rotation speed of the collection mandrel during fiber electrospinning was varied to define fiber alignment ($n \geq 5$ matrices). (**h**) Post height was varied to define post bending stiffness. (i) LAP photoinitiator concentration was tuned to generate matrices of physiologically relevant stiffnesses. (**j**) Tissue seeding was unaffected by the mechanical inputs, as quantified by the number of cells that compose each tissue 7 days after seeding. All data presented as mean ± std; * $p < 0.05$.

While matrix stiffness has been extensively studied using polymeric hydrogel or elastomer surfaces (Engler et al. 2008; McCain et al. 2012; Pandey et al. 2018; A. J. S. Ribeiro et al. 2015;

Tsan et al. 2021), little is known about how the stiffness of assemblies of fibers influences iPSC-CM tissue formation and function. The discrete nature of fibrous matrices engenders distinct behavior compared to elastic, continuum-like materials (Baker et al. 2015). Although here we provide measurements of bulk modulus to demonstrate mechanical tunability, these values cannot be directly extrapolated to continuum-like materials. Of note, these matrix fibers are individually quite stiff (~100's of MPa) despite the soft bulk stiffness of the overall matrix given its high void fraction. This is in contrast to hydrogel or elastomer materials where mechanics are fairly uniform from bulk to cell length-scales (C.D. Davidson et al. 2020). The cell-scale mechanics of these fibers, which we view as most relevant to CM mechanosensing, are therefore within the range of values reported for common natural biomaterials such as perimysial collagen fibers in the heart (Guthold et al. 2007; MacKenna, Vaplon, and McCulloch 1997; L. Yang et al. 2007). Furthermore, because our fibroTUG platform is predicated upon predefined synthetic matrices that facilitate robust integrin engagement to guide assembly of myocardial syncytia that are structurally similar to stratified muscle layers in the myocardium, we were able to generate and monitor functional myocardial tissues composed of pure iPSC-CMs, highlighting the utility of this system in studying the impact of mechanical cues on cell- and tissue-scale function over long-term culture (up to 3 weeks) (**Supplementary Figure 5.3, Supplementary Figure 5.11, Supplementary Figure 5.12**) (Karbassi et al. 2020).

To demonstrate the general utility of this mechanically tunable platform for studying microenvironmental inputs on other types of tissues beyond EHTs, we also seeded fibroTUGs with varying fiber stiffness with tendon progenitor cells (TPC) to examine whether fiber stiffness influences tenogenic differentiation (**Supplementary Methods**) (Kent et al. 2022). We found that TPCs cultured on stiff fibers expressed higher levels of scleraxis, a key marker of tenogenic

differentiation (**Supplementary Figure 5.4**). Additionally, treatment of tissues on stiff matrices with pro-tenogenic TGF-β3 resulted in a further increase in tenogenic differentiation, supporting the general observation that a combination of physical and soluble cues potentiate stem cell differentiation (**Supplementary Figure 5.4**). These results highlight the broad applicability of highly tunable microtissue platforms for understanding cellular mechanosensing in a variety of contexts.

5.4.2 Mechanical inputs impact tissue mechanical function, organization, and maturation

After thorough mechanical characterization of our fibroTUG platform, we examined how altering key architectural and mechanical inputs – specifically matrix alignment, matrix stiffness, and post stiffness – affect iPSC-CM tissue assembly, organization, and function (**Figure 4.2**). Tuning each of these parameters orthogonally enables controlled study of their respective influence and enables insights into physiologically relevant microenvironmental factors experienced by CMs. For example, disorganized collagenous ECM found in fibrotic scars after myocardial infarction has been suggested to promote disease by mitigating CM contractility and inducing pathogenic signaling (Bowers, Meng, and Molkentin 2022; Bugg et al. 2020; Coeyman, Richardson, and Bradshaw 2022; Neff and Bradshaw 2021; Perestrelo et al. 2021). ECM stiffness has similarly been shown to increase dramatically in fibrotic conditions, while gradually increasing throughout heart development and maturation (Coeyman, Richardson, and Bradshaw 2022; Jacot, Martin, and Hunt 2010; Neff and Bradshaw 2021; Perestrelo et al. 2021; Young and Engler 2011). Finally, changes in post stiffness model changes in tissue afterload that occur throughout tissue development concurrent with CM maturation and are further increased in various forms of cardiac disease (Leonard et al. 2018; Struijk et al. 2008). While previously established EHT platforms enable the study of some of these mechanical perturbations, our

system allows for orthogonal tuning of all these inputs in fibrous matrices that better recapitulate the perimysial matrix. This ability opens the door to understanding how each input alone impacts tissue function and how combinations of these inputs may impact tissue signaling involved in iPSC-CM maturation. To assess resulting tissue function in various mechanical environments, contractility of tissues after 7 days of culture was quantified by measuring post deflections from time-lapse imaging of contracting tissues (**Supplementary Movies 1-5**). Myofibril organization and density were quantified as previously described to assess the impact of physical microenvironmental cues on tissue organization (DePalma et al. 2021; Jilberto et al. 2023).

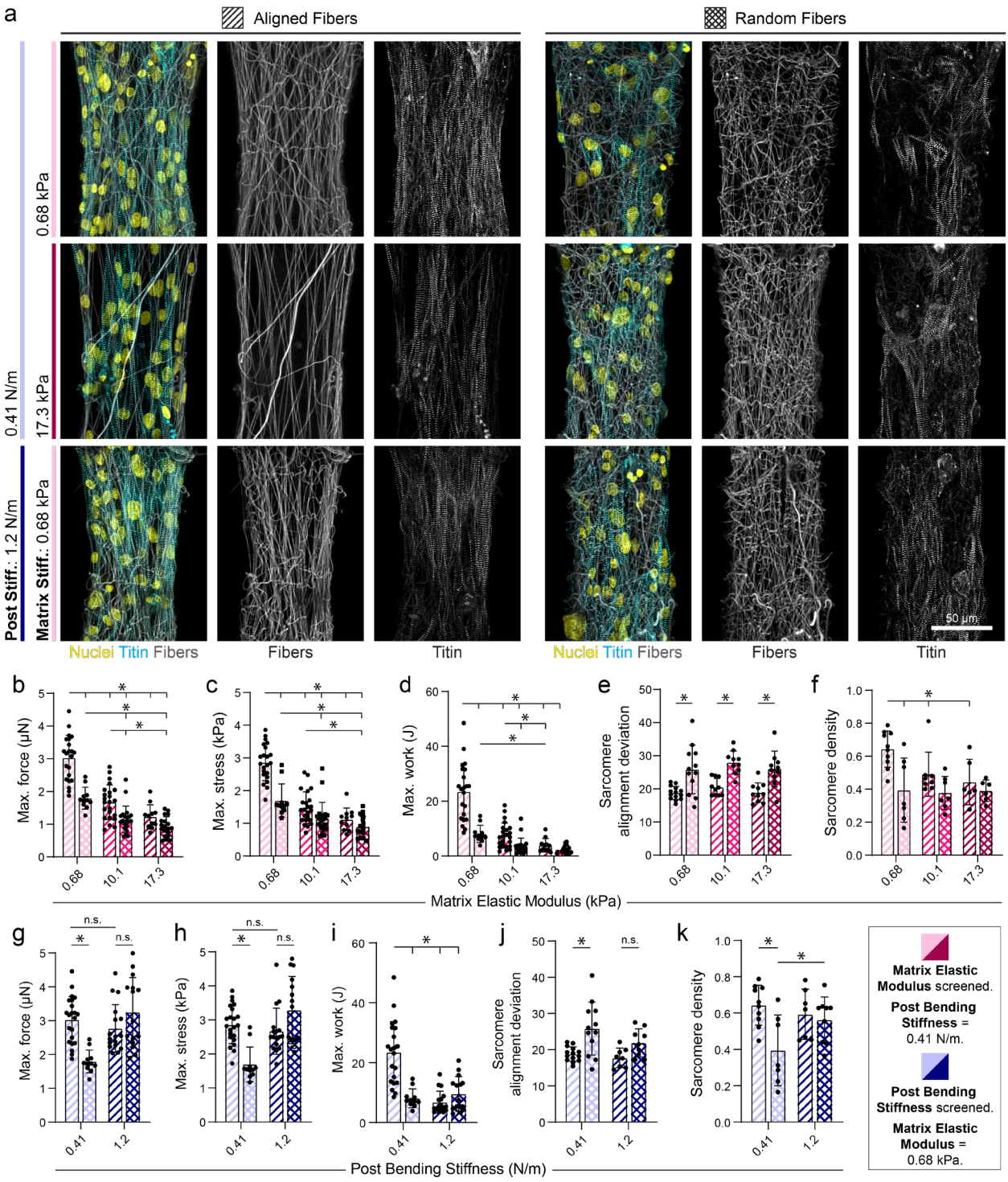

Figure 5.2: Fibrous matrix alignment and stiffness influences iPSC-CM tissue assembly and force generation. (**a**) Confocal fluorescent images of fibroTUG tissues of varied fiber alignment, fiber stiffness, and post stiffness seeded with iPSC-CMs possessing a GFP-TTN reporter. All images show a region located at the center of each tissue. Maximum contractile (**b**) force, (**c**) stress, and (**d**) work quantified in tissues with constant post stiffness (0.41 N/m) with

varied fiber alignment and fiber stiffness (n ≥ 11 tissues). (**e**) Sarcomere alignment deviation and (**f**) sarcomere density quantified in tissues with constant post stiffness (0.41 N/m) and varying fiber alignment and fiber stiffness (n ≥ 10 tissues). Maximum contractile (**g**) force, (**h**) stress, and (**i**) work quantified in tissues with constant matrix stiffness (0.68 kPa) with varied fiber alignment and post stiffness (n ≥ 11). (**j**) Sarcomere alignment deviation and (**k**) sarcomere density quantified in tissues with constant matrix stiffness (0.68 kPa) with varied fiber alignment and post stiffness (n ≥ 8). All data presented as mean ± std; * $p < 0.05$.

Regardless of matrix conditions, all tissues contracted uniaxially, as evidenced by inward post deflections (**Supplementary Movies S1-S9**), similar to established rectangular micropatterned 2D and 3D tissues (Boudou et al. 2012; McCain et al. 2012; A. J. S. Ribeiro et al. 2015; Ronaldson-Bouchard et al. 2018; Tsan et al. 2021). Examining fibroTUGs formed on aligned fibrous matrices spanning soft (0.41 N/m) posts, we noted a decrease in tissue contractile force, contractile stress, and work as a function of increasing matrix stiffness (**Figure 5.2b-d; Supplementary Movie 4.2:** Calcium transients of iPSC-CMs seeded a varying densities on aligned DVS matrices.). Exploring the effect of matrix fiber alignment (via pre-defining aligned vs. randomly oriented fibers), we noted diminished tissue contractility on soft (0.68 kPa) matrices with randomly oriented fibers as compared to matrices composed of aligned fibers of equivalent fiber stiffness (**Figure 5.2b-d; Supplementary Movie 5.2, Supplementary Movie 5.3**). On stiffer matrices, differences in tissue stress arising from fiber alignment was less prominent, potentially indicating that iPSC-CMs may be unable to deform stiffer matrices or efficiently assemble myofibrils independent of matrix fiber alignment. Additionally, contraction velocity and duration were highest on soft, aligned matrices (**Supplementary Figure 5.5a-d**). We next quantified myofibril organization within these tissues and observed a decrease in sarcomere alignment on randomly oriented fiber matrices regardless of matrix stiffness, as quantified by a higher sarcomere deviation (DePalma et al. 2021) (**Figure 5.2a,e,f**). Additionally, sarcomere density decreased on

random matrices compared to aligned matrices across all stiffnesses tested (**Figure 5.2a,e,f**). Finally, we examined the influence of tissue boundary stiffness on resulting tissue contractility by maintaining a constant stiffness of aligned matrices at 0.68 kPa while increasing post stiffness (**Figure 5.2g-i; Supplementary Movie 5.4, Supplementary Movie 5.5**). While contractile force and stress remained constant in tissues formed between both soft (0.41 N/m) and stiff (1.2 N/m) posts, the effective work produced by tissues contracting against stiffer boundaries was greatly reduced (**Figure 5.2g-i**). Contraction velocity and time were also decreased in tissues formed between stiff (1.2 N/m) posts (**Supplementary Figure 5.5e-h**). However, tissues formed on randomly oriented, soft fiber matrices tethered between stiff posts surprisingly revealed no differences in contractile force and stress as compared to aligned, soft matrices suspended between stiff posts (**Figure 5.2g,h**). This finding may be explained by a greater relative influence of increased uniaxial workload against the stiff posts, given that these tissues also exhibited enhanced myofibril assembly and alignment compared to tissues formed on random matrices under soft boundary conditions (**Figure 5.2j,k**). This surprising result suggests that iPSC-CMs contracting against stiffer boundary constraints can form aligned myofibrils regardless of the topographical alignment of the underlying matrix, as has been shown previously in 3D tissues (Bliley et al. 2021; Huebsch et al. 2022; Ronaldson-Bouchard et al. 2018). However, as these tissues demonstrated limited fractional shortening and work, this condition may represent a diseased or supraphysiologic mechanical environment (Leonard et al. 2018).

We next explored how microenvironmental mechanics impact iPSC-CM EHT maturation. To assess structural maturation, we immunostained tissues formed in different mechanical environments for connexin-43, the predominant cardiac gap junction protein, and the myosin regulatory light chain MLC-2v, which is known to be enriched in adult ventricular CMs (Karbassi

et al. 2020) (**Figure 5.3a-d**). Corroborating our measurements of fibroTUG contractility and myofibril assembly, tissues formed on soft (0.68 kPa), aligned matrices and soft (0.41 N/m) posts expressed the highest levels of connexin-43 and MLC-2v compared to tissues formed on stiff aligned matrices, soft non-aligned matrices, or between stiff posts (**Figure 5.3a-d**). Long term culture of tissues under these conditions in OxPhos media yielded a progressive increase in both MLC-2v and connexin-43 expression until day 21 (**Supplementary Figure 5.6)**. Additionally, cardiac troponin T expression was also most abundantly expressed in tissues formed on soft (0.68 kPa) aligned matrices and soft (0.41 N/m) posts (**Supplementary Figure 5.7**).

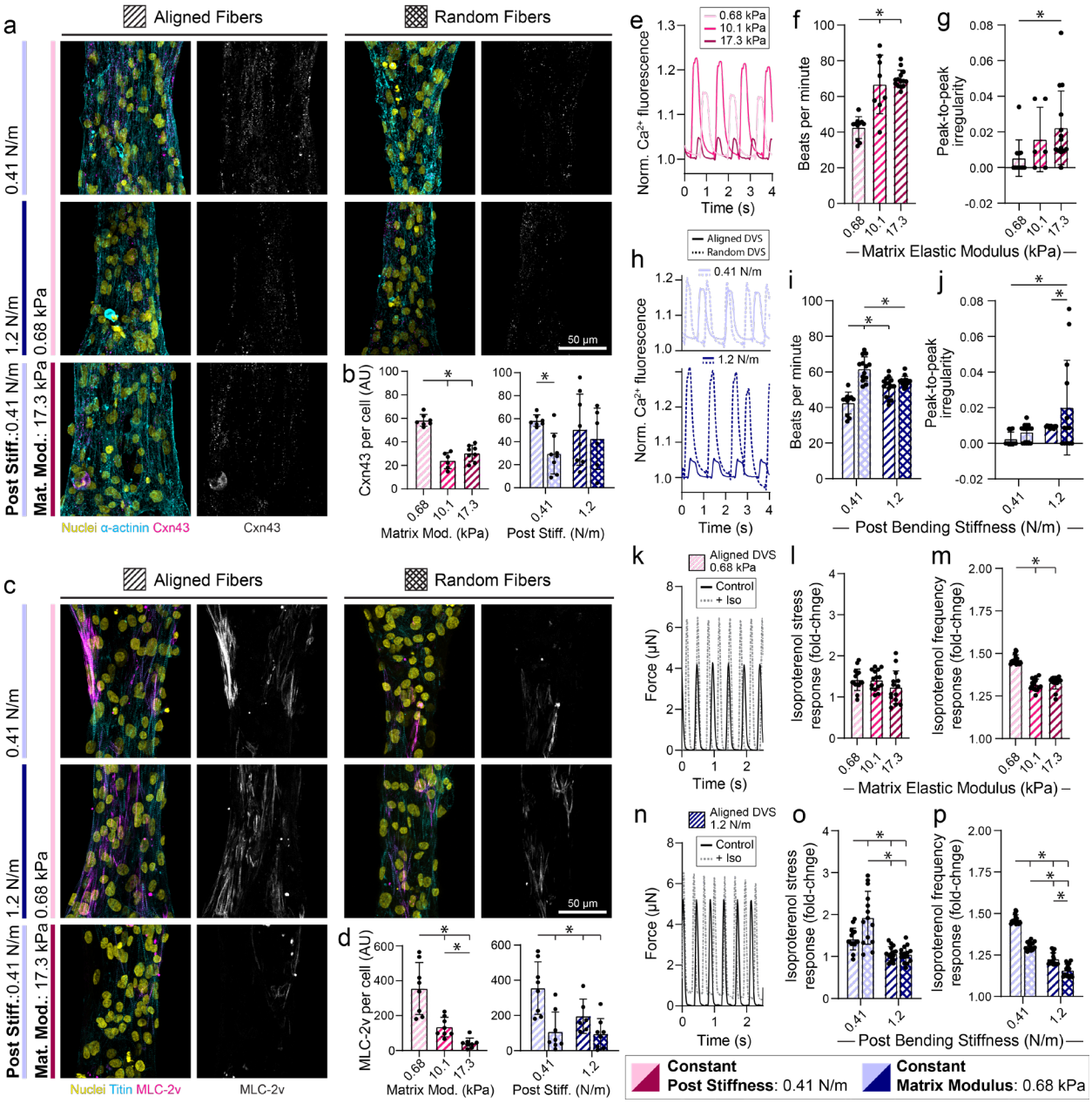

Figure 5.3: Fibrous matrix alignment, stiffness, and mechanical constraints influence iPSC-CM tissue development. (**a**) Confocal fluorescent images of fibroTUG tissues of varied fiber alignment, fiber stiffness, and post stiffness immunostained for α-actinin and connexin-43. All images show a region located at the center of each tissue. (**b**) Quantification of connexin-43 (Cxn43) expression (n ≥ 6). (**c**) Confocal fluorescent images of fibroTUG tissues of varied fiber alignment, fiber stiffness, and post stiffness seeded with iPSC-CMs containing a GFPtitin reporter and immunostained for MLC-2v. Again, all images show a region located at the center of each tissue. (**d**) Quantification of MLC-2v expression (n ≥ 6). Calcium flux dynamics were analyzed, with representative flux traces shown in (**e**) and (**h**), to determine (**f,i**) contraction frequency (n ≥ 8) and (**g,j**) peak-to-peak irregularity, as quantified by the standard deviation of time interval

between peaks ($n \geq 6$). Contractile dynamics in response to isoproterenol treatment (10 nM) were analyzed, with representative contraction traces shown in (**k**) and (**n**), to determine the fold change in (**l,o**) contractile force and (**m,p**) contractile frequency ($n \geq 14$). Blue hatching within bar plots indicates where post stiffness was held constant at 0.41 N/m in **(b,d,e-g,k-m**) to explore the impact of matrix alignment and post stiffness on tissue development. Pink hatching within bar plots indicates matrix stiffness was held constant at 0.68 kPa in (**b,d,h-j,n-p**) to explore the impact of matrix alignment and fiber stiffness on tissue development. All data presented as mean ± std; * $p < 0.05$.

To further corroborate these findings, we next assessed calcium handling of tissues formed with the fibroTUG platform. Briefly, tissues were incubated with a calcium sensitive dye and imaged at high frame rates > 65 frames/sec. Quantification of calcium flux dynamics indicated tissues formed on soft (0.68 kPa) aligned matrices with soft (0.41 N/m) posts contracted at the lowest frequency and at the most regular intervals (in contrast to heightened peak-to-peak irregularity observed on tissues formed on stiff or random matrices, suggestive of heightened arrythmogenic activity); of note, decrease contraction frequency and regularity are both considered to be characteristic of more mature iPSC-CMs (Karbassi et al. 2020) (**Figure 5.3e-j; Supplementary Movie 5.6, Supplementary Movie 5.7, Supplementary Movie 5.8**). Additional analysis indicates that increased matrix and increased matrix stiffness also results in changes in flux rise time, decay time, and full width half max (**Supplementary Figure 5.8**). We also treated tissues with the β-adrenergic agonist isoproterenol to further analyze tissue maturation and function (**Figure 5.3k-p**). As β-adrenergic signaling plays a critical role in regulating cardiomyocyte contractility and calcium handling, robust responses to agonists of this pathway, such as increased contractile frequency and stress, are generally indicative of a more mature phenotype (Jung et al. 2016; Karbassi et al. 2020; Ronaldson-Bouchard et al. 2018; Tsan et al. 2021). Across all conditions tested, tissues demonstrated chronotropic and inotropic responses to isoproterenol (**Figure 5.3k-p; Supplementary Movie 5.9**). Importantly, isoproterenol induced a

greater force-frequency response in tissues formed on soft (0.68 kPa), aligned matrices with soft (0.41 N/m) posts as compared to tissues formed on stiffer aligned matrices, soft non-aligned matrices, or stiffer posts (**Figure 5.3k-p**).

These findings highlight the value of a bioengineered platform that enables orthogonal tuning of various microenvironmental mechanical inputs, as each input appeared to have unique effects on tissue structure and function. Collectively, the results presented herein support the claim that tissues formed on soft, aligned fibrous matrices contracting against soft boundaries resulted in the most structurally and functionally mature EHTs. Additionally, these studies also reveal that each mechanical perturbation impacts tissue function, assembly, and maturation and in unique ways. Specifically, disrupting fiber alignment reduces both myofibril organization and density resulting in less contractile tissues. Increases in fiber stiffness also yield less dense myofibril networks, promote an arrhythmogenic phenotype, and decrease cell-matrix adhesions in contrast to findings from studies tuning hydrogel substrate stiffness. Increased post stiffness also resulted in a more prominent arrhythmogenic phenotype, but only when tissues were formed on random matrices between stiff pillars. Studies using this highly controlled system also showed that combinations of mechanical and architectural inputs can alter tissue structure and function in complex and non-intuitive ways. For example, while randomly oriented fibers in most combinations with post and fiber stiffness led to decreased tissue contractility and disorganized myofibrils, surprisingly, randomly oriented fibers spanning stiff posts resulted in aligned myofibrils and tissues with heightened contractility. Despite mirroring the highest functioning tissues in terms of contractile stress and myofibril organization, these tissues displayed substantial contractile frequency irregularity consistent with a pro-arrhythmic phenotype and expressed lower levels of connexin-43 and MLC-2v (**Figure 5.2, Figure 5.3**). Leonard et al. showed that gradually

increasing cantilever stiffness yields increases in contractile force to a point where the boundary stiffness reached potentially pathologic levels (Leonard et al. 2018). Additionally, increased mechanical loading of tissues has been shown to increase myofibril organization (Bliley et al. 2021; Ramachandran et al. 2023), further supporting the fact that high boundary stiffness may be driving this phenotype. While established EHT platforms have been used to examine the impact of individual mechanical perturbations, we can explore the combinatorial effects of this wide array of physiologically relevant biophysical parameters via the unique combination of predefined synthetic ECM-mimetic fibers integrated with microfabricated pillars. Finally, while these studies indicate the importance of control over mechanical features and matrix architecture in driving iPSC-CM maturation, other maturation techniques such as electrical pacing and metabolic programming are likely essential in deriving tissues that more closely approach the function of healthy adult myocardium (Correia et al. 2017; Feyen et al. 2020; Ronaldson-Bouchard et al. 2018). Indeed, culturing fibroTUGs formed with varying post stiffnesses in media that promotes oxidative phosphorylation (OxPhos) yielded tissues with greater contractile force after 7 and 14 days in culture as compared to those cultured in standard media (Tsan et al. 2021) (**Supplementary Figure 5.3**). While tissues cultured in baseline RPMI-1640 medium supplemented with B27 appear to adapt their contractile machinery to exhibit similar levels of force on posts of increasing stiffness, tissues cultured in OxPhos medium for 14 days between 0.9 N/m posts had the highest contractile function compared to tissues formed between 0.41 N/m and 1.2 N/m (**Supplementary Figure 5.3c-d**). These results are consistent with previous studies showing that metabolic maturation can increase the levels of tissue contractile force and further suggest that iPSC-CM tissues will adapt to increasing post stiffness by increasing their contractility

until the tissue's boundary stiffness approaches a stiffness regime reflecting pathological conditions (J. Guo et al. 2021; Leonard et al. 2018; Z. Ma et al. 2018; Tsan et al. 2021).

5.4.3 Tissue specific modeling of fibroTUG reveals altered cellular response to matrix stiffness

The ability to orthogonally tune mechanical and architectural inputs to EHT formation enables investigation into how iPSC-CMs sense and respond to distinct physical microenvironmental cues. However, a limitation of many EHT platforms (including ours) is that tissue-scale contractile force readouts are determined by measuring post deflections. While this affords a direct measure of dynamic tissue contractility, these measurements fail to capture stresses and strains at the cell and subcellular levels. This is best illustrated by an example of highly contractile CMs contracting on rigid matrices, where limited post deflections would misleadingly suggest low CM contractility. The discrepancy between tissue contractility and cell force/stress thus limits our interpretation of how iPSC-CMs may be responding to matrix alignment, matrix stiffness, or boundary constraints. To overcome this challenge, we generated tissue-specific computational models of fibroTUGs that enable quantification of the active cell stresses generated by iPSC-CMs within these tissues based on the input parameters of composite force, myofibrillar structure, and the underlying fiber structure. Detailed methods on how tissue-specific models were generated and validated can be found in Jilberto et al. (2023) (Jilberto et al. 2023). Briefly, to generate these computational models, an image analysis pipeline was developed to extract key matrix and cell parameters including fiber density, alignment, and dispersion; sarcomere density and alignment; and tissue displacements (i.e. post deflections) from time-lapse imaging (DePalma et al. 2021) (**Figure 5.4a-c**). From these metrics, a non-linear hyperelastic finite element model that accounts for tissue-specific fiber and cell mechanics was constructed. The contraction of each

tissue was simulated while computing the active stress of CMs required to generate the experimentally determined contractile dynamics (**Supplementary Movie 5.10**). By design, the model captures the contractile behavior experimentally measured at the posts (**Figure 5.4d**) and the active stress curve generated by the model describes the heterogenous local contractile function that the CMs generate given the tissue-specific inputs described above (**Figure 5.4e**).

In comparing tissues formed with soft vs. stiff fibers, we found that CMs on stiff matrices in fact generated lower active cell stresses than those on soft matrices (**Figure 5.4f**), suggesting that a cellular mechanoresponse to matrix stiffness in part explains the observed reduced force output. The extent to which decreased post-derived force measurements on stiff matrices is a product of an adaptive cellular response as opposed to the mechanics of the fiber matrices is unknown. However, the magnitude of the decrease in post force on stiff matrices compared to soft was greater than the magnitude of the decrease in the cellular active stress on stiff matrices (**Figure 5.4f**), highlighting a combination of cellular mechanosensing in addition to matrix stiffness and structure in defining tissue force measured by post deflections. Post stiffness, however, did not significantly change the relationship between tissue and active cell stresses, as expected (**Figure 5.4g**). Further exploration of insights gained from the computational model are discussed in the concurrent manuscript (Jilberto et al. 2023). Here, we delved deeper into the discussed result and its implications – that matrix stiffness impacts how CMs generate intercellular forces and forces applied extracellularly to the underlying matrix.

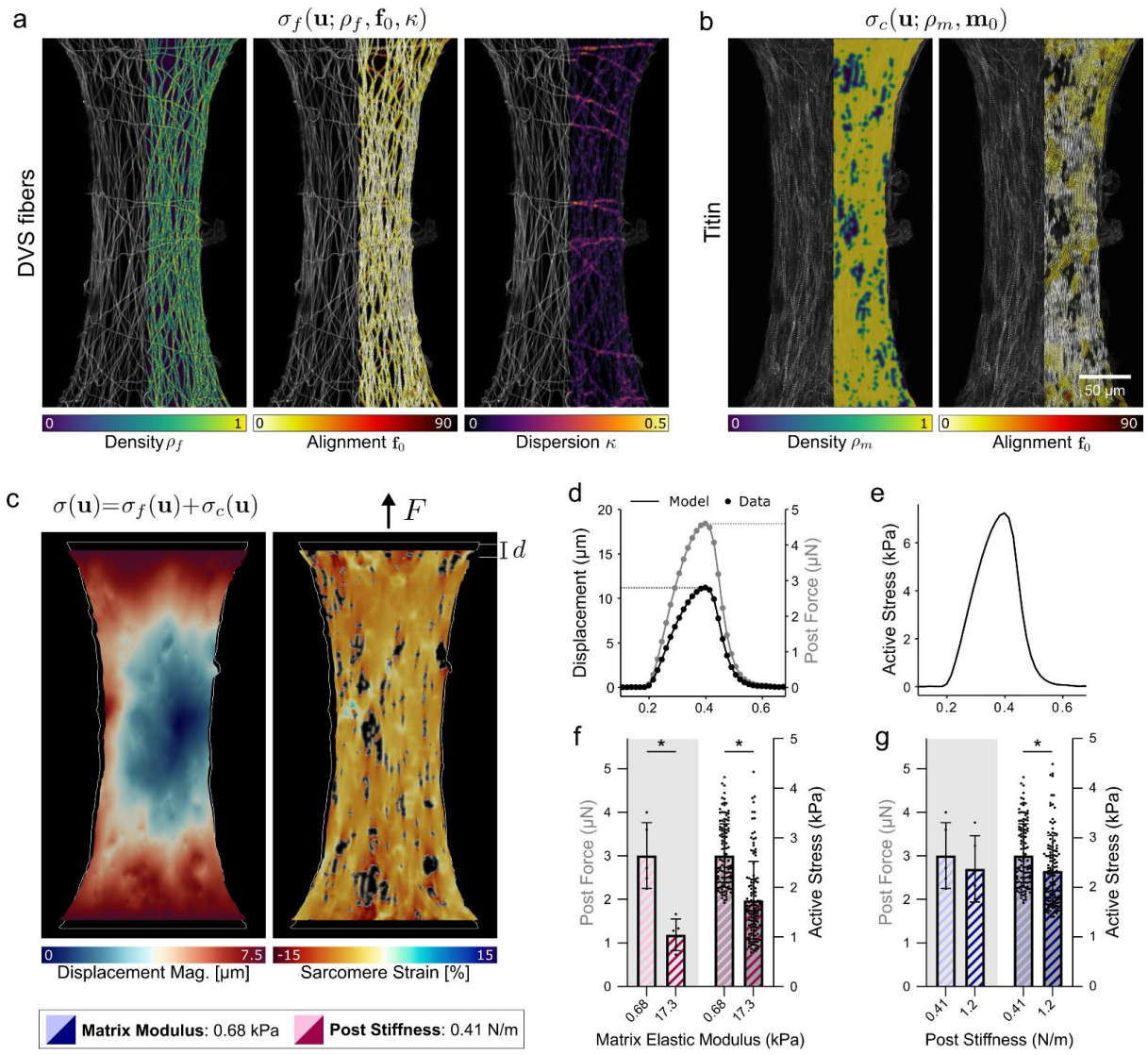

Figure 5.4: Tissue-specific computational modeling of fibroTUGs shows altered cellular contractility on matrices of varied stiffness. (**a**) Density, alignment, and dispersion fields characterizing the structure of the fibrous matrix. (**b**) Sarcomere density and alignment characterizing the structure of the myofibril network. (**c**) Results of the simulation for representative tissue showing inner displacement magnitude (left), and sarcomere strain (right). (**d**) Simulated post displacement and force time traces matching the experimental data for one simulation, where post displacement and force data are the simulation input. (**e**) The resulting mean active stress curve exerted by sarcomeres in the model to match the data in (**d**). (**f-g**) Post-force input (left two bars on gray background) compared with the computed active stress (right two bars on white background) for n>100 simulations with varied fiber stiffness (**f**) and varied post-stiffness (**g**). All data presented as mean ± std; * $p < 0.0001$ by unpaired t-tests.

5.4.4 Matrix stiffness impacts cell-ECM interactions and costamere formation

The preceding studies demonstrate that matrix stiffness significantly impacts EHT formation and function (**Figure 5.2, Figure 5.3**), expression of markers associated with maturation (**Figure 5.3**), and active cell stresses (**Figure 5.4**). As the fibroTUG platform provides a means to probe how the mechanics of the fibrous ECM impacts tissue assembly and maturation, we next examined if cell-ECM interactions might differ in tissues formed on soft compared to stiff matrices. Previous work from Chopra et al. implicated FAs or protocostameres as critical nucleation points for sarcomere and myofibril assembly in iPSC-CMs cultured on 2D micropatterns (Chopra et al. 2018). Moreover, Fukuda et al. examined the role of vinculin, a mechanosensitive protein that localizes to cell-matrix adhesions as well as adherens junctions, in zebrafish heart development (Fukuda et al. 2019). Their results indicate that mechanical strain upregulates vinculin expression, which is known to mediate myofibril maturation throughout development. We thus hypothesized that altered cell-matrix interactions as a function of fibrous matrix stiffness could impact FA and myofibril assembly. Further building upon this previous work and our findings highlighting changes in iPSC-CM function and maturation on matrices of varying mechanics, we also hypothesized that changes in FA assembly may coincide with changes in myofibril maturation at later time points (Day 7).

To test these hypotheses, we generated tissues between soft posts, on aligned soft (0.68 kPa) or stiff (17.3 kPa) matrices and assessed after 1, 3, or 7 days of culture. Immunostaining for vinculin, a marker of mechanoresponsive FAs and key regulator of cardiac development (Fukuda et al. 2019), and quantification of FA size, shape, and overall abundance via 3D segmentation of confocal z-stacks revealed marked stiffness-mediated differences in cell-matrix interactions during tissue assembly and maturation (**Fig. 5**). At day 1, during initial myofibril assembly, FAs were

observed to colocalize with matrix fibers and the number of vinculin-rich FAs, average size of FAs, total vinculin expression, and the eccentricity of each adhesion all were significantly greater on soft matrices as compared to stiff (**Figure 5.5a-e**). Further, initially formed immature myofibrils were more disorganized on stiff matrices than on soft (**Figure 5.2a, Supplementary Figure 5.9**). At days 3 and 7, the average FA size and total FA signal, as determined by vinculin immunostaining, decreased slightly independently of matrix stiffness (**Figure 5.5c,d**). At these later timepoints, vinculin localized to z-discs most prevalently in tissues formed on soft matrices as quantified by colocalization with the z-disc protein titin. This co-localization suggesting the formation of costameres to our knowledge has not been previously reported for iPSC-CM EHTs (**Figure 5.5a,e-g**). In native myocardium, costameres physically link myofibrils to the surrounding ECM at each z-disc, enabling force transmission to adjacent tissue (Samarel 2005; Shakp et al. 1997; Simpson et al. 1993). These structures are known to play a critical role in regulating myocardial contractile function and their formation during development may be regulated in part by mechanical strain within the tissue (Fukuda et al. 2019; Kaushik et al. 2015). We also observed an increase over time in the expression of the β1D integrin splice isoform uniquely in soft matrices (**Supplementary Figure 5.10**). Integrin β1D is specific to cardiac and striated muscle cells and has previously been associated with cardiac maturation (Belkin et al. 1996; Van Der Flier et al. 1997; Israeli-Rosenberg et al. 2014). Taken together, the formation of costameres and increased expression of β1D integrin may indicate a more mature CM adhesive state regulated by matrix mechanics that corresponds to the formation of more mature myofibrils (**Figure 5.3c,d**).

To further explore the connection between tissue maturation and costamere formation, we cultured fibroTUG tissues generated on soft, aligned matrices spanning soft posts in OxPhos media for 21 days to test the potential for further iPSC-CM maturation (Correia et al. 2017; Tsan et al.

2021). Fixing and imaging tissues immunostained for vinculin and GFP-titin at days 1, 3, 7, 14, and 21 revealed that vinculin colocalization with the z-disc persists at later time points as the tissues continue to mature (**Supplementary Figure 5.11a,e,f, Supplementary Figure 5.5**). As was the case in tissues cultured in standard RPMI B27 media, FA average size trended downward over time as did adhesion eccentricity, supportive of a transition in CM adhesion from proto-costameres to costameres (**Supplementary Figure 5.11b,d**). However, the total volume of vinculin-enriched structures in the tissue increased at later time points, suggesting continued remodeling of cell-matrix adhesions in conditions that drive tissue maturation (**Supplementary Figure 5.11d**). As previously described, costameres are composed of various proteins that play specific roles in processes such as cellular mechanosensing and signal transduction. We thus confirmed our previous findings by additionally immunostaining for zyxin, an adhesion protein associated with adhesion maturation that regulates actin polymerization (Al-Hasani et al. 2022; Shi, Wang, et al. 2022; Shi, Wu, et al. 2022). In contrast to vinculin, average zyxin volume remained relatively constant while total zyxin expression and eccentricity increased over time (Fig. 12a-d). Additionally, zyxin localization to costameres (based on co-localization with titin) lagged behind vinculin, peaking at day 14 as opposed to day 7 (**Supplementary Figure 5.12a,e-f**). This is consistent with the notion that zyxin is recruited to more mature adhesions based on previous observations of zyxin recruitment to adhesions following vinculin and paxillin, both of which are more rapidly recruited (C. K. Choi et al. 2008; Legerstee et al. 2019).

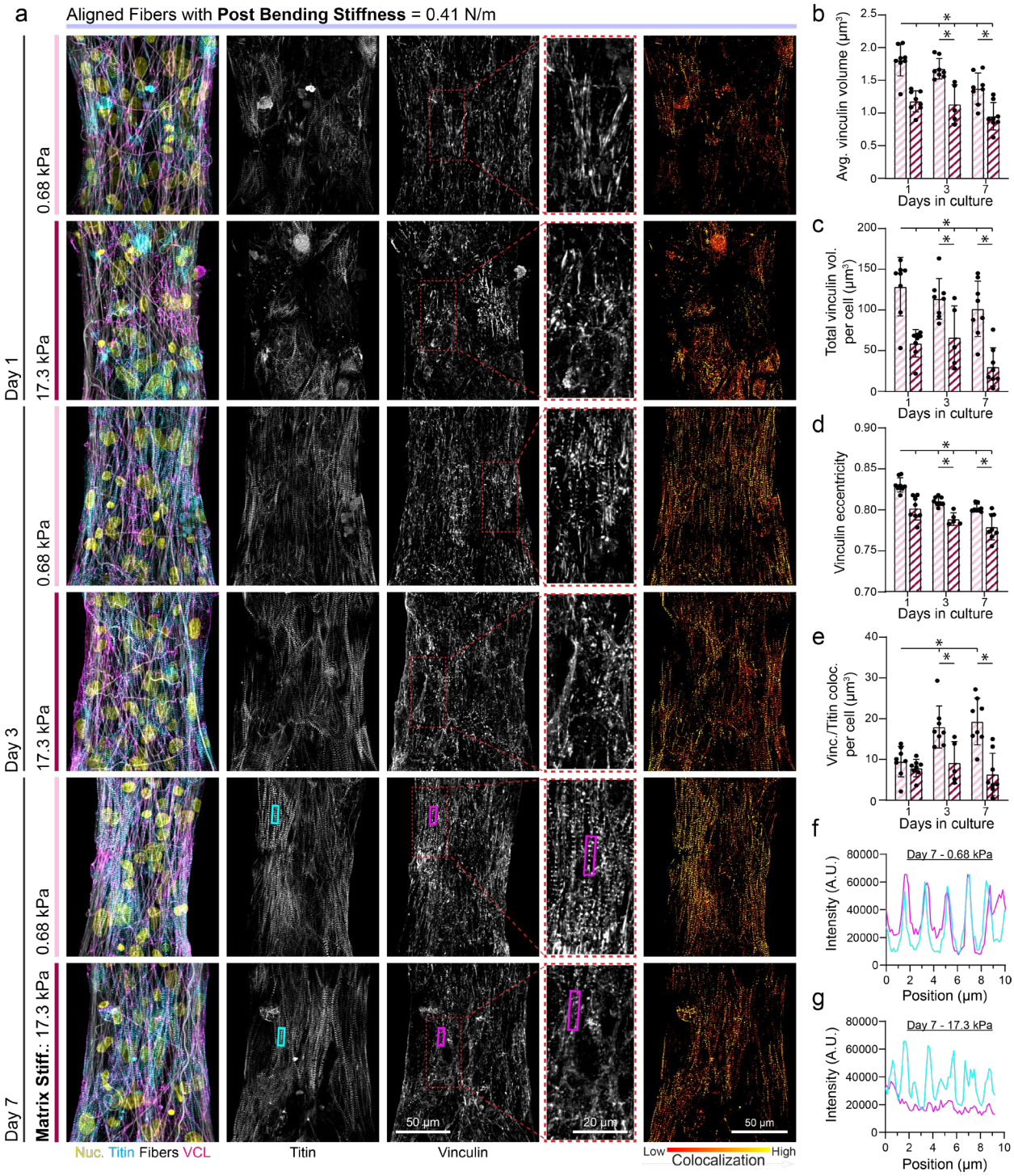

Figure 5.5: Matrix mechanics influence costamere formation which regulates myofibril assembly and maturation. (**a**) Confocal fluorescent images of fibroTUG tissues fixed at day 1, 3 and 7 post seeding on either soft (0.68 kPa) or stiff (17.1 kPa) aligned fiber matrices (post stiffness was held constant at 0.41 N/m). All images show a region located at the center of each tissue. (**b**) Average vinculin volume, (**c**) total vinculin volume, (**d**) and vinculin eccentricity were quantified

from the fluorescent images of immunostained vinculin ($n \geq 5$). (**e**) Costamere formation was assessed by quantifying vinculin colocalization with titin. Colocalization of vinculin and titin on day 7 was visualized via fluorescence intensity plots of titin (cyan) and vinculin (magenta) on (**f**) 0.68 kPa matrices and (**g**) 17.1 kPa matrices from lines drawn along the major axis of regions indicated by the rectangles overlayed on images in panel a. All data presented as mean ± std; * $p < 0.05$.

As vinculin also localizes to adherens junctions, we co-immunostained tissues fixed at days 1, 3, and 7 for N-cadherin and vinculin to examine whether N-cadherin (N-cad) and vinculin co-localization to the intercalated disc was also influenced by matrix stiffness (**Figure 5.6a-d**). Total N-cadherin expression increased comparably over culture time in tissues formed on both soft and stiff matrices (**Figure 5.6a,b**). Expression of desmoplakin, a key desmosomal protein, also increased similarly with time on soft and stiff matrices (**Supplementary Figure 5.13**). Localization of vinculin to N-cadherin, however, was greatest on soft matrices at days 3 and 7, potentially indicating the formation of more robust and mechanically engaged intercalated discs (**Figure 5.6a,c**). When normalizing the intensity of vinculin at intercalated discs to costameric vinculin, differences between the two matrix conditions were not apparent, indicating that vinculin expression is upregulated in both locations in the more contractile tissues formed on soft matrices (**Figure 5.6d**). This idea is supported by findings from Fukuda et al. that indicate vinculin localization to both costameres and cell-cell junctions is upregulated in CMs that experience mechanical strain during development (Fukuda et al. 2019).

Using high resolution imaging, we identified three distinct locations to which vinculin localizes in fibroTUG tissues: 1) FAs, most prevalent upon initial cell adhesion and during myofibril assembly (day 1), 2) intercalated discs, and 3) costameres, which were evident by day 7 following myofibril formation (Simpson et al. 1993) (**Figure 5.6e-g, Supplementary Figure 5.14**). Of note, vinculin localized to z-discs to form costameres preferentially in soft matrices by

day 7, suggesting myofibril maturation may be associated with the formation of these critical cell-ECM adhesions (**Figure 5.6e**). Vinculin was present at N-cadherin-rich adherens junctions in both soft and stiff matrices by day 7 (**Figure 5.6f, Supplementary Figure 5.14**), despite the lower amount of N-cadherin colocalization with vinculin observed in stiff tissues more broadly (**Figure 5.6c**). Finally, we observed vinculin localization to FAs distinct from z-discs based on the lack of titin and instead co-localization with non-muscle myosin-IIB (NMM-IIB) (**Figure 5.6g**). FAs were particularly prominent in assembling tissues on day 1 and more commonly observed on stiff matrices across all time points (**Figure 5.6g**), in line with decreased vinculin localization to titin noted on stiff matrices (**Figure 5.5e**). Furthermore, these complexes were larger and more elongated on soft matrices than stiff matrices at day 1, suggesting more robust adhesion to soft matrices, as previously described (**Figure 5.6g, Figure 5.5d**). These three vinculin-enriched adhesive structures were first observed by Simpson and colleagues in adult feline CM cultures (Simpson et al. 1993). Their results suggest that contractile behavior and the formation of cell-cell junctions regulate vinculin distribution and potentially myofibril assembly (Chopra et al. 2018; Merkel et al. 2019; Shakp et al. 1997; Simpson et al. 1993). Our observations indicate that cellular mechanosensing of the surrounding ECM drives the expression and localization of vinculin to distinct cellular domains within iPSC-CMs and further supports the role that contractile activity plays in regulating vinculin distribution (**Figure 5.5, Figure 5.6**).

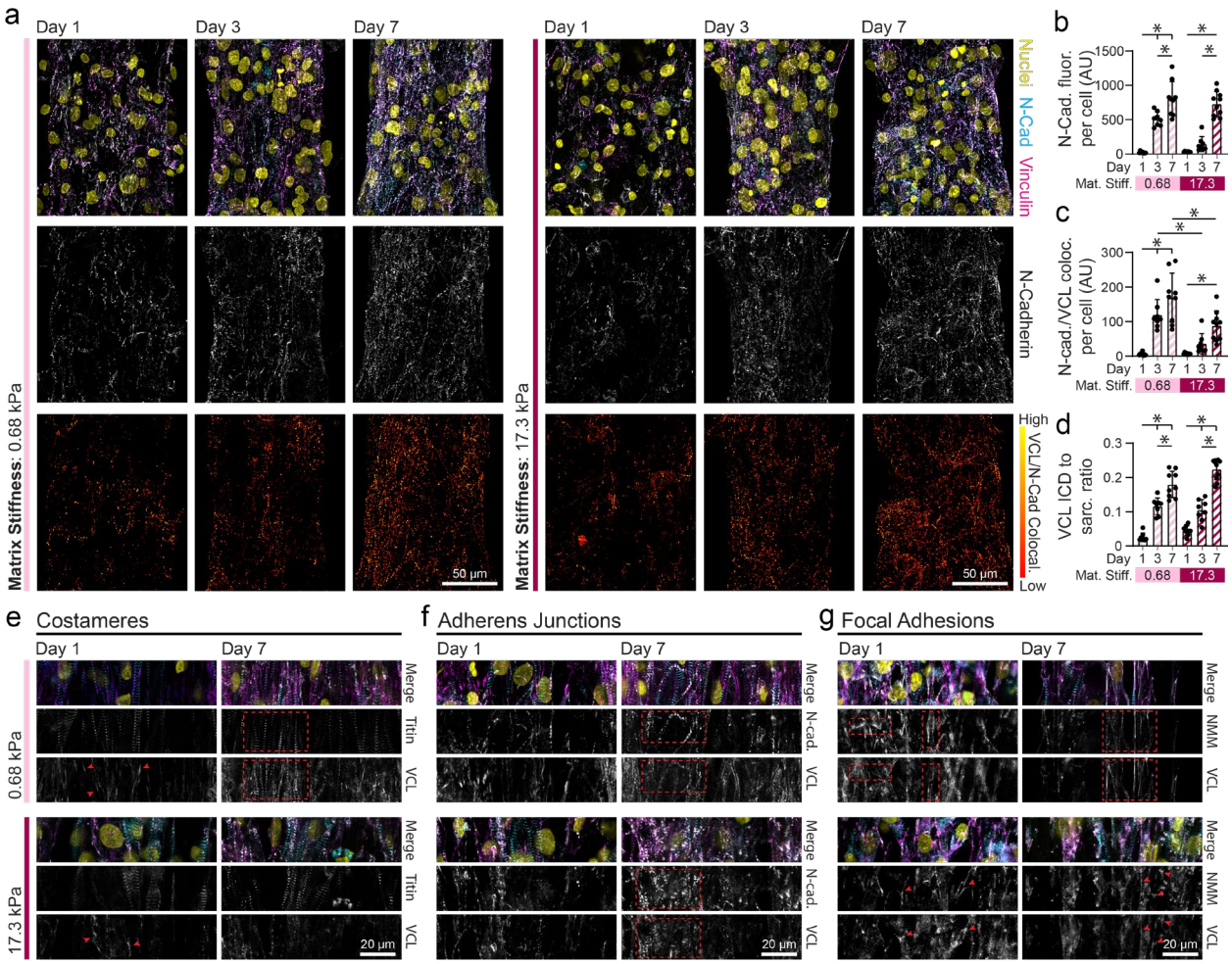

Figure 5.6: Microenvironmental mechanics regulate vinculin localization to costameres, adherens junctions and focal adhesions. (**a**) Confocal fluorescent images of fibroTUG tissues fixed at day 1, 3 and 7 after seeding on either soft (0.68 kPa) or stiff (17.1 kPa) aligned fiber matrices (post stiffness was held constant at 0.41 N/m). All images show a region located at the center of each tissue. (**b**) N-cadherin (N-Cad) fluorescence was quantified from the fluorescent images of immunostained N-cadherin ($n \geq 8$). (**c**) Vinculin localization to adherens junctions was quantified by analyzing vinculin and N-cadherin immunostained images. (**d**) Ratio of vinculin that localized to intercalated discs (ICD) to vinculin localized to costameres or sarcomere z-discs. Representative confocal fluorescent images of vinculin localization at days 1 or 7 to (**e**) costameres (i.e., vinculin colocalization to titin), (**f**) adherens junctions (i.e., vinculin colocalization to N-cadherin), and (**g**) focal adhesions (i.e., vinculin colocalization to NMM-IIB) not associated with either N-cadherin or titin staining, as indicated by red arrow heads and boxes. All data presented as mean ± std; * $p < 0.05$.

5.4.5 Tissue contractility drives myofibril maturation and costamere formation in soft matrices

In the preceding studies, soft (0.68 kPa), aligned fibrous matrices yielded the most contractile tissues and localization of vinculin to costameres, an adhesive phenotype not previously reported in EHTs derived from iPSC-CMs (**Figure 5.2, Figure 5.5, Figure 5.6**). As prior studies implicated myosin contractility as being critical for myofibril assembly and maturation (Chopra et al. 2018; Fenix et al. 2018; Taneja, Neininger, and Burnette 2020; Tsan et al. 2021), we next examined if myosin contractility also plays a role in regulating myofibril stability and costamere formation. iPSC-CMs seeded on soft matrices were treated with blebbistatin (50 μM) beginning at day 3, an inhibitor of both non-muscle myosins and cardiac myosins, or mavacamten (500 nM), a cardiac myosin specific inhibitor, to test whether myosin contractility is required for myofibril maturation and concomitant vinculin localization to costameres (**Figure 5.7**). Comparisons were made to tissues formed on stiff matrix conditions, which exhibited less costameric vinculin and overall lower myofibril density (**Figure 5.5**). Tissues were analyzed on day 8 to assess diastolic stress, vinculin localization, and myofibril assembly. In only untreated tissues on soft matrices, we observed a decrease in diastolic tissue length implying enhanced tissue contractility (**Figure 5.7b**). In contrast, blebbistatin and mavacamten treated tissues both increased in length, indicating relaxation and lower diastolic stress (**Figure 5.7c-d**). Further, the number of vinculin-enriched adhesions, total vinculin expression, and eccentricity of adhesive structures decreased in tissues treated with both blebbistatin and mavacamten from days 3-8, implying disrupted maturation of cell-cell and cell-ECM adhesions (**Figure 5.7e-g**). FA organization and vinculin localization in treated tissues formed on soft matrices were similar to that of untreated stiff matrix tissues, suggesting that

diminished CM contractility on stiff matrices may limit FA maturation (**Figure 5.7e-g**). No effect was observed when treating tissues from only days 7-8, most likely due to the shorter treatment duration that was not long enough to allow significant disassembly of cell-ECM adhesions and myofibrils which may happen more gradually (**Supplementary Figure 5.15**). Additionally, myofibril organization and density, along with non-muscle myosin IIB expression, decreased upon myosin inhibition, supporting a role for actomyosin contractility in myofibril maintenance (**Figure 5.7h,i, Supplementary Figure 5.16**). Finally, vinculin localization to z-discs decreased in treated tissues, implying that actomyosin contractility is critical for the formation of costameres (**Figure 5.7j**).

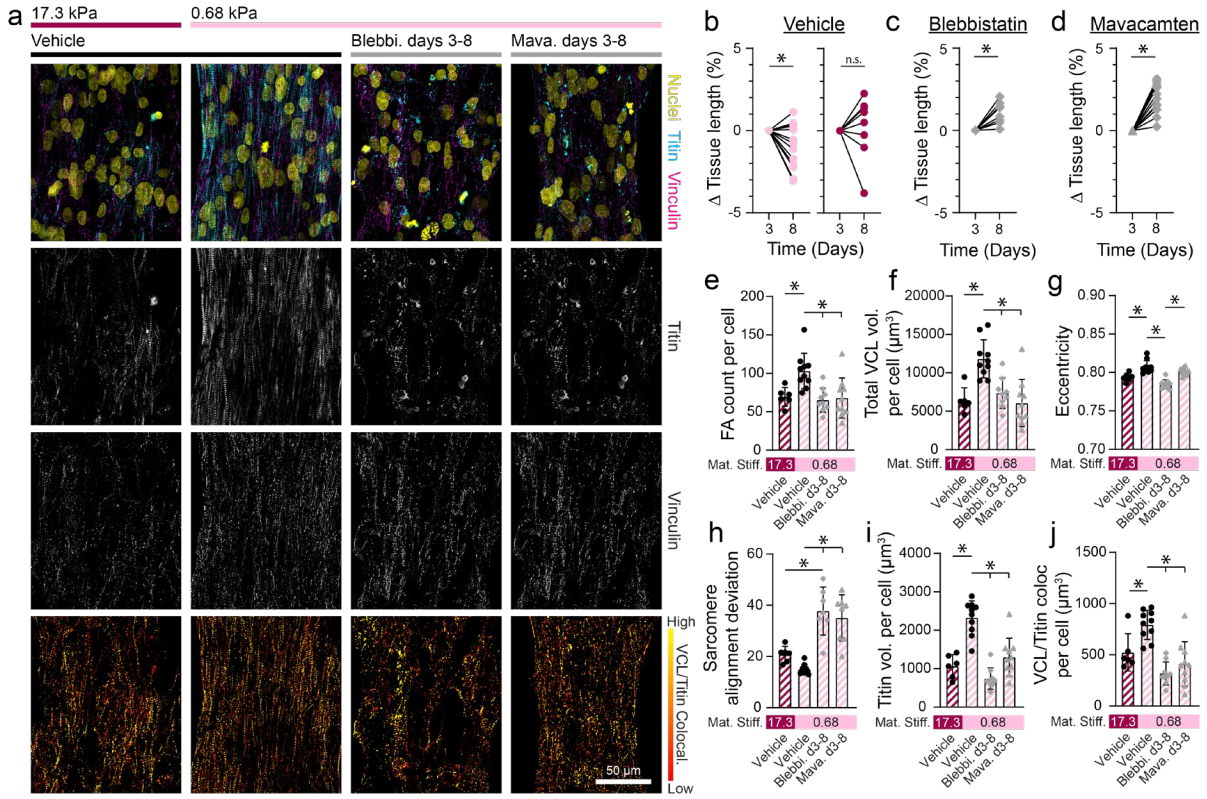

Figure 5.7: Tissue contractility drives the maturation and maintenance of myofibrils and costameres. (**a**) Confocal fluorescent images of fibroTUG tissues treated with blebbistatin (50µM) or mavacamten (500 nM). All images show a region located at the center of each tissue. (**b**)

Diastolic tissue length on day 3 and 8 of tissues seeded on soft (0.68 kPa) and stiff (17.1 kPa) aligned fiber matrices (post stiffness was held constant at 0.41 N/m) without treatment with the contractile inhibitors. (c,d) Diastolic tissue length of tissues seeded on soft matrices on day 3 before treatment with contractile inhibitors, (c) blebbistatin or (d) mavacamten, and day 8 after 5 days of treatment ($n \geq 8$). (e) Focal adhesion count, (f) vinculin volume per cell, and (g) focal adhesion eccentricity were quantified from the fluorescent images of immunostained vinculin ($n \geq 6$). (h) Sarcomere alignment deviation and (i) titin volume per cell quantified from fluorescent images of titin-GFP reporter ($n \geq 6$). Vinculin colocalization with titin per cell quantified from titin and vinculin images ($n \geq 6$). All data presented as mean ± std; * $p < 0.05$.

Variants in β-cardiac myosin (MYH7) and other regulators of contractility are associated with hypertrophic cardiomyopathies (HCM) and dilated cardiomyopathies (DCM). In fact, nearly a third of all known HCM variants arise from mutations in MYH7, in line with our findings that myosin driven CM contractility is critical for myofibril assembly, maturation, and overall structural integrity (Jordan et al. 2021; Nakamura and Sadoshima 2018). Additionally, many costameric proteins including vinculin and filamin C, are strongly implicated in dilated cardiomyopathies (Agarwal et al. 2021; Jordan et al. 2021; Sarker et al. 2019). Studying the impact of these mutations on tissue function requires accurate models of the myocardium that possess adult-like function and structure (Karbassi et al. 2020). The fibroTUG platform provides the mechanical control and ECM-like architecture of fibrous matrices necessary for driving a mature cell-adhesive phenotype that may be critical to a deeper understanding of the mechanisms of such diseases.

5.4.6 Costamere formation is associated with more mature myofibrils

As costameres are the sole mediator of CM-ECM adhesion in the mature adult myocardium, we next tested the hypothesis that MLC-2v expression directly correlates with costamere formation (**Figure 5.8**). Shared expression of costameric vinculin and MLC-2v could

suggest that robust cell adhesion to the matrix along the myofibril facilitates myofibril maturation via recruitment of the more mature myosin light chain isoform. We seeded iPSC-CMs containing a GFP-titin reporter on both soft and stiff aligned matrices tethered between soft posts and immunostained for MLC-2v and vinculin after 7 days of culture (**Figure 5.8**). As before, we observe increased MLC-2v expression and vinculin localization to z-discs on soft matrices. In contrast, iPSC-CMs on stiff matrices revealed significantly lower MLC-2v expression (**Figure 5.8a,b**). Interestingly, examining the ratio of MLC-2v colocalized with vinculin-rich costameres, we found that the percentage is high in both soft and stiff matrices, despite decreased overall expression of MLC-2v in stiff matrices, indicating a relationship between myofibril maturation and costamere formation (**Figure 5.8c**). To confirm this quantification, we segmented the tissue into subsections comparable to the area inhabited by a single spread CM. For each of these subregions, MLC-2v expression was plotted against costameric vinculin and fit to a linear regression model (**Figure 5.8d,e**). On both soft and stiff matrices, correlation between these two metrics was positive and significant; however, a higher linear regression slope was noted for tissues formed on soft matrices, indicating that the highest level of both costameric vinculin MLC-2v was attained in tissues on soft matrices (**Figure 5.8d,e**). Taken together, these data indicate that the formation of costameres is coupled with myofilament maturation, though costamere formation does not necessarily lead to myofibrillar maturation. This highlights the critical relationship between CM cell-matrix adhesion and myofibril maturation that hand in hand define CM and overall tissue contractility.

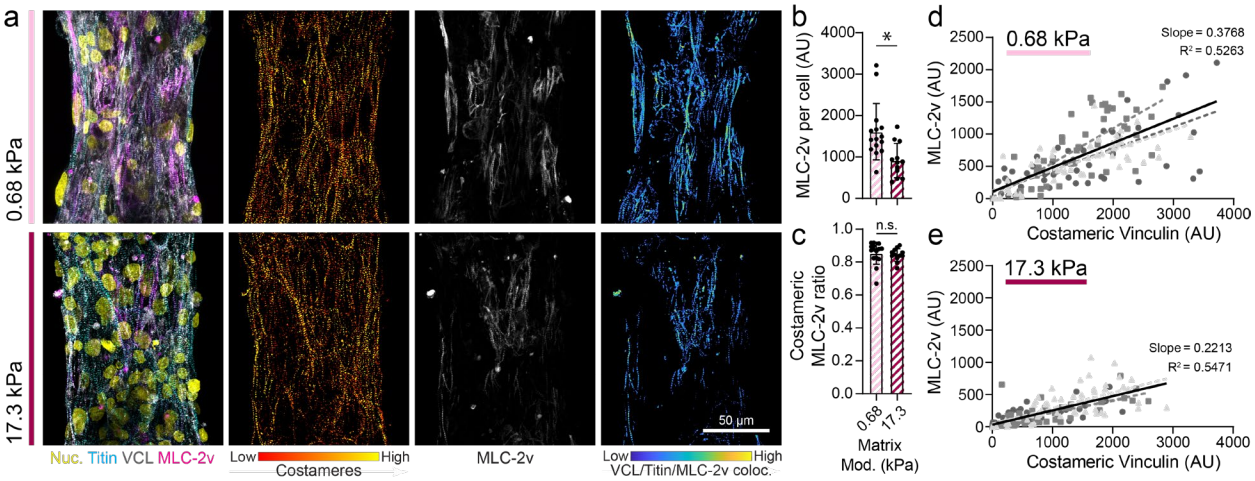

Figure 5.8: Costamere formation is associated with more mature myofibrils. (**a**) Confocal fluorescent images of fibroTUG tissues fixed at day 7 after seeding on either soft (0.68 kPa) or stiff (17.1 kPa) aligned fiber matrices (post stiffness was held constant at 0.41 N/m). (**b**) Quantification of MLC-2v expression per cell ($n \geq 12$). (**c**) Ratio of MLC-2v expressing myofibrils that are associated with robust costamere formation ($n \geq 12$). For tissues formed on (**d**) soft and (**e**) stiff matrices, correlation between MLC-2v expression and costameric vinculin was assessed by segmenting tissues into regions equal to roughly the size of one CM and MLC-2v and costameric vinculin expression was quantified within each of these regions. Each point on the plot represents a single subregion on one of three representative tissues. Linear regressions for data from each individual tissue are indicated by different colored dashed lines while linear regression of the data from these three tissues pooled together is indicated by the solid black line. The slope and R^2 value for this pooled data are also noted in the plots. All data presented as mean ± std; * $p < 0.05$.

5.5 Discussion

Despite many recent advances, studying the impact of biophysical cues on iPSC-CM tissue assembly and maturation remains challenging. Current 2D models provide an excellent setting for certain applications, but typically cannot recapitulate native tissue mechanics and architecture. Common 2D culture platforms such as micropatterned ECM proteins, for example, lack the fibrous topography and mechanical heterogeneity present in native myocardial tissues (McCain et al. 2012; A. J. S. Ribeiro et al. 2015; Tsan et al. 2021). Other electrospun scaffolds have limited

mechanical control, as materials such as polycaprolactone are much stiffer than fibrillar proteins in the ECM and lack mechanical tunability (Allen et al. 2019; Fleischer et al. 2015; Wanjare et al. 2017). Additionally, while widely used 3D constructs more closely mimic the dimensionality of native environmental conditions and enable control of some relevant mechanical inputs such as boundary stiffness, isolating the impact of tissue-relevant mechanical and architectural cues on CMs in these models is intractable due to the use of natural biomaterials (Cho et al. 2022; Tenreiro et al. 2021). Thus, new EHT platforms that capture the fibrous architecture of the native ECM while enabling orthogonal tuning of boundary stiffness, matrix alignment and stiffness (over a physiologic range) may provide new insights into iPSC-CM mechanosensing, function, and structural maturation. Thus, we created a 2.5D tunable iPSC-CM tissue platform composed of mechanically tunable synthetic fiber matrices suspended between two elastomeric posts, enabling the study of key physical microenvironmental inputs to tissue assembly and function: tissue boundary constraints, matrix fiber alignment, and matrix stiffness.

Unlike other approaches to engineering cardiac tissues, the orthogonal tunability of the fibroTUG cardiac microtissue platform allowed for careful dissection of how individual biophysical cues impact CM organization and function. While several studies have examined how mechanical inputs impact iPSC-CM function and tissue assembly, previously established platforms lack the ability to isolate the effects of relevant discrete physical properties in a setting that faithfully recapitulates the architecture of the myocardial microenvironment. Furthermore, the formation of thin fibroTUG tissues (~15 μm thick) between elastomeric posts permits comprehensive image-based analysis of both contractile function and subcellular structural development of the tissues, which enabled insights into the distinct impacts each mechanical input has on tissue assembly, contractility, and maturation.

More specifically, each mechanical perturbation made possible by the fibroTUG platform corresponds to various microenvironmental states that occur in native tissue development and disease progression. Our studies exploring the influence of fiber stiffness provide insight into how changes in ECM mechanics during cardiac development or disease progression may impact cardiac tissue organization and function. Alternatively, matrix alignment is known to play a critical role in tissue function where disorganized fibrotic ECM deposited due to myocardial injury has been suggested to contribute to abnormal myocardial biomechanics and disease-associated signaling (Kong, Christia, and Frangogiannis 2014; Karl T. Weber 1989). Finally, control over post stiffness to define tissue boundary constraints may reflect tissue remodeling associated with altered cardiac afterload, which is known to alter heart function in various contexts (Bliley et al. 2021; Leonard et al. 2018; Nakamura and Sadoshima 2018; Ramachandran et al. 2023; Toischer et al. 2010).

Importantly, many cardiac microtissue platforms require the inclusion of stromal cells for tissue assembly and compaction (Boudou et al. 2012; Giacomelli et al. 2020; J. Guo et al. 2021; Ronaldson-Bouchard et al. 2018; Tenreiro et al. 2021; Thavandiran et al. 2013; Tiburcy et al. 2017). However, their random distribution amongst contractile CMs does not accurately recapitulate the organization of the native myocardium where CMs and stromal cells are segregated (Costa et al. 1999; Pope et al. 2008; Karl T. Weber 1989), and furthermore confounds clear insights into how various biophysical cues impact specifically CM development and maturation. Additionally, these tissues typically exhibit limited stability over time in culture due to stromal cell proliferation, contraction, and tissue delamination (Karbassi et al. 2020; Tenreiro et al. 2021). In our fibroTUG platform, predefining matrix properties before seeding enables the assembly of robust iPSC-CM tissues without the addition of stromal cells. There is mounting

evidence to suggest that CM-fibroblast crosstalk via both direct cell-cell connections and paracrine signaling can drive iPSC-CM maturation(Giacomelli et al. 2020; Uscategui Calderon, Gonzalez, and Yutzey 2023). Expanding on this idea, these studies show that, independent of other biochemical signals, CM mechanosensing of synthetic matrices that recapitulate fibroblast secreted perimysial collagen fibers can significantly impact CM development and function. Future studies using this platform will be focused on comparing tissues formed from pure iPSC-CM populations to those containing fibroblasts to probe how fibroblasts might impact iPSC-CM maturation.

We found that tissues formed on soft (0.68 kPa), aligned matrices suspended between soft (0.41 N/m) posts were the most mature, as evidenced by myofibril density and contractility (**Figure 5.2, Figure 5.3**). These optimized mechanical conditions yielded tissues with comparable contractile stress output to tissues generated in other studies (Bliley et al. 2021; Huebsch et al. 2016; Leonard et al. 2018; Melby et al. 2021; Ronaldson-Bouchard et al. 2018; Ruan et al. 2016; Shadrin et al. 2017). However, most of these approaches yield tissues that were much larger and therefore composed of substantially more CMs (often >1e6 CMs) as compared to our tissues composed of an average of 100 CMs. Further, our fibroTUG microtissues contract with higher stress than myocardial tissues strips obtained from human newborn and infant hearts (~0.9 kPa) (Wiegerinck et al. 2009). Taken together, this mechanically tunable platform can drive the formation of functional iPSC-CM tissues.

Each mechanical input we explored had distinct effects on tissue assembly, maturation, and contractility, suggesting that different mechanosensing mechanisms may be involved in responding to various mechanical signals. First, altered contractile function of tissues formed in aligned vs. random fiber matrices is likely a result of disrupted myofibril density and organization.

(**Figure 5.2**). By isolating matrix alignment from matrix and boundary stiffness perturbations, we can conclude that iPSC-CM interactions with disorganized matrices leads to impaired formation of aligned myofibrils. Specifically, we found that increased fiber alignment improved myofibril alignment and density, independent of fiber stiffness and post stiffness. Secondly, isolating the impact of altered matrix stiffness in our tissue platform revealed that contractility of CMs on soft vs. stiff fiber matrices is in part defined by differential mechanosensing and CM-matrix interactions. Using non-degradable, mechanically defined, and well-characterized synthetic fibers that can be easily imaged facilitated the creation of tissue-specific modeling the provided precise analysis of how matrix architecture and mechanics impact iPSC-CM contractile function (Jilberto et al. 2023). This integration of finite element models of our fibroTUG platform provided further insights into how iPSC-CMs respond to this specific mechanical perturbation and confirmed that CMs on stiff matrices indeed individually generating less stress (**Figure 5.4**). Specifically, we found that differences in tissue contractility as measured by elastomeric posts were not only caused by changes in matrix deformability, but also a cellular contractile response to changes in matrix stiffness, as measured by changes in cellular active stresses (**Figure 5.4**). Further supporting this claim, cell adhesions, and more specifically the formation of costameres, proved sensitive to matrix stiffness, implying that cellular mechanosensing dictates the formation of distinct adhesive structures that may influence tissues assembly and structural maturation (**Figure 5.5**). Current computational modeling efforts are focused on integrating cell-ECM and cell-cell adhesions into the system with the goal of better understanding how tissue mechanosensing impacts tissue growth or disease progression[67]. Lastly, while increasing post stiffness did not impact cellular active stress or post-force measurements, stiff boundary constraints appear to be sufficient in driving myofibril alignment regardless of matrix organization, despite low levels of fractional shortening.

Fiber alignment plays a key role in the development of fibroTUG tissues, and previously developed techniques including electrospun scaffolds, nano- and micro-grooved surfaces, or micropatterning have been shown to drive alignment and subsequent maturation of iPSC-CMs (Allen et al. 2019; Carson et al. 2016; DePalma et al. 2021; A. J. S. Ribeiro et al. 2015; Tsan et al. 2021). Additionally, many groups have explored how matrix stiffness impacts CM maturation and contractile function, culminating in the observation that CMs contract most robustly on hydrogels of physiologic stiffness (~8-10 kPa) (Engler et al. 2008; A. J. S. Ribeiro et al. 2015). In our studies, soft, fibrous matrices (0.68 kPa) that more closely mimic the stiffness of fetal heart tissue yielded the most contractile tissues (Engler et al. 2008). This discrepancy could be explained by the distinct architecture and local mechanics of fibrous matrices as compared to isotropic, continuum-like hydrogel or elastomer surfaces that lack discrete fibrous structure and topography (DePalma et al. 2021). In addition to better modeling CM responses the native tissue microenvironment, this tissue model may also better mimic the mechanics of other 3D EHT constructs made from fibrous hydrogels such as fibrin or collagen. Furthermore, in our platform, tissues formed on soft, aligned matrices with soft boundary conditions displayed the highest levels of fractional shortening, a key regulator of iPSC-CM maturation (Bliley et al. 2021; Ruan et al. 2016; Tsan et al. 2021). Caution should be taken, however, when attempting to compare elastic moduli of hydrogels and other in vitro culture platforms with the modulus of native tissues, as characterization techniques vary widely across settings (e.g. testing in compression vs. tension, or at different length-scales). Additionally, as highlighted here, cells sense and respond to many mechanical properties of a material that are not captured in a simple elastic modulus measurement. Previous work from our group showcases this idea, demonstrating that fibroblasts or mesenchymal stem cells cultured on fibrous scaffolds generate more robust focal adhesions when individual fibers and resulting

matrices are softer rather than stiffer, in contrast to previous studies showing great focal adhesions formation on stiffer elastic hydrogel or elastomer surfaces (Baker et al. 2015; C.D. Davidson et al. 2020). As it is well accepted that iPSC-CMs are most comparable to fetal CMs, the results presented here supports the concept of initiating CMs in a soft environment to allow them to assemble properly prior to gradually increasing matrix mechanics to promote CM growth and maturation, as has been previously explored using elastic hydrogels (Young and Engler 2011).

One aspect of this mechanoresponse involves the formation and modulation of costameres. In agreement with previous work (Chopra et al. 2018; Taneja, Neininger, and Burnette 2020), we observed that protocostamere formation corresponds with initial myofibril assembly. However, our experiments examined timepoints beyond early spreading of iPSC-CMs mediated by proto-costameres in a multicellular, tissue-like context. Intriguingly, we found that costamere formation, as evidenced by vinculin and zyxin localization to the z-disc, is maximized when tissues are maintained on soft (0.68 kPa) fiber matrices (**Figure 5.5**). Previous results obtained by culturing single iPSC-CMs on soft vs stiff hydrogels indicated that the stiffness of the hydrogel surface did not impact costamere formation, supporting the idea that iPSC-CMs interact differently with fibrous matrices compared to isotropic hydrogel surfaces (Shi, Wang, et al. 2022). Further, these findings support a dynamic interplay between adhesion myofibrillar proteins where protocostameres give rise to myofibrils followed by a redistribution of adhesion proteins to along the myofibril under particular mechanical conditions. Additionally, we found that iPSC-CMs possessing more costameres also demonstrated increased expression of MLC-2v, a marker of mature myofibrils in ventricular CMs (**Figure 5.8**). As costameres play a critical role in transmitting force generated by the myofibril to the surrounding matrix, these results suggest that mechanical inputs from the microenvironment keenly influence the formation of distinct types of

matrix adhesions and myofibrillar content. Despite observing that MLC-2v expression and costameres correlate on a per cell basis (**Figure 5.8**), the connection between the two remains to be explored.

Our results may inform the design of larger-scale tissue patches and translatable regenerative therapies, where interactions between iPSC-CMs and biomaterials are likely critical to the proper assembly of functional, mature myocardial syncytia. Future work translating the identified optimal mechanical parameters to fully 3D tissue constructs with therapeutic potential will be essential. Previous work developing 3D EHT constructs lacked close examination of cell-ECM interactions, at least in part due to imaging challenges inherent to these thick tissue constructs. However, it is critical to understand how CMs interact with their microenvironment in these constructs, as focal adhesions and costameres are likely required for not only native tissue-like contractile function of EHTs but also robust integration of EHTs with native tissue upon implantation due to their critical roles in force transmission. Scaffolds design features such as the incorporation of soft, aligned fibers should be considered, especially in light of prior studies testing scaffold-free implants which resulted in arrhythmic activity (Liu et al. 2018; Shiba et al. 2016). Motivated by the findings in this work, we are currently working to integrate synthetic fibers into fibrin- or collagen-based 3D iPSC-CM tissue constructs to examine whether findings presented in these studies translate to the biofabrication of larger scale tissue patches.

Furthermore, as alterations in myocardial matrix organization and mechanics are a hallmark of many forms of cardiac disease, the high mechanical tunability of the fibroTUG platform could enable key insights into the mechanisms of disease and in the longer term, facilitate the development of better treatment options. Of note, mutations in mechanosensitive proteins, including vinculin, have been shown to cause various forms of heart disease such as dilated or

hypertrophic cardiomyopathies(Jordan et al. 2021; Nakamura and Sadoshima 2018). Ongoing studies are being conducted to better understand how changes in tissue mechanics may exacerbate disease phenotypes observed in patients with genetic cardiomyopathies, specifically in proteins of the costamere or intercalated disc(Jordan et al. 2021; Lyon et al. 2015; Nakamura and Sadoshima 2018). Finally, in vitro CM tissue models, such as the fibroTUG platform presented here show promise as platforms for screening drugs for potential cardiotoxicity or effective in treating heart disease. Here, we show that tissue response to isoproterenol, a clinically approved inotrope used to treat patients with heart failure, is impacted by altered tissue mechanics, highlighting a requirement for the informed design of drug screening platforms.

In conclusion, we developed a mechanically tunable iPSC-CM microtissue platform that we used to investigate the impacts of specific, physiologically relevant microenvironmental states. Platforms such as this can help progress the field of cardiac tissue engineering by providing mechanistic insights into how CMs interact with both their native ECM and engineered scaffolds to generate more effective *in vitro* tissue models of disease and regenerative therapies.

5.6 Materials and Methods

5.6.1 Reagents

All reagents were purchased from Sigma Aldrich and used as received, unless otherwise stated.

5.6.2 Elastomeric cantilever array fabrication

Arrays of poly(dimethylsiloxane) (PDMS; Dow Silicones Corporation, Midland, MI) postswere fabricated by soft lithography as previously described [cite DexVS paper and bdon nat mat]. Briefly, silicon wafer masters possessing SU-8 photoresist (Microchem, Westborough, MA) were produced by standard photolithography and used to generate PDMS stamps. Following silanization with trichloro(1H,1H,2H,2H-perfluorooctyl)silane, stamps were used to emboss uncured PDMS onto oxygen plasma-treated coverslips. Cantilever arrays were methacrylated with vapor-phase silanization of 3-(trimethoxysilyl)propyl methacrylate in a vacuum oven at 60 °C for at least 6 h to promote fiber adhesion to PDMS.

5.6.3 DVS fiber matrix fabrication

DVS polymer was synthesized as previously described by our lab (C.D. Davidson et al. 2020). Briefly, dextran was reacted with divinyl sulfone and the product was dialyzed and lyophilized. For electrospinning, DVS was dissolved at 0.7 g mL^{-1} in a 1:1 mixture of milli-Q water and dimethylformamide with 0.6% (w/v) lithium phenyl-2,4,6-trimethylbenzoylphosphinate (LAP; Colorado Photopolymer Solutions) photoinitiator, 2.5% (v/v) methacrylated rhodamine (25 mM; Polysciences, Inc., Warrington, PA), and 5.0% (v/v) glycidyl methacrylate. This solution was electrospun on coverslips containing microfabricated cantilever arrays affixed to a custom-built rotating mandrel with a hexagonal geometry driven by an AC motor with controllable speed

(DePalma et al. 2021). Electrospinning was conducted in an environmental chamber at 35% humidity with a flow rate of 0.2 ml h^{-1}, voltage of 7.0 kV, and a gap distance of ~5 cm to the grounded mandrel. After collection, fibers were stabilized by primary crosslinking under UV (100 mW cm^{-2}) through a microfabricated photomask for 20 s, such that only the fibers suspended in the region spanning two posts would be crosslinked. Upon hydration, uncrosslinked fibers were dissolved away leaving isolated suspended microtissues adhered to the posts. Fiber matrices were subsequently placed in LAP photoinitiator solutions of varying concentrations and exposed again to UV (100 mW cm^{-2}) for 20 s to tune fiber stiffness and sterilize substrates.

Matrices were functionalized with cell adhesive peptides cyclized [Arg-Gly-Asp-D-Phe-Lys(Cys)] (cRGD; Peptides International) via Michael-Type addition to available vinyl sulfone groups. Peptides were dissolved at 200 μM in milli-Q water containing HEPES (50 mM), phenol red (10 μg mL^{-1}), and 1 M NaOH to bring the pH to 8.0. A volume of 150 μL was added to each substrate and incubated at room temperature for 30 min.

5.6.4 Mechanical characterization

PDMS cantilever mechanics were characterized by deflecting individual posts with a ~100μm diameter tungsten rod of known elastic modulus attached to a micromanipulator (SmarAct) (**Supplementary Figure 5.1a-c**). Bending stiffness was calculated by measuring the cantilever deflection and the force applied by the tungsten rod using custom Matlab scripts. Bending stiffness was approximated using the following equations:

$$F_{rod} = \frac{3dEI_{rod}}{L^3} \qquad I_{rod} = \frac{\pi r^4}{4} \qquad \boldsymbol{Bending\ stiffness\ (k) = \frac{F_{rod}}{\delta}}$$

where d = rod deflection, E = elastic modulus of rod, L = length of the rod, r = radius of the rod, δ = post deflection, F_{rod} = force applied by the rod, and I_{rod} = moment of inertia of the rod. Rod

deflection (d) was quantified by subtracting the distance that the PDMS post moved (δ) from the distance moved by the micromanipulator holding the rod.

Matrix modulus was determined by pressing a microfabricated SU8 rectangle measuring 20 x 250 μm across the center of the fiber matrices to apply tension to the matrix (**Fig. S1d-f**). Using custom Matlab scripts, matrix modulus was extrapolated from the applied force (measured by the PDMS post's deflection) and the resulting tensile stretch of the fiber matrix. Matrix modulus was approximated using the following equations. First, the resultant length of half of the stretched fiber matrix L_f was geometrically defined as:

$$L_f = \sqrt{(\Delta h)^2 + (\frac{L_0}{2} - \delta)^2}$$

where Δh = indentation depth, L_0 = initial length of the fiber matrix, and δ = post deflection. As the resultant post deflection is the result of a force balance between the cantilever and resistance arising from tension in the stretched fiber matrix, we define the force on each post F_p as:

$$F_p = T\ sin\theta$$

where T = tension in the fiber matrix and θ = angle between the indenter and the fiber matrix. Tension in the matrix can thus be defined as follows:

$$T = F_p \frac{L_f}{\frac{L_0}{2} - \delta}$$

Next, we define elastic modulus of the fiber matrix, $E = \frac{\sigma}{\varepsilon}$, in terms of our measured parameters, where σ = stress and ε = strain.

$$\sigma = \frac{T}{A} = \frac{F_p L_f}{A(\frac{L_0}{2} - \delta)}$$

$$\varepsilon = \frac{2L_f - L_0}{L_0}$$

$$E = \frac{TL_0}{A(2L_f - L_0)}$$

More details on this calculation and mechanical testing set up can be found in **Supplementary Figure 5.1**.

5.6.5 iPSC culture and iPSC-CM differentiation

Induced pluripotent stem cells containing a GFP-titin reporter (Sharma, Toepfer, Ward, et al. 2018) (PGP1; gift from the Seidman Lab) or GFP-DSP reporter (WTC; Allen Institute AICS-0017 cl.6) were cultured in mTeSR1 media (StemCell Technologies) on Matrigel (Corning) coated tissue culture plastic and differentiated via temporal Wnt modulation as previously described (Burridge et al. 2014; Lian et al. 2012). Briefly, differentiation was initiated when iPSCs reached 90% confluency in RPMI 1640 media supplemented with B27 minus insulin on day 0 with the addition of 12 μM CHIR99021 for 24 hours. On day 3, CDM3 media containing 5 uM IWP4 on day 3 for 48 hours. Retinol inhibitor BMS 453 (Cayman Chemical, 1 μM) was also added for days 3-6 to minimize atrial lineage differentiation (Tsan et al. 2021; Q. Zhang et al. 2010). Cultures were then maintained in CDM3 media until contractions began between day 8 and 10. iPSC-CMs cultures were then transferred to RPMI 1640 media lacking glucose and glutamine (Captivate Bio) supplemented with 4 mM DL-lactate, 500 ug/mL human serum albumin (Sciencell Research Labs), and 213 ug/mL L-ascorbic acid 2-phosphate trisodium salt on day 11 for 4 days. Following purification, iPSC-CMs were replated as monolayers (300,000 cells/cm^2) on growth factor reduced Matrigel (Corning) in RPMI 1640 media supplemented with B27 for 7 additional days before seeding into tissues.

5.6.6 Microtissue seeding and culture

Due to the suspended nature of the fibrous matrices, it was determined that iPSC-CMs must directly land on the top of the matrices by patterning the cells through a microfabricated cell seeding mask to prevent cells from "rolling" off the tops of the matrices and landing on the substrate beneath. Additionally, this technique significantly reduced the number of iPSC-CMs needed to efficiently seed all the tissue on the substrate. To fabricate the seeding mask, 3D printed molds were designed in SolidWorks and printed via stereolithography (Protolabs). PDMS (1:10 crosslinker:base ratio) devices were replica cast from these molds. Prior to seeding the tissues, cell seeding masks were plasma treated for 5 minutes to generate highly hydrophilic surfaces that allow water to wick through the small microtissue scale wells in the mask. Vacuum grease was then applied to the edge of the seeding mask to ensure a watertight seal between the seeding mask and the substate prior to placing the mask on the tissue array substrate such that the holes in the mask sit directly above each suspended fiber matrix.

After aligning the seeding masks, iPSC-CMs were dissociated by 0.25% Trypsin-EDTA (Gibco) with 5% (v/v) Liberase for 5 min, stopped by an equal volume of 20% FBS/1 mM EDTA/PBS. Cells were triturated by gently pipetting with a p1000 pipette eight times to obtain a near single-cell suspension and centrifuged (200 g, 4 min). iPSC-CMs were resuspended in replating media (RPMI plus B27 supplement with 2% FBS and 5μM Y-27632 (Santa Cruz Biotechnology)) and 125,000 cells were seeded per fibroTUG substrate through the top of the cell seeding mask in approximately 200 μL of media. Cultures were then moved to the incubator and left undisturbed overnight to allow the iPSC-CMs to attach to the tissues before removing the seeding masks. Cultures were maintained in RPMI media plus B27 supplement and replenished every other day for the duration of studies. All studies were carried out for 7 days unless otherwise specified.

5.6.7 Contractile force analysis

Time-lapse videos of the microtissue's spontaneous contractions were acquired at 65 Hz on Zeiss LSM800 equipped with an Axiocam 503 camera while maintaining a temperature of 37 ℃ and 5% CO2. Maximum contractile force, contractile stress, contraction kinetics, and contraction frequency were calculated using a custom Matlab script based on the deflection of the posts and the measured post bending stiffness, as described previously (Boudou et al. 2012). For isoproterenol challenge, the same tissues were imaged prior to the addition of 10 nM isoproterenol and again 30 minutes after the addition of the drug for comparison.

5.6.8 Calcium imaging

Calcium handling analysis was performed by incubating cells for 1 hour at 37 ℃ with 5 μM Cal520-AM (AAT Bioquest). Cells were then returned to conditioned media preserved prior to adding the calcium sensitive dye and allowed to equilibrate for >30 min at 37 ℃ and 5% CO_2. Following equilibration, tissues were imaged under epifluorescence at 65 Hz while maintaining temperature and CO_2. Time-lapse movies of calcium flux were analyzed with custom Matlab scripts as previously described(DePalma et al. 2021). Briefly, average fluorescent profiles over time were determined for each tissue and parameters such as beats per minute, peak-to-peak irregularity, flux rise time, flux decay time, and peak full width half max were calculated. Contraction correlation coefficient was determined by dividing the entire tissue into 16 regions of equal area and calculating the average Pearson's correlation coefficient between the flux profiles of each of these regions.

5.6.9 Immunofluorescence staining

Samples were fixed in 2% paraformaldehyde for 10 min at RT. Samples were then permeabilized in PBS solution containing Triton X-100 (0.2% v/v), sucrose (10% w/v), and magnesium chloride (0.6% w/v) for 10 min and blocked in 1% (w/v) bovine serum albumin. Alternatively, to extract cytoplasmic vinculin, samples were simultaneously fixed and permeabilized in 2% paraformaldehyde in a buffer containing 1,4-piperazinediethanesulfonic acid (PIPES, 0.1 M), ethylene glycol-bis(2-aminoethylether)-N,N,N',N'-tetraacetic acid (EGTA, 1 mM), magnesium sulfate (1 mM), poly(ethylene glycol) (4 % w/v), and triton X-100 (1% v/v) for 10 min at room temperature, prior to blocking in 1% (w/v) bovine serum albumin. Tissues were incubated with rabbit monoclonal anti-N-cadherin (1:500; Abcam Ab18203), rabbit monoclonal anti-connexin43 (1:1000; Millipore Sigma AB1728), mouse monoclonal anti-α-actinin (1:500; Abcam ab9465), mouse monoclonal anti-cardiac troponin T (1:500; ThermoFisher MA5-12960), mouse monoclonal anti-vinculin (1:1000; Millipore Sigma V9264), rabbit polyclonal anti-myosin light chain 2 (1:500; Proteintech 10906-1-AP), rabbit polyclonal anti-non-muscle myosin II-B (1:1000; Biolegend 909902), mouse monoclonal anti-integrin β1D (1:1000; Abcam ab8991), rabbit polyclonal anti-zyxin (1:200; Millipore Sigma HPA004835), or mouse anti-dextran (1:500; STEMCELL Technologies 60026) antibodies for 1 hour at RT, followed by goat anti-mouse Alexa Fluor 647 (1:1000; Life Technologies A21236), goat anti-mouse Alex Fluor 546 (1:1000, Life Technologies A11030), or goat anti-rabbit Alexa Fluor 647 secondary antibodies (1:1000; Life Technologies A21245) and DAPI for 1 hour at RT.

5.6.10 Microscopy and image analysis

Fluorescent images were captured on a Zeiss LSM800 confocal microscope. Sarcomere alignment was quantified via custom Matlab scripts as previously described (DePalma et al. 2021). Briefly, images of titin-GFP reporter were thresholded and individual z-discs segmented. Z-discs

were subsequently grouped with neighboring z-discs based on proximity and orientation to identify myofibrils within the image. The orientation of all identified myofibrils within a field of view was fit to a Gaussian distribution. Sarcomere alignment deviation was defined at the standard deviation of this distribution using circular/angular statistics. Myofibril density was calculated by determining the percent area of each tissue containing titin-rich myofibril structures.

Vinculin and N-cadherin morphology and colocalization analysis was also performed using custom Matlab scripts. Because of the 3D nature of these tissues due to the intercalation of iPSC-CMs into matrix pores, confocal z-stacks of fibroTUG tissues formed with iPSC-CMs containing a GFP-titin live-reporter and immunostained for vinculin and N-cadherin were segmented in 3D for vinculin-, N-cadherin-, and titin-enriched structures. Custom Matlab functions were implemented to extract volume, eccentricity, and other parameters for these structures. Where applicable, quantifications were normalized to cell number in each field of view.

5.6.11 Computational modeling

The development of a tissue specific finite element model of fibroTUG tissues is described in detail by Jilberto et al. in an accompanying manuscript (Jilberto et al. 2023). Briefly, the images of the DVS fibers and titin were processed using Matlab/Python scripts to quantify the specific fiber structure and a probabilistic characterization of the myofibril organization (Kobeissi et al. 2023). This information was projected into a 2D triangular finite element mesh. Using these quantities, and following a continuum mechanics approach, non-linear constitutive relationships for the fibers and cells were defined. The mechanical response of the tissue was taken to be the sum of these two components. We then adapted methods similar to those presented in Miller et al. (2021) (Miller et al. 2021) to find the necessary active stress that the cells are exerting to generate the observed boundary tractions and displacement conditions. Using the experimental data for each

of the permutations of interest (soft/stiff fibers with soft/stiff post), we generated more than a hundred *in-silico* tissues for each of them by combining image-derived fibrous matrix with probabilistic-generated myofibril fields and experimentally measured force responses specific for each condition. We then compile the results to obtain a distribution of active stress for each mechanical environment.

5.6.12 Tendon progenitor cell isolation and culture

Tendon progenitor cells were isolated and cultured as previously described(Kent et al. 2022). For all animal procedures, the Institutional Animal Care and Use Committee (IACUC) guidelines for survival surgery in rodents and the IACUC Policy on Analgesic Use in Animals Undergoing Surgery were followed (Protocol #PRO00009868). Murine cells used in this work were harvested from 12x 6-9 week-old C57BL/6 mice (6 female,6 male). A ScxGFP mouse colony was maintained by breeding ScxGFP+/− heterozygotes modified from a C57BL/6 background with WT C57BL/6J mice, and progeny were genotyped (ScxGFP+/-versus ScxGFP−/−) using a Dual Fluorescent Protein Flashlight (Model DFP-1, Nightsea, Lexington, MA). Tail tendons were removed from euthanized mice and then encapsulated in a 2 mg mL-1 type I collagen hydrogel(Denduluri et al. 2016). Encapsulated tissues were cultured in an incubator (37°C and 5% CO2) in DMEM containing L-glutamine (ThermoFisher, Waltham, MA), 1 v/v% penicillin/streptomycin/fungizone, and 10 v/v% fetal bovine serum for 10 days to allow tendon progenitor cells (TPCs) to migrate from tendons into the collagen gel. Following isolation and expansion of TPCs, collagen gels were digested in 0.25 mg mL-1 collagenase from C. histolyticum with 0.025 w/v% trypsin-EDTA. The resulting slurry was filtered through a cell strainer and then plated. Adherent TPCs were cultured in basal media, and cells at passage 1 were used for all experiments.

5.6.13 Statistical analysis

Statistical significance was determined by t-tests and one-way or two-way analysis of variance (ANOVA) with post-hoc analysis (Tukey test), where appropriate, with significance indicated by $p < 0.05$. Studies were conducted a minimum of 3 times in each experiment. The data presented are representative data sets from one of these replicate studies. Specific sample size is indicated within corresponding figure legends and all data are presented as mean ± standard deviation.

5.7 Supplementary Figures

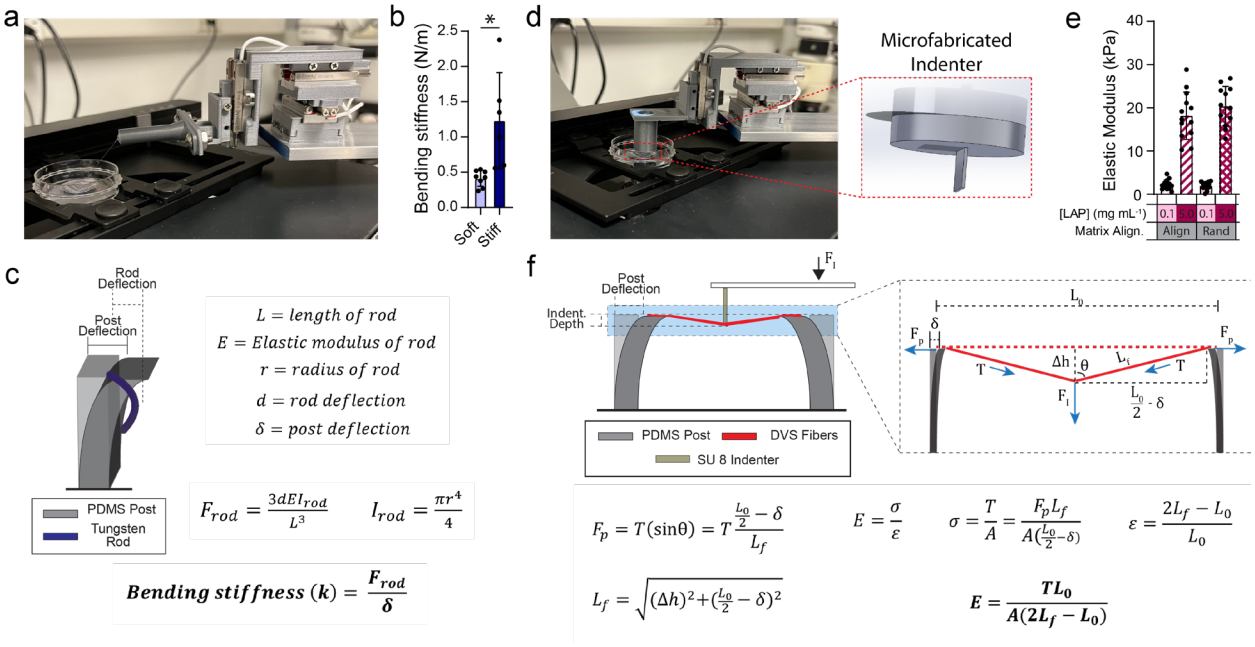

Supplementary Figure 5.1: Mechanical characterization of fibroTUG platform. (**a**) Image of PDMS post mechanical characterization setup. (**b**) Measured bending stiffness of soft and stiff PDMS posts. (**c**) Schematic of post mechanical testing scheme and equations used to calculate post bending stiffness. (**d**) Image of fiber matrix mechanical characterization setup. (**e**) Measured elastic modulus of various fiber matrices. (**f**) Schematic of fiber matrix mechanical testing scheme and equations used to calculate matrix elastic modulus. All data presented as mean ± std; * $p < 0.05$.

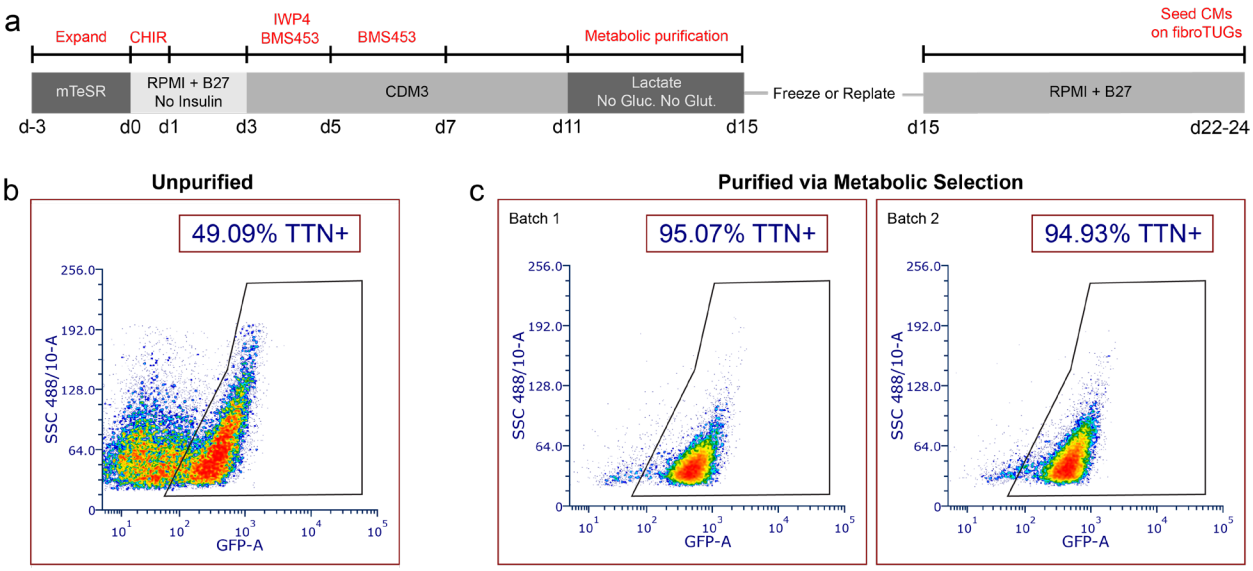

Supplementary Figure 5.2: Differentiation and purification of iPSC-CM cultures. (**a**) Timeline illustrating differentiation of iPSC to CMs, metabolic purification of iPSC-CMs populations, and seeding of CMs on fibroTUG tissues. (**b**) Flow cytometry analysis of unpurified iPSC-CM populations measured at day 22 in the differentiation protocol showed that ~49% of cells expressed the CM marker TTN. (**c**) Flow cytometry analysis of metabolically selected iPSC-CM populations measured at day 22 in the differentiation protocol showed that ~95% of cells expressed the CM marker TTN. Analysis is shown for two separate differentiations to illustrate the consistency of this purification method.

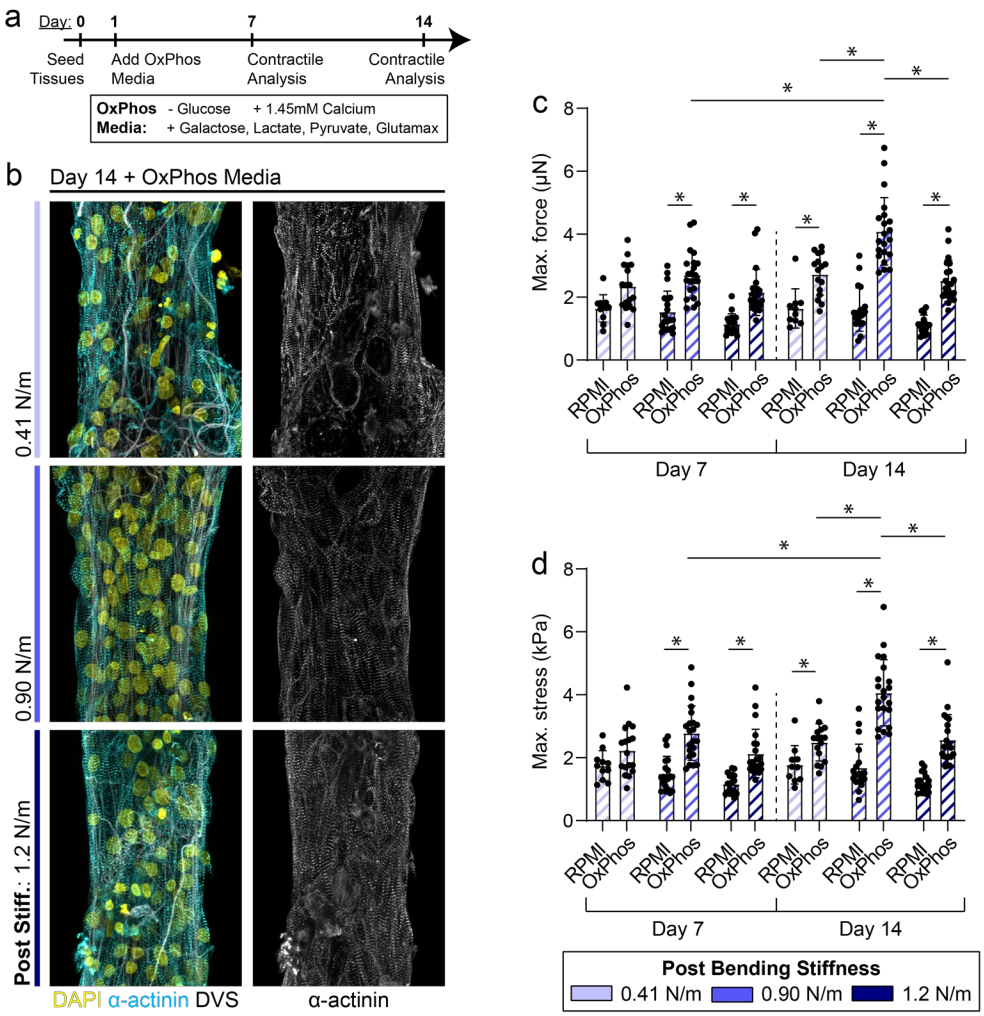

Supplementary Figure 5.3: fibroTUG platform supports long-term culture of iPSC-CMs with metabolic maturation media. (**a**) Experimental timeline. (**b**) Confocal fluorescent images of fibroTUG tissues after 14 days in culture with OxPhos metabolic maturation media. (**c**) Max contractile force and (**d**) max contractile stress of tissues between various post stiffnesses in both RPMI B27 and OxPhos media. All data presented as mean ± std; * $p < 0.05$.

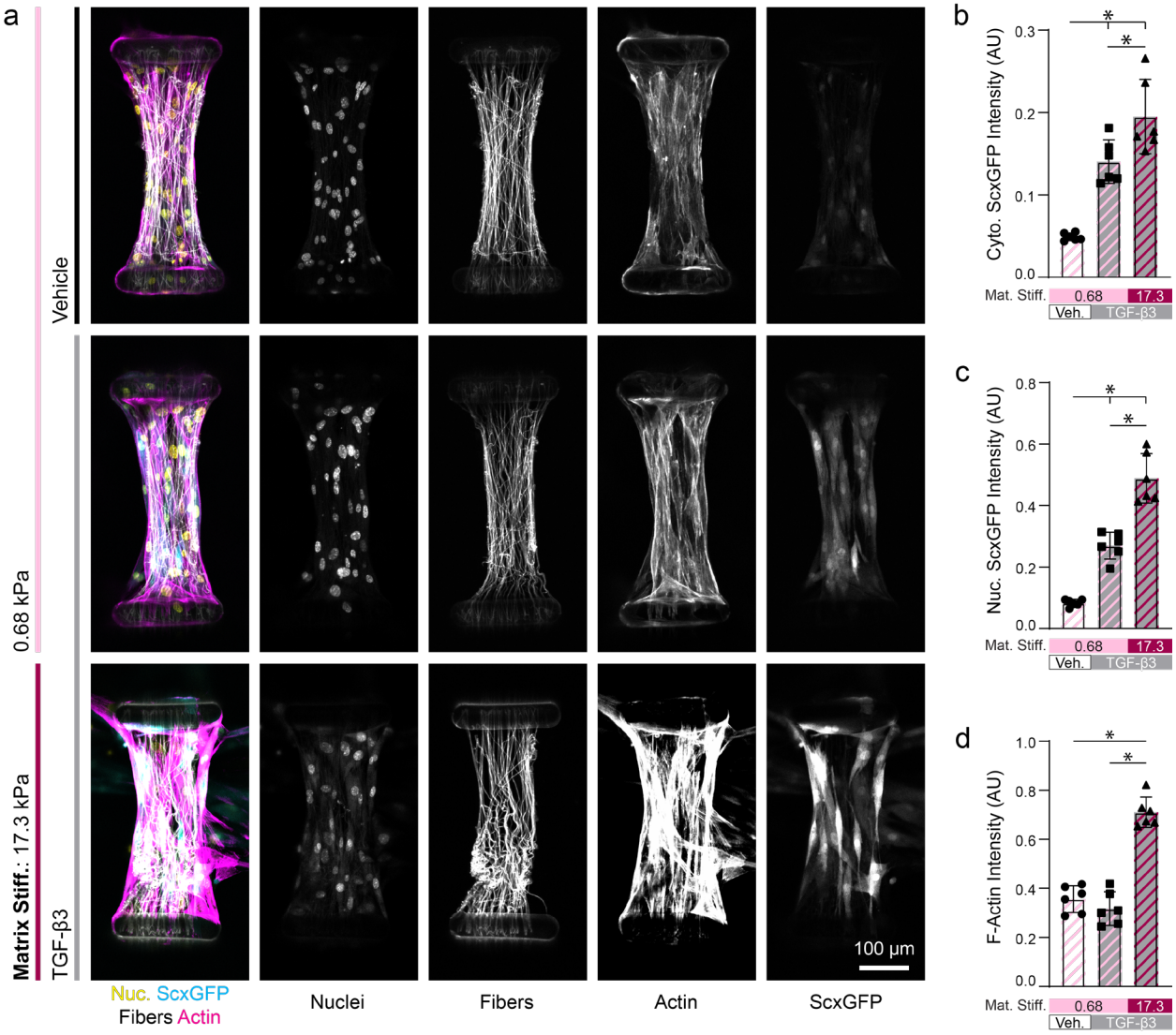

Supplementary Figure 5.4: Matrix stiffness drive tenogenic differentiation of tendon progenitor cells (TPCs) in fibroTUG platform. (**a**) Confocal fluorescent images of fibroTUG tissues with stiff (1.2 N/m) posts, due to the high baseline contractility of TCPs, and aligned fibers of varying stiffness. TCPs were isolated from mice engineered to express a live GFP-scleraxis (Scx) report and were stained for actin using phalloidin. Tissues were also treated with T3 to induce further tenogenic differentiation. Quantification of cytosolic scleraxis expression (**b**), nuclear scleraxis expression (**c**), and actin expression (**d**) ($n \geq 6$). All data presented as mean ± std; * $p < 0.05$.

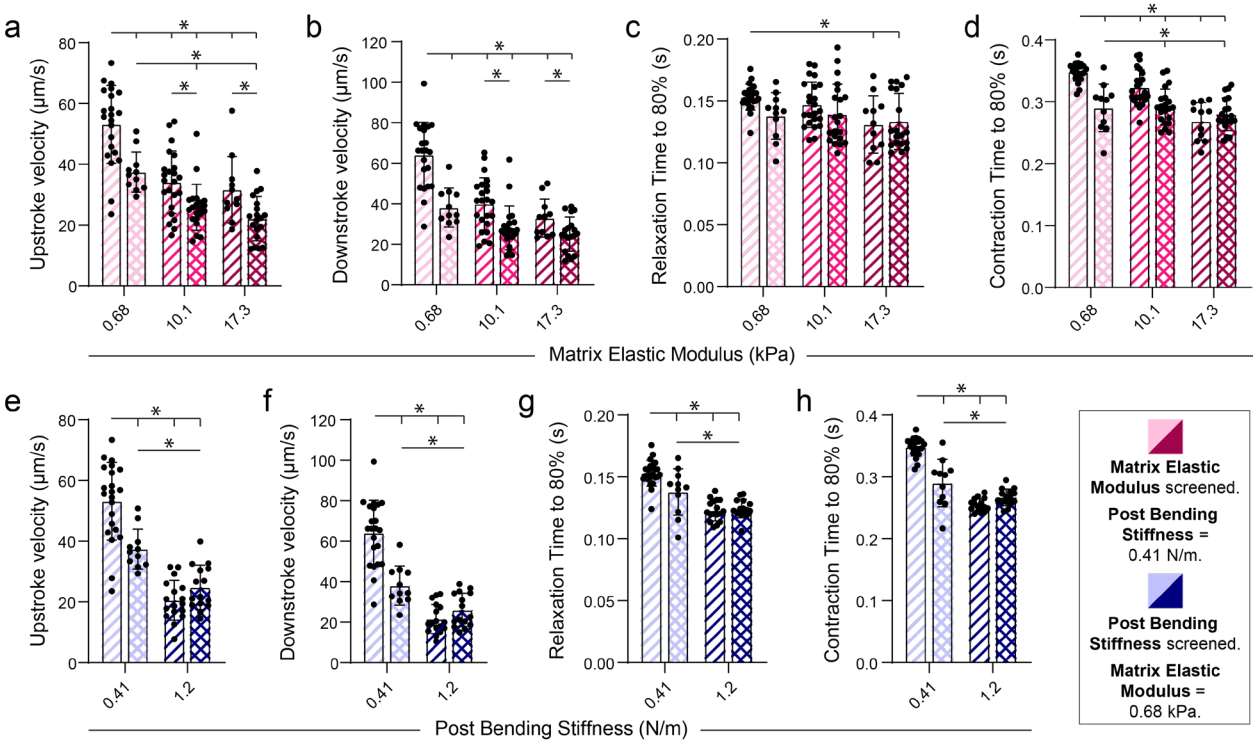

Supplementary Figure 5.5: Fibrous matrix alignment and stiffness influences iPSC-CM tissue contractile dynamics. Upstroke velocity (**a**), downstroke velocity (**b**), relaxation time to 80% relaxation (**c**), and contraction time to 80% relaxation (**d**) quantified in tissues with constant post stiffness (0.41 N/m) with varied fiber alignment and fiber stiffness ($n \geq 11$ tissues). Upstroke velocity (**e**), downstroke velocity (**f**), relaxation time to 80% relaxation (**g**), and contraction time to 80% relaxation (**h**) quantified in tissues with constant matrix stiffness (0.68 kPa) with varied fiber alignment and post stiffness ($n \geq 11$). All data presented as mean ± std; * $p < 0.05$.

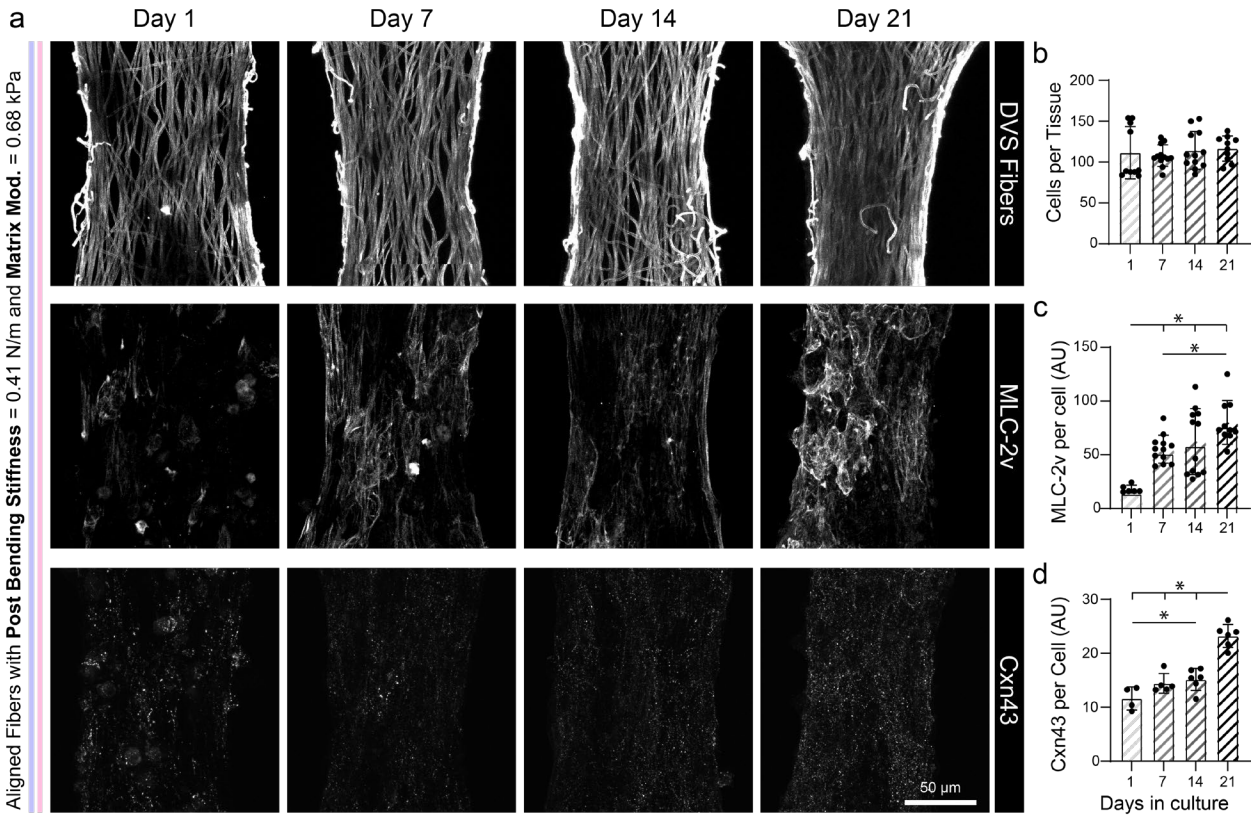

Supplementary Figure 5.6: Long-term culture of fibroTUG tissues in maturation medium leads to progressive structural maturation. (**a**) Confocal fluorescent images of fibroTUG tissues with soft (0.68 kPa), aligned fibers and soft (0.41 N/m) post after 1, 7, 14, and 21 days in culture with OxPhos metabolic maturation medium immunostained for dextran (DVS fibers), MLC-2v, and connexin-43. (**b**) Quantification of the number of cells per tissue over time ($n \geq 12$). (**c**) Quantification of MLC-2v expression ($n \geq 12$). (**d**) Quantification of connexin-43 expression ($n \geq 6$). All data presented as mean ± std; * $p < 0.05$.

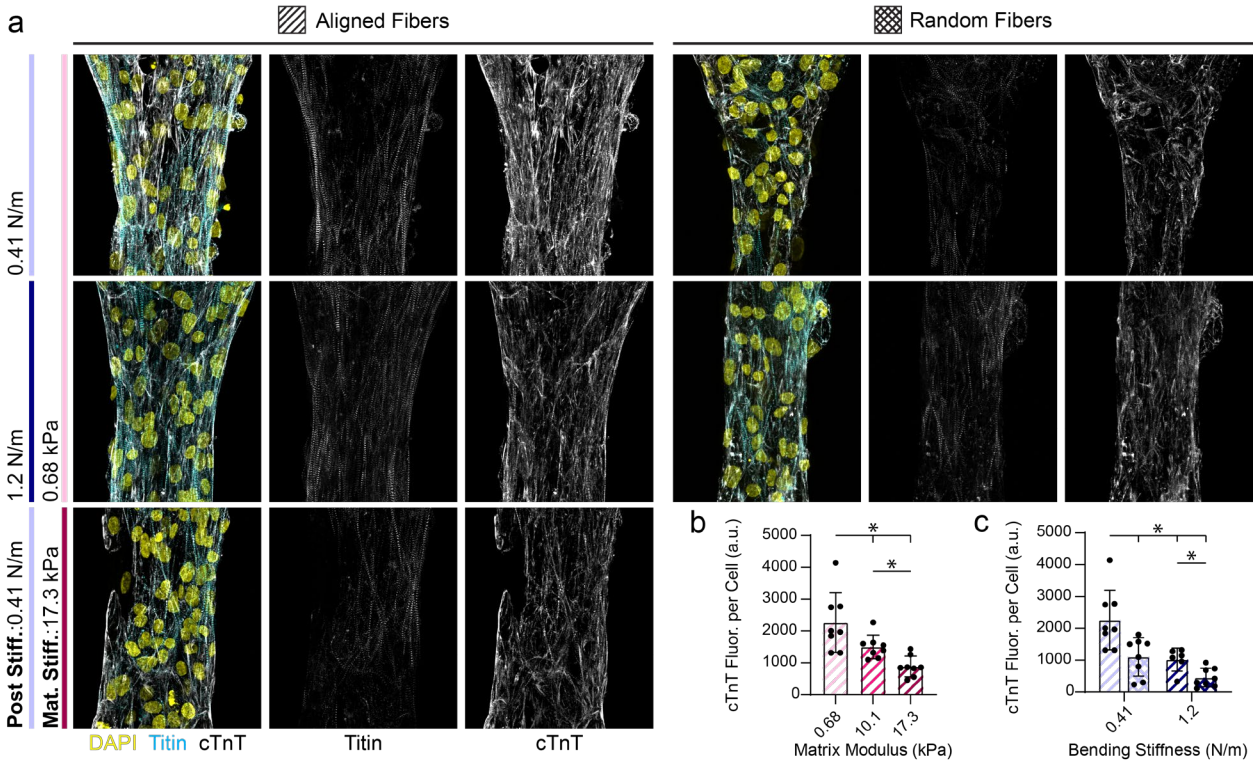

Supplementary Figure 5.7: Cardiac troponin expression in fibroTUG tissues. (**a**) Confocal fluorescent images of fibroTUG tissues of varying mechanics immunostained for cTnT. Quantification of cTnT fluorescence per cell in tissues with (**b**) varied matrix stiffness and (**c**) bending stiffness. All data presented as mean ± std; * $p < 0.05$.

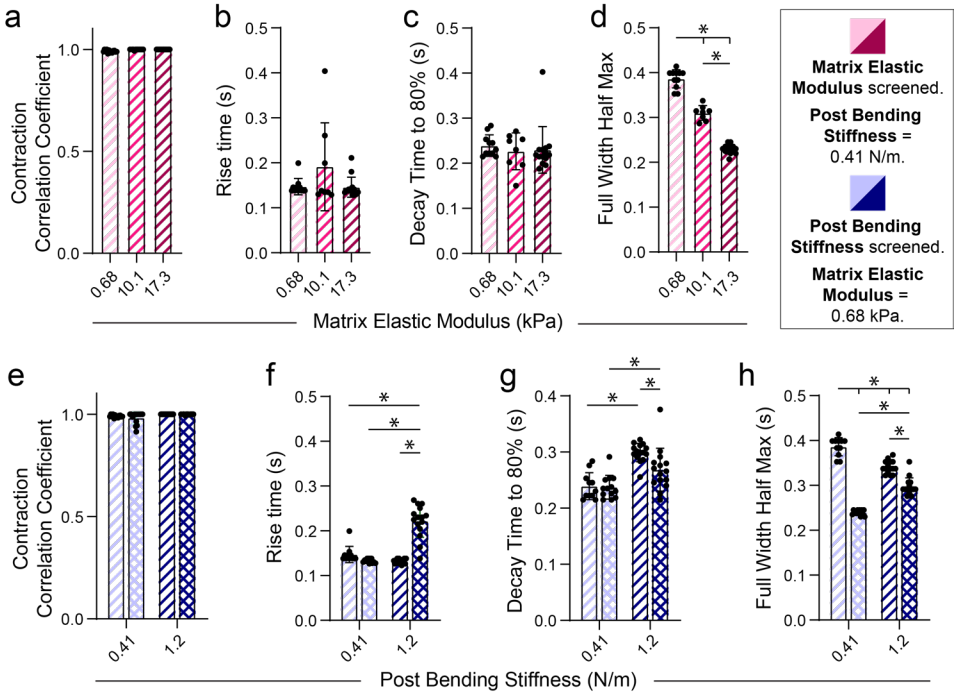

Supplementary Figure 5.8: Fibrous matrix alignment and stiffness influences iPSC-CM tissue calcium flux dynamics. Contraction correlation coefficient (**a**), calcium flux rise time (**b**), decay time to 80% relaxation (**c**), full width half max (**d**) quantified in tissues with aligned fibers and constant post stiffness (0.41 N/m) with varied fiber stiffness ($n \geq 11$). Contraction correlation coefficient (**e**), calcium flux rise time (**f**), decay time to 80% relaxation (**g**), full width half max (**h**) quantified in tissues with constant fiber stiffness (0.68 kPa) with varied post stiffness and fiber alignment ($n \geq 11$). All data presented as mean ± std; * $p < 0.05$.

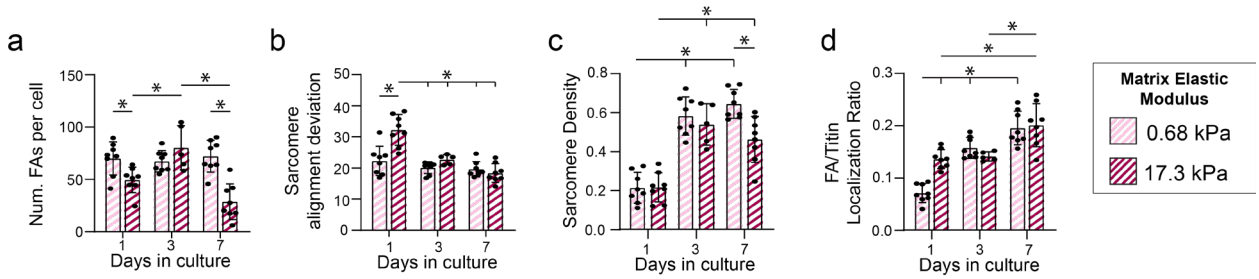

Supplementary Figure 5.9: Matrix mechanics influence costamere formation and sarcomere formation over time. Quantification of number of (**a**) focal adhesions per cell, (**b**) sarcomere alignment, (**c**) sarcomere density, (**d**) and the fraction of vinculin that is colocalized with titin in tissues formed on aligned soft and stiff matrices suspended between 0.41 N/m posts fixed at 1-, 3-, and 7-days post seeding ($n \geq 5$). All data presented as mean ± std; * $p < 0.05$.

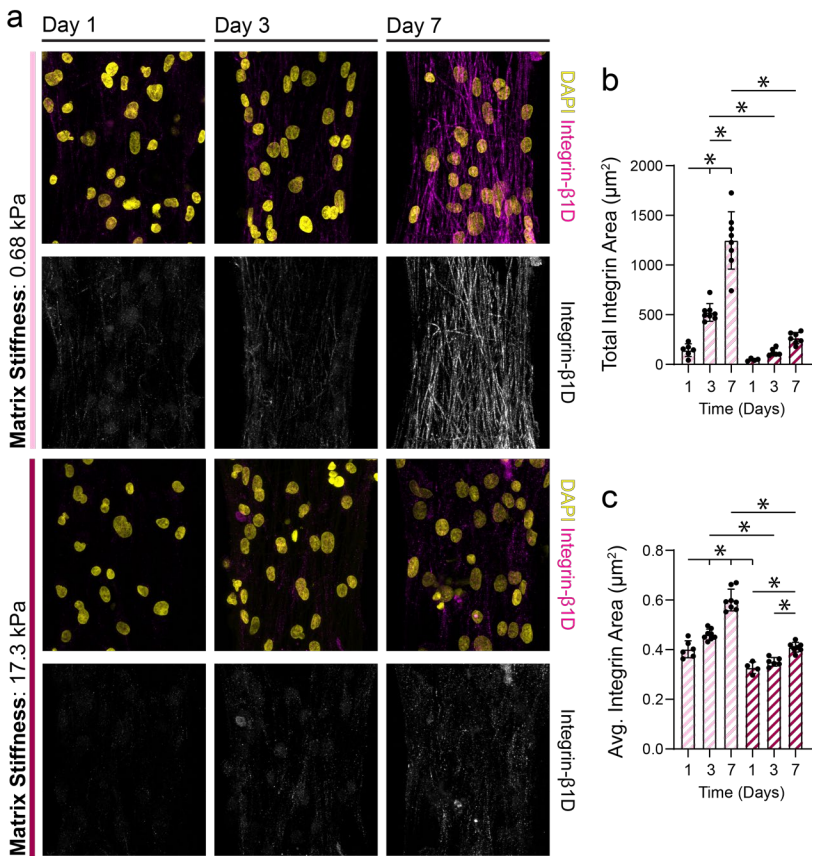

Supplementary Figure 5.10: Quantification of β1D integrin expression in fibroTUG tissues. (**a**) Confocal fluorescent images of fibroTUG tissues fixed at day 1, 3 and 7 post seeding on either soft (0.68 kPa) or stiff (17.1 kPa) aligned fiber matrices (post stiffness was held constant at 0.41 N/m). Quantification of (**b**) total integrin area and (**c**) average integrin size ($n \geq 5$). All data presented as mean ± std; * $p < 0.05$.

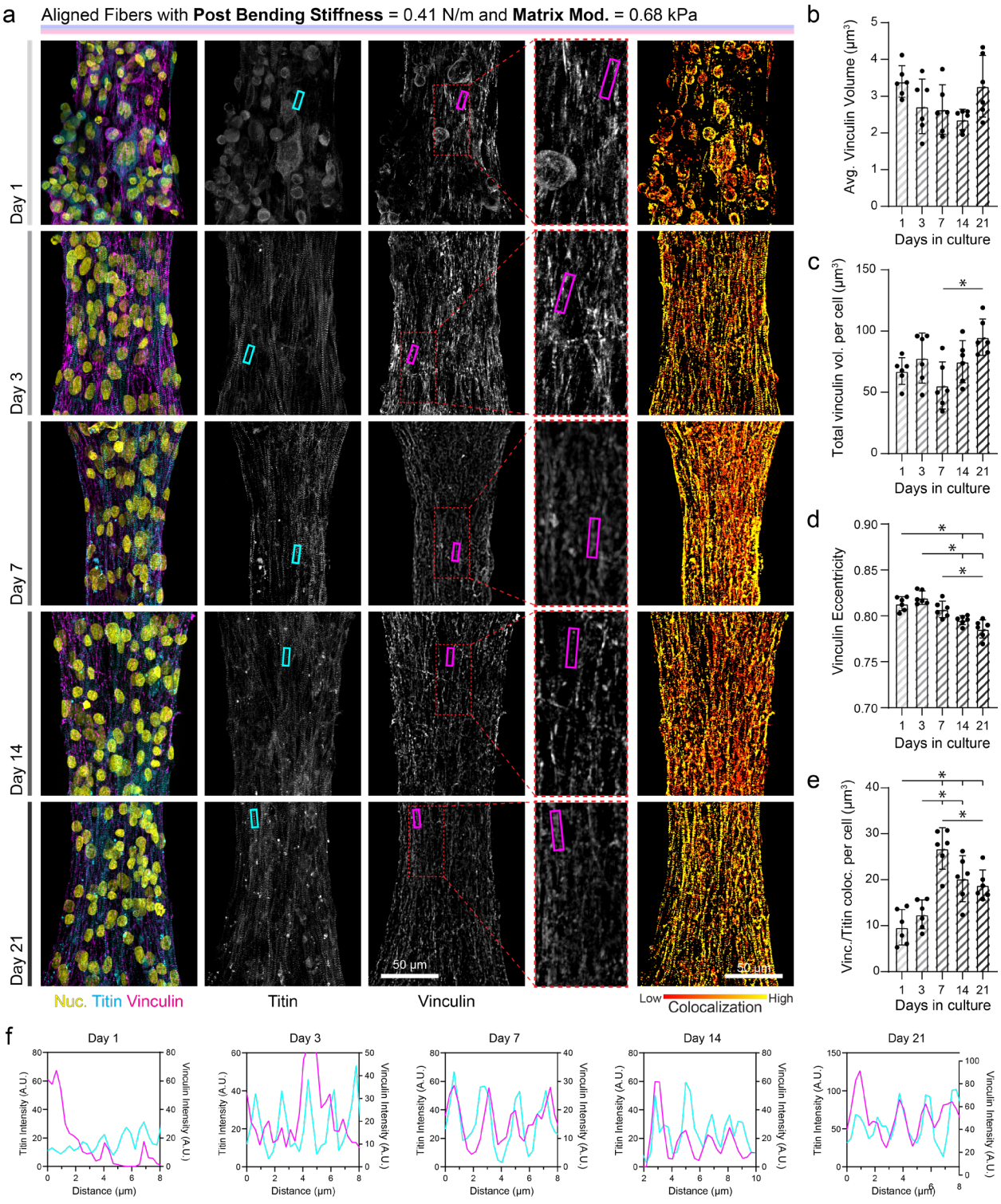

Supplementary Figure 5.11: Soft, aligned fibers and soft posts facilitate robust costamere formation in long term culture. (**a**) Confocal fluorescent images of fibroTUG tissues reporter fixed at day 1, 3, 7, 14, and 21 post seeding on aligned, soft (0.68 kPa) matrices between soft (0.41 N/m) posts containing a GFP-titin and immunostained for vinculin. Tissues were cultured

in OxPhos maturation medium. (**b**) Average vinculin volume, (**c**) total vinculin volume, (**d**) and vinculin eccentricity were quantified from the fluorescent images of immunostained vinculin ($n \geq 6$). (**e**) Costamere formation was assessed by quantifying vinculin colocalization with titin ($n \geq 6$). (**f**) Colocalization of vinculin and titin was visualized via fluorescence intensity plots of titin (cyan) and vinculin (magenta) at all time points from lines drawn along the major axis of regions indicated by the rectangles overlayed on images in panel a. All data presented as mean ± std; * $p < 0.05$. All data presented as mean ± std; * $p < 0.05$.

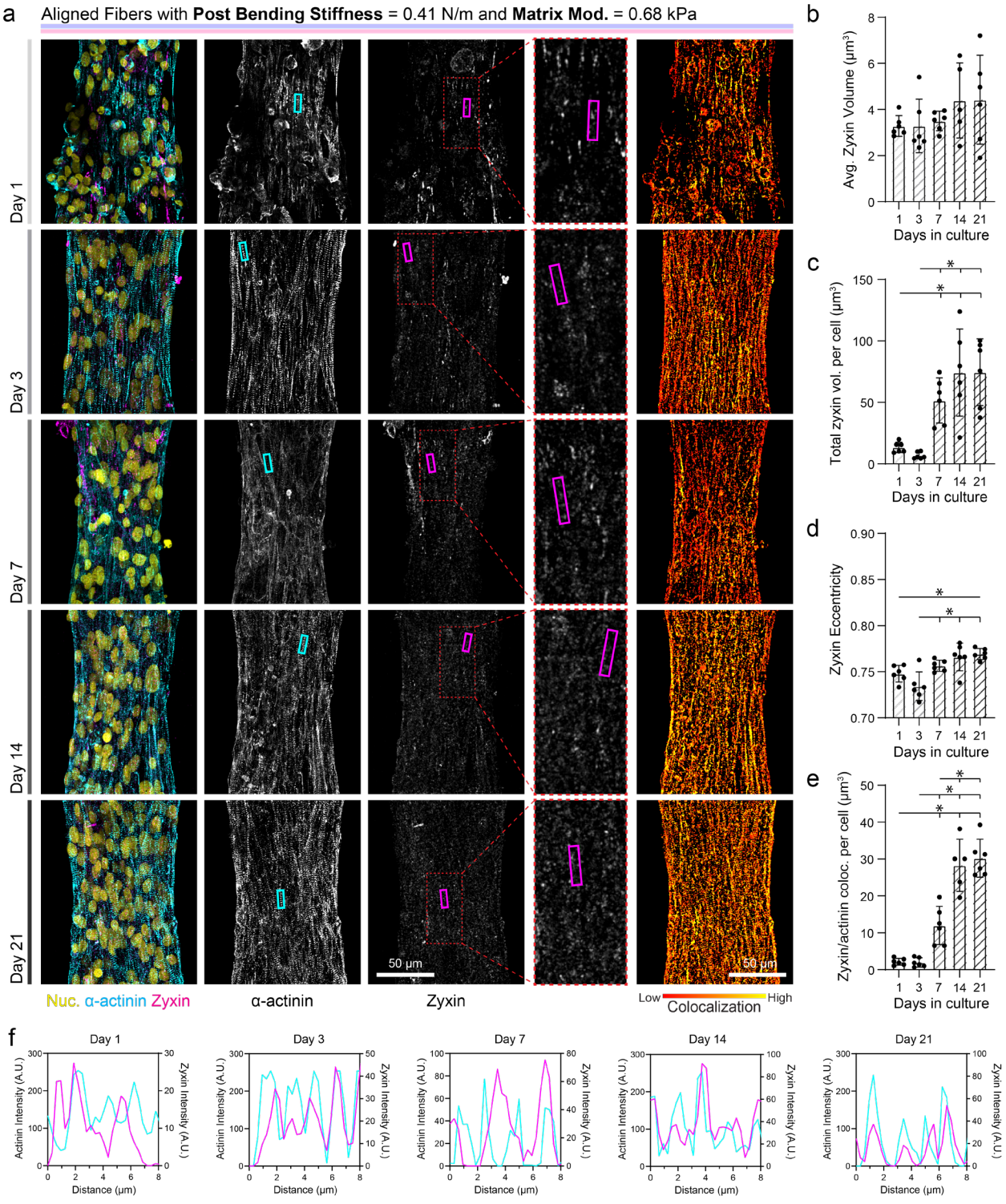

Supplementary Figure 5.12: Soft, aligned fibers and soft posts facilitate robust zyxin localization to costameres in long term culture. (**a**) Confocal fluorescent images of fibroTUG tissues fixed at day 1, 3, 7, 14, and 21 post seeding on aligned, soft (0.68 kPa) matrices between soft (0.41 N/m) posts immunostained for α-actinin and zyxin. Tissues were cultured in OxPhos

maturation medium. (**b**) Average zyxin volume, (**c**) total zyxin volume, (**d**) and zyxin eccentricity were quantified from the fluorescent images of immunostained zyxin ($n \geq 6$). (**e**) Costamere formation was assessed by quantifying zyxin colocalization with α-actinin ($n \geq 6$). (**f**) Colocalization of zyxin and α-actinin was visualized via fluorescence intensity plots of α-actinin (cyan) and zyixin (magenta) at all time points from lines drawn along the major axis of regions indicated by the rectangles overlayed on images in panel a. All data presented as mean ± std; * $p < 0.05$. All data presented as mean ± std; * $p < 0.05$.

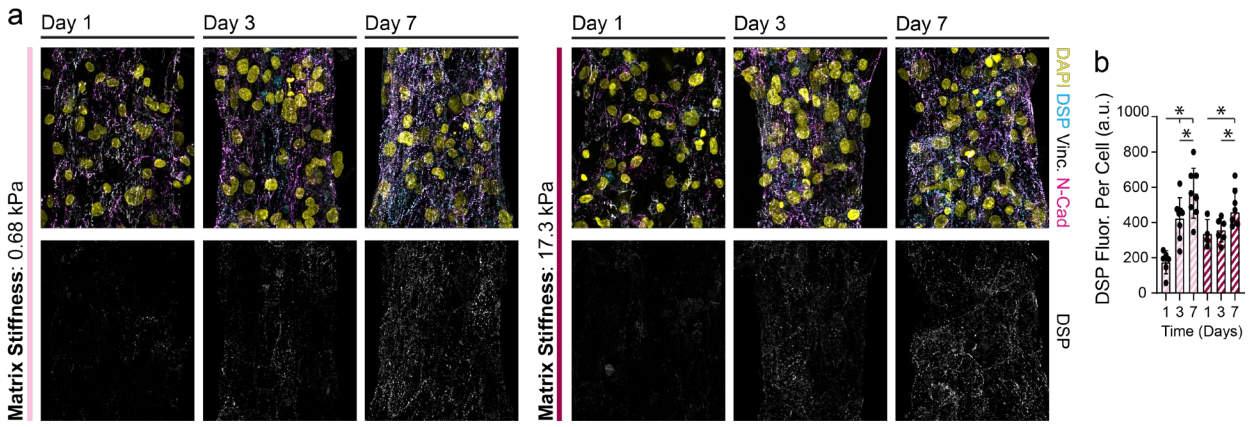

Supplementary Figure 5.13: Intercalated disc formation over time on soft and stiff fiber matrices. (**a**) Confocal fluorescent images of fibroTUG tissues fixed at day 1, 3 and 7 post seeding on either soft (0.68 kPa) or stiff (17.1 kPa) aligned fiber matrices (post stiffness was held constant at 0.41 N/m). (**b**) Quantification of DSP fluorescence per cell ($n \geq 8$). All data presented as mean ± std; * $p < 0.05$.

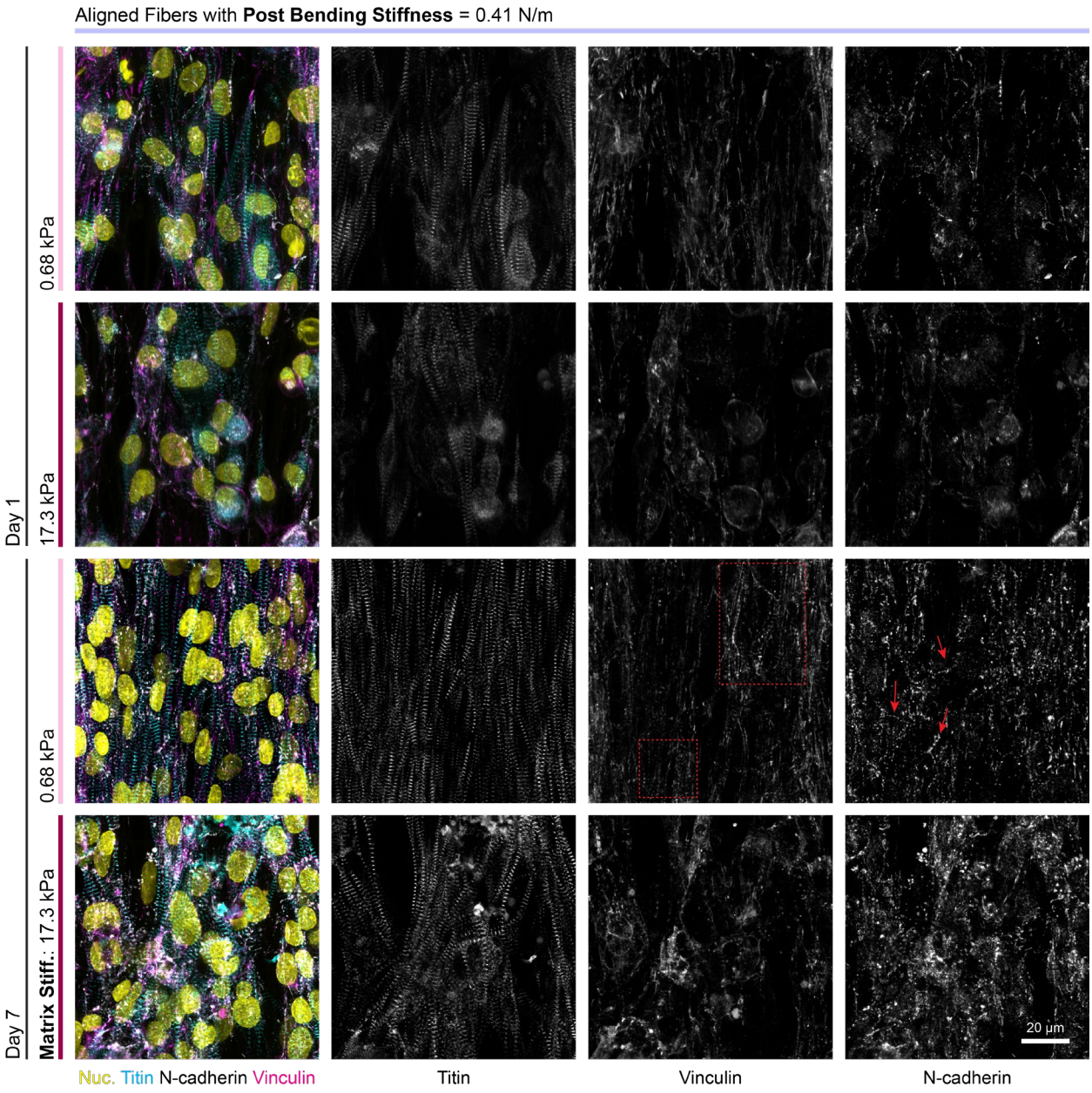

Supplementary Figure 5.14: High magnification images of fibroTUG tissues show robust costamere and intercalated disc formation on soft, aligned fiber matrices. (**a**) Confocal fluorescent images of fibroTUG tissues fixed at day 1 and 7 after seeding on either soft (0.68 kPa) or stiff (17.1 kPa) aligned fiber matrices (post stiffness was held constant at 0.41 N/m) acquired at 63x magnification. All images show a region located at the center of each tissue.

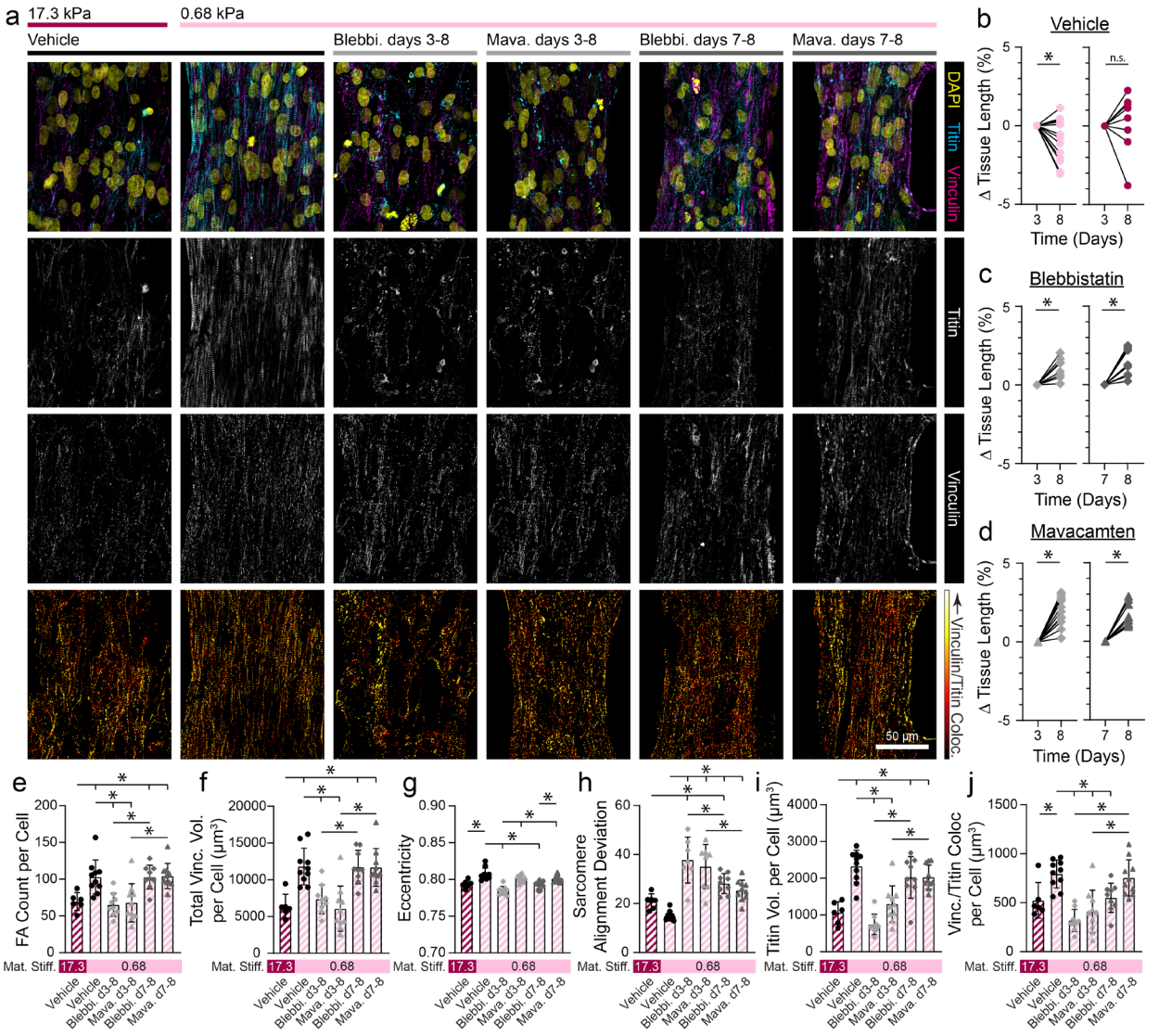

Supplementary Figure 5.15: Treatment with contractile inhibitors at day 3 and day 7. (**a**) Confocal fluorescent images of fibroTUG tissues treated with blebbistatin (50uM) or mavacamten (500 nM) starting at either day 3 or day 7post seeding. (**b**) Diastolic tissue length on day 3 and 8 of tissues seeded on soft (0.68 kPa) and stiff (17.1 kPa) aligned fiber matrices (post stiffness was held constant at 0.41 N/m) without treatment with the contractile inhibitors. (**c,d**) Diastolic tissue length of tissues seeded on soft matrices on day 3 or day 7 before treatment with a contractile inhibitor, (**c**) blebbistatin or (**d**) mavacamten, and day 8 after 5 or 1 days of treatment,($n \geq 8$). (**e**) Focal adhesion count, (**f**) vinculin volume per cell, and (**g**) focal adhesion eccentricity were quantified from the fluorescent images of immunostained vinculin ($n \geq 6$). (**h**) Sarcomere alignment deviation and (**i**) titin volume per cell quantified from fluorescent images of titin-GFP reporter ($n \geq 6$). (**j**) Vinculin colocalization with titin per cell quantified from titin and vinculin images ($n \geq 6$). All data presented as mean ± std; * $p < 0.05$.

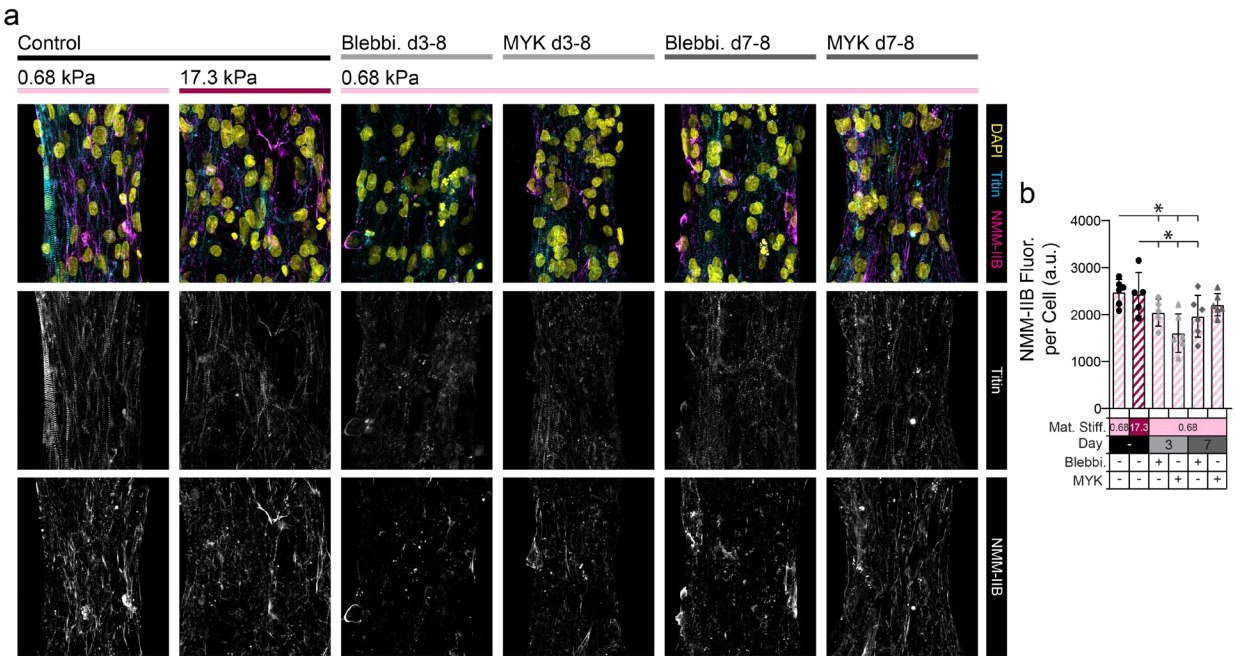

Supplementary Figure 5.16: Treatment with myosin inhibitors at day 3 decreases non-muscle myosin IIB (NMM-IIB) expression. (a) Confocal fluorescent images of fibroTUG tissues treated with blebbistatin (50 μM) or mavacamten (500 nM). (**b**) Quantification of NMM-IIB expression per cell ($n \geq 6$). All data presented as mean ± std; * $p < 0.05$.

5.8 Supplementary Movies

Supplementary Movie 5.1: Representative brightfield video of an array of contracting fibroTUG tissues formed on aligned, soft (0.68 kPa) fiber matrices suspended between soft (0.41 N/m) posts. (https://www.biorxiv.org/content/10.1101/2023.10.20.563346v1)

Supplementary Movie 5.2: Representative brightfield videos of contracting fibroTUG tissues formed on aligned fiber matrices of varying stiffness suspended between soft (0.41 N/m) posts. (https://www.biorxiv.org/content/10.1101/2023.10.20.563346v1)

Supplementary Movie 5.3: Representative brightfield videos of contracting fibroTUG tissues formed on random fiber matrices of varying stiffness suspended between soft (0.41 N/m) posts. (https://www.biorxiv.org/content/10.1101/2023.10.20.563346v1)

Supplementary Movie 5.4: Representative brightfield videos of contracting fibroTUG tissues formed on aligned, soft (0.68 kPa) fiber matrices suspended between posts of varying stiffness. (https://www.biorxiv.org/content/10.1101/2023.10.20.563346v1)

Supplementary Movie 5.5: Representative brightfield videos of contracting fibroTUG tissues formed on random, soft (0.68 kPa) fiber matrices suspended between posts of varying stiffness. (https://www.biorxiv.org/content/10.1101/2023.10.20.563346v1)

Supplementary Movie 5.6: Representative videos of calcium fluxes in fibroTUG tissues treated with Cal520-AM dye formed on aligned fiber matrices of varying stiffness suspended between soft (0.41 N/m) posts. (https://www.biorxiv.org/content/10.1101/2023.10.20.563346v1)

Supplementary Movie 5.7: Representative videos of calcium fluxes in fibroTUG tissues treated with Cal520-AM dye formed on aligned, soft (0.68 kPa) fiber matrices suspended between posts of varying stiffness. (https://www.biorxiv.org/content/10.1101/2023.10.20.563346v1)

Supplementary Movie 5.8: Representative videos of calcium fluxes in fibroTUG tissues treated with Cal520-AM dye formed on random, soft (0.68 kPa) fiber matrices suspended between posts of varying stiffness. (https://www.biorxiv.org/content/10.1101/2023.10.20.563346v1)

Supplementary Movie 5.9: Representative brightfield videos of contracting fibroTUG tissues formed on aligned, soft (0.68 kPa) fiber matrices suspended between soft (0.41 N/m) posts before and after isoproterenol treatment.
(https://www.biorxiv.org/content/10.1101/2023.10.20.563346v1)

Supplementary Movie 5.10: Videos depicting computational models of a fibroTUG tissue. The top video shows measured tissue displacements used to verify the model's accuracy while the bottom videos show maps simulated tissue displacements and sarcomere strain. (https://www.biorxiv.org/content/10.1101/2023.10.20.563346v1)

Chapter 6: Dissecting Heterocellular Communication Between Cardiac Fibroblasts and iPSC-Cardiomyocytes in a Compartmentalized Biomimetic Tissue

6.1 Authors

Samuel J. DePalma, Darcy D. Huang, Anya G. Coffeen Vandeven, Austin E. Stis, Jingyi Xia, Robert N. Kent III, Adam S. Helms, Brendon M. Baker

6.2 Abstract

Homeostatic maintenance of the cardiac extracellular matrix required for healthy tissue function depends on cardiac fibroblast (CF) communication with cardiomyocytes (CMs). Given the challenges involved in parsing the dynamic and multifactorial heterocellular interactions underlying tissue homeostasis versus fibrosis, we engineered a compartmentalized, bilayer cardiac tissues where iPSC-derived CMs and CFs can be cultured on either side of a shared mechanically tunable, synthetic fibrous ECM to study CM-CF communication. Electrospun dextran vinyl sulfone (DVS) fibers were collected on arrays on microfabricated wells with channels linking neighboring wells underneath the fibers to allow for seeding of both sides of the fiber matrix with cells. Results show stiff, aligned matrices enhance MF differentiation, but the presence of CMs significantly reduces MF formation, even in a pro-fibrotic environment, indicating protective intercellular communication. These findings suggest that CM-CF crosstalk plays a critical role in

preventing fibrosis, and further research is being conducted to identify specific communication pathways involved.

6.3 Introduction

The myocardium is composed of multiple distinct cell types, including cardiomyocytes (CMs), fibroblasts, endothelial cells, and immune cells, that all work in concert to maintain proper heart function (Litviňuková et al. 2020). In particular, cardiac fibroblasts (CFs) play a central role in healthy, homeostatic cardiac structure and function by synthesizing and remodeling the hierarchically assembled collagen-rich extracellular matrix (ECM) found within the heart (Baudino et al. 2006; Bowers, Meng, and Molkentin 2022; Rienks et al. 2014). CFs are situated within the endomysial and perimysial collagen networks that segregate individual CMs and syncytial CM bundles, respectively (Goldsmith et al. 2004; Hall et al. 2021). In the healthy myocardium, mechanical and biochemical cues encoded by this highly organized network of collagen fibers surrounding CMs are essential to the organization and resulting anisotropic contractions of the tissue (Pope et al. 2008; Karl T. Weber 1989; Karl T. Weber et al. 1994). In addition to maintaining the collagenous matrix and associated signals, CFs also bi-directionally communicate via paracrine signals with neighboring CMs (Baudino et al. 2006; Goldsmith et al. 2004; Souders, Bowers, and Baudino 2009). It is thought that homeostatic maintenance of the ECM required for healthy tissue function depends heavily upon CF communication with other cell types including CMs via secreted factors and direct electromechanical coupling (Baudino et al. 2006; Cartledge et al. 2015; Giacomelli et al. 2020; Hall et al. 2021). Conversely, disruption to these modes of CM-CF communication is believed to play a critical role in driving fibrotic disease progression (Hall et al. 2021).

During cardiac fibrosis, alterations and dysregulation of the tissue microenvironment leads to aberrant CF behavior including excessive deposition of stiff, disorganized ECM that ultimately mechanically impairs heart function. These pathologic changes to the ECM are driven by CFs that differentiate or activate into myofibroblasts (MFs) in response to chemical and mechanical cues encoded by other cells in the tissue, including CMs and immune cells such as macrophages (Kong, Christia, and Frangogiannis 2014; Travers et al. 2016). For example, after myocardial infarction, significant numbers of CMs undergo apoptosis due to ischemic conditions (Frangogiannis 2014, 2015). Prior to apoptosis, these CMs secrete fibrogenic factors such as TGF-β1 that initiate the activation of fibroblasts into MFs (Hanna and Frangogiannis 2019; Rainer et al. 2014; Karl T. Weber et al. 2012). CM necrosis also induces immune cell activation, which further amplifies the activation of CFs to MFs (Frangogiannis 2012, 2014). Activated MFs then begin to produce various ECM proteins and other paracrine factors, which in turn impairs the functionality of surviving CMs (Pathak et al. 2001; Perestrelo et al. 2021; Spinale et al. 2016; Karl T. Weber et al. 2012). In chronic conditions such as hypertrophic cardiomyopathy (HCM) and dilated cardiomyopathy (DCM), fibrosis will manifest in early stages of disease progression (Lyon et al. 2015; Nakamura and Sadoshima 2018; Schultheiss et al. 2019; Teekakirikul et al. 2012). While the specific triggers of increased myocardial fibrosis in these conditions remain unclear, increased expression of profibrotic factors such as TGF-β1, angiotensin II, and IL-6 and other fibrogenic or inflammatory paracrine signals likely contributes to MF activation and subsequent CM dysfunction (Cartledge et al. 2015; Hall et al. 2021; Pellman, Zhang, and Sheikh 2016). Yet, our knowledge of the signaling between CMs and CFs in the heart remains incomplete, as parsing the reciprocal heterocellular interactions underlying tissue homeostasis versus fibrosis is difficult

given the dynamic and multifactorial nature of the many soluble, insoluble, and mechanical cues involved.

Despite each having intrinsic limitations, both *in vivo* and *in vitro* models of the myocardium have been established towards identifying specific signaling pathways central to tissue homeostasis vs. fibrotic disease progression. First, *in vivo* models of cardiac fibrosis, though critical for pathway validation, are not ideal for dissecting heterocellular communication given the many cellular players present (Pellman, Zhang, and Sheikh 2016; Rai et al. 2016). While numerous mouse and rat models have demonstrated that electrical coupling of CMs and CFs in addition to paracrine signaling via the TGF-β pathway affect cardiac tissue repair, the unavoidable presence of other cell types, especially immune cells, and challenges targeting specific cardiac fibroblast populations confound the identification of specific, critical pathways for therapeutic targeting (Hall et al. 2021; Kong et al. 2013; Quinn et al. 2016; Souders, Bowers, and Baudino 2009; Takeda et al. 2010).

Reductionist *in vitro* co-culture platforms provide better opportunities to isolate cellular players and their respective signaling. Studies using this approach have confirmed the importance of CM-CF paracrine signaling, for example by treating CMs with conditioned media from activated MFs or conversely, CFs with conditioned media from hypertrophic CMs (Herum et al. 2017; H. Zhang et al. 2019). These studies have identified critical signaling feedback loops present between CMs and CFs and demonstrated that profibrotic signaling can drive disrupted mechanical and electrical coupling between fibroblasts and CMs (Kaur et al. 2013; LaFramboise et al. 2007; Quinn et al. 2016; Thompson et al. 2011; Vasquez et al. 2010). Additionally, co-culture models incorporating tunable ECM-like substrates have shown how aberrant mechanical cues associated with myocardial infarct can drive CF activation into MFs (Herum et al. 2017). While easy to

implement, these platforms fail to recapitulate cardiac tissue architecture and mechanics, which likely are a major factor in modulating heterocellular communication. For example, traditional transwell culture enables paracrine signaling but prevents direct cell-cell interactions (Pellman, Zhang, and Sheikh 2016). Further, traditional 2D co-culture typically randomly intermix CMs and CFs across a culture substrate, and as such, fail to recapitulate the physiologic segregation of each cell population by fibrous ECM. This same issue persists in 3D engineered tissue constructs, limiting their relevance as models to study matrix-mediated CM-CF communication (Giacomelli et al. 2020; E. Y. Wang et al. 2019). As such, many established models may possess limited potential to capture relevant communication networks that are operative in native tissues during homeostasis and after tissue injury.

Thus, in this work we established a compartmentalized, bilayer tissue (BLT) fabrication method whereby iPSC-derived CMs and CFs are co-cultured on opposing sides of a shared, tunable synthetic fibrous matrix, reflecting the cellular segregation within native myocardium. Using this co-culture model, we find that ECM mechanics directly modulates CF activation into MFs in the absence of CMs. Next, by tuning the architecture and mechanics of these matrices to model healthy and disease tissue states in CF/CM co-cultures, we found that culturing CFs and CMs on a shared ECM-mimetic synthetic matrix facilitates heterocellular communication that prevents MF activation and thereby supports tissue homeostasis, despite the introduction of a potent fibrogenic soluble cue (TGF-β1). Finally, we establish a role for paracrine signaling between CMs and CFs in the maintenance of CF quiescence in this model. Taken together, these studies describe a platform that enables the identification and study of heterocellular communication pathways in an environment that better recapitulates the cellular and extracellular organization of the native myocardium.

6.4 Results

6.4.1 Collagen networks of the human myocardium in healthy and diseased tissues

As previously described, significant remodeling of the myocardial ECM is a hallmark of many forms of cardiac disease. Many studies examining the dynamics of this process after myocardial infarction have highlighted significant spatial heterogeneity in collagen alignment and density across various fibrotic regions of the heart (Bugg et al. 2020; Goergen et al. 2016; Richardson and Holmes 2016). To further assess changes in ECM structure and composition that occur in human heart disease, we obtained sections of the human left ventricular myocardial wall from healthy and diseased donors. Diseased tissue sections were obtained from patients with dilated or hypertrophic cardiomyopathy resulting from mutations in DSP (DCM) or TTN (HCM), respectively. Tissues were fixed, embedded in agarose, and sectioned by vibratome to generate approximately 200 μm thick slices. We then applied advanced CUBIC clearing methods to enable immunofluorescence staining and high magnification imaging of these thick tissue sections (Matsumoto et al. 2019) **(Figure 6.1a**). Tissue stacks approximately 100 μm were acquired and analyzed using custom MATLAB analysis scripts that filtered, thresholded and segmented 3D image stacks (**Figure 6.1b-d**). First, fibroblasts were visualized by immunostaining for vimentin. Vimentin volume increased in both DCM and HCM myocardial tissues compared to healthy control tissue, with a significant increase in fibroblast presence observed heterogeneously across HCM tissue sections (**Figure 6.1a,b**), reflecting the spatial heterogeneity observed in other species (Bugg et al. 2020; Goergen et al. 2016). Further highlighting this heterogeneity, an increase in α-smooth muscle actin (αSMA) positive MFs were only observed in select regions of the tissue

(**Figure 6.1c**). Additionally, we observed a significant increase in collagen I expression in both the DCM and HCM tissues compared to the healthy control while fibronectin expression was much more heterogeneous, increasing in some regions of the HCM heart (**Figure 6.1a,d,e**).

Corresponding to the increase in collagen I deposition, we observed an increase in collagen fiber crimping and greater disorganization compared to the healthy tissue sections, where fibers were thinner and more aligned (**Figure 6.1a**). Even within these relatively small regions imaged for this analysis, the organization of the ECM was far from uniform. Additionally, previous studies in mice have also indicated that after myocardial infarction, there are regions of disorganized collagen matrices within the scar tissue and highly aligned collagen fibers located at the border zone between the scar and surrounding functional myocardial tissue (Bugg et al. 2020). Increased numbers of MFs were observed in these latter regions compared to the disorganized scar tissue, in line with previous studies indicating that fibrosis may be initiated within tissue zones bordering the infarct region (Van Den Borne et al. 2009). The finding presented here, in conjunction with a number of previous studies that indicate high levels of heterogeneity to the density and organization of fibrotic ECM in the heart (Goergen et al. 2016; Holmes, Borg, and Covell 2005; Richardson and Holmes 2016), motivate the use of tunable fibrous matrix platforms to dissect how microenvironmental cues arising from the matrix either promote or limit MF activation.

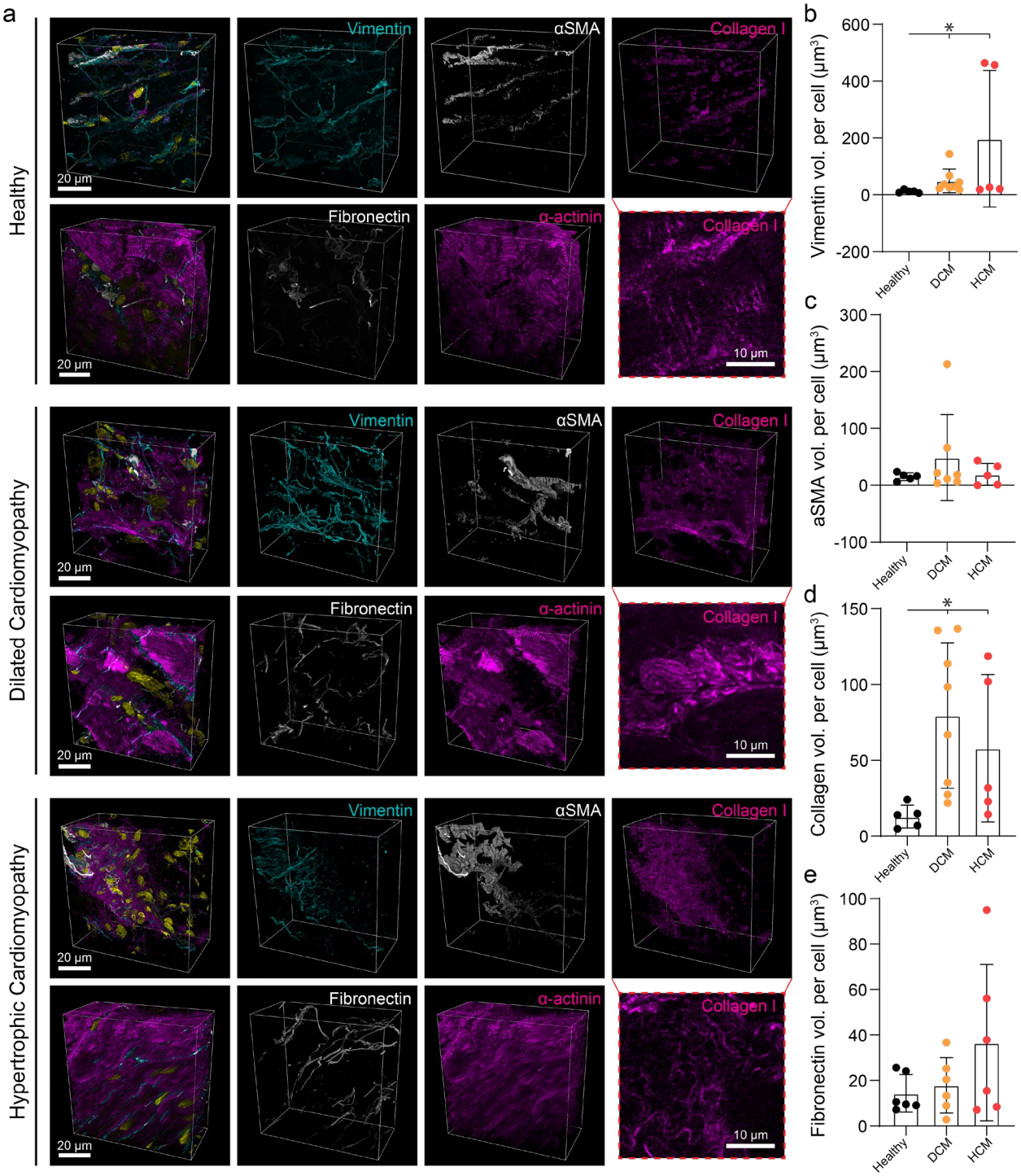

Figure 6.1: Increased extracellular matrix accumulation in diseased human heart tissue compared to healthy control tissue. (**a**) Confocal fluorescent images of vibratome section human myocardial tissue from a healthy donor and patients with dilated cardiomyopathy and hypertrophic cardiomyopathy. (**b**) Quantification of vimentin volume per cell number in each tissue region. (**c**) Quantification of αSMA volume per cell number in each tissue region. (**d**) Quantification of

collagen volume per cell per cell number. (**e**) Quantification of fibronectin volume per cell. For all conditions, $n \geq 6$ unique regions obtained from 3 different tissue slices. All data presented as mean ± std; * $p < 0.05$.

6.4.2 Mechanics of synthetic fibrous matrices impact myofibroblast differentiation

Developing a platform to better understand how biophysical properties of the ECM impact MF activation requires an approach to controlling fibrous architecture and mechanics to recapitulate the ECM in healthy or disease states. Previously, our group has established synthetic matrices composed of dextran vinyl sulfone (DVS) polymeric fibers with tunable architecture and mechanics (C.D. Davidson et al. 2020; DePalma et al. 2021). These fibers are comparable in mechanics and geometry to perimysial collagen fibers, which are networks of ~1 μm diameter fibers that surround bundles of CMs and support the anisotropic contractions of cardiac tissue (Pope et al. 2008; Karl T. Weber 1989; Karl T. Weber et al. 2012). Additionally, these perymisial networks have been shown to become disrupted in fibrotic disease (Karl T. Weber 1989; Karl T. Weber et al. 2012). Using this biomaterial platform, we have previously shown that matrix mechanics and alignment are critical iPSC-CM tissue assembly and their subsequent organization, function, and maturation (DePalma et al. 2021, 2023). Additionally, we have shown that the stiffness of disorganized fiber matrices alters lung fibroblast differentiation to MFs again by influencing cell-ECM interactions (Baker et al. 2015; C.D. Davidson et al. 2020).

Motivated by these findings and previous work describing the architecture of the ECM in both healthy and diseased myocardium, we adopted this approach enabling control of both fiber alignment and stiffness to explore how these distinct cues known to change with myocardial disease impact CF activation to MFs. Electrospun DVS fibers were collected on microfabricated arrays of square 2 mm by 2 mm PDMS wells creating dense matrices with subcellular pore sizes

such that cells seeded onto matrices and did not fall through prior to adhering (**Figure 6.2a**) (C.D. Davidson et al. 2020; Christopher D. Davidson et al. 2024). To control fiber matrices, substrates were attached to a mandrel rotating at various speeds, as previously described (DePalma et al. 2021, 2023). Matrix stiffness was controlled by modulating the concentration of lithium phenyl-2,4,6-trimethylbenzoylphosphinate (LAP) photoinitiator present during exposure to UV light. Crosslinking parameters were identified to generate matrices with stiffnesses corresponding to healthy (0.1 mg/mL LAP; 0.68 kPa) or diseased (5.0 mg/mL LAP; 17.4 kPa) myocardium, as characterized by microindentation measurements (DePalma et al. 2023).

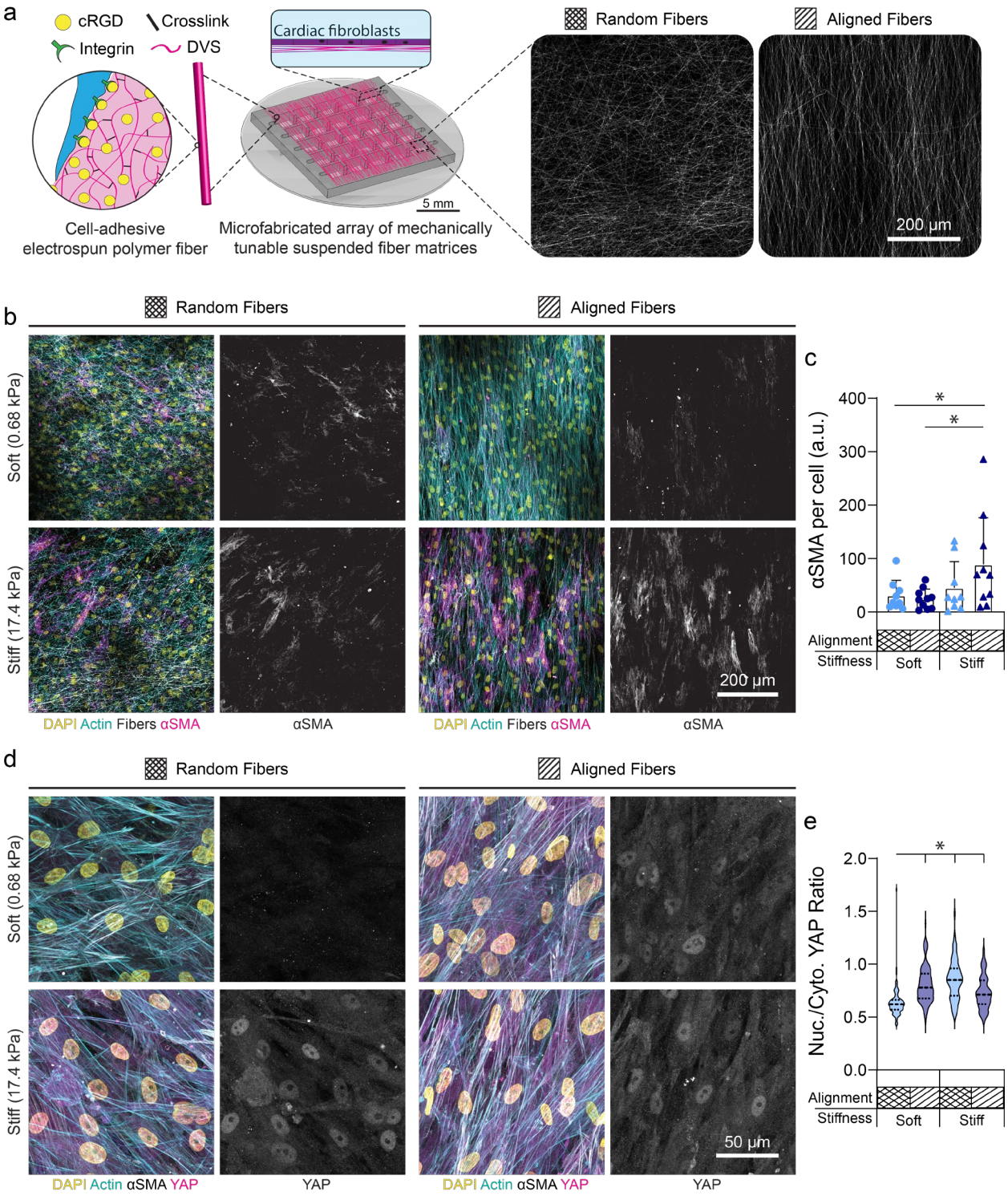

Figure 6.2: Stiff, aligned fibers drive robust differentiation of primary human cardiac fibroblasts in the presence of TGF-β1. (**a**) Schematic of microfabricated fibrous tissue array. Stiffness can be tuned by controlling the amount of crosslinks in the fibers and alignment can be tuned by altering the rotation speed of the collection mandrel. (**b**) Confocal fluorescent images of

primary cardiac fibroblasts (NHCF1) cultured on fiber matrices of varying stiffness and alignment immunostained for αSMA. (**c**) Quantification of αSMA expression per cell. ($n \geq 9$ regions from separate wells in the microfabricated substrate). (**d**) Confocal fluorescent images of primary cardiac fibroblasts (NHCF1) cultured on fiber matrices of varying stiffness and alignment immunostained for YAP. (**e**) Quantification of YAP nuclear to cytosolic ratio. ($n \geq 81$ nuclei from 9 individual wells.) All data presented as mean ± std; * $p < 0.05$.

Following functionalization of fibers with cell-adhesive cyclic-RGD, normal human CFs were seeded on matrices with varied alignment and stiffness and cultured in the presence of a vehicle control, fibrogenic TGF-β1 (10 ng/mL), and a TGF-β inhibitor SB431542 (10 μM) for 7 days (**Figure 6.2**). When expanded on tissue culture plastic prior to seeding, we observed that CFs spontaneously activated into MFs (**Supplementary Figure 6.1**). To prevent unintended activation, CFs were maintained in media supplemented with the TGF-β inhibitor SB431542 (10 μm) which was removed 24 prior to the beginning of experiments (**Supplementary Figure 6.1**). Control and SB431542 treated samples expressed little αSMA, regardless of matrix conditions (**Supplementary Figure 6.2**). In samples cultured with TGF-β1 for 7 days, expression of αSMA increased on all matrix conditions compared to vehicle control or SB431542 counterparts (**Supplementary Figure 6.2**). However, CFs cultured on matrices composed of stiff and aligned fibers yielded the highest levels of αSMA expression when exposed to TGF-β1 as compared to all matrix conditions tested (**Fig. 2b,c**). These results were consistent for a second CF donor line (**Supplementary Figure 6.2**). In this other donor lines however, the impact of fiber alignment on was even more pronounced. With stiff, aligned fibers maintaining high levels of αSMA expression overall, significant increases in αSMA were also observed in CFs cultured on soft, aligned fibers compared to random fibers, further supporting fiber alignment as a major driver of CF activation to MFs (**Supplementary Figure 6.2**). Additionally, immunostaining for YAP expression, an early marker of MF activation (Ragazzini et al. 2022; Del Re 2022; Reichardt et al. 2021), in samples

treated with TGF-β1 after 3 days in culture revealed reduced YAP nuclear to cytosolic ratio only in tissues cultured on soft, random matrices (**Figure 6.2d,e**). This suggests a role for multiple mechanosensing pathways in driving MF differentiation in response to changes in matrix alignment and mechanics.

6.4.3 Heterocellular crosstalk with iPSC-CMs inhibits MF activation

As it has been previously established that CM and CF communication is central to healthy tissue function but can promote fibrosis when disrupted, we next generated matrix-segregated cocultures of iPSC-CMs and CFs (Bowers, Meng, and Molkentin 2022; Cartledge et al. 2015). We aimed to establish a co-culture model that recapitulates the organization of CMs and CFs in the myocardium, where the two cell types are separated by thin layers of collagen fibers (Goldsmith et al. 2004). To accomplish this, we incorporated seeding channels connecting individual wells beneath the fiber matrices within the microfabricated well array. After seeding purified cultures of iPSC-CMs on top of the fiber matrices and allowing them to begin to assemble into multicellular tissues for 3 days, CFs were pipetted into these channels through small ports and distributed throughout the channels and wells by gently rocking (**Figure 6.3a**). Samples were quickly inverted and cultured upside down to allow CFs to adhere to the underside of the matrix, after which samples were cultured right-side up for the duration of the experiment. The resultant bilayer tissue contains iPSC-CMs and CFs separated by a thin porous synthetic matrix of DVS fibers not only mimics the distribution of these two cell types *in vivo* and allows for CM-CF hetereocellular communication via secreted paracrine factors, direct connections via gap junctions through small pores in the matrix, and mechanical signals transmitted through the ECM (Bowers, Meng, and Molkentin 2022; Cartledge et al. 2015; Hall et al. 2021; Herum et al. 2017; Ruwhof et al. 2000).

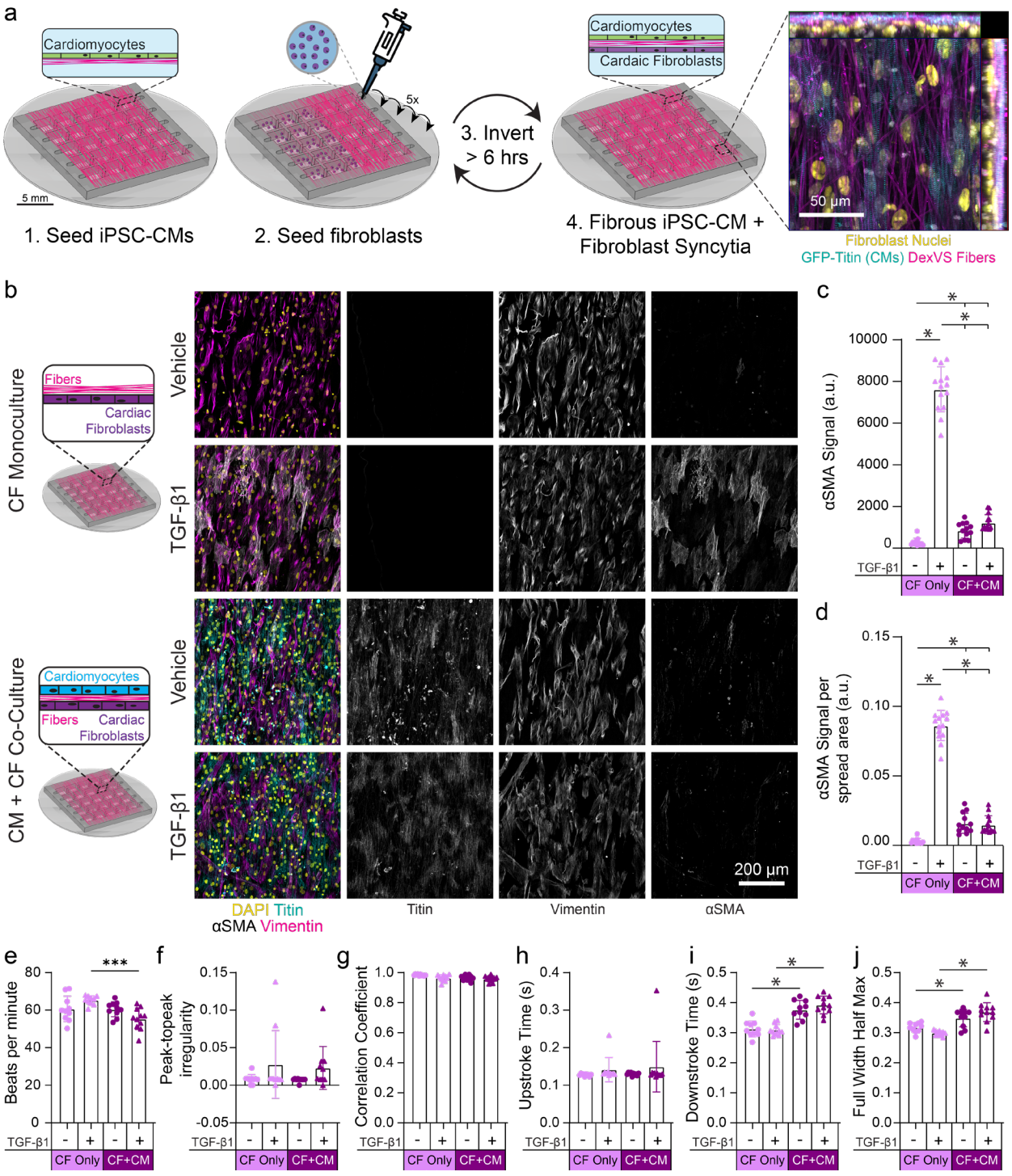

Figure 6.3: iPSC-CMs mitigate CF differentiation to MF when cultured on a shared soft, aligned fibrous matrix. (**a**) Schematic of microfabricated bilayer fibrous tissue array. Pure populations of iPSC-CMs were seeded on the top of the matrix, followed by CF seeding on the bottom of the matrix 3 days later. Fluorescent confocal image of bilayer tissue with the fibroblast

nuclei labeled in yellow and the cardiomyocytes labeled in cyan. Segregation of the two layers on either side of the matrix observable in the orthogonal projection. (**b**) Confocal fluorescent images of primary cardiac fibroblasts (NHCF3) cultured on the bottom of the fiber matrices alone or with iPSC-CMs (PGP1) on top. (**c**) Quantification of total αSMA expression and (**d**) αSMA expression pre spread area. ($n \geq 10$ regions from separate wells in the microfabricated substrate). (**e**) Calcium flux dynamics were analyzed, to determine (**e**) contraction frequency, (**f**) peak-to-peak irregularity, (**g**) correlation coefficient, (**h**) upstroke time, (**i**) downstroke time to 80% relaxation, and (**j**) full width half max. ($n \geq 10$). All data presented as mean ± std; * $p < 0.05$.

In comparing CM and CF monocultures with bilayer co-cultures, we chose soft, aligned fiber matrices, as they best reflect healthy myocardial matrix and have previously been shown to best facilitate the assembly of organized iPSC-CM tissues (DePalma et al. 2023). CFs on the bottom of the soft, aligned fiber matrices without iPSC-CMs present differentiated into αSMA positive MFs when exposed to TGF- β1, as described above (**Figure 6.3b-d**). However, when iPSC-CMs were present on the opposing side of matrices, to our surprise MF activation of CF was significantly inhibited despite the presence of TGF-β1, as quantified by a decrease in αSMA expression in vimentin positive fibroblasts (**Figure 6.3b-d**). These results were consistent across various combinations of two iPSC-CM donors and three CF donors (**Figure 6.3, Figure 6.4**). Additionally, MF differentiation was also negligible when the positioning of CMs and CFs was reversed, with CFs positioned on top of the matrix and CMs on the bottom (**Figure 6.3**). These results suggest crosstalk between CMs and CFs that prevents the activation of MFs, thereby promoting tissue homeostasis. As there are many signals known to initiate fibrotic disease progression, it is possible that other factors beyond TGF-β1 are necessary for MF activation (Cartledge et al. 2015; Hall et al. 2021; Herum et al. 2017; Pellman, Zhang, and Sheikh 2016). Further, protective signals iPSC-CMs may prevent initial activation through either paracrine or mechanical means. Mass spectrometry conducted on conditioned media from CF monocultures and CM-CF cocultures treated with TGF-β1 showed significant increases in secreted extracellular

matrix proteins such as fibronectin and collagen in CF monocultures as compared to the coculture with CMs (data not shown), further indicating reduced activation of CFs in the presence of CMs.

To examine the impact that co-culture with CFs had on iPSC-CM function, we assessed calcium handling of iPSC-CM monocultures or in BLTs containing CFs. Tissues were incubated with a calcium sensitive dye and imaged at high frame rates > 65 frames/sec. Decreased contractile frequency was observed in co-culture conditions only in the presence of TGF-β1 (**Figure 6.3e**). Additionally, the presence of TGF-β1 increased the arrhythmogenic potential, as quantified by heightened peak-to-peak irregularity (DePalma et al. 2021) of iPSC-CMs with or without CFs present, suggesting a detrimental impact of TGF-β1 on iPSC-CMs (**Figure 6.3f**). No differences in the contraction correlation and upstroke time were observed (**Figure 6.3g,h**). However, co-culture with CFs increased both downstroke time and full width half max of calcium fluxes (**Figure 6.3i,j**). These results indicate that TGF-β1 negatively influences iPSC-CM function but that co-culture with CFs may promote electrophysiological maturation of iPSC-CMs, potentially due to direct connection via gap junctions (Frangogiannis 2022; Hanna and Frangogiannis 2019; Vasquez et al. 2010).

6.4.4 Cellular crosstalk via secreted factors prevents myofibroblast differentiation

With distinctions noted between monocultures of iPSC-CMs and CFs compared to BLTs containing both cell types, we next explored the mode of signaling underlying these differences. To potentially isolate paracrine signaling as a key regulator of homeostatic crosstalk between iPSC-CMs and CFs, we first treated CF cultures with conditioned media from iPSC-CM monocultures and BLTs treated TGF-β1, all cultured on soft, aligned matrices (**Figure 6.4a**). Conditioned media was collected after 24 hours of CM culture and transferred to CF

monocultures seeded on soft, aligned fiber matrices, repeated daily for the duration of the study. Treatment with CM-conditioned media did not result in the same mitigation of MF activation in CF monocultures, evident by heightened αSMA expression (**Figure 6.4a-c**). However, it is possible that the protective effect observed in BLTs is mediated by short range paracrine signaling or other communication mechanisms between iPSC-CMs and CFs, either through gap junctions or direct mechanical signaling. To isolate short range paracrine signaling as a potential mediator of this effect, we generated samples containing iPSC-CMs and CFs that did not share a matrix by seeding soft, aligned fiber matrices with iPSC-CMs as before, but seeding CFs onto the PDMS surface below suspended fiber matrices (**Figure 6.4d**). As we showed previously that CFs differentiate to MFs on stiff tissue culture plastic in normal culture conditions (**Supplementary Figure 6.1**), we expect robust MF activation as marked by αSMA expression in the presence of TGF-β1. However, with iPSC-CMs positioned on fiber matrices ~350 μm above the CFs, differentiation to MFs was again diminished, suggesting paracrine communication between iPSC-CMs and CFs in preventing MF activation and maintaining tissue homeostasis (**Figure 6.4**). These experiments do not rule out the potential role for mechanical communication or electrochemical signaling through gap junctions as possible means of communication but rather highlight the importance of secreted factors in limiting CF activation. Further, the discrepant results from conditioned media and separated co-culture experiments suggests that constant, dynamic paracrine crosstalk between iPSC-CMs and CFs is critical to maintaining CF quiescence.

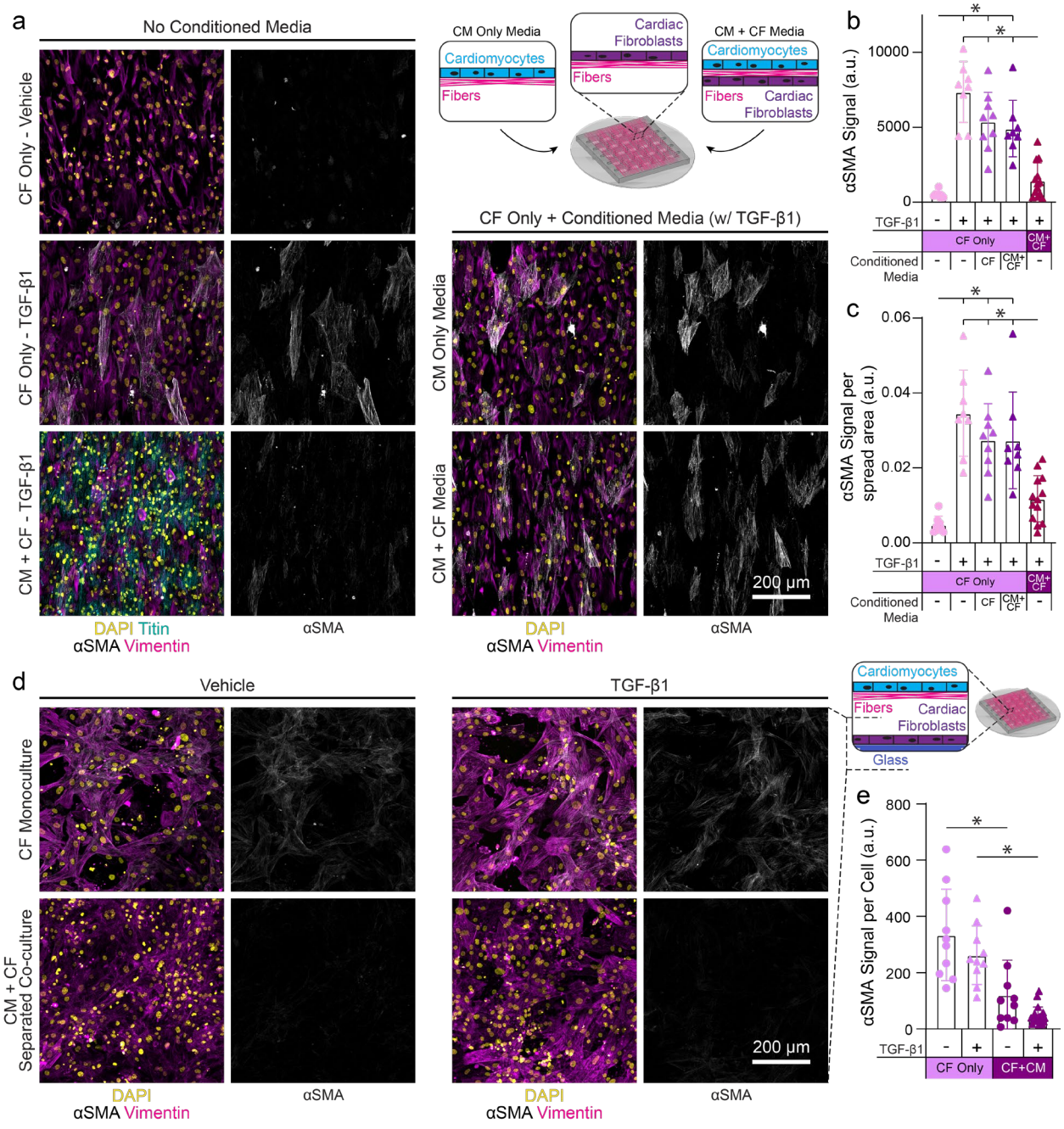

Figure 6.4: Paracrine factors from iPSC-CMs prevent MF differentiation. (**a**) Confocal fluorescent images of primary cardiac fibroblasts (NHCF3) cultured alone on the bottom side of the fiber matrix or with iPSC-CMs (PGP1) on the top of the matrix. (**b**) Quantification of total αSMA. These samples served as control to compare the samples of only cardiac fibroblasts that received conditioned media from either iPSC-CMs or iPSC-CM + CF biolayer tissue. (c) Quantification of αSMA expression per cell. (**d**) Confocal fluorescent images of primary cardiac fibroblasts (NHCF3) cultured on the glass surface beneath the suspended fiber matrix with iPSC-

CMs (PGP1). (**e**) Quantification of αSMA expression per cell. ($n \geq 9$ regions from separate wells in the microfabricated substrate). All data presented as mean ± std; * $p < 0.05$.

6.5 Discussion

In the healthy myocardium, resident fibroblasts are responsible for maintenance of the ECM, which is critical to the normal mechanical function of the heart (Travers et al. 2016). In response to pathological signals both soluble and physical, these fibroblasts become activated and differentiate into highly contractile MFs that are associated with the secretion of large amounts of disorganized matrix, leading to disruption of tissue function (Hinz 2006; Travers et al. 2016). Additionally, secreted signals from activated MFs are believed to further propagate pathogenesis by signaling directly to other cell types including CMs via physical contact and paracrine signaling (Cadosch et al. 2024; Kong, Christia, and Frangogiannis 2014; Shinde and Frangogiannis 2014; Travers et al. 2016). However, previous models of cardiac disease make it difficult to precisely dissect these interactions due to limited control of physical microenvironment cues. Here, we integrated synthetic biomaterials with microfabrication techniques to generate 2.5D fibrous matrices that can accurately mimic the architectural and mechanical features of the ECM associated with tissues states while segregating CMs and CFs in a manner reflective of physiology.

Immunostaining for ECM proteins in healthy and diseased human heart sections revealed that the increase in matrix accumulation in the interstitial space between CMs in tissues samples from patients with DCM and HCM, and more broadly ECM remodeling associated with fibrosis observed across the myocardium, is quite heterogeneous (**Figure 6.1**). Despite other recent studies identifying variable architecture and density of these fibrotic regions in mouse models of cardiac fibrosis, there is little known about the causes of this heterogeneity and the impact of specific

microenvironmental conditions on fibrotic disease progression (Holmes, Borg, and Covell 2005; Richardson and Holmes 2016). This is in part because previously established *in vitro* models used to study cardiac disease often fail to recapitulate the fibrous architecture and complex mechanics of the cardiac microenvironment (Pope et al. 2008; Karl T. Weber 1989). By seeding CFs on synthetic fibrous matrices of various alignment and stiffness mimicking the various tissue states overserved in healthy and fibrotic tissue, we found that CFs differentiate more efficiently to MFs on aligned, stiff fibers (**Figure 6.2**). Surprisingly, little activation was noted in CFs seeded on both soft and stiff matrices composed of randomly oriented fibers which reflect the disorganized matrices often associated with cardiac fibrosis (Karl T. Weber 1989; Karl T. Weber et al. 2012). Supporting our findings, MF differentiation has been correlated with collagen I alignment in the scar border zone after myocardial infarction in mouse hearts (Van Den Borne et al. 2009; Bugg et al. 2020). Additionally, Bugg et al. presented results in agreement with the ones presented here, describing that culturing primary human CFs on aligned nanotopographical substrates increased MF differentiation compared to CFs cultured on flat surfaces or substrates with a disorganized topography (Bugg et al. 2020). More elongated CFs on aligned samples were shown to have increased tension at focal adhesions that induced enhanced p38-YAP-TEAD signaling which supported MF activation. Previous work from our group culturing primary human lung fibroblasts on fibrous DVS matrices of varying stiffness noted that enhanced vinculin expression corresponded with increased MF differentiation (C.D. Davidson et al. 2020). Additionally, focal adhesion kinase (FAK), a mechanosensitive protein associated with integrin signaling, has been shown to be key regular in MF activation (Baudino et al. 2006; Schroer and Merryman 2015). As such, future studies investigating links between matrix cues and key regulators of signaling at CF focal adhesions could provide insights into matrix-mediated MF activation.

In addition to tuning of matrix alignment, the fibrous biomaterial platform presented here enables orthogonal tuning of matrix mechanics. We found that aligned, stiff matrices increased MF differentiation compared to aligned soft matrices (**Figure 6.2**). Many studies using mechanically tunable hydrogel substrates such as polyacrylamide have shown that increased matrix stiffness supports MF activation of CFs and fibroblasts of varied tissue origins (Balestrini et al. 2012; Caliari et al. 2016; Goffin et al. 2006; van Putten, Shafieyan, and Hinz 2016), while long term culture on soft hydrogels maintains fibroblast quiescence and limit proliferation (Felisbino et al. 2024; Godbout et al. 2020; H. Wang et al. 2013). Conversely, our group has shown that random, soft fibrous DVS matrices, support MF activation of primary human lung fibroblasts compared to stiff matrices in the presence of TGF-β1, likely due to increased fiber recruitment, resulting ligand densification, and enhanced integrin-mediated adhesion to fibers (C.D. Davidson et al. 2020; Schroer and Merryman 2015). When interpreting these divergent results, caution must be taken when directly comparing continuum-like isotropic hydrogel substrates as compared to matrices composed of discrete fibers, as the mechanical properties of the 2.5D synthetic fiber matrices are vastly different than elastic hydrogel samples (Baker et al. 2015; C.D. Davidson et al. 2020). Multiple culture platforms, including our fibrous platform described herein (**Figure 6.2**), have been utilized to highlight the importance fiber alignment in driving CF differentiation to MFs, and thus suggest that cellular anisotropy may be a key cue for MF activation (Bugg et al. 2020). Additionally, when comparing how biophysical cues impact MF activation, it is important to consider that fibroblasts of different tissue origin may respond differently to changes in the mechanical environment.

As previously described, CF communication with other cell types present in the myocardium is critical to maintaining healthy tissue function and when dysregulated can drive

remodeling during disease (Hall et al. 2021). However current models of cardiac disease fail to recapitulate the segregation of CFs and CMs in the native myocardium, where CFs are interspersed throughout the endomysial collagen networks between CMs (Goldsmith et al. 2004; Kanzaki et al. 2010; Pellman, Zhang, and Sheikh 2016). These models can be broadly categorized into 3 major groups: 2D *in vitro* models, 3D *in vitro* models, and *in vivo* systems (Pellman, Zhang, and Sheikh 2016). Simple 2D systems include admixed CFs and CMs on traditional tissue culture plastic, hydrogel surfaces, transwell platforms, and micropatterned samples utilized to organize or align tissues (Caliari et al. 2016; Cartledge et al. 2015; Felisbino et al. 2024; Godbout et al. 2020; van Putten, Shafieyan, and Hinz 2016). While these platforms have helped identify regulators of fibrotic disease progression, they suffer from various limitations, including the improper organization of CFs and CMs and limited mechanical tunability. Despite increased complexity, both scaffold-based and scaffold-free 3D systems suffer from similar limitations to 2D systems, with limited control of mechanical properties, tissue organization, and limited ability to isolate specific cell-cell interactions (Pellman, Zhang, and Sheikh 2016).

The BLT co-culture platform presented here overcomes many of these limitations by utilizing a mechanically tunable ECM-mimetic biomaterial and microfabrication approach that recapitulates the structure of myocardial endomysial collagen fibers and enables the segregation of CF and CMs in a physiologic manner (**Figure 6.3**) (Fleischer and Dvir 2013; Kanzaki et al. 2010; Karl T. Weber 1989). Culturing CMs and CFs on opposing sides of a synthetic fibrous matrix with tunable mechanical properties facilitated the generation of model of both healthy and diseased tissues states. Aligned, soft matrices, that we have previously shown to drive robust assembly and maturation of iPSC-CMs and mimic the healthy cardiac ECM, were chosen for initial coculture studies to better understand hoe CMs and CFs communicate in homeostatic conditions

(**Figure 6.3**). Additionally, by introducing the profibrotic growth factor TGF-β1, we explored how initial fibrogenic soluble cues influence MF activation. Interestingly, we found that even with exposure to fibrogenic TGF-β1, crosstalk with iPSC-CMs through a shared fibrous matrix prevented MF differentiation in contrast to CF monocultures maintained under identical conditions (**Figure 6.3, Supplementary Figure 6.3, Supplementary Figure 6.4)**. While there are reports on how CMs and CFs communicate to promote fibrosis, there far fewer insights into how CM-CF crosstalk maintains tissue homeostasis (Cadosch et al. 2024; Pesce et al. 2022). Both paracrine communication and direct connections through gap junctions between CFs and iPSC-CMs have been identified as important for iPSC-CM maturation, implying a role for these communication pathways in maintaining overall tissue homeostasis as well (Beauchamp et al. 2020; Giacomelli et al. 2020). Additionally, alterations in mechanical signaling between CMs and CFs can lead to increased FGF expression and thus more collagen expression, showing the importance of mechanical connections between these two cell types (Cadosch et al. 2024).

In our BLT platform, iPSC-CMs and CFs can communicate in different ways by secreting paracrine factors, interacting with the shared deformable ECM to transmit mechanical signals, and direct cell-cell connections through small pores present within the matrix (Hall et al. 2021; Kakkar and Lee 2010; Pellman, Zhang, and Sheikh 2016). By controlling the positioning of both cell types, we identified paracrine signaling between CFs and CMs as critical to homeostatic signaling. Specifically, we removed the potential for mechanical crosstalk by removing CFs from the shared fibrous ECM and culturing them on the glass surface beneath the fibers, a surface we showed to be quite amenable to MF differentiation (**Figure 6.4; Supplementary Figure 6.1**). While CMs prevented CF differentiation to MFs while cultured on a shared fibrous matrix, differentiation was also mitigated when CMs were cultured on -soft fibrous matrices ~350 μm above CFs cultured on

glass in the presence of TGF-β1, suggesting the presence of homeostatic paracrine crosstalk between CFs and CMs (**Figure 6.4**). In response to profibrotic factors such as TGF-β1, CFs typically will begin to become more contractile and secrete additional proinflammatory factors such as angiotensin II, initiating a positive feedback loop that leads to further activation (Nakamura and Sadoshima 2018; Talman and Ruskoaho 2016; Travers et al. 2016). Exploration into secreted factors that antagonize this feedback loop using our co-culture platform could therefore help identify potential therapeutic targets to prevent or reverse fibrotic progression.

While the importance of paracrine signaling in maintaining CF quiescence is clear from these studies, isolating direct mechanical crosstalk between CMs and CFs is more challenging in this platform, as disrupting all paracrine signaling may disrupt normal cellular functions and confound results. Mechanical actuation of individual cultures of CMs and CFs have indicated that excessive strain initiates the secretion of profibrotic factors and extracellular matrix proteins (Herum et al. 2017; Pathak et al. 2001; Pellman, Zhang, and Sheikh 2016; Ruwhof et al. 2000; Souders, Bowers, and Baudino 2009). Additionally, cellular contractility has been shown to activate latent matrix-bound TGF-β1, a key driver of MF differentiation in cardiac disease (Khalil et al. 2017; Wipff et al. 2007). Direct mechanical signaling between CMs and CFs, either through adherens junctions or ECM-mediated force transmission, is also likely critical in driving disease progression (Hall et al. 2021; Pellman, Zhang, and Sheikh 2016). For example, highly contractile MFs can apply increased tension on CMs, leading to disrupted electrophysiological function of tissues (Mahoney, Mezzano, and Morley 2016; Quinn et al. 2016; Rubart et al. 2018; Thompson et al. 2011; Y. Wang et al. 2023). However, how these interactions may promote hemostatic maintenance and provide protection from initial fibrotic signaling merits further investigation.

In conclusion, we developed a microfabricated, biomimetic co-culture platform to examine CM-CF communication underlying tissue homeostasis versus fibrosis. We found that the mechanical properties and alignment of the fibrous ECM modulates MF differentiation. Further, CM-CF paracrine crosstalk inhibited MF differentiation on soft, aligned fibrous matrices that recapitulate the healthy cardiac ECM. Ongoing studies are focused on identifying the operative heterocellular communication pathways via mass spectrometry and RNA sequencing analysis of the CM-CF secretory and transcription.

6.6 Materials and Methods

6.6.1 Reagents

All reagents were purchased from Sigma Aldrich and used as received, unless otherwise stated.

6.6.2 Human myocardial tissue sectioning, clearing, and immunostaining

Human myocardial tissue was sectioned into 200 μm slices using a vibratome. Tissue sections were then cleared using a modified advanced cubic clearing method(Matsumoto et al. 2019). Specifically, sections were cleared in dH2O with 50%CUBIC-L containing 10% N-butyldiethanolamine(w/w), and 10% TritonX-100 (w/w) in dH2O for one day, then switched to 100% CUBIC-L for 3 more days, replacing the solution every 24 hours. Following clearing, tissues were permeabilized for two days in PBS solution containing 20% DMSO, 0.1% tween 20, 0.1% TritonX-100, 0.02% SDS, + 0.1% deoxycholate(w/v) and + 0.1% tergitol NP40 (w/v). Then tissues were blocked and stored in PBS solution containing 0.2% TritonX-100, 6% goat serum, and 10% DMSO for at least 24 hours or until staining. Primary and secondary antibody solutions were diluted in the same blocking solution and samples were treated with both primary and secondary antibodies for 48 hours, refreshing the antibody solution after 24 hours.

6.6.3 PDMS well array fabrication

Arrays of poly(dimethylsiloxane) (PDMS; Dow Silicones Corporation, Midland, MI) posts were fabricated by soft lithography as previously described (Baker et al. 2015; C.D. Davidson et al. 2020). Briefly, silicon wafer masters possessing SU-8 photoresist (Microchem, Westborough, MA) were produced by standard photolithography and used to generate PDMS stamps. Following silanization with trichloro(1H,1H,2H,2H-perfluorooctyl)silane, stamps were used to emboss

uncured PDMS onto oxygen plasma-treated coverslips. Cantilever arrays were methacrylated with vapor-phase silanization of 3-(trimethoxysilyl)propyl methacrylate in a vacuum oven at 60 °C for at least 6 h to promote fiber adhesion to PDMS.

6.6.4 DVS fiber matrix fabrication

DVS polymer was synthesized as previously described by our lab(C.D. Davidson et al. 2020). Briefly, dextran was reacted with divinyl sulfone and the product was dialyzed and lyophilized. For electrospinning, DVS was dissolved at 0.7 g mL^{-1} in a 1:1 mixture of milli-Q water and dimethylformamide with 0.6% (w/v) lithium phenyl-2,4,6-trimethylbenzoylphosphinate (LAP; Colorado Photopolymer Solutions) photoinitiator, 2.5% (v/v) methacrylated rhodamine (25 mM; Polysciences, Inc., Warrington, PA), and 5.0% (v/v) glycidyl methacrylate. This solution was electrospun on coverslips containing microfabricated cantilever arrays affixed to a custom-built rotating mandrel with a hexagonal geometry driven by an AC motor with controllable speed (DePalma et al. 2021). Electrospinning was conducted in an environmental chamber at 35% humidity with a flow rate of 0.2 ml h^{-1}, voltage of 7.0 kV, and a gap distance of ~5 cm to the grounded mandrel. After collection, fibers were stabilized by primary crosslinking under UV (100 mW cm^{-2}) through a microfabricated photomask for 20 s, such that only the fibers suspended in the region spanning two posts would be crosslinked. Fiber matrices were subsequently placed in LAP photoinitiator solutions of varying concentrations and exposed again to UV (100 mW cm^{-2}) for 20 s to tune fiber stiffness and sterilize substrates.

Matrices were functionalized with cell adhesive peptides cyclized [Arg-Gly-Asp-D-Phe-Lys(Cys)] (cRGD; Peptides International) via Michael-Type addition to available vinyl sulfone groups. Peptides were dissolved at 200 μM in milli-Q water containing HEPES (50 mM), phenol

red (10 μg mL^{-1}), and 1 M NaOH to bring the pH to 8.0. A volume of 150 μL was added to each substrate and incubated at room temperature for 30 min.

6.6.5 iPSC culture and iPSC-CM differentiation

Induced pluripotent stem cells containing a GFP-titin reporter 79 (PGP1; gift from the Seidman Lab) or GFP-DSP reporter (WTC; Allen Institute AICS-0017 cl.6) were cultured in mTeSR1 media (StemCell Technologies) on Matrigel (Corning) coated tissue culture plastic and differentiated via temporal Wnt modulation as previously described 80,81. Briefly, differentiation was initiated when iPSCs reached 90% confluency in RPMI 1640 media supplemented with B27 minus insulin on day 0 with the addition of 12 μM CHIR99021 for 24 hours. On day 3, CDM3 media containing 5 uM IWP4 on day 3 for 48 hours. Retinol inhibitor BMS 453 (Cayman Chemical, 1 μM) was also added for days 3-6 to minimize atrial lineage differentiation82,83. Cultures were then maintained in CDM3 media until contractions began between day 8 and 10. iPSC-CMs cultures were then transferred to RPMI 1640 media lacking glucose and glutamine (Captivate Bio) supplemented with 4 mM DL-lactate, 500 ug/mL human serum albumin (Sciencell Research Labs), and 213 ug/mL L-ascorbic acid 2-phosphate trisodium salt on day 11 for 4 days. Following purification, iPSC-CMs were replated as monolayers (300,000 cells/cm2) on growth factor reduced Matrigel (Corning) in RPMI 1640 media supplemented with B27 for 7 additional days before seeding into tissues.

6.6.6 Cardiac fibroblast culture

Normal human ventricular cardiac fibroblasts (NHCF) (Lonza) were thawed and expanded in FGM-3 medium (Lonza) supplemented with 10 μm SB431542 to prevent differentiation to myofibroblasts. Three cell lines were utilized in these studies to ensure robustness of

theexperimental findings (labeled NHCF1, NHCF2, and NHCF3). Despite treatment with SB431542, fibroblasts were not used for experiments past passage 6. NHCFs were passaged using 0.05% trysin. Cells were cultured at 37 °C and 5% CO2.

6.6.7 Microtissue seeding and culture

When conducting experiments with only cardiac fibroblasts, CFs were seeded on top of the fiber matrices and allowed to adhere to the fibers for 24 h. Following cell attachment, basal media was supplemented with TGF-β1 (10 ng mL−1) and cultured for an additional 6 days, unless otherwise noted. Media was replaced every 2 days. For seeding cells on the bottom side of the matrix, cells were resuspended at a high concentration (10,000 cells /10 μL for NHCFs or 25,000 cell/10μL for iPSC-CMs) and 10 μL of cell suspension was quickly injected into each of the 5 channels on the sample. The sample was quickly inverted and rocked back and forth to ensure even distribution of cells. Next, 300 μL of RPMI-B27 media was then placed on a piece of parafilm in dish. The samples were then placed on the drop of media such that it floats on the top with the fibers facing down, a left to let set for 24 hours, allowing the cells to settle and adhere to the bottom of the matrix. Samples were then moved to a 12 well dish where all tissues for experiments, coculture or not, were conducted in RPMI B27 media. For conditioned media experiments, media was transferred to new samples daily starting at day 1 in culture until day 7, unless otherwise noted.

6.6.8 Calcium imaging

Calcium handling analysis was performed by incubating cells for 1 hour at 37 ℃ with 5 μM Cal520-AM (AAT Bioquest). Cells were then returned to conditioned media preserved prior to adding the calcium sensitive dye and allowed to equilibrate for >30 min at 37 ℃ and 5% CO_2. Following equilibration, tissues were imaged under epifluorescence at 65 Hz while maintaining

temperature and CO_2. Time-lapse movies of calcium flux were analyzed with custom Matlab scripts as previously described(DePalma et al. 2021). Briefly, average fluorescent profiles over time were determined for each tissue and parameters such as beats per minute, peak-to-peak irregularity, flux rise time, flux decay time, and peak full width half max were calculated. Contraction correlation coefficient was determined by dividing the entire tissue into 16 regions of equal area and calculating the average Pearson's correlation coefficient between the flux profiles of each of these regions.

6.6.9 Immunofluorescence staining of *in vitro* culture platforms

Samples were fixed in 2% paraformaldehyde for 10 min at RT. Samples were then permeabilized in PBS solution containing Triton X-100 (0.2% v/v), sucrose (10% w/v), and magnesium chloride (0.6% w/v) for 10 min and blocked in 1% (w/v) bovine serum albumin. Alternatively, to extract cytoplasmic vinculin, samples were simultaneously fixed and permeabilized in 2% paraformaldehyde in a buffer containing 1,4-piperazinediethanesulfonic acid (PIPES, 0.1 M), ethylene glycol-bis(2-aminoethylether)-N,N,N',N'-tetraacetic acid (EGTA, 1 mM), magnesium sulfate (1 mM), poly(ethylene glycol) (4 % w/v), and triton X-100 (1% v/v) for 10 min at room temperature, prior to blocking in 1% (w/v) bovine serum albumin. Tissues were incubated with rabbit monoclonal anti-N-cadherin (1:500; Abcam Ab18203), rabbit monoclonal anti-connexin43 (1:1000; Millipore Sigma AB1728), mouse monoclonal anti-α-actinin (1:500; Abcam ab9465), mouse monoclonal anti-cardiac troponin T (1:500; ThermoFisher MA5-12960), mouse monoclonal anti-vinculin (1:1000; Millipore Sigma V9264), rabbit polyclonal anti-myosin light chain 2 (1:500; Proteintech 10906-1-AP), rabbit polyclonal anti-non-muscle myosin II-B (1:1000; Biolegend 909902), mouse monoclonal anti-integrin β1D (1:1000; Abcam ab8991), rabbit polyclonal anti-zyxin (1:200; Millipore Sigma HPA004835), or mouse anti-dextran (1:500;

STEMCELL Technologies 60026) antibodies for 1 hour at RT, followed by goat anti-mouse Alexa Fluor 647 (1:1000; Life Technologies A21236), goat anti-mouse Alex Fluor 546 (1:1000, Life Technologies A11030), or goat anti-rabbit Alexa Fluor 647 secondary antibodies (1:1000; Life Technologies A21245) and DAPI for 1 hour at RT.

6.6.10 Microscopy and image analysis

Fluorescent images were captured on a Zeiss LSM800 confocal microscope. Sarcomere alignment was quantified via custom Matlab scripts as previously described (DePalma et al. 2021). Briefly, images of titin-GFP reporter were thresholded and individual z-discs segmented. Z-discs were subsequently grouped with neighboring z-discs based on proximity and orientation to identify myofibrils within the image. The orientation of all identified myofibrils within a field of view was fit to a Gaussian distribution. Sarcomere alignment deviation was defined at the standard deviation of this distribution using circular/angular statistics. Myofibril density was calculated by determining the percent area of each tissue containing titin-rich myofibril structures.

Vinculin and N-cadherin morphology and colocalization analysis was also performed using custom Matlab scripts. Because of the 3D nature of these tissues due to the intercalation of iPSC-CMs into matrix pores, confocal z-stacks of fibroTUG tissues formed with iPSC-CMs containing a GFP-titin live-reporter and immunostained for vinculin and N-cadherin were segmented in 3D for vinculin-, N-cadherin-, and titin-enriched structures. Custom Matlab functions were implemented to extract volume, eccentricity, and other parameters for these structures. Where applicable, quantifications were normalized to cell number in each field of view.

6.6.11 Statistical analysis

Statistical significance was determined by t-tests and one-way or two-way analysis of variance (ANOVA) with post-hoc analysis (Tukey test), where appropriate, with significance indicated by $p < 0.05$. Studies were conducted a minimum of 3 times in each experiment. The data presented are representative data sets from one of these replicate studies. Specific sample size is indicated within corresponding figure legends and all data are presented as mean ± standard deviation.

6.7 Supplementary Figures

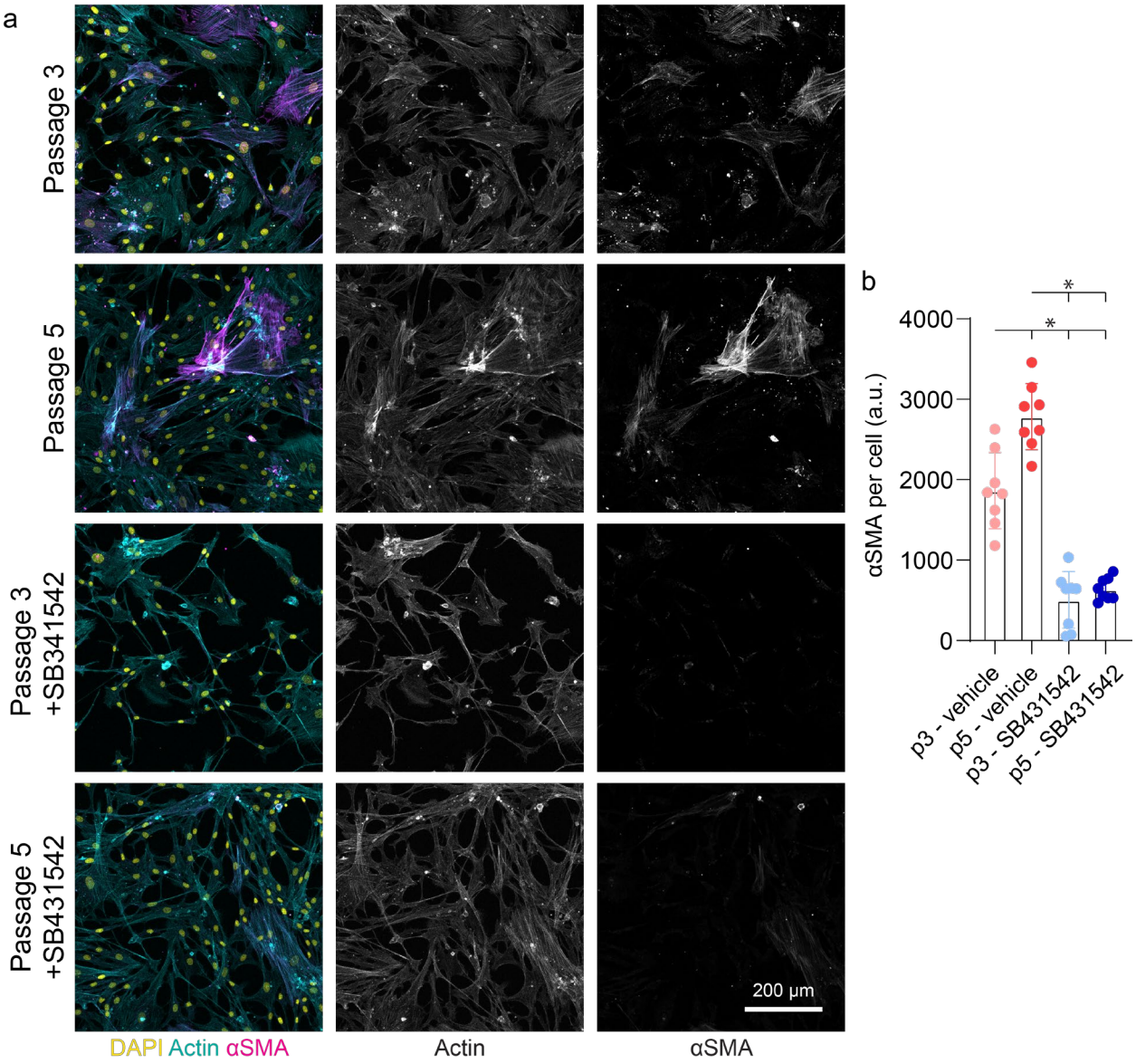

Supplementary Figure 6.1: Cardiac fibroblasts differentiation to MFs when expanded on tissue culture plastic. (**a**) Confocal fluorescent images of cardiac fibroblasts (NHCF1) on tissue culture plastic. Samples that were treated with 10 µm SB431542 were always expanded in the inhibitor starting at passage 1. (**b**) Quantification of αSMA per cell. ($n \geq 10$ regions from separate wells in the microfabricated substrate). All data presented as mean ± std; * $p < 0.05$.

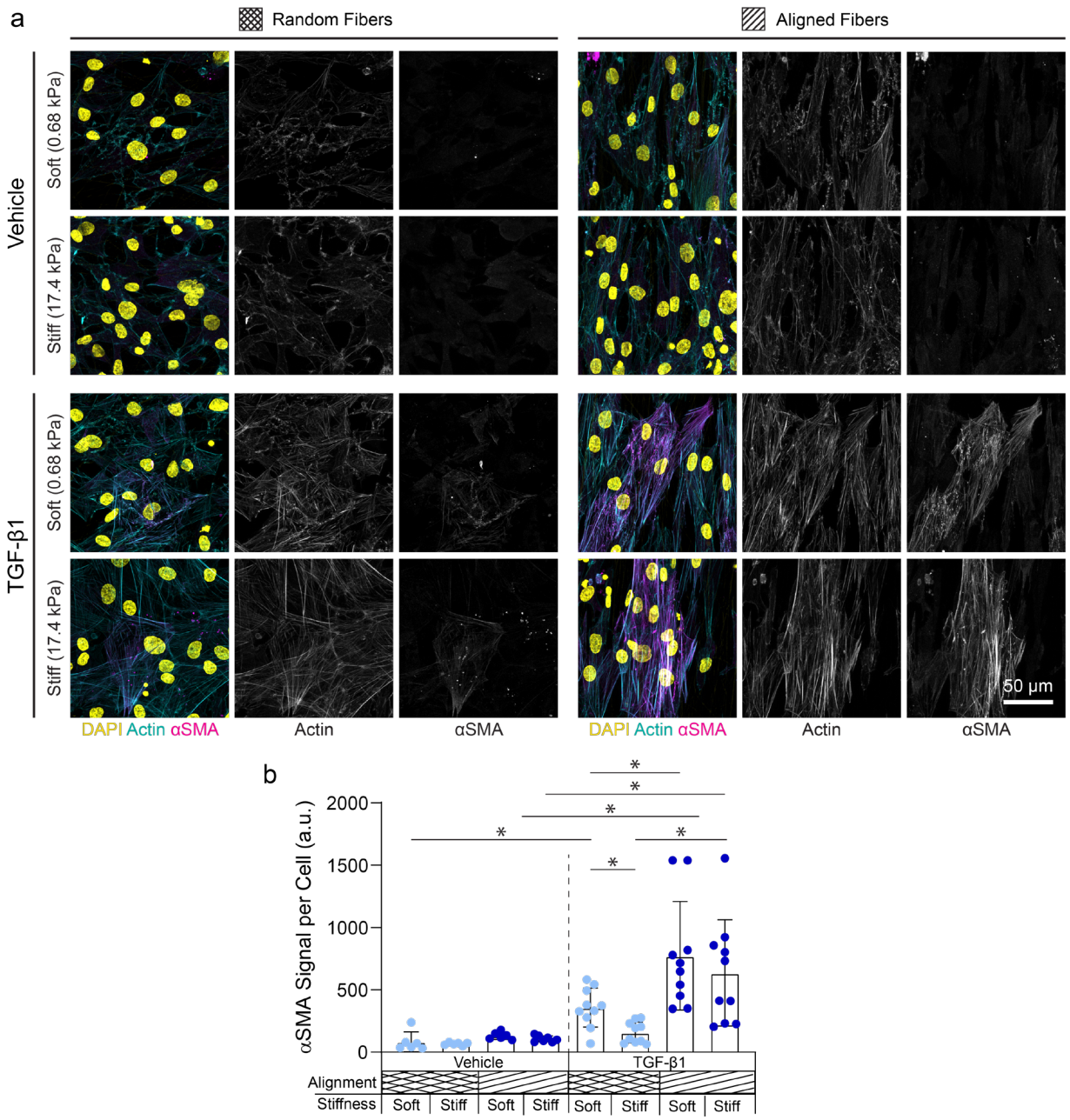

Supplementary Figure 6.2: Aligned fibers drive robust differentiation of primary human cardiac fibroblasts from a second donor in the presence of TGF-β1. (**a**) Confocal fluorescent images of primary cardiac fibroblasts (NHCF3) cultured on fiber matrices of varying stiffness and alignment immuostained for αSMA. (**b**) Quantification of αSMA expression per cell. ($n \geq 10$ regions from separate wells in the microfabricated substrate). All data presented as mean ± std; * $p < 0.05$.

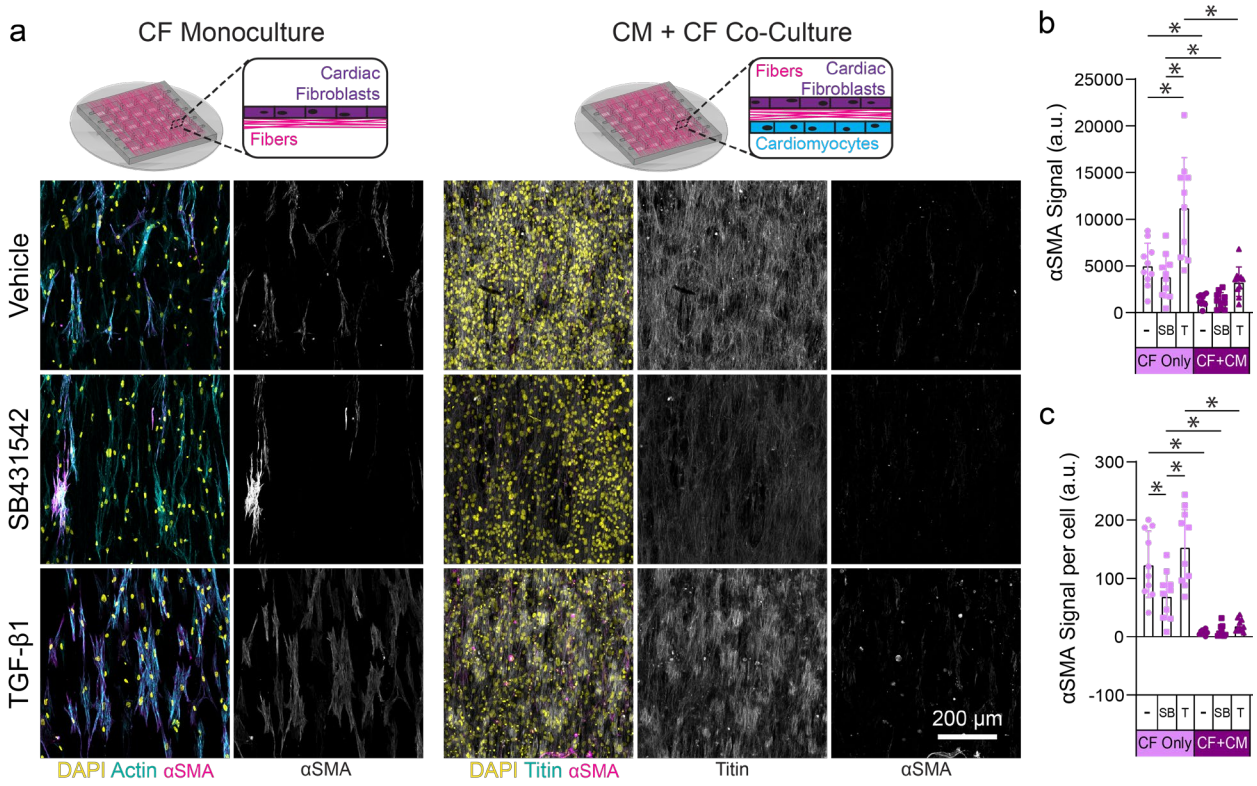

Supplementary Figure 6.3: iPSC-CMs mitigate CF differentiation to MF when cultured on a shared soft, aligned fibrous matrix, regardless of what cell type is on top of the matrix. (**a**) Schematics of microfabricated bilayer fibrous tissue arrays indicating that CMs (PGP1) were seeded on the bottom of the fiber matrices with fibroblasts (NHCF1) seeded on top. Confocal fluorescent images of primary cardiac fibroblasts (NHCF1) cultured on the top of the fiber matrices alone or with iPSC-CMs (PGP1) on bottom. (**b**) Quantification of total αSMA expression. (**c**) Quantification of total αSMA expression per cell. $n \geq 10$. All data presented as mean ± std; * $p < 0.05$.

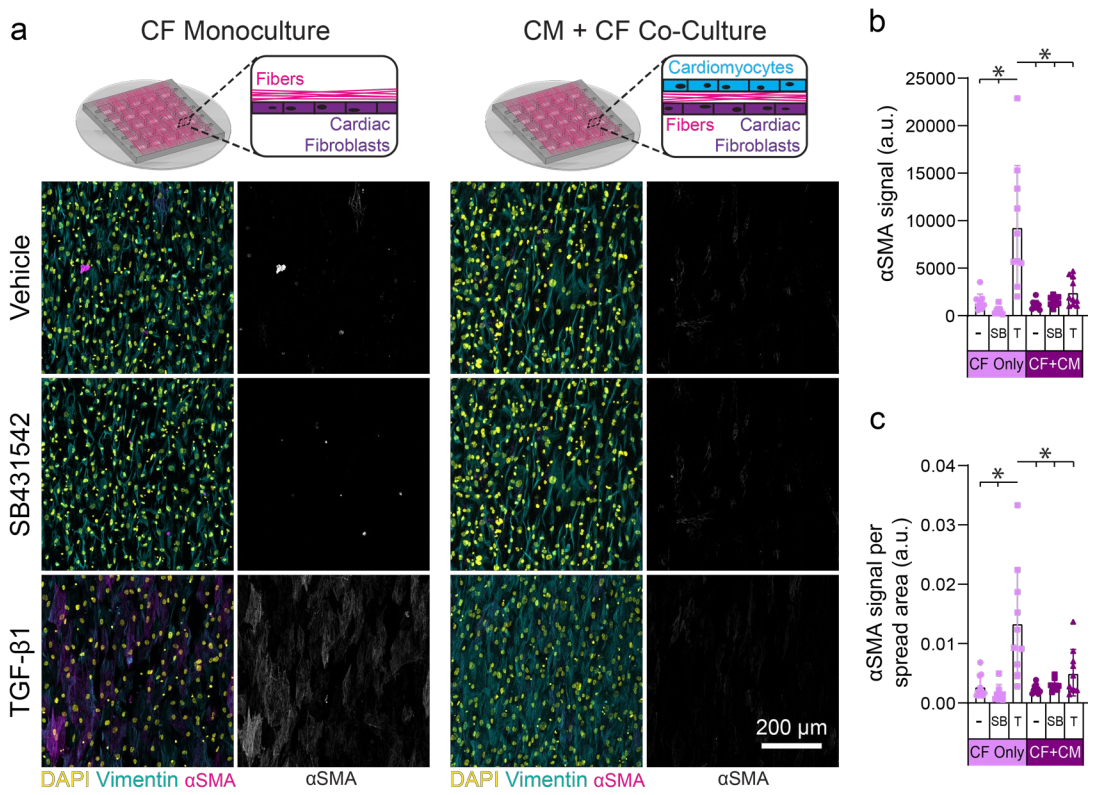

Supplementary Figure 6.4: iPSC-CMs mitigate CF differentiation to MF when cultured on a shared soft, aligned fibrous matrix, regardless of what cell type is on top of the matrix. (**a**) Schematics of microfabricated bilayer fibrous tissue arrays indicating that CMs (WTC11) were seeded on the top of the fiber matrices with fibroblasts (NHCF3) seeded on the bottom. Confocal fluorescent images of all tissues stained for αSMA. (**b**) Quantification of total αSMA expression. (**c**) Quantification of total αSMA expression per spread area. $n \geq 10$. All data presented as mean ± std; * $p < 0.05$.

Chapter 7: Summary and Future Directions

7.1 Summary

Overall, this thesis aimed to design cardiac microtissue platforms composed of extracellular matrix (ECM) mimetic synthetic biomaterials to investigate the role of mechanical signaling in cardiomyocyte (CM) maturation and cardiac disease. Chapter 2 provided background on the structure and function of the myocardial ECM and how the dynamic biophysical properties of the ECM facilitate cardiac development and fibrotic disease progression. Additionally, Chapter 2 summarized current biomaterial platforms used to model the cardiac ECM and known mechanosensing mechanisms involved in myofibril assembly processes, tissue regeneration, and pathogenesis. Specifically, this thesis integrated synthetic biomaterials composed of electrospun fibrous matrices with microfabrication techniques to develop several cardiac microtissue platforms of varying complexity to recapitulate various tissue states. These platforms, combined with stem cell biology, confocal microscopy, and image analysis techniques, enabled the study of how mechanical and biological microenvironmental cues drive myocardial function.

Chapter 3 examined the state of the field of cardiac tissue engineering and the current platforms used to model the cardiac ECM in greater detail by conducting a comprehensive quantitative review of > 300 manuscripts that implemented induced pluripotent stem cell-derived CMs (iPSC-CMs) (J. Ewoldt, S.J. DePalma et al. 2023). Chapter 4 explored how changing mechanical properties of synthetic fiber networks influence iPSC-CM tissue assembly and functionality (DePalma et al. 2021). Chapter 5 worked towards advancing the mechanical

tunability of these electrospun fibrous scaffolds, by employing microfabrication techniques to create arrays of suspended cardiac microtissues with real-time contractile force readouts (DePalma et al. 2023). Here, we also build upon the results in Chapter 4 to define a set of mechanical inputs that drive the most robust tissue assembly, function, and maturation. Lastly, Chapter 6 focused on incorporating cardiac fibroblasts (CFs) into these fibrous biomaterial platforms to investigate how communication between CFs and CMs is altered by various biophysical cues to maintain tissue homeostasis and propagate fibrotic feedback loops. Overall, studies utilizing these platforms have improved understanding of the mechanobiological drivers of myocardial function and provided new insights towards the design of engineered heart tissues for disease modeling, drug screening, and regenerative therapies.

7.2 Limitations and Future Directions

7.2.1 Towards a deeper understanding of cardiomyocyte mechanobiology

Continuing to advance our understanding of how cells in the heart sense and respond to dynamic mechanical changes that occur throughout tissue development and disease will require integration of multidisciplinary characterization techniques to probe complex mechanosensing pathways. Starting at the cell-scale, implementing Förster resonance energy transfer (FRET)-based molecular tension sensors could provide key insights into mechanotransduction by enabling measurement of tensions across various cytoskeletal proteins. This technique has been implemented most extensively for the cell adhesion protein vinculin, a protein that plays a critical role in CM mechanosensing (Grashoff et al. 2010). Additionally, FRET-tension sensors have been developed to quantify tension across desmoplakin in pathological mechanical conditions (Price et

al. 2018). Combining these approaches with our mechanically tunable fibrous scaffolds and live-cell imaging could enhance our understanding of how mechanical signals are transmitted throughout the cell as myofibrils assemble and mature. Further, implementation of these molecular tension probes could elucidate mechanisms by which CMs adapt to aberrant mechanical changes in the cardiac microenvironment that in various cardiomyopathies.

In combination with molecular tension sensors, high throughput imaging protocols could be implemented to begin to understand the relationships between a greater number of the many mechanosensitive proteins involved in cardiac tissue development and disease. Several cell-ECM and cell-cell junction proteins, in addition to various myofibril proteins, have been connected to various forms of cardiomyopathy because of the important role that they play in generating and transmitting forces throughout the myocardium (Jordan et al. 2021; Maron and Maron 2013; Walsh et al. 2021). By adapting previously developed iterative immunostaining protocols with high-dimensional data analysis techniques, we can take advantage of our ability to easily image and assess the structural organization of our fibrous cardiac microtissues (Freeburne et al. 2023; Gut, Herrmann, and Pelkmans 2018). Machine learning techniques could also be applied to begin to correlate tissue scale functional metrics such as tissue contractile force with the expression and organization of specific proteins (Schmitt et al. 2024; Tao et al. 2023). Overall, the continued implementation and development of new techniques for analyzing *in vitro* cardiac models, such as the ones presented in this thesis and throughout the literature, will be essential to uncovering additional important mechnosensing processes in the heart.

7.2.2 Improving tissue maturity for improved disease modeling and drug screening

A limitation of the work presented here that is persistent in other engineered heart tissue models as well is the immaturity of iPSC-CMs used to generate these tissues (Karbassi et al. 2020).

As described in Chapter 3 of this thesis, iPSC-CMs more closely mimic fetal CMs than adult CMs in both their structural and functional phenotypes, which can limit their utility in modeling cardiac diseases and drugs screening applications. The work presented in Chapter 4 and Chapter 5 defined key mechanical parameters that can facilitate the maturation of iPSC-CM tissues. While these mechanical inputs alone do in fact support the formation of tissues that are of similar functionality to other tissues generated in the field (DePalma et al. 2023; J. Ewoldt et al. 2023), there is still a significant gap in maturity between these tissues and the adult myocardium (Karbassi et al. 2020).

Therefore, it is necessary to explore how other maturation techniques can complement the mechanical maturation techniques explored in this thesis to generate adult-like cardiac tissues *in vitro*. Combining other maturation techniques with mechanically tunable platforms that do not require the addition of support cells besides iPSC-CMs could also enable careful dissection of the mechanism by which each maturation technique is generating more mature tissues. More specifically, electrical pacing, mechanical actuation, and metabolic reprogramming have been shown to drive iPSC-CM maturation and could be easily implemented into most established engineered heart tissue systems, including the platforms presented here (Correia et al. 2017; Ronaldson-Bouchard et al. 2018; Ruan et al. 2016). Additionally, exploring iPSC-CM interactions with other cell types such as fibroblasts and endothelial cells will also be important for generating more complex cardiac models (Beauchamp et al. 2020; Giacomelli et al. 2020).

However, it remains an open question as to how mature is mature enough for many disease modeling and drug toxicity testing applications. In many cases, more complex engineered heart tissue models result in more mature tissues, while simultaneously sacrificing throughput (**Figure 2.3**) (Cho et al. 2022). For *in vitro* engineered heart tissue models to be broadly applicable in this context, they will need to be able to screen many conditions simultaneously which will require the

design of simpler, highly reproducible platforms that are mature enough recapitulate specific phenotypes of interest. Many studies have suggested that specific types of maturation may be necessary to model certain diseases or responses to drugs; mechanical maturation may be necessary when modeling cardiomyopathies caused by cell-cell junction proteins while metabolic maturation may be necessary when testing the toxicity of drugs that interact with various ion channels (Bliley et al. 2021; Correia et al. 2017). As such, tunable model systems that can be adapted depending on the question being explored at a given time will be extremely valuable as the translational applications of these models continues to expand. Additionally, platforms like the ones presented in this thesis that enable real-time functional readouts of tissue structure and function will be critical to optimizing and improving the platforms for such applications.

7.2.3 Scaling-up to generate 3D engineered regenerative therapies

In addition to generating *in vitro* models for studying tissue development and disease, iPSC-CMs show great promise as regenerative therapies to restore functionality of damaged myocardium. However, simply injecting singularized iPSC-CMs or aggregates of immature iPSC-CMs can result in arrythmias due to inefficient integration of the new iPSC-CMs with the host tissue (Liu et al. 2018). This suggests the need for engineered scaffolding that can facilitate proper maturation of the tissue before implantation and provide structural support once implanted (Tzahor and Poss 2017). As such, mechanically tunable scaffolds should continue to be leveraged to explore the specific mechanical parameters required to generate highly functional cardiac syncytia. However, the 2.5D fibrous scaffolds described throughout this thesis are limited in their ability to be directly scaled up to a functional cardiac patch because of their thin structure. The development of 3D material systems with similar levels of mechanical control will therefore be necessary to successfully generate functional engineered cardiac tissue patches (Jianyi Zhang et al. 2018).

Furthermore, understanding how other cell types such as fibroblasts and endothelial cells interact with CMs in these complex environments will be critical to ensuring proper integration and survival of the engineered therapy upon implantation (Giacomelli et al. 2020). Overall, the continued advancement of tunable engineered heart tissue platforms will provide fundamental insights necessary for the intelligent design of next generation engineered tissue constructs for drug screening, disease modeling, and regenerative medicine applications.

Appendix A: MATLAB Scripts

Sarcomere Alignment Quantification

```
function [sarcCount, avgSarcArea, sd, maxAngle,
avgSarcSpace,sarcGroup,sarcGroupNew,sarcGroupMask,sarcAngCent,sarcContent,sarcInt,gro
upMaskAngle] =
sarcomere_v12(sarcFilename,nucFilename,fiberFilename,root,pathname,dirOut,imgCount)

cd(pathname)

%% HARDCODED VARIABLES
minSarcArea = 15; %pixels
maxSarcArea = 1000; %pixels
clusterSens = 8; % 4 or 8 connectivity
backSize = 50;

pixelDim = 0.195; %microns/pixel
sarcDistMax = 2.5; %microns. Guess how far each z-disc is to each other.
sarcAreaGuess = 40; %pixels. To estimate number of sarcomeres per group in code.
searchDist = 2.5; %microns. How far to search for next sarcomere.



%% SAROMERE IMAGE PROCESSING

% parse file
sarcScale = [14000 50000];
nucScale = [5000 60000];
fiberScale = [0 20000]; %sarcScale;
sarcImg = double(mat2gray(squeeze(imread(sarcFilename)), sarcScale));
nucImg = double(mat2gray(squeeze(imread(nucFilename)), nucScale));
fiberImg = double(mat2gray(squeeze(imread(fiberFilename)), fiberScale));
sarcImgNoFilt = sarcImg; %(:,:,2); %Save unfilter image for finding background.

% Creating tissue mask of sarcomeres, nuclei, and fibers...

tissueImage = sarcImg + nucImg + fiberImg;


% Selecting a tolerance for thresholding ... seemed to work well ...
    TOL = max(max(tissueImage)) * 0.01;  %0.1

    % Create a mask ...
    m = (tissueImage > TOL);
```

```
    % Cap the ends and fill in the holes ...
    m(1,:) = 1; m(end,:) = 1;

    % Define the micro-tissue region ...
    bk = imfill(m,'holes');
    bk = imfill(bk,'holes');

    % Making sure we select the largest singular region as the background ...
    cc = bwconncomp(bk);
    for i = 1:cc.NumObjects
        pixnum(i) = length(cc.PixelIdxList{i});
    end
    mxpix = find(pixnum == max(pixnum));
    bk(:,:) = 0;
    bk(cc.PixelIdxList{mxpix}) = 1;

    % Focus only on areas in the defined tissue region (ignoring scattered
    % pixels) ...
    m = m .* bk;


% image cleanup
backH = fspecial('gaussian',backSize,backSize/3);
background = imfilter(sarcImg,backH,'symmetric');
sarcImg = sarcImg - background;
sarcImg(sarcImg<0) = 0;
sarcImg = sarcImg .* bk;

% [sarcGradMag,sarcGradDir] = imgradient(sarcImg);
figure(1)
imshow(sarcImg); pause(0.5);

sarcInt = sum(sum(sarcImg));

% initial guess for threshold
threshVal = 0.1;

% initializations
button = 1;
peakLocMat = [];
circCount = 1;


% Threshold image
% continue to whileloop until user hits enter (which makes button empty)
while isempty(button) ~= 1
    % clear nucCount here so that a value is always stored at the end of
    % the loop
    sarcCount = 1;

    % filter cell img to get rid of stuff that's too small to be a cell
    sarcMask = im2bw(sarcImg,threshVal); %%%sarcImg
%     sarcMask = imfill(sarcMask,'holes');
    [clusterLabel,totalLabels] = bwlabel(sarcMask,clusterSens);
```

```
    allStats =
regionprops(clusterLabel,'Area','PixelIdxList','PixelList','Centroid','Orientation','
Eccentricity');
    centroid = [];
    orient = [];
    ecc = [];
    pixelSize = [];
    for i=1:totalLabels

        if allStats(i,1).Area < minSarcArea || allStats(i,1).Area > maxSarcArea ||
allStats(i,1).Eccentricity < 0.8 %|| minRefValue > 10
            sarcMask(allStats(i,1).PixelIdxList)=0;
        else
            centroid(i,:) = allStats(i,1).Centroid; % if they're the right size,
record their centroid and increment sarcCount
            pixelSize(sarcCount) = allStats(i,1).Area;
            orient(i,:) = allStats(i,1).Orientation;
            ecc(i,:) = allStats(i,1).Eccentricity;
            pixList{i} = allStats(i,1).PixelList; %structure containing all pixels of
each z-disc
            sarcCount = sarcCount + 1;
        end
    end


    if sarcCount == 0
        avgSarcArea = 0;
    else
        pixelSizeMod = pixelSize(pixelSize~=0);
        avgSarcArea = mean(pixelSizeMod);
    end

    % generate a composite mask and display on the right
    figure(1)
    set(gcf, 'Units', 'Normalized', 'OuterPosition', [0 0 1 1]);
    impanel(sarcImg,sarcMask);

    % display number of counts
    title(num2str(sarcCount));

    % switch on click (can't use actual switch because of breakout)
    [x,y,button] = ginput(1);

    % arrow keys to adjust threshold value
    if button == 30 % up arrow
        threshVal = threshVal + .01;
    end
    if button == 31 % down arrow
        threshVal = threshVal - .01;
        if threshVal  <= 0
            threshVal = 0.01;
        end
    end
    if button == 28 % left arrow
        threshVal = threshVal - .05;
```

```
        if threshVal  <= 0
            threshVal = 0.01;
        end
    end
    if button == 29 % right arrow
        threshVal = threshVal + .05;
    end
    % need to clear cluster stats so no residual data
    clear clusterLabel pixelSize


end
close


%% Group z-discs into sarcomeres

sarcGroupNum = 1;
badCentroid = centroid;
[yPix,xPix] = size(sarcMask);
groupMask = zeros(size(sarcMask));
groupColor = jet(30);
for sarcLoop = 1:length(badCentroid)
    plusStop = 0;
    negStop = 0;
    whileCount = 0;
    whileCountNeg = 0;
    firstCentroid = badCentroid(sarcLoop,:);
    firstOrient = orient(sarcLoop)+90;

    % Find z-discs in "plus" direction
    while plusStop == 0
        if whileCount == 0
            currCentroid = firstCentroid;
            currOrient = firstOrient;
        else
        end

        if currCentroid(1,1) == 0 && currCentroid(1,2) == 0
            plusStop = 1;
        else
            % Add first centroid to the group
            if whileCount == 0
                whileCount = whileCount+1;
                sarcGroup{sarcGroupNum}(whileCount,:) = allStats(sarcLoop);
                groupMask(allStats(sarcLoop,1).PixelIdxList) = 1;
            end

            cosOrient = cosd(currOrient);
            sinOrient = sind(currOrient);
            xcoords = ceil(currCentroid(1,1) + searchDist/pixelDim * [cosOrient -
cosOrient]);
            ycoords = ceil(currCentroid(1,2) + searchDist/pixelDim * [-sinOrient
sinOrient]);
```

```
            distVecRefPlus = sqrt((badCentroid(:,1)-xcoords(1)).^2 +
((badCentroid(:,2)-ycoords(1)).^2));
            [minPlus, indexPlus] = min(nonzeros(distVecRefPlus));

            if minPlus < sarcDistMax/pixelDim && minPlus > 0.005/pixelDim &&
xcoords(1)>=0 && ycoords(1)>=0

                if allStats(indexPlus).Eccentricity ==
sarcGroup{sarcGroupNum}(whileCount,:).Eccentricity
                    groupMask(allStats(indexPlus,1).PixelIdxList) = 1;
                    badCentroid(badCentroid==currCentroid(1,1)) = 0; %Remove current
centroid from the list of centroids so it doesn't find it again
                    badCentroid(badCentroid==currCentroid(1,2)) = 0;
                    currCentroid = badCentroid(indexPlus,:);
                    currOrient = orient(indexPlus)+90;
                else
                    whileCount = whileCount+1;
                    sarcGroup{sarcGroupNum}(whileCount,:) = allStats(indexPlus);
                    groupMask(allStats(indexPlus,1).PixelIdxList) = 1;
                    badCentroid(badCentroid==currCentroid(1,1)) = 0; %Remove current
centroid from the list of centroids so it doesn't find it again
                    badCentroid(badCentroid==currCentroid(1,2)) = 0;
                    currCentroid = badCentroid(indexPlus,:);
                    currOrient = orient(indexPlus)+90;
                end

            elseif minPlus > sarcDistMax/pixelDim || minPlus < 0.005/pixelDim
                plusStop = 1;
            else
                plusStop = 1;
            end

        end
    end

    % Find z-discs in "negative" direction
    while negStop == 0
        if whileCountNeg == 0
            currCentroid = firstCentroid;
            currOrient = firstOrient;
        else
        end

        if currCentroid(1,1) == 0 && currCentroid(1,2) == 0
            negStop = 1;
        else

            cosOrient = cosd(currOrient);
            sinOrient = sind(currOrient);
            xcoords = ceil(currCentroid(1,1) + searchDist/pixelDim * [cosOrient -
cosOrient]);
            ycoords = ceil(currCentroid(1,2) + searchDist/pixelDim * [-sinOrient
sinOrient]);
```

```
            distVecRefNeg = sqrt((badCentroid(:,1)-xcoords(2)).^2 +
((badCentroid(:,2)-ycoords(2)).^2));
            [minNeg, indexNeg] = min(nonzeros(distVecRefNeg));

            if minNeg < sarcDistMax/pixelDim && minNeg > 0.005/pixelDim &&
xcoords(2)>=0 && ycoords(2)>=0
                if allStats(indexNeg).Eccentricity ==
sarcGroup{sarcGroupNum}(whileCount+whileCountNeg,:).Eccentricity
                    groupMask(allStats(indexNeg,1).PixelIdxList) = 1;
                    badCentroid(badCentroid==currCentroid(1,1)) = 0; %Remove current
centroid from the list of centroids so it doesn't find it again
                    badCentroid(badCentroid==currCentroid(1,2)) = 0;
                    currCentroid = badCentroid(indexNeg,:);
                    currOrient = orient(indexNeg)+90;
                else
                    whileCountNeg = whileCountNeg+1;
                    sarcGroup{sarcGroupNum}(whileCount+whileCountNeg,:) =
allStats(indexNeg);
                    groupMask(allStats(indexNeg,1).PixelIdxList) = 1;
                    badCentroid(badCentroid==currCentroid(1,1)) = 0; %Remove current
centroid from the list of centroids so it doesn't find it again
                    badCentroid(badCentroid==currCentroid(1,2)) = 0;
                    currCentroid = badCentroid(indexNeg,:);
                    currOrient = orient(indexNeg)+90;
                end
            elseif minNeg > sarcDistMax/pixelDim || minNeg < 0.005/pixelDim
                negStop = 1;
            else
                negStop = 1;
            end
        end
    end

    if currCentroid(1,2) == 0 && currCentroid(1,1) == 0 %&& currCentroidNeg(1,1) == 0
&& currCentroidNeg(1,2) == 0

    else
        sarcGroupNum = sarcGroupNum + 1;
    end
end



%% Remove groups with only 1 z-disc

newGroupCount = 1;
for ii = 1:length(sarcGroup)
    if length(sarcGroup{ii}) > 2
        sarcGroupNew(newGroupCount) = sarcGroup(ii); %Combo
        newGroupCount = newGroupCount+1;
    else
    end
end
```

```
%% Make new mask for each group
[r,c] = size(sarcMask);
sarcGroupMaskAllX = zeros(r,c);
sarcGroupMaskAllY = zeros(r,c);
sarcGroupMaskAllZ = zeros(r,c);
sarcGroupMask = zeros(r,c,length(sarcGroupNew));

groupColor = colormap(lines(20));

for jj = 1:length(sarcGroupNew)
    sarcGroupMaskCurr = zeros(r,c);
    random = randi([1,20]);
    for kk = 1:length(sarcGroupNew{jj})
        sarcGroupMaskCurr(sarcGroupNew{jj}(kk,1).PixelIdxList) = 1;
        sarcGroupMaskAllX(sarcGroupNew{jj}(kk,1).PixelIdxList) =
groupColor(random,1);
        sarcGroupMaskAllY(sarcGroupNew{jj}(kk,1).PixelIdxList) =
groupColor(random,2);
        sarcGroupMaskAllZ(sarcGroupNew{jj}(kk,1).PixelIdxList) =
groupColor(random,3);
    end
    sarcGroupMask(:,:,jj) = sarcGroupMaskCurr;
end
sarcGroupMaskAll = cat(3,sarcGroupMaskAllX,sarcGroupMaskAllY,sarcGroupMaskAllZ);


figure(1)
imshow(sarcGroupMaskAll)

figure(2)
imshow(sarcMask)


%% Manually select/delete/combine/separate groups

% initializations
button = 1;
update = 1;
cellCount = 0;
finalMask = zeros(r,c);
xlsOut=zeros(1,9);
groupMaskAngle = zeros(r,c);
groupMaskRand = zeros(r,c);

% continue to whileloop until user hits enter (which makes button empty)
while isempty(button) ~= 1
    if update == 1
        clear groupProps groupCentroid groupOrient
        groupMaskAngle = zeros(r,c);
        groupMaskRand = zeros(r,c);
        sarcMaskFinal = zeros(r,c);

%%%%%%%%%%%%%%%%%%%%%%%%%%%%%%%%%%%%%%%%%%%%%%%%%%%%%%%%%%%%%%%%%%%%%%%%%%%%%%%
        % Take orientation of each group
```

```
        [~,~,groupNum] = size(sarcGroupMask);

        for xx = 1:groupNum %length(sarcGroupNew)
            groupProps(xx) =
regionprops(sarcGroupMask(:,:,xx),'Area','BoundingBox','Orientation','Centroid','Pixe
lIdxList','SubarrayIdx');
            groupOrient(xx,:) = groupProps(xx).Orientation;
            groupArea(xx,:) = groupProps(xx).Area;
            groupCentroid(xx,:) = groupProps(xx).Centroid;
            thisOrient = abs(ceil(groupOrient(xx)));
            groupMaskAngle(groupProps(xx).PixelIdxList) = thisOrient;
            groupMaskAnglePosAndNeg(groupProps(xx).PixelIdxList) = groupOrient(xx,:);
            groupMaskRand(groupProps(xx).PixelIdxList) = randi([1,20]);
            sarcMaskFinal(groupProps(xx).PixelIdxList) = 1; %for masking image later
to quantify total sarcomere content
        end
        groupColor = colormap(autumn(20));
        groupMaskRandColor = label2rgb(groupMaskRand,groupColor,'k');
        groupColorAngle = colormap(jet(90));
        groupMaskAngleColor = label2rgb(groupMaskAngle,groupColorAngle,'k');


%%%%%%%%%%%%%%%%%%%%%%%%%%%%%%%%%%%%%%%%%%%%%%%%%%%%%%%%%%%%%%%%%%%%%%%%%%%%%%%
        % Plot groups with orientation on them

        sarcAngle = groupOrient;
        sarcAngleVals = nonzeros(sarcAngle);
        meanSarcAngle = circ_mean(sarcAngle);

        L = 15; %length of lines to be plotted


        figure(3)
        set(gcf, 'Units', 'Normalized', 'OuterPosition', [0 0 1 1]);
        %imshow(zeros(size(sarcMask)))
        imshow(groupMaskRandColor)
        hold on
        plotColor = colormap(cool(100));
        % colormap jet
        % colorbar
        lineCount = 1;
        for sarcNum = 1:length(sarcAngle)
            if groupCentroid(sarcNum,1) == 0 && groupCentroid(sarcNum,2) == 0

            else
                lineCenter2 = groupCentroid(sarcNum,:);

                alpha = sarcAngle(sarcNum);
                alphaDiff = abs(alpha-meanSarcAngle);
                alphaDiffVec(sarcNum) = alphaDiff;
                alphaRound = ceil(alphaDiff);

                x1=abs(lineCenter2(1,1)-(L*cosd(alpha)));
                y1=abs(lineCenter2(1,2)+(L*sind(alpha)));
                x2=abs(lineCenter2(1,1)+(L*cosd(alpha)));
```

```
                y2=abs(lineCenter2(1,2)-(L*sind(alpha))); %These values are only used
for plotting
                                                          %abs is intended to
eliminate negatives that mess up plotting
                alphaColor = alphaRound;
                alphaVec(sarcNum) = alphaRound;
                plot([x1,x2],[y1,y2],'color',plotColor(alphaColor,:,:))

                lineCount = lineCount+1;
            end
        end
    end
%%%%%%%%%%%%%%%%%%%%%%%%%%%%%%%%%%%%%%%%%%%%%%%%%%%%%%%%%%%%%%%%%%%%%%%%%%%%
    % to avoid cluster filtering everytime a cell is extracted:

        [xButton,yButton,button] = ginputc(1,'Color','w','LineStyle',':');

        % Delete unwanted groups
        if button == 3 %right click
            [value,index] = min(sqrt((groupCentroid(:,1)-
xButton).^2+(groupCentroid(:,2)-yButton).^2));
            sarcGroupMask(:,:,index) = []; %remove from current mask

            update = 1;
        end

        % Combine nearby groups
        if button == 1 %left click
            [value1,index1] = mink(sqrt((groupCentroid(:,1)-
xButton).^2+(groupCentroid(:,2)-yButton).^2),2);
            sarcGroupMask(:,:,index1(1)) = sarcGroupMask(:,:,index1(1)) +
sarcGroupMask(:,:,index1(2));
            mat = sarcGroupMask(:,:,index1(1));
            mat(mat==2) = 1; %account for potentially overlapping pixels
            sarcGroupMask(:,:,index1(1)) = mat;
            sarcGroupMask(:,:,index1(2)) = [];

            update = 1;
        end

        if button == 2 %center click


            update = 1;
        end

end

sarcAlignFig = figure(4);
imshow(groupMaskAngleColor)


%% Plot histograms of angles

figure(8)
```

```
circ_plot(sarcAngle)
% figure(9)
% CircHist(sarcAngle,45)

%Normalize area of each group to approx area of each sarc.
allAngles = [];
for gg = 1:length(sarcAngle)
    currAngleVec = [];
    currAngle = sarcAngle(gg);
    currArea = groupArea(gg);
    currNumSarc = ceil(currArea/sarcAreaGuess);
    currAngleVec(1:currNumSarc) = currAngle;
    allAngles = horzcat(allAngles,currAngleVec); %Create vector of angles for each z-
disc
end

allAngles = allAngles'; %make column vector for histfit later

binNum = 45;
sarcAngleVals = allAngles; %(allAngles~=0);
sarcAng90 = sarcAngleVals+90;
figure(5)
angHist = histogram(sarcAng90,binNum);

meanAngle = circ_mean(sarcAngleVals);
maxAngle = find(max(angHist.Values)==angHist.Values)*180/binNum;


sarcAngCent = sarcAng90-maxAngle(1); %Index only first element in case there are two
max angles
for centCount = 1:length(sarcAngCent)
    if sarcAngCent(centCount) < -90
        sarcAngCent(centCount) = sarcAngCent(centCount)+180;
    elseif sarcAngCent(centCount) > 90
        sarcAngCent(centCount) = sarcAngCent(centCount)-180;
    end
end

sarcHist = figure(6);
histogram(sarcAngCent,binNum)
xlim([-95 95])
xlabel('Sarcomere angle from mean orientation (degrees)')
ylabel('Number of sarcomeres')
hold on
histfit(sarcAngCent,binNum,'normal')
hold off
angHistFit = fitdist(sarcAngCent,'normal');
sd = angHistFit.sigma;


%% Find the average distance between z-discs
sarcDist = [];
sarcDistNum = 1;

for sarcNum2 = 1:length(centroid)
```

```
    if centroid(sarcNum2,1) == 0 && centroid(sarcNum2,2) == 0

    else
        sarcCent = centroid(sarcNum2,:);
        distVec = sqrt((centroid(:,1)-sarcCent(1,1)).^2 + ((centroid(:,2)-
sarcCent(1,2)).^2));
        distVec(distVec == 0) = inf;
        [value,index] = min(distVec);

        angDiff = abs(orient(sarcNum2)-orient(index));

        if angDiff <= 5 && value*pixelDim >= 1 && value*pixelDim <= 3
            sarcDist(sarcDistNum) = value;
            sarcDistNum = sarcDistNum + 1;
        end

    end
end

    sarcSpace = sarcDist.*pixelDim;
    avgSarcSpace = mean(sarcSpace);


%% Calculate total sarcomere content
% Mask original sarcomere image with the sarcomere mask generated(sarcMaskFinal)

maskedSarcImage = sarcImg .* sarcMaskFinal;
sarcContentFluor = sum(sum(maskedSarcImage));

% New SarcContent Calculation
% Sum the area of the original image mask (sarcMask) ignoring fluor int
sarcContent = sum(sum(sarcMask));



%% image output
cd(dirOut);
imwrite(sarcMask,strcat(root(1:end),num2str(imgCount),'_threshSarcImg.tif'),'TIFF')
imwrite(sarcGroupMaskAll,strcat(root(1:end),num2str(imgCount),'_sarcGroupImg.tif'),'T
IFF')
print(sarcAlignFig,strcat(root(1:end),num2str(imgCount),'_sarcAngleImg.png'),'-dpng')
%-dmeta for .emf
print(sarcHist,strcat(root(1:end),num2str(imgCount),'_sarcHist.png'),'-dpng')
%saveas(sarcMapFig,strcat(root,num2str(imgCount),'sarcMap.png'))

save(strcat(root(1:end),num2str(imgCount),'workspace.mat'))



end
```

Cardiomyocyte Calcium Transient Analysis

```
%% ========================================================================
% CalciumImaging_v16


%% ========================================================================
% WORKSPACE INITIALIZATION

close all;
clear all;

%% ========================================================================
% DIRECTORY INITIALIZATION

% EXPORT FILES AS .MAT %

% Specify image directory.
% Set of files should be stored in one folder.
% All file names should have the same # of characters.
[filename, pathname, filterIndex] = uigetfile('*.*', 'Open Image');
cd(pathname);
direct=dir;              % Initialize current directory
% create output directery
dirOut = 'calciumQuant';
mkdir(dirOut);

%% Hard coded variables
pixelSize = 0.908;  %micron/pixel
                    % Axiocam 503 Parameters at 10x:
                    % 1x1 = 0.454
                    % 2x2 = 0.908
                    % 3x3 = 1.362
                    % 4x4 = 1.816
                    % 4x4 @ 40x = 0.709
subAreaDim = 10;    % Num of regions the ROI is broken into for contraction
                    % correlation coefficient.
rotateAngle = -50; %Rotate image to enable more accurate tissue selection.
frameRate = 65.28; %frames per second
videoThresh = [150 1000];

%% ========================================================================
% Save File Info Initiation
saveFileName = 'Calcium Imaging Data.xls';
bpmT = [];
bpmstdT = [];
timingIrregT = [];
meanCorrT = [];
fwhmT = [];
fileT = [];
downstroke90T = [];
downstroke80T = [];
upstrokeT= [];
down80veloT = [];
```

```
upstrokeVeloT = [];
normAmpT = [];

% establish excel file for outputs
% cd(dirOut);
% dataOut = 'excel_data';
% mkdir(dataOut);
% cd(dataOut);
headers = {'Sample Name' 'bpm' 'bpm std','timing irreg','Correlation',...
    'Upstroke Time','Downstroke Time 90','Downstroke Time 80','fwhm',...
    'Downstroke 80 Velo','Upstroke Velo','Amplitude Normalized'};
xlswrite(saveFileName,headers,1,'A1');


%% ========================================================================

n=1; % Counter for each file in directory, includes non-image files
count=1; % Counter for analyzed images, max(j) = # images in folder


for m=1:length(dir)             % FOR each file in directory @ cd
    cd(pathname)
    if direct(m).bytes < 1000000   % Filter based on filesize
        n=n+1;                  % Skip small files (headers & text)
    else                        % Continue if large enough to be an image
        button = 1;

        %Initialize other variables
        bpm = [];
        bpmSTD = [];
        timingIrreg = [];
        meanCorr = [];
        fwhm = [];
        downstrokeTime90 = [];
        downstrokeTime80 = [];
        upstrokeTime= [];
        down80velo = [];
        upstrokeVelo = [];
        normAmp = [];


        stackFile = load(direct(m).name); %Load in .mat file converted from .czi
file.
        numFrames = length(stackFile.data{1,1});

        raw = [];
        frames = [];
        ALLframeMean = [];
        for s = 1:numFrames
            raw(:,:,s) = stackFile.data{1,1}{s,1}; % Read video
            raw(:,:,s) = mat2gray(raw(:,:,s), videoThresh);
            raw(:,:,s) = horzcat(raw(:,515:end,s),raw(:,1:514,s)); %fix messed up
videos
            frames(:,:,s) = imgaussfilt(raw(:,:,s));
            ALLframeMean(s) = mean2(frames(:,:,s));
```

```
        end
        file = direct(m).name;
        time = numFrames/frameRate;

        rateInverse = 1/frameRate;
        t = [];
        t = 0:rateInverse:numFrames*rateInverse-rateInverse;


%         frames = [];
%         for s = 1:numFrames
%             video = read(raw,s);
%             video = imgaussfilt(video);
%             frames(:,:,s) = video(:,:,2); %only care about the green channel
%             ALLframeMean(s) = mean2(frames(:,:,s));
%         end

        [maxFrameInitial,maxFrameIndexInitial] = max(ALLframeMean);


        % Rotate video to make selection of tissue easier
        framesRot = imrotate(frames,-rotateAngle);

        % select region of the image that you would like to analyze

        figure(1);   imshow(framesRot(:,:,maxFrameIndexInitial),[]);     %Display raw
frame with max intensity

        rect = imrect;
        imgRect = wait(rect); % imgRect = [xmin ymin width height]
        imgRectRound = floor(imgRect);
        rectMat = zeros(imgRectRound(4),imgRectRound(3),numFrames);
        ymax = imgRectRound(2) + imgRectRound(4)-1;
        xmax = imgRectRound(1) + imgRectRound(3)-1;

        %Make new matrix containing only chosen area
        for nn = 1:numFrames
            rectMat(:,:,nn) =
framesRot(imgRectRound(2):ymax,imgRectRound(1):xmax,nn);
            rectMean(nn) = mean2(rectMat(:,:,nn));
        end

        % Filer mean with Savitzky-Golay Filter
        frameMeanFilt = sgolayfilt(rectMean,7,21);

        [maxFrame,maxFrameIndex] = max(frameMeanFilt); %find frame with max intesity
for display
        [minFrame,minFrameIndex] = min(frameMeanFilt);

        peakPromThresh = (maxFrame(1)-minFrame(1))/5;

        meanFramLoc = [];
        [meanFramePks,meanFrameLoc] =
findpeaks(frameMeanFilt,'MinPeakProminence',peakPromThresh);
        meanFramePksTime = meanFrameLoc/frameRate;
```

```
        meanPeakNum = length(meanFrameLoc);
        bpm = meanPeakNum/time*60;
        peakDiffs = diff(meanFrameLoc)/frameRate;
        bpmSTD = std(peakDiffs);
        timingIrreg = bpmSTD/mean(peakDiffs);

        minFramePks = [];
        [minFramePks,minFrameLoc] = findpeaks(-
frameMeanFilt,'MinPeakProminence',peakPromThresh);
        minFramePks = -minFramePks;
        minFramePksTime = minFrameLoc/frameRate;

        if length(minFramePks) > 1
        % Normalize plot to min values before each peak.
        % Also, save each peak as its own vector in cell array.
        dataSection{1} = frameMeanFilt(1:minFrameLoc(1))/minFramePks(1);
        normMeanFilt = [];
        normMeanFilt(1:minFrameLoc(1)) =
frameMeanFilt(1:minFrameLoc(1))/minFramePks(1);
        for sectionNum = 1:length(minFrameLoc)-1
            startPoint = minFrameLoc(sectionNum)+1;
            endPoint = minFrameLoc(sectionNum+1);
            dataSection{sectionNum} =
frameMeanFilt(startPoint:endPoint)/minFramePks(sectionNum);
            normMeanFilt(startPoint:endPoint) =
frameMeanFilt(startPoint:endPoint)/minFramePks(sectionNum);
        end
        dataSection{sectionNum+1} =
frameMeanFilt(minFrameLoc(sectionNum+1):end)/minFramePks(sectionNum+1);
        normMeanFilt(minFrameLoc(sectionNum+1):numFrames) =
frameMeanFilt(minFrameLoc(sectionNum+1):end)/minFramePks(sectionNum+1);


        % Find peak amplitudes on normalized plot.
        % Peak locations should not change from above.
        [maxNorm,maxNormIndex] = max(normMeanFilt);
        %min value will always be 1 because of normalization
        normPkThresh = (maxNorm(1)-1)/5; %set peak threshold value as 1/3 the max
peak prominence

        normPks = [];
        [normPks,normPkLoc] =
findpeaks(normMeanFilt,'MinPeakProminence',normPkThresh);
        meanNormTime = normPkLoc/frameRate;

        minNormPks = [];
        [minNormPks,minNormLoc] = findpeaks(-
normMeanFilt,'MinPeakProminence',normPkThresh);
        minNormTime = minNormLoc/frameRate;
        minNormPks = -minNormPks;


        figure(2)
        plot(t,normMeanFilt)
        hold on
```

```
        plot(meanNormTime,normPks,'go')
        plot(minFramePksTime,minNormPks(1:length(minFramePksTime)),'bo')
        xlabel('Time (s)')
        ylabel('Nomalized Fluorescence Intensity (a.u)')

%         % click if there is offset in peaks for upstroke calculation.
%         [xPoint0,yPoint0] = ginput(); %click where first upstroke ends if necessary
%         if length(xPoint0) > 0
%             topOffset = meanNormTime(1)-xPoint0(1);
%             meanNormTime = meanNormTime-topOffset;
%         end

        hold off

%% Upstroke/downstroke time calculations

        %Peak start and max for upstroke are identified and plotted above.
%         if length(meanNormTime) ~= length(minNormTime)
%             inputNumVals = min([length(meanNormTime),length(minNormTime)]);
%             meanNormTime = meanNormTime(1:inputNumVals);
%             normPks = normPks(1:inputNumVals);
%             minNormTime = minNormTime(1:inputNumVals);
%             minNormPks = minNormPks(1:inputNumVals);
%         else
%         end
        if minNormTime(1) < meanNormTime(1) %min detected first
            meanFramePksCrop = meanNormTime;
            normPksCrop = normPks;
            minFramePksCrop = minNormTime;
            minNormPksCrop = minNormPks;
            upstrokeTimeVec = meanFramePksCrop-
minFramePksCrop(1:length(meanFramePksCrop));
            upstrokeAmpVec = normPksCrop-minNormPksCrop(1:length(meanFramePksCrop));
            upstrokeTime = mean(upstrokeTimeVec);
        elseif minNormTime(1) > meanNormTime(1) && length(meanNormTime) ~=
length(minNormTime)
            meanFramePksCrop = meanNormTime; %(2:end);
            normPksCrop = normPks; %(2:end);
            minFramePksCrop = minNormTime; %(1:end-1);
            minNormPksCrop = minNormPks; %(1:end-1);
            upstrokeTimeVec = meanFramePksCrop(2:end)-minFramePksCrop;
            upstrokeAmpVec = normPksCrop(2:end)-minNormPksCrop;
            upstrokeTime = mean(upstrokeTimeVec);
        else
            meanFramePksCrop = meanNormTime; %(2:end);
            normPksCrop = normPks; %(2:end);
            minFramePksCrop = minNormTime; %(1:end-1);
            minNormPksCrop = minNormPks; %(1:end-1);
            upstrokeTimeVec = meanFramePksCrop(2:end)-minFramePksCrop(1:end-1);
            upstrokeAmpVec = normPksCrop(2:end)-minNormPksCrop(1:end-1);
            upstrokeTime = mean(upstrokeTimeVec);
        end

        % Next, we need to find the start of the downstroke.
        % On first peak, click once to define the offset time before
```

```
        % downstroke.

        startLoc = [];
        downStartAmp = [];
        downstrokeTimeVec = [];
        downStartTime = [];
        amp90Time = [];
        amp90Vec = [];

        % update figure with cropped peaks plotted
        figure(3)
        plot(t,normMeanFilt)
        hold on
        title('Click where downstroke begins after plateau on first peak:')
        plot(meanFramePksCrop,normPksCrop,'go')
        plot(minFramePksCrop,minNormPksCrop,'go')
        xlabel('Time (s)')
        ylabel('Nomalized Fluorescence Intensity (a.u)')

        [xPoint1,yPoint1] = ginput(); %click where first downstroke starts after the
        xPointDiff = xPoint1 - meanFramePksCrop(1);
        for ii = 1:length(meanFramePksCrop)-1
            downStart = meanFramePksCrop(ii) + xPointDiff;
            [startVal,startLoc(ii)] = min(abs(t-downStart));
            downStartAmp(ii) = normMeanFilt(startLoc(ii)); %
            if minNormTime(1) < meanNormTime(1) && minNormTime(end) <
meanNormTime(end)%min detected first and not last
                minIndex = ii+1;
            elseif minNormTime(1) < meanNormTime(1) && minNormTime(end) >
meanNormTime(end) %min detected first and last
                minIndex = ii+2;
            else
                minIndex = ii;
            end
            downEndAmp(ii) = minNormPksCrop(minIndex);
            amp90 = (downStartAmp(ii)-downEndAmp(ii))*.10 + downEndAmp(ii); % Down
stroke to 90% peak fluor. (100-90=10%)
            amp80 = (downStartAmp(ii)-downEndAmp(ii))*.20 + downEndAmp(ii); % Down
stroke to 90% peak fluor. (100-80=20%)

            % Find a the first two points on the down stroke surrounding
            % 90% amplitude.
            thisRange =
normMeanFilt(meanFramePksCrop(ii)*frameRate:minFramePksCrop(minIndex)*frameRate);
            first90 = 0; %initialize
            first80 = 0;
            for jj = 1:length(thisRange)-1
                point1 = thisRange(jj);
                point2 = thisRange(jj+1);
                if point1 > amp90 && point2 < amp90 && first90 == 0
                    point90(ii) = meanFramePksCrop(ii)*frameRate + jj;
                    % make sure point64 is integer for indexing later
                    first90 = 1; %prevents code from finding another value
                end
```

```
            if point1 > amp80 && point2 < amp80 && first80 == 0
                point80(ii) = meanFramePksCrop(ii)*frameRate + jj;
                % make sure point64 is integer for indexing later
                first80 = 1; %prevents code from finding another value
            end

        end

        downstrokeTimeVec(ii) = (point90(ii)-startLoc(ii))/frameRate;
        downStartTime(ii) = t(startLoc(ii));
        amp90Time(ii) = t(int64(point90(ii))); %int64(overallLoc(ii)));
        amp90Vec(ii) = normMeanFilt(int64(point90(ii))); %overallLoc(ii));

        downstrokeTimeVec80(ii) = (point80(ii)-startLoc(ii))/frameRate;
        downStartTime80(ii) = t(startLoc(ii));
        amp80Time(ii) = t(int64(point80(ii))); %int64(overallLoc(ii)));
        amp80Vec(ii) = normMeanFilt(int64(point80(ii))); %overallLoc(ii));

    end
    downstrokeTime90 = mean(downstrokeTimeVec);
    downstrokeTime80 = mean(downstrokeTimeVec80);

    plot(downStartTime,downStartAmp,'ro')
    plot(amp80Time,amp80Vec,'ro')
    hold off

    %Calculate upstroke and downstroke velocities
    down80velo = mean((downStartAmp-amp80)./downstrokeTimeVec80);
    upstrokeVelo = mean((upstrokeAmpVec)./upstrokeTimeVec);
    normAmp = mean(normPksCrop);



%% Full width half max calculation

    if minNormTime(1) < meanNormTime(1) %min detected first
        minStart = minFrameLoc(1); %start at first identified min val
        maxStart = meanFrameLoc(1);

    elseif minNormTime(1) > meanNormTime(1) && length(meanNormTime) ~=
length(minNormTime)
        minStart = minFrameLoc(1); %start at first identified min val
        maxStart = meanFrameLoc(2);

    else %max detected first and same amount of min and max peaks
        minStart = minFrameLoc(1); %start at first identified min val
        maxStart = meanFrameLoc(2);

    end

    minStart = minFrameLoc(1); %start at first identified min val
    halfMax = (minFrame(1) + maxFrame(1))/2;
    halfMaxFrame = find(rectMean(minStart:end)>halfMax);
    jumpIndex = diff(halfMaxFrame) > 2;
    findJumpIndex = find(jumpIndex==1);
```

```
        if length(findJumpIndex) < 2
            meanPeakWidth = findJumpIndex;
        else
            meanPeakWidth = mean(diff(findJumpIndex));
        end
        fwhm = meanPeakWidth/frameRate;

        %% Plot filter data and save raw data to csv
        rawDataOut = [t' normMeanFilt'];
        rawDataName = strcat(file(1:end-4),'_RawData.xls');
        xlswrite(rawDataName,rawDataOut,1,'A1');
        hold off

        else
        fprintf('No peaks detected! \n')

        %% Plot filter data and save raw data to csv
        rawDataOut = [t' frameMeanFilt'];
        rawDataName = strcat(file(1:end-4),'_RawData.xls');
        xlswrite(rawDataName,rawDataOut,1,'A1');
        hold off


        end
%% Calculate Contraction Correlation
% Divide image into regions of a defined size (subAreaDim).
% Find intensity profiles of those regions.
% Calculate a Pearson's Correlation coefficient across matrix of profiles.

        [r,c] = size(frames(:,:,1));
        peakShift = zeros(r,c);
        peakNumDiff = zeros(r,c);
        rSubArea = floor(r/subAreaDim);
        cSubArea = floor(c/subAreaDim);
        subArea = zeros(rSubArea,cSubArea,numFrames); %divide image into 4x4 grid

        areaNum = 1;
        filterAreaNum = 1;
        areaNumRecord = [];
        filterMeanMat = [];
        for rIndex = 1:subAreaDim
            for cIndex = 1:subAreaDim
                for f = 1:numFrames
                    subArea(:,:,f) = frames((rIndex-
1)*rSubArea+1:rIndex*rSubArea,(cIndex-1)*cSubArea+1:cIndex*cSubArea,f);
                    meanMat(f,areaNum) = mean2(subArea(:,:,f)); %matrix with mean of
each area in column
                end
                [maxFrameCorr,maxFrameIndex] = max(meanMat(:,areaNum)); %find frame
with max intesity for display
                [minFrameCorr,minFrameIndex] = min(meanMat(:,areaNum));
                peakPromThreshCorr = (maxFrameCorr(1)-minFrameCorr(1))/2;
                [subAreaPks,subAreaLocs] =
findpeaks(meanMat(:,areaNum),'MinPeakProminence',peakPromThreshCorr);
                if length(subAreaLocs) < meanPeakNum-5
```

```
                else
                    filterMeanMat(:,filterAreaNum) = meanMat(:,areaNum);
                    areaNumRecord(filterAreaNum) = areaNum; %to record which areas
are kept
                    filterAreaNum = filterAreaNum + 1;
                end
                areaNum = areaNum + 1;
            end
        end

        correlation = corrcoef(filterMeanMat); %Pearson's Corr. Coef.
        meanCorr = mean2(correlation);


%% Output ==========================================================

%         imageName = raw.name;
%         imageNameT = vertcat(imageNameT,imageName);
        fileT = vertcat(fileT,file);
        bpmT = vertcat(bpmT,bpm);
        bpmstdT = vertcat(bpmstdT,bpmSTD);
        timingIrregT = vertcat(timingIrregT,timingIrreg);
        meanCorrT = vertcat(meanCorrT,meanCorr);
        fwhmT = vertcat(fwhmT,fwhm);
        upstrokeT = vertcat(upstrokeT,upstrokeTime);
        downstroke90T = vertcat(downstroke90T,downstrokeTime90);
        downstroke80T = vertcat(downstroke80T,downstrokeTime80);
        down80veloT = vertcat(down80veloT,down80velo);
        upstrokeVeloT = vertcat(upstrokeVeloT,upstrokeVelo);
        normAmpT = vertcat(normAmpT,normAmp);

        %imwrite(pixelPeakNumColor,strcat(filename(1:end-
4),num2str(m),'_numBeatsMap.tif'),'TIFF')
        ALLDATA = horzcat(fileT,bpmT,bpmstdT,timingIrregT,...
            meanCorrT,upstrokeT,downstroke90T,downstroke80T,fwhmT,...
            down80veloT,upstrokeVeloT,normAmpT);
        xlsOut = {file,bpm,bpmSTD,timingIrreg,meanCorr,upstrokeTime,...
            downstrokeTime90,downstrokeTime80,fwhm,down80velo,...
            upstrokeVelo,normAmp};
        xlsRow = strcat('A',num2str(count+1));
%         cd(dirOut);
        xlswrite(saveFileName,xlsOut,1,xlsRow);

        count = count+1;
    end

    % Clear all variables after each itteration excepts ones defined before
    %reading files.
    clearvars -except filename pathname filterIndex direct dirOut pixelSize...
        saveFileName n count rotateAngle subAreaDim bpmT bpmstdT timingIrregT...
        meanCorrT fwhmT fileT downstroke90T downstroke80T upstrokeT...
        down80veloT upstrokeVeloT normAmpT frameRate videoThresh

end
```

Focal Adhesion and Costamere Formation Analysis

```
function [] =
vincloc3(Filename,experiment_title,root,dirOut,dataOut,pathname,imgCount,locNum)

%% INPUT nuc, FA, actinin and adherens junctions data ====================
faScale = [14000 65000];
actininScale = [3000 50000];
ncadScale = [2500 50000];
nucScale = [2000 40000];

% Account for offset in LSM800 channels
offsetVec = [1 2 5 0]; % [405 488 555 647] = [1 2 5 0] @ 40x
offsetMax = max(offsetVec);
offsetMin = min(offsetVec);

maxVincArea = 10000;
maxfaVolume = 100000; % 4166 pixels = 100um^2
numChannel = 3; % Number of channels in the stack.

stackFile = load(Filename); %Load in .mat file converted from .czi file.

numslice = length(stackFile.data{1,1})/numChannel;

[r,c] = size(stackFile.data{1,1}{1,1});
%  r = 1024;
%  c = 1024;
maxNumslice = numslice-offsetMax;
nucImage = zeros(r,c,maxNumslice);
actininImage = zeros(r,c,maxNumslice);
faImage = zeros(r,c,maxNumslice);
ncadImage = zeros(r,c,maxNumslice);



for j = 1:maxNumslice
    %Channel for each image indicated in comments
    %Move channel names around to depending on what is stained in each

    %3 Channel Images
    nucImage(:,:,j) = imresize(mat2gray(stackFile.data{1,1}{3*(j+offsetVec(1))-
2,1},nucScale),[r c]); %405
    actininImage(:,:,j) = imresize(mat2gray(stackFile.data{1,1}{3*(j+offsetVec(2))-
1,1},actininScale),[r c]); %488
    faImage(:,:,j) =
imresize(mat2gray(stackFile.data{1,1}{3*(j+offsetVec(4)),1},faScale),[r c]); %555 or
647
    ncadImage(:,:,j) =
imresize(mat2gray(stackFile.data{1,1}{3*(j+offsetVec(4)),1},ncadScale),[r c]); %647
(ignore for 3 channnel)

    %4 Channel Images
    % nucImage(:,:,j) = imresize(mat2gray(stackFile.data{1,1}{4*(j+offsetVec(1))-
3,1},nucScale),[r c]); %405
```

```
    % actininImage(:,:,j) = imresize(mat2gray(stackFile.data{1,1}{4*(j+offsetVec(2))-
2,1},actininScale),[r c]); %488
    % faImage(:,:,j) = imresize(mat2gray(stackFile.data{1,1}{4*(j+offsetVec(3))-
1,1},faScale),[r c]); %555
    % ncadImage(:,:,j) =
imresize(mat2gray(stackFile.data{1,1}{4*(j+offsetVec(4)),1},ncadScale),[r c]); %647
end

%% Filter and Display Images ===============================================

% Filter fa imaage
fanoiseSize = 3; % range=1-10
fabackSize = 20; % range=10-200 (was 50 before)
[faClean, faThresh] = gfilt(faImage, fanoiseSize, fabackSize);
% filter out adhesions < 1 micron^2
faMask = double(bwareaopen(faThresh,10)); % 20 pixels = 0.5 um^2 for 40x
maxfaMask = max(faMask,[],3);
maxfaClean = max(faClean,[],3);
maxfaImage = max(faImage,[],3);
figure(1)
impanel(maxfaImage,maxfaClean,maxfaMask);

% Filter ncad image
ncadnoiseSize = 3; % range=1-10
ncadbackSize = 20; % range=10-200 (was 50 before)
[ncadClean, ncadThresh] = gfilt(ncadImage, ncadnoiseSize, ncadbackSize);
% filter out adhesions < 1 micron^2
ncadMask = double(bwareaopen(ncadThresh,20)); % 20 pixels = 0.5 um^2 for 40x
maxncadMask = max(ncadMask,[],3);
maxncadClean = max(ncadClean,[],3);
maxncadImage = max(ncadImage,[],3);

totalNcadArea = sum(sum(maxncadMask));

figure(2)
impanel(maxncadImage,maxncadClean,maxncadMask);

% Filter actinin image
actininnoiseSize = 3; % range=1-10
actininbackSize = 20; % range=10-200 (was 50 before)
[actininClean, actininThresh] = gfilt(actininImage, actininnoiseSize,
actininbackSize);
% filter out adhesions < 1 micron^2
actininMask = double(bwareaopen(actininThresh,20)); % 20 pixels = 0.5 um^2 for 40x
maxactininThresh = max(actininThresh,[],3);
maxactininMask = max(actininMask,[],3);
maxactininClean = max(actininClean,[],3);
maxactininImage = max(actininImage,[],3);

totalActininArea = sum(sum(maxactininMask));

figure(3)
impanel(maxactininImage,maxactininClean,maxactininMask);

% Filter nuc image
```

```
nucnoiseSize = 3; % range=1-10
nucbackSize = 20; % range=10-200 (was 50 before)
[nucClean, nucThresh] = gfilt(nucImage, nucnoiseSize, nucbackSize);
% filter out adhesions < 1 micron^2
nucMask = double(bwareaopen(nucThresh,40)); % 20 pixels = 0.5 um^2 for 40x
maxnucMask = max(nucMask,[],3);
maxnucClean = max(nucClean,[],3);
maxnucImage = max(nucImage,[],3);

figure(4)
impanel(maxnucImage,maxnucClean,maxnucMask);

%% Count the number of nuclei from max projection

[nucCount, avgNucArea] =
vincloc3nuccounter(maxnucImage,pathname,dirOut,imgCount,root,locNum);


%% Extract FA metrics from 3D reconstruction ==============================
[faLabel, faCount] = bwlabeln(faMask,18);
faStats3 =
regionprops3(faLabel,'Volume','SurfaceArea','PrincipalAxisLength','Orientation','Cent
roid','VoxelIdxList');
for i=1:faCount
    if faStats3(i,1).Volume > maxfaVolume
        %faLabel(faStats3(i,1).VoxelIdxList)=0;
    else
        rawAdh3D(i,1) = faStats3.Volume(i);
        rawAdh3D(i,2) = faStats3.SurfaceArea(i);
        rawAdh3D(i,3:5) = faStats3.PrincipalAxisLength(i,:);
        rawAdh3D(i,6:8) = faStats3.Orientation(i,:);
        rawAdh3D(i,8:10) = faStats3.Centroid(i,:);
    end
end

% CALCULATE 3D ADHESION STATISTICS
faCountperCell = faCount/nucCount;
volMean = mean(rawAdh3D(:,1));
volStd = std(rawAdh3D(:,1));
saMean = mean(rawAdh3D(:,2));
saStd = std(rawAdh3D(:,2));

totalAdhVol = sum(rawAdh3D(:,1));
totalAdhVolperCell = totalAdhVol/nucCount;
totalAdhSA = sum(rawAdh3D(:,2));
totalAdhSAperCell = totalAdhSA/nucCount;


% Extract some 2D metrics from max projection as well ====================
[faLabel2, faCount2] = bwlabel(maxfaMask,8);
adhStats =
regionprops(faLabel2,'Area','Eccentricity','Orientation','MajorAxisLength','MinorAxis
Length','PixelIdxList');
for i=1:faCount2
    if adhStats(i,1).Area > maxVincArea
```

```
        faLabel2(adhStats(i,1).PixelIdxList)=0;
    else
        rawAdh2D(i,1) = adhStats(i,1).Area;
        rawAdh2D(i,2) = adhStats(i,1).Eccentricity;
        rawAdh2D(i,3) = adhStats(i,1).Orientation;
        rawAdh2D(i,4) = adhStats(i,1).MajorAxisLength;
        rawAdh2D(i,5) = adhStats(i,1).MinorAxisLength;
    end
end

% CALCULATE 2D ADHESION STATISTICS
areaMean = mean(rawAdh2D(:,1));
areaStd = std(rawAdh2D(:,1));
eccMean = mean(rawAdh2D(:,2));
eccStd = std(rawAdh2D(:,2));
aspectMean = mean(rawAdh2D(:,3));
aspectStd = std(rawAdh2D(:,3));
angMean = rad2deg(circ_mean(deg2rad(rawAdh2D(:,4))));
angDisp = rad2deg(circ_std(deg2rad(rawAdh2D(:,4))));

totalAdhArea = sum(sum(maxfaMask));
totalAdhAreaPerCell = totalAdhArea/nucCount;
totalActininAreaPerCell = totalActininArea/nucCount;
totalNcadAreaPerCell = totalNcadArea/nucCount;



%% FA - Actinin Colocalization Data

fa_actinin_mask = faMask.*actininMask;
[faActininLabel, faActininCount] = bwlabeln(fa_actinin_mask,18);
faActininStats = regionprops3(faActininLabel,'Volume','SurfaceArea','Centroid');

total_fa_actinin_vol = sum(faActininStats.Volume);
total_fa_actinin_vol_perCell = total_fa_actinin_vol./nucCount;
faActininLocRatio = total_fa_actinin_vol./totalAdhVol;

% Make FA/Actinin colocalization images
faMaskRed = zeros(r,c,3,maxNumslice);
faMaskRed(:,:,1,:) = faMask*255;
actininMaskGreen = zeros(r,c,3,maxNumslice);
actininMaskGreen(:,:,2,:) = actininMask*255;

fa_actinin_combine_color = faMaskRed+actininMaskGreen;
fa_actinin_combine_color_max = max(fa_actinin_combine_color,[],4);
figure(6)
imshow(fa_actinin_combine_color_max)

% % Set up orthosliceviewer
faMaskRed_ortho = zeros(r,c,maxNumslice,3);
faMaskRed_ortho(:,:,:,1) = faMask*255;
actininMaskGreen_ortho = zeros(r,c,maxNumslice,3);
actininMaskGreen_ortho(:,:,:,2) = actininMask*255;
fa_actinin_combine_color_ortho = faMaskRed_ortho+actininMaskGreen_ortho;
% figure(101)
```

```
% orthoslice_faActinin = orthosliceViewer(fa_actinin_combine_color_ortho);

colocImg = mat2gray(actininThresh.*faClean,[0,0.1]);
colocImg = max(colocImg,[],3);



%% FA - N-Cad Colocalization Data

fa_ncad_mask = faMask.*ncadMask;
[faNcadLabel, faNcadCount] = bwlabeln(fa_ncad_mask,18);
faNcadStats = regionprops3(faNcadLabel,'Volume','SurfaceArea','Centroid');

total_fa_ncad_vol = sum(faNcadStats.Volume);
total_fa_ncad_vol_perCell =total_fa_ncad_vol./nucCount;
faNcadLocRatio = total_fa_ncad_vol./totalAdhVol;

% Make FA/N-Cad colocalization images
ncadMaskGreen = zeros(r,c,3,maxNumslice);
ncadMaskGreen(:,:,2,:) = ncadMask*255;

fa_ncad_combine_color = faMaskRed+ncadMaskGreen;
fa_ncad_combine_color_max = max(fa_ncad_combine_color,[],4);
figure(7)
imshow(fa_ncad_combine_color_max)

% % Set up orthosliceviewer
% faMaskRed_ortho = zeros(r,c,maxNumslice,3);
% faMaskRed_ortho(:,:,:,1) = faMask*255;
% ncadMaskGreen_ortho = zeros(r,c,maxNumslice,3);
% ncadMaskGreen_ortho(:,:,:,2) = ncadMask*255;
% figure(102)
% fa_ncad_combine_color_ortho = faMaskRed_ortho+ncadMaskGreen_ortho;
% orthoslice_fancad = orthosliceViewer(fa_ncad_combine_color_ortho);


%% Write data to spreadsheet ==============================================
cd(dataOut);
xlsOut = {Filename faCount faCountperCell volMean volStd saMean saStd totalAdhVol
totalAdhVolperCell totalAdhSA totalAdhSAperCell...
    areaMean areaStd eccMean eccStd aspectMean aspectStd angMean angDisp nucCount
totalAdhArea totalAdhAreaPerCell...
    totalActininArea totalActininAreaPerCell totalNcadArea totalNcadAreaPerCell...
    total_fa_actinin_vol total_fa_actinin_vol_perCell faActininLocRatio
total_fa_ncad_vol total_fa_ncad_vol_perCell faNcadLocRatio};
xlsFilename = strcat(experiment_title,'new.xls');
xlsRow = strcat('A',num2str(imgCount+1));
xlswrite(xlsFilename,xlsOut,1,xlsRow);


%% Image Exports
cd(pathname);
cd(dirOut);
imwrite(maxfaMask,
strcat(root,num2str(imgCount),'_faMask.tif'),'Compression','none');
```

```
imwrite(maxfaClean,
strcat(root,num2str(imgCount),'_faClean.tif'),'Compression','none');
imwrite(maxactininMask,
strcat(root,num2str(imgCount),'_actininMask.tif'),'Compression','none');
imwrite(maxncadMask,
strcat(root,num2str(imgCount),'_ncadMask.tif'),'Compression','none');
imwrite(fa_actinin_combine_color_max,
strcat(root,num2str(imgCount),'_fa_actinin_coloc.tif'),'Compression','none');
imwrite(fa_ncad_combine_color_max,
strcat(root,num2str(imgCount),'_fa_ncad_coloc.tif'),'Compression','none');

imwrite(colocImg,strcat(root,num2str(imgCount),'_coloc.tif'),'TIFF','Compression','no
ne');
imwrite(ind2rgb(round(colocImg*255),jet(256)),strcat(root,num2str(imgCount),'_coloc_j
et.tif'),'TIFF','Compression','none');
imwrite(ind2rgb(round(colocImg*255),autumn(256)),strcat(root,num2str(imgCount),'_colo
c_autumn.tif'),'TIFF','Compression','none');
imwrite(ind2rgb(round(colocImg*255),parula(256)),strcat(root,num2str(imgCount),'_colo
c_parula.tif'),'TIFF','Compression','none');

save(strcat(root,num2str(imgCount),'_colocImg.mat'),'colocImg')

save(strcat(root,num2str(imgCount),'_workspace.mat'))

end
```

Alpha Smooth Muscle Quantification

```
function [ actin_signal, asma_signal, nucCount, actinCell, asmaCell, asmaArea ] =
asmaquant(asmaFilename, nucFilename, actinFilename, threshVal, pathname, dirOut,
imgCount)

% INPUT
asmaScale = [40 255];
actinScale = [1 35];
asmaImage = mat2gray(imread(asmaFilename),asmaScale);
actinImage = mat2gray(imread(actinFilename),actinScale);

% THRESHOLD ACTIN IMAGE AND REMOVE BACKGROUND NOISE
cell = im2bw(imin(actinFilename),threshVal);
cell = bwmorph(cell, 'close');
[objects, totalObjects] = bwlabel(cell, 4);
stats = regionprops(objects, 'Area', 'PixelIdxList');
for i = 1:totalObjects
    if stats(i,1).Area < 100 %GET RID OF NOISE THAT IS NOT THE CELL NETWORK
        cell(stats(i,1).PixelIdxList) = 0;
    end
end
cell = bwmorph(cell, 'spur');

% CALCULATE aSMA AND ACTIN SIGNAL (MASKED BY CELL AREA)
```

```
cellArea = sum(sum(cell));
asmaMask = asmaImage .* cell;
asma_signal = sum(sum(asmaMask(:,:,1)));
actinMask = actinImage .* cell;
actin_signal = sum(sum(actinMask(:,:,1)));

% GET CELL COUNT BY COUNTING NUMBER OF NUCLEI
[nucCount, avgNucArea] = asmanuccounter(nucFilename,pathname,dirOut,imgCount);

% CALCULATE aSMA AND ACTIN SIGNAL PER CELL
actinCell = actin_signal ./ nucCount;
asmaCell = asma_signal ./ nucCount;
asmaArea = asma_signal ./ cellArea;
end
```

Bibliography

Abecasis, Bernardo, Patrícia Gomes-Alves, Susana Rosa, Pedro J. Gouveia, Lino Ferreira, Margarida Serra, and Paula M. Alves. 2019. 'Unveiling the Molecular Crosstalk in a Human Induced Pluripotent Stem Cell-Derived Cardiac Model'. *Biotechnology and Bioengineering* 116(5): 1245–52. doi:10.1002/bit.26929.

Abilez, Oscar J., Evangeline Tzatzalos, Huaxiao Yang, Ming Tao Zhao, Gwanghyun Jung, Alexander M. Zöllner, Malte Tiburcy, et al. 2018. 'Passive Stretch Induces Structural and Functional Maturation of Engineered Heart Muscle as Predicted by Computational Modeling'. *Stem Cells* 36(2): 265–77. doi:10.1002/stem.2732.

Afzal, Junaid, Yamin Liu, Wenqiang Du, Yasir Suhail, Pengyu Zong, Jianlin Feng, Visar Ajeti, et al. 2022. 'Cardiac Ultrastructure Inspired Matrix Induces Advanced Metabolic and Functional Maturation of Differentiated Human Cardiomyocytes'. *Cell Reports* 40(4). doi:10.1016/j.celrep.2022.111146.

Agarwal, Radhika, Joao Paulo, Christopher N Toepfer, Jourdan K Ewoldt, Subramanian Sundaram, Anant Chopra, Qi Zhang, et al. 2021. 'Filamin C Cardiomyopathy Variants Cause Protein and Lysosome Accumulation'. *Circulation Research*. doi:10.1161/CIRCRESAHA.120.317076.

Ahmed, Donia W., Madeline K. Eiken, Samuel J. DePalma, Adam S. Helms, Rachel L. Zemans, Jason R. Spence, Brendon M. Baker, and Claudia Loebel. 2023. 'Integrating Mechanical Cues with Engineered Platforms to Explore Cardiopulmonary Development and Disease'. *iScience* 26(12): 108472. doi:10.1016/J.ISCI.2023.108472.

Ahrens, John H., Sebastien G.M. Uzel, Mark Skylar-Scott, Mariana M. Mata, Aric Lu, Katharina T. Kroll, and Jennifer A. Lewis. 2022. 'Programming Cellular Alignment in Engineered Cardiac Tissue via Bioprinting Anisotropic Organ Building Blocks'. *Advanced Materials* 34(26). doi:10.1002/adma.202200217.

Ahrens, John, Sebastien Uzel, Mark Skylar-Scott, Mariana Mata, Aric Lu, Katharina Kroll, Jennifer A Lewis, and John A Paulson. 2022. 'Programming Cellular Alignment in Engineered Cardiac Tissue via Bioprinting Anisotropic Organ Building Blocks'. *Advanced Materials*: 2200217. doi:10.1002/ADMA.202200217.

Al-Hasani, Jaafar, Carla Sens-Albert, Subhajit Ghosh, Felix A. Trogisch, Taslima Nahar, Prisca A.P. Friede, Jan Christian Reil, and Markus Hecker. 2022. 'Zyxin Protects from Hypertension-Induced Cardiac Dysfunction'. *Cellular and Molecular Life Sciences* 79(2): 1–14. doi:10.1007/S00018-022-04133-4/FIGURES/7.

Allen, Alicia C.B., Elissa Barone, Nima Momtahan, Cody O. Crosby, Chengyi Tu, Wei Deng, Krista Polansky, and Janet Zoldan. 2019. 'Temporal Impact of Substrate Anisotropy on Differentiating Cardiomyocyte Alignment and Functionality'. *Tissue Engineering Part A* 25(19–20): 1426–37. doi:10.1089/ten.tea.2018.0258.

Arnold, Marco, Elisabetta Ada Cavalcanti-Adam, Roman Glass, Jacques Blümmel, Wolfgang Eck, Martin Kantlehner, Horst Kessler, and Joachim P. Spatz. 2004. 'Activation of Integrin Function by Nanopatterned Adhesive Interfaces'. *ChemPhysChem* 5(3): 383–88. doi:10.1002/cphc.200301014.

Bajaj, Piyush, Xin Tang, Taher A. Saif, and Rashid Bashir. 2010. 'Stiffness of the Substrate Influences the Phenotype of Embryonic Chicken Cardiac Myocytes'. *Journal of Biomedical Materials Research Part A* 95A(4): 1261–69. doi:10.1002/jbm.a.32951.

Baker, Brendon M, Britta Trappmann, William Y Wang, Mahmut S Sakar, Iris L Kim, Vivek B Shenoy, Jason A Burdick, and Christopher S Chen. 2015. 'Cell-Mediated Fibre Recruitment Drives Extracellular Matrix Mechanosensing in Engineered Fibrillar Microenvironments'. *Nature Materials* 14: 1262–68. doi:10.1038/NMAT4444.

Balestrini, Jenna L., Sidharth Chaudhry, Vincent Sarrazy, Anne Koehler, and Boris Hinz. 2012. 'The Mechanical Memory of Lung Myofibroblasts'. *Integrative Biology* 4(4): 410–21. doi:10.1039/C2IB00149G.

Bargehr, Johannes, Lay Ping Ong, Maria Colzani, Hongorzul Davaapil, Peter Hofsteen, Shiv Bhandari, Laure Gambardella, et al. 2019. 'Epicardial Cells Derived from Human Embryonic Stem Cells Augment Cardiomyocyte-Driven Heart Regeneration'. *Nature Biotechnology* 37(8): 895–906. doi:10.1038/s41587-019-0197-9.

Barnes, Ashlynn M., Tessa B. Holmstoen, Andrew J. Bonham, and Teisha J. Rowland. 2022. 'Differentiating Human Pluripotent Stem Cells to Cardiomyocytes Using Purified Extracellular Matrix Proteins'. *Bioengineering* 9(12): 720. doi:10.3390/BIOENGINEERING9120720/S1.

Bassat, Elad, Yara Eid Mutlak, Alex Genzelinakh, Ilya Y. Shadrin, Kfir Baruch Umansky, Oren Yifa, David Kain, et al. 2017. 'The Extracellular Matrix Protein Agrin Promotes Heart Regeneration in Mice'. *Nature* 547(7662): 179–84. doi:10.1038/nature22978.

Baudino, Troy A., Wayne Carver, Wayne Giles, and Thomas K. Borg. 2006. 'Cardiac Fibroblasts: Friend or Foe?' *https://doi.org/10.1152/ajpheart.00023.2006* 291(3): 1015–26. doi:10.1152/AJPHEART.00023.2006.

Beauchamp, Philippe, Christopher B. Jackson, Lijo Cherian Ozhathil, Irina Agarkova, Cristi L. Galindo, Douglas B. Sawyer, Thomas M. Suter, and Christian Zuppinger. 2020. '3D Co-Culture of HiPSC-Derived Cardiomyocytes With Cardiac Fibroblasts Improves Tissue-Like Features of Cardiac Spheroids'. *Frontiers in Molecular Biosciences* 7: 14. doi:10.3389/fmolb.2020.00014.

Belkin, Alexey M., Natalia I. Zhidkova, Fiorella Balzac, Fiorella Altruda, Daniela Tomatis, Alfred Maier, Guido Tarone, Victor E. Koteliansky, and Keith Burridge. 1996. 'Beta 1D Integrin Displaces the Beta 1A Isoform in Striated Muscles: Localization at Junctional Structures and Signaling Potential in Nonmuscle Cells.' *Journal of Cell Biology* 132(1): 211–26. doi:10.1083/JCB.132.1.211.

Berens, Philipp. 2009. 'CircStat : A MATLAB Toolbox for Circular Statistics '. *Journal of Statistical Software* 31(10): 1–21. doi:10.18637/jss.v031.i10.

Bergmann, Olaf, Ratan D. Bhardwaj, Samuel Bernard, Sofia Zdunek, Fanie Barnabé-Heide, Stuart Walsh, Joel Zupicich, et al. 2009. 'Evidence for Cardiomyocyte Renewal in Humans'. *Science* 324(5923): 98–102. doi:10.1126/SCIENCE.1164680/SUPPL_FILE/BERGMANN.SOM.PDF.

Bershadsky, Alexander D., Nathalie Q. Balaban, and Benjamin Geiger. 2003. 'Adhesion-Dependent Cell Mechanosensitivity'. *Annual Review of Cell and Developmental Biology* 19(Volume 19, 2003): 677–95. doi:10.1146/ANNUREV.CELLBIO.19.111301.153011/CITE/REFWORKS.

Bhagwan, Jamie R., Emma Collins, Diogo Mosqueira, Mine Bakar, Benjamin B. Johnson, Alexander Thompson, James G.W. Smith, and Chris Denning. 2019. 'Variable Expression and Silencing of CRISPR-Cas9 Targeted Transgenes Identifies the AAVS1 Locus as Not an Entirely Safe Harbour'. *F1000Research* 8: 1911. doi:10.12688/f1000research.19894.1.

Bian, Liming, Murat Guvendiren, Robert L. Mauck, and Jason A. Burdick. 2013. 'Hydrogels That Mimic Developmentally Relevant Matrix and N-Cadherin Interactions Enhance MSC Chondrogenesis'. *Proceedings of the National Academy of Sciences of the United States of America* 110(25): 10117–22. doi:10.1073/pnas.1214100110.

Bird, S. D., P. A. Doevendans, M. A. Van Rooijen, A. Brutel De La Riviere, R. J. Hassink, R. Passier, and C. L. Mummery. 2003. 'The Human Adult Cardiomyocyte Phenotype'. *Cardiovascular Research* 58(2): 423–34. doi:10.1016/S0008-6363(03)00253-0.

Blazeski, Adriana, Justin Lowenthal, Renjun Zhu, Jourdan Ewoldt, Kenneth R. Boheler, and Leslie Tung. 2019. 'Functional Properties of Engineered Heart Slices Incorporating Human Induced Pluripotent Stem Cell-Derived Cardiomyocytes'. *Stem Cell Reports* 12(5): 982–95. doi:10.1016/j.stemcr.2019.04.002.

Bliley, Jacqueline M., Mathilde C. S. C. Vermeer, Rebecca M. Duffy, Ivan Batalov, Duco Kramer, Joshua W. Tashman, Daniel J. Shiwarski, et al. 2021. 'Dynamic Loading of Human Engineered Heart Tissue Enhances Contractile Function and Drives a Desmosome-Linked Disease Phenotype'. *Science Translational Medicine* 13(603): eabd1817. doi:10.1126/SCITRANSLMED.ABD1817.

Block, Travis, Jeffery Creech, Andre Monteiro da Rocha, Milos Marinkovic, Daniela Ponce-Balbuena, Eric N. Jiménez-Vázquez, Sy Griffey, and Todd J. Herron. 2020. 'Human Perinatal Stem Cell Derived Extracellular Matrix Enables Rapid Maturation of HiPSC-CM Structural and Functional Phenotypes'. *Scientific Reports 2020 10:1* 10(1): 1–15. doi:10.1038/s41598-020-76052-y.

Bonnans, Caroline, Jonathan Chou, and Zena Werb. 2014. 'Remodelling the Extracellular Matrix in Development and Disease'. *Nature Reviews Molecular Cell Biology 2014 15:12* 15(12): 786–801. doi:10.1038/nrm3904.

Van Den Borne, Susanne W.M., Javier Diez, W. Matthijs Blankesteijn, Johan Verjans, Leo Hofstra, and Jagat Narula. 2009. 'Myocardial Remodeling after Infarction: The Role of Myofibroblasts'. *Nature Reviews Cardiology 2010 7:1* 7(1): 30–37. doi:10.1038/nrcardio.2009.199.

Bornhorst, Dorothee, Peng Xia, Hiroyuki Nakajima, Chaitanya Dingare, Wiebke Herzog, Virginie Lecaudey, Naoki Mochizuki, et al. 2019. 'Biomechanical Signaling within the Developing Zebrafish Heart Attunes Endocardial Growth to Myocardial Chamber Dimensions'. *Nature Communications 2019 10:1* 10(1): 1–10. doi:10.1038/s41467-019-12068-x.

Boudou, Thomas, Wesley R. Legant, Anbin Mu, Michael A. Borochin, Nimalan Thavandiran, Milica Radisic, Peter W. Zandstra, et al. 2012. 'A Microfabricated Platform to Measure and Manipulate the Mechanics of Engineered Cardiac Microtissues'. *Tissue Engineering Part A* 18(9–10): 910–19. doi:10.1089/ten.tea.2011.0341.

Bowers, Stephanie L. K., Qinghang Meng, and Jeffery D. Molkentin. 2022. 'Fibroblasts Orchestrate Cellular Crosstalk in the Heart through the ECM'. *Nature Cardiovascular Research 2022 1:4* 1(4): 312–21. doi:10.1038/s44161-022-00043-7.

Brady, Eileen L., Olivia Prado, Fredrik Johansson, Shannon N. Mitchell, Amy M. Martinson, Elaheh Karbassi, Hans Reinecke, et al. 2023. 'Engineered Tissue Vascularization and Engraftment Depends on Host Model'. *Scientific Reports* 13(1). doi:10.1038/s41598-022-23895-2.

Branco, Mariana A., João P. Cotovio, Carlos A.V. Rodrigues, Sandra H. Vaz, Tiago G. Fernandes, Leonilde M. Moreira, Joaquim M.S. Cabral, and Maria Margarida Diogo. 2019. 'Transcriptomic Analysis of 3D Cardiac Differentiation of Human Induced Pluripotent Stem Cells Reveals Faster Cardiomyocyte Maturation Compared to 2D Culture'. *Scientific Reports* 9(1). doi:10.1038/s41598-019-45047-9.

Briganti, Francesca, Han Sun, Wu Wei, Jingyan Wu, Chenchen Zhu, Martin Liss, Ioannis Karakikes, et al. 2020. 'IPSC Modeling of RBM20-Deficient DCM Identifies Upregulation of RBM20 as a Therapeutic Strategy'. *Cell Reports* 32(10). doi:10.1016/j.celrep.2020.108117.

Bugg, Darrian, Ross C Bretherton, Peter Kim, Emily Olszewski, Abigail Nagle, Austin E Schumacher, Nickolas Chu, et al. 2020. 'Infarct Collagen Topography Regulates Fibroblast Fate Via P38-Yap-TEAD Signals.' *Circulation research*: CIRCRESAHA.119.316162. doi:10.1161/CIRCRESAHA.119.316162.

Buikema, Jan W., Soah Lee, William R. Goodyer, Renee G. Maas, Orlando Chirikian, Guang Li, Yi Miao, et al. 2020. 'Wnt Activation and Reduced Cell-Cell Contact Synergistically Induce Massive Expansion of Functional Human IPSC-Derived Cardiomyocytes'. *Cell Stem Cell* 27(1): 50-63.e5. doi:10.1016/j.stem.2020.06.001.

Burnett, Sarah D., Alexander D. Blanchette, Fabian A. Grimm, John S. House, David M. Reif, Fred A. Wright, Weihsueh A. Chiu, and Ivan Rusyn. 2019. 'Population-Based Toxicity Screening in Human Induced Pluripotent Stem Cell-Derived Cardiomyocytes'. *Toxicology and Applied Pharmacology* 381. doi:10.1016/j.taap.2019.114711.

Burridge, Paul W., Elena Matsa, Praveen Shukla, Ziliang C. Lin, Jared M. Churko, Antje D. Ebert, Feng Lan, et al. 2014. 'Chemically Defined Generation of Human Cardiomyocytes'. *Nature Methods 2014 11:8* 11(8): 855–60. doi:10.1038/nmeth.2999.

Cadosch, Nadine, Cristina Gil-Cruz, Christian Perez-Shibayama, and Burkhard Ludewig. 2024. 'Cardiac Fibroblastic Niches in Homeostasis and Inflammation'. *Circulation research* 134(12): 1703–17. doi:10.1161/CIRCRESAHA.124.323892.

Caliari, Steven R., Maryna Perepelyuk, Brian D. Cosgrove, Shannon J. Tsai, Gi Yun Lee, Robert L. Mauck, Rebecca G. Wells, and Jason A. Burdick. 2016. 'Stiffening Hydrogels for

Investigating the Dynamics of Hepatic Stellate Cell Mechanotransduction during Myofibroblast Activation'. *Scientific Reports 2016 6:1* 6(1): 1–10. doi:10.1038/srep21387.

Campostrini, Giulia, Laura M. Windt, Berend J. van Meer, Milena Bellin, and Christine L. Mummery. 2021. 'Cardiac Tissues From Stem Cells'. *Circulation Research* 128(6): 775–801. doi:10.1161/circresaha.121.318183.

Carafoli, Ernesto, Luigia Santella, Donata Branca, and Marisa Brini. 2001. 'Generation, Control, and Processing of Cellular Calcium Signals'. *Critical Reviews in Biochemistry and Molecular Biology* 36(2): 107–260. doi:10.1080/20014091074183.

Carson, Daniel, Marketa Hnilova, Xiulan Yang, Cameron L. Nemeth, Jonathan H. Tsui, Alec S.T. Smith, Alex Jiao, et al. 2016. 'Nanotopography-Induced Structural Anisotropy and Sarcomere Development in Human Cardiomyocytes Derived from Induced Pluripotent Stem Cells'. *ACS Applied Materials and Interfaces* 8(34): 21923–32. doi:10.1021/acsami.5b11671.

Cartledge, James E., Christopher Kane, Priyanthi Dias, Meron Tesfom, Lucy Clarke, Benjamin Mckee, Samha Al Ayoubi, et al. 2015. 'Functional Crosstalk between Cardiac Fibroblasts and Adult Cardiomyocytes by Soluble Mediators'. *Cardiovascular Research* 105(3): 260–70. doi:10.1093/CVR/CVU264.

Chan, Clarence E., and David J. Odde. 2008. 'Traction Dynamics of Filopodia on Compliant Substrates'. *Science* 322(5908): 1687–91. doi:10.1126/science.1163595.

Chen, Yizhou, Jennifer P.Y. Chan, Jun Wu, Ren Ke Li, and J. Paul Santerre. 2022. 'Compatibility and Function of Human Induced Pluripotent Stem Cell Derived Cardiomyocytes on an Electrospun Nanofibrous Scaffold, Generated from an Ionomeric Polyurethane Composite'. *Journal of Biomedical Materials Research - Part A* 110(12): 1932–43. doi:10.1002/jbm.a.37428.

Cho, Sangkyun, Dennis E. Discher, Kam W. Leong, Gordana Vunjak-Novakovic, and Joseph C. Wu. 2022. 'Challenges and Opportunities for the next Generation of Cardiovascular Tissue Engineering'. *Nature Methods 2022 19:9* 19(9): 1064–71. doi:10.1038/s41592-022-01591-3.

Choi, Colin K., Miguel Vicente-Manzanares, Jessica Zareno, Leanna A. Whitmore, Alex Mogilner, and Alan Rick Horwitz. 2008. 'Actin and α-Actinin Orchestrate the Assembly and Maturation of Nascent Adhesions in a Myosin II Motor-Independent Manner'. *Nature Cell Biology 2008 10:9* 10(9): 1039–50. doi:10.1038/ncb1763.

Choi, Suji, Keel Yong Lee, Sean L. Kim, Luke A. MacQueen, Huibin Chang, John F. Zimmerman, Qianru Jin, et al. 2023. 'Fibre-Infused Gel Scaffolds Guide Cardiomyocyte

Alignment in 3D-Printed Ventricles'. *Nature Materials 2023 22:8* 22(8): 1039–46. doi:10.1038/s41563-023-01611-3.

Chopra, Anant, Matthew L. Kutys, Kehan Zhang, William J. Polacheck, Calvin C. Sheng, Rebeccah J. Luu, Jeroen Eyckmans, et al. 2018. 'Force Generation via β-Cardiac Myosin, Titin, and α-Actinin Drives Cardiac Sarcomere Assembly from Cell-Matrix Adhesions'. *Developmental Cell* 44(1): 87-96.e5. doi:10.1016/j.devcel.2017.12.012.

Chopra, Anant, Erdem Tabdanov, Hersh Patel, Paul A. Janmey, and J. Yasha Kresh. 2011. 'Cardiac Myocyte Remodeling Mediated by N-Cadherin-Dependent Mechanosensing'. *American Journal of Physiology - Heart and Circulatory Physiology* 300(4): 1252–66. doi:10.1152/AJPHEART.00515.2010/SUPPL_FILE/FIGURES.

Coeyman, Samuel J., William J. Richardson, and Amy D. Bradshaw. 2022. 'Mechanics and Matrix: Positive Feedback Loops between Fibroblasts and ECM Drive Interstitial Cardiac Fibrosis'. *Current Opinion in Physiology* 28: 100560. doi:10.1016/J.COPHYS.2022.100560.

Cohn, Rachel, Ketan Thakar, Andre Lowe, Feria A. Ladha, Anthony M. Pettinato, Robert Romano, Emily Meredith, et al. 2019. 'A Contraction Stress Model of Hypertrophic Cardiomyopathy Due to Sarcomere Mutations'. *Stem Cell Reports* 12(1): 71–83. doi:10.1016/J.STEMCR.2018.11.015.

Colatsky, Thomas, Bernard Fermini, Gary Gintant, Jennifer B. Pierson, Philip Sager, Yuko Sekino, David G. Strauss, and Norman Stockbridge. 2016. 'The Comprehensive in Vitro Proarrhythmia Assay (CiPA) Initiative — Update on Progress'. *Journal of Pharmacological and Toxicological Methods* 81: 15–20. doi:10.1016/j.vascn.2016.06.002.

Conant, Genevieve, Benjamin Fook Lun Lai, Rick Xing Ze Lu, Anastasia Korolj, Erika Yan Wang, and Milica Radisic. 2017. 'High-Content Assessment of Cardiac Function Using Heart-on-a-Chip Devices as Drug Screening Model'. *Stem Cell Reviews and Reports 2017 13:3* 13(3): 335–46. doi:10.1007/S12015-017-9736-2.

Corbin, Elise A., Alexia Vite, Eliot G. Peyster, Myan Bhoopalam, Jeffrey Brandimarto, Xiao Wang, Alexander I. Bennett, et al. 2019. 'Tunable and Reversible Substrate Stiffness Reveals a Dynamic Mechanosensitivity of Cardiomyocytes'. *ACS Applied Materials & Interfaces* 11(23): 20603–14. doi:10.1021/acsami.9b02446.

Correia, Cláudia, Alexey Koshkin, Patrícia Duarte, Dongjian Hu, Ana Teixeira, Ibrahim Domian, Margarida Serra, and Paula M. Alves. 2017. 'Distinct Carbon Sources Affect Structural and Functional Maturation of Cardiomyocytes Derived from Human Pluripotent Stem Cells'. *Scientific Reports* 7(1). doi:10.1038/s41598-017-08713-4.

Costa, Kevin D., Yasuo Takayama, Andrew D. McCulloch, and James W. Covell. 1999. 'Laminar Fiber Architecture and Three-Dimensional Systolic Mechanics in Canine Ventricular Myocardium'. *American Journal of Physiology - Heart and Circulatory Physiology* 276(2 45-2). doi:10.1152/AJPHEART.1999.276.2.H595/ASSET/IMAGES/LARGE/AHEA40226010X.JPEG.

Cruz Walma, David A., and Kenneth M. Yamada. 2020. 'The Extracellular Matrix in Development'. *Development (Cambridge)* 147(10). doi:10.1242/DEV.175596/224217.

Cui, Haitao, Chengyu Liu, Timothy Esworthy, Yimin Huang, Zu-Xi Yu, Xuan Zhou, Hong San, et al. 2020. *H E A L T H A N D M E D I C I N E 4D Physiologically Adaptable Cardiac Patch: A 4-Month in Vivo Study for the Treatment of Myocardial Infarction*. https://www.science.org.

Cui, Ning, Fujian Wu, Wen Jing Lu, Rui Bai, Bingbing Ke, Taoyan Liu, Lei Li, Feng Lan, and Ming Cui. 2019. 'Doxorubicin-Induced Cardiotoxicity Is Maturation Dependent Due to the Shift from Topoisomerase IIα to IIβ in Human Stem Cell Derived Cardiomyocytes'. *Journal of Cellular and Molecular Medicine* 23(7): 4627–39. doi:10.1111/jcmm.14346.

Cui, Yueli, Yuxuan Zheng, Xixi Liu, Liying Yan, Xiaoying Fan, Jun Yong, Yuqiong Hu, et al. 2019. 'Single-Cell Transcriptome Analysis Maps the Developmental Track of the Human Heart'. *Cell Reports* 26(7): 1934-1950.e5. doi:10.1016/J.CELREP.2019.01.079.

Cyganek, Lukas, Malte Tiburcy, Karolina Sekeres, Kathleen Gerstenberg, Hanibal Bohnenberger, Christof Lenz, Sarah Henze, et al. 2018. 'Deep Phenotyping of Human Induced Pluripotent Stem Cell-Derived Atrial and Ventricular Cardiomyocytes'. *JCI insight* 3(12). doi:10.1172/jci.insight.99941.

Dangman, Kenneth H, Peter Danilo, Allan J Hordof, Luc Mary-rabine, Robert F Reder, and Michael R Rosen. 1982. 65 *Electrophysiologic Characteristics of Human Ventricular and Purkinje Fibers*. http://ahajournals.org.

Danowski, B. A., K. Imanaka-Yoshida, J. M. Sanger, and J. W. Sanger. 1992. 'Costameres Are Sites of Force Transmission to the Substratum in Adult Rat Cardiomyocytes.' *Journal of Cell Biology* 118(6): 1411–20. doi:10.1083/JCB.118.6.1411.

Davidson, C.D., D.K.P. Jayco, D.L. Matera, S.J. DePalma, H.L. Hiraki, W.Y. Wang, and B.M. Baker. 2020. 'Myofibroblast Activation in Synthetic Fibrous Matrices Composed of Dextran Vinyl Sulfone'. *Acta Biomaterialia* 105: 78–86. doi:10.1016/j.actbio.2020.01.009.

Davidson, Christopher D., Firaol S. Midekssa, Samuel J. DePalma, Jordan L. Kamen, William Y. Wang, Danica Kristen P. Jayco, Megan E. Wieger, and Brendon M. Baker. 2024.

‘Mechanical Intercellular Communication via Matrix-Borne Cell Force Transmission During Vascular Network Formation’. *Advanced Science* 11(3): 2306210. doi:10.1002/ADVS.202306210.

Davidson, Christopher D., William Y. Wang, Ina Zaimi, Danica Kristen P. Jayco, and Brendon M. Baker. 2019. ‘Cell Force-Mediated Matrix Reorganization Underlies Multicellular Network Assembly’. *Scientific Reports* 9(1). doi:10.1038/s41598-018-37044-1.

Davidson, Matthew D., Jason A. Burdick, and Rebecca G. Wells. 2020. ‘Engineered Biomaterial Platforms to Study Fibrosis’. *Advanced Healthcare Materials*: 1901682. doi:10.1002/adhm.201901682.

Davis, Justin, Ahmad Chouman, Jeffery Creech, Andre Monteiro da Rocha, Daniela Ponce-Balbuena, Eric N. Jimenez Vazquez, Ruthann Nichols, et al. 2021. ‘In Vitro Model of Ischemic Heart Failure Using Human Induced Pluripotent Stem Cell–Derived Cardiomyocytes’. *JCI Insight* 6(10). doi:10.1172/JCI.INSIGHT.134368.

Delmar, Mario, and William J. McKenna. 2010. ‘The Cardiac Desmosome and Arrhythmogenic Cardiomyopathies: From Gene to Disease’. *Circulation Research* 107(6): 700–714. doi:10.1161/CIRCRESAHA.110.223412.

Denduluri, Sahitya K., Bryan Scott, Joseph D. Lamplot, Liangjun Yin, Zhengjian Yan, Zhongliang Wang, Jixing Ye, et al. 2016. ‘Immortalized Mouse Achilles Tenocytes Demonstrate Long-Term Proliferative Capacity While Retaining Tenogenic Properties’. *Tissue Engineering. Part C, Methods* 22(3): 280. doi:10.1089/TEN.TEC.2015.0244.

DePalma, Samuel J., Christopher D. Davidson, Austin E. Stis, Adam S. Helms, and Brendon M. Baker. 2021. ‘Microenvironmental Determinants of Organized IPSC-Cardiomyocyte Tissues on Synthetic Fibrous Matrices’. *Biomaterials Science* 9(1): 93–107. doi:10.1039/D0BM01247E.

DePalma, Samuel J, Javiera Jillberto, Austin E Stis, Darcy D Huang, Jason Lo, Christopher D Davidson, Aamilah Chowdhury, et al. 2023. ‘Matrix Architecture and Mechanics Regulate Myofibril Organization, Costamere Assembly, and Contractility of Engineered Myocardial Microtissues’. *bioRxiv*: 2023.10.20.563346. doi:10.1101/2023.10.20.563346.

Derrick, Christopher J., and Emily S. Noel. 2021. ‘The ECM as a Driver of Heart Development and Repair’. *Development (Cambridge)* 148(5). doi:10.1242/DEV.191320/237489.

Dickerson, Darryl A. 2022. ‘Advancing Engineered Heart Muscle Tissue Complexity with Hydrogel Composites’. *Advanced Biology*. doi:10.1002/adbi.202200067.

Dou, Wenkun, Li Wang, Manpreet Malhi, Haijiao Liu, Qili Zhao, Julia Plakhotnik, Zhensong Xu, et al. 2021. 'A Microdevice Platform for Characterizing the Effect of Mechanical Strain Magnitudes on the Maturation of IPSC-Cardiomyocytes'. *Biosensors and Bioelectronics* 175. doi:10.1016/j.bios.2020.112875.

Drouin, Emmanuel, Flavien Charpentier, Chantal Gauthier, Karine Laurent, and Herve Le Marec. 1995. 'Electrophysiologic Characteristics of Cells Spanning the Left Ventricular Wall of Human Heart: Evidence for Presence of M Cells'. *Journal of the American College of Cardiology* 26(1): 185–92. doi:10.1016/0735-1097(95)00167-X.

Engler, Adam J., Christine Carag-Krieger, Colin P. Johnson, Matthew Raab, Hsin Yao Tang, David W. Speicher, Joseph W. Sanger, Jean M. Sanger, and Dennis E. Discher. 2008. 'Embryonic Cardiomyocytes Beat Best on a Matrix with Heart-like Elasticity: Scar-like Rigidity Inhibits Beating'. *Journal of Cell Science* 121(22): 3794–3802. doi:10.1242/JCS.029678.

Ergir, Ece, Jorge Oliver-De La Cruz, Soraia Fernandes, Marco Cassani, Francesco Niro, Daniel Pereira-Sousa, Jan Vrbský, et al. 2022. 'Generation and Maturation of Human IPSC-Derived 3D Organotypic Cardiac Microtissues in Long-Term Culture'. *Scientific Reports* 12(1). doi:10.1038/s41598-022-22225-w.

Eschenhagen, Thomas, and Florian Weinberger. 2024. 'Challenges and Perspectives of Heart Repair with Pluripotent Stem Cell-Derived Cardiomyocytes'. *Nature Cardiovascular Research 2024 3:5* 3(5): 515–24. doi:10.1038/s44161-024-00472-6.

Ewoldt, Jourdan, Samuel DePalma, Brendon Baker, and Chen. Christopher. 2023. 'Induced Pluripotent Stem Cell-Derived Cardiomyocyte in Vitro Models: Tissue Fabrication Protocols, Assessment Methods, and Quantitative Maturation Metrics for Benchmarking Progress [Dataset].' *Dryad*.

Ewoldt, Jourdan K., Samuel J. DePalma, Maggie E. Jewett, M. Cagatay Karakan, Yih-Mei Lin, Paria Mir Hashemian, Xining Gao, et al. 2023. 'Induced Pluripotent Stem Cell-Derived Cardiomyocyte in Vitro Models: Tissue Fabrication Protocols, Assessment Methods, and Quantitative Maturation Metrics for Benchmarking Progress [Dataset].' *Dryad*.

Fan, Dong, Abhijit Takawale, Jiwon Lee, and Zamaneh Kassiri. 2012. 'Cardiac Fibroblasts, Fibrosis and Extracellular Matrix Remodeling in Heart Disease.' *Fibrogenesis & tissue repair* 5(1): 15. doi:10.1186/1755-1536-5-15.

Farhadian, Farahnaz, Francis Contard, Alain Corbier, Alice Barrieux, Lydie Rappaport, and Jane Lyse Samuel. 1995. 'Fibronectin Expression during Physiological and Pathological Cardiac

Growth'. *Journal of Molecular and Cellular Cardiology* 27(4): 981–90. doi:10.1016/0022-2828(95)90067-5.

Feaster, Tromondae K., Adrian G. Cadar, Lili Wang, Charles H. Williams, Young Wook Chun, Jonathan E. Hempel, Nathaniel Bloodworth, et al. 2015. 'A Method for the Generation of Single Contracting Human-Induced Pluripotent Stem Cell-Derived Cardiomyocytes'. *Circulation Research* 117(12): 995–1000. doi:10.1161/CIRCRESAHA.115.307580.

Felisbino, Marina B., Marcello Rubino, Joshua G. Travers, Katherine B. Schuetze, Madeleine E. Lemieux, Kristi S. Anseth, Brian A. Aguado, and Timothy A. McKinsey. 2024. 'Substrate Stiffness Modulates Cardiac Fibroblast Activation, Senescence, and Proinflammatory Secretory Phenotype'. *American journal of physiology. Heart and circulatory physiology* 326(1): H61–73. doi:10.1152/AJPHEART.00483.2023/ASSET/IMAGES/LARGE/AJPHEART.00483.2023_F006.JPEG.

Fenix, Aidan M, Abigail C Neininger, Nilay Taneja, Karren Hyde, Mike R Visetsouk, Ryan J Garde, Baohong Liu, et al. 2018. 'Muscle-Specific Stress Fibers Give Rise to Sarcomeres in Cardiomyocytes'. *eLife* 7. doi:10.7554/eLife.42144.

Feric, Nicole T., Isabella Pallotta, Rishabh Singh, Danielle R. Bogdanowicz, Marietta M. Gustilo, Khuram W. Chaudhary, Robert N. Willette, et al. 2019. 'Engineered Cardiac Tissues Generated in the Biowire II: A Platform for Human-Based Drug Discovery'. *Toxicological Sciences* 172(1): 89–97. doi:10.1093/toxsci/kfz168.

Feric, Nicole T., and Milica Radisic. 2016. 'Maturing Human Pluripotent Stem Cell-Derived Cardiomyocytes in Human Engineered Cardiac Tissues'. *Advanced Drug Delivery Reviews* 96: 110–34. doi:10.1016/j.addr.2015.04.019.

Feyen, Dries A.M., Wesley L. McKeithan, Arne A.N. Bruyneel, Sean Spiering, Larissa Hörmann, Bärbel Ulmer, Hui Zhang, et al. 2020. 'Metabolic Maturation Media Improve Physiological Function of Human IPSC-Derived Cardiomyocytes'. *Cell Reports* 32(3). doi:10.1016/j.celrep.2020.107925.

Figtree, Gemma A., Kristen J. Bubb, Owen Tang, Eddy Kizana, and Carmine Gentile. 2017. 'Vascularized Cardiac Spheroids as Novel 3D in Vitro Models to Study Cardiac Fibrosis'. *Cells Tissues Organs* 204(3–4): 191–98. doi:10.1159/000477436.

Fishman, G I, E L Hertzberg, D C Spray, and L A Leinwand. 1991. 'Expression of Connexin43 in the Developing Rat Heart.' *Circulation Research* 68(3): 782–87. doi:10.1161/01.RES.68.3.782.

Fleischer, Sharon, and Tal Dvir. 2013. 'Tissue Engineering on the Nanoscale: Lessons from the Heart'. *Current Opinion in Biotechnology* 24(4): 664–71. doi:10.1016/j.copbio.2012.10.016.

Fleischer, Sharon, Jacob Miller, Haley Hurowitz, Assaf Shapira, and Tal Dvir. 2015. 'Effect of Fiber Diameter on the Assembly of Functional 3D Cardiac Patches'. *Nanotechnology* 26(29): 1–10. doi:10.1088/0957-4484/26/29/291002.

Fleischer, Sharon, Assaf Shapira, Ron Feiner, and Tal Dvir. 2017. 'Modular Assembly of Thick Multifunctional Cardiac Patches'. *Proceedings of the National Academy of Sciences of the United States of America* 114(8): 1898–1903. doi:10.1073/pnas.1615728114.

Van Der Flier, Arjan, Ana C Gaspar, So´lveig So´, So´lveig Thorsteinsdo´ttir, Thorsteinsdo´ Thorsteinsdo´ttir, Christian Baudoin, Els Groeneveld, Christine L Mummery, and Arnoud Sonnenberg. 1997. 'Spatial and Temporal Expression of the 1D Integrin During Mouse Development'. *Dev. Dyn* 210: 472–86. doi:10.1002/(SICI)1097-0177(199712)210:4.

Floy, Martha E., Kaitlin K. Dunn, Taylor D. Mateyka, Isabella M. Reichardt, Alexandra B. Steinberg, and Sean P. Palecek. 2022. 'Direct Coculture of Human Pluripotent Stem Cell-Derived Cardiac Progenitor Cells with Epicardial Cells Induces Cardiomyocyte Proliferation and Reduces Sarcomere Organization'. *Journal of Molecular and Cellular Cardiology* 162: 144–57. doi:10.1016/j.yjmcc.2021.09.009.

Frangogiannis, Nikolaos G. 2012. 'Regulation of the Inflammatory Response in Cardiac Repair' ed. Anthony Rosenzweig. *Circulation Research* 110(1): 159–73. doi:10.1161/CIRCRESAHA.111.243162.

Frangogiannis, Nikolaos G. 2014. 'The Inflammatory Response in Myocardial Injury, Repair, and Remodelling'. *NATURE REVIEWS | CARDIOLOGY* 11: 255–65. doi:10.1038/nrcardio.2014.28.

Frangogiannis, Nikolaos G. 2015. 'Pathophysiology of Myocardial Infarction'. *Comprehensive Physiology* 5(4): 1841–75. doi:10.1002/cphy.c150006.

Frangogiannis, Nikolaos G. 2017. 'The Extracellular Matrix in Myocardial Injury, Repair, and Remodeling'. *The Journal of Clinical Investigation* 127(5): 1600–1612. doi:10.1172/JCI87491.

Frangogiannis, Nikolaos G. 2019. 'The Extracellular Matrix in Ischemic and Nonischemic Heart Failure'. *Circulation Research* 125(1): 117–46. doi:10.1161/CIRCRESAHA.119.311148.

Frangogiannis, Nikolaos G. 2022. 'Transforming Growth Factor-β in Myocardial Disease'. *Nature Reviews Cardiology 2022*: 1–21. doi:10.1038/s41569-021-00646-w.

Frantz, Christian, Kathleen M. Stewart, and Valerie M. Weaver. 2010. 'The Extracellular Matrix at a Glance'. *Journal of Cell Science* 123(24): 4195–4200. doi:10.1242/JCS.023820.

Freeburne, Emily, Seth Teague, Hina Khan, Bolin Li, Siyuan Ding, Bohan Chen, Adam Helms, and Idse Heemskerk. 2023. 'Spatial Single Cell Analysis of Proteins in 2D Human Gastruloids Using Iterative Immunofluorescence'. *Current Protocols* 3(10): e915. doi:10.1002/CPZ1.915.

Fukuda, Ryuichi, Felix Gunawan, Radhan Ramadass, Arica Beisaw, Anne Konzer, Sri Teja Mullapudi, Alessandra Gentile, et al. 2019. 'Mechanical Forces Regulate Cardiomyocyte Myofilament Maturation via the VCL-SSH1-CFL Axis'. *Developmental Cell* 51(1): 62-77.e5. doi:10.1016/J.DEVCEL.2019.08.006.

Fukushima, Hiroyuki, Miki Yoshioka, Masahide Kawatou, Victor Lopez-Davila, Masafumi Takeda, Yasunari Kanda, Yuko Sekino, Yoshinori Yoshida, and Jun K. Yamashita. 2020. 'Specific Induction and Long-Term Maintenance of High Purity Ventricular Cardiomyocytes from Human Induced Pluripotent Stem Cells'. *PLoS ONE* 15(11 November). doi:10.1371/journal.pone.0241287.

Funakoshi, Shunsuke, Kenji Miki, Tadashi Takaki, Chikako Okubo, Takeshi Hatani, Kazuhisa Chonabayashi, Misato Nishikawa, et al. 2016. 'Enhanced Engraftment, Proliferation, and Therapeutic Potential in Heart Using Optimized Human IPSC-Derived Cardiomyocytes'. *Scientific Reports* 6(1): 1–14. doi:10.1038/srep19111.

Gaetani, Roberto, Eric Adriano Zizzi, Marco Agostino Deriu, Umberto Morbiducci, Maurizio Pesce, and Elisa Messina. 2020. 'When Stiffness Matters: Mechanosensing in Heart Development and Disease'. *Frontiers in Cell and Developmental Biology* 8: 334. doi:10.3389/fcell.2020.00334.

Gao, Ling, Zachery R. Gregorich, Wuqiang Zhu, Saidulu Mattapally, Yasin Oduk, Xi Lou, Ramaswamy Kannappan, et al. 2018. 'Large Cardiac Muscle Patches Engineered from Human Induced-Pluripotent Stem Cell-Derived Cardiac Cells Improve Recovery from Myocardial Infarction in Swine'. *Circulation* 137(16): 1712–30. doi:10.1161/CIRCULATIONAHA.117.030785.

Gao, Ling, Molly E. Kupfer, Jangwook P. Jung, Libang Yang, Patrick Zhang, Yong Da Sie, Quyen Tran, et al. 2017. 'Myocardial Tissue Engineering with Cells Derived from Human-Induced Pluripotent Stem Cells and a Native-Like, High-Resolution, 3-Dimensionally Printed Scaffold'. *Circulation Research* 120(8): 1318–25. doi:10.1161/CIRCRESAHA.116.310277/-/DC1.

Garay, Bayardo I., Sophie Givens, Phablo Abreu, Man Liu, Doğacan Yücel, June Baik, Noah Stanis, et al. 2022. 'Dual Inhibition of MAPK and PI3K/AKT Pathways Enhances Maturation of Human IPSC-Derived Cardiomyocytes'. *Stem Cell Reports*. doi:10.1016/J.STEMCR.2022.07.003.

Garbern, Jessica C., Aharon Helman, Rebecca Sereda, Mohsen Sarikhani, Aishah Ahmed, Gabriela O. Escalante, Roza Ogurlu, et al. 2020. 'Inhibition of MTOR Signaling Enhances Maturation of Cardiomyocytes Derived From Human-Induced Pluripotent Stem Cells via P53-Induced Quiescence'. *Circulation* 141(4): 285–300. doi:10.1161/CIRCULATIONAHA.119.044205.

Geng, Le, Zidun Wang, Chang Cui, Yue Zhu, Jiaojiao Shi, Jiaxian Wang, and Minglong Chen. 2018. 'Rapid Electrical Stimulation Increased Cardiac Apoptosis through Disturbance of Calcium Homeostasis and Mitochondrial Dysfunction in Human Induced Pluripotent Stem Cell-Derived Cardiomyocytes'. *Cellular Physiology and Biochemistry* 47(3): 1167–80. doi:10.1159/000490213.

George, Elizabeth L., Elisabeth N. Georges-Labouesse, Ramila S. Patel-King, Helen Rayburn, and Richard O. Hynes. 1993. 'Defects in Mesoderm, Neural Tube and Vascular Development in Mouse Embryos Lacking Fibronectin'. *Development* 119(4): 1079–91. doi:10.1242/DEV.119.4.1079.

Giacomelli, Elisa, Milena Bellin, Luca Sala, Berend J. van Meer, Leon G.J. Tertoolen, Valeria V. Orlova, and Christine L. Mummery. 2017. 'Three-Dimensional Cardiac Microtissues Composed of Cardiomyocytes and Endothelial Cells Co-Differentiated from Human Pluripotent Stem Cells'. *Development (Cambridge)* 144(6): 1008–17. doi:10.1242/dev.143438.

Giacomelli, Elisa, Viviana Meraviglia, Giulia Campostrini, Amy Cochrane, Xu Cao, Ruben W.J. van Helden, Ana Krotenberg Garcia, et al. 2020. 'Human-IPSC-Derived Cardiac Stromal Cells Enhance Maturation in 3D Cardiac Microtissues and Reveal Non-Cardiomyocyte Contributions to Heart Disease'. *Cell Stem Cell* 26(6): 799–801. doi:10.1016/j.stem.2020.05.004.

Godbout, Elena, Dong Ok Son, Stephanie Hume, Stellar Boo, Vincent Sarrazy, Sophie Clément, Andras Kapus, et al. 2020. 'Kindlin-2 Mediates Mechanical Activation of Cardiac Myofibroblasts'. *Cells 2020, Vol. 9, Page 2702* 9(12): 2702. doi:10.3390/CELLS9122702.

Goergen, Craig J., Howard H. Chen, Sava Sakadžić, Vivek J. Srinivasan, and David E. Sosnovik. 2016. 'Microstructural Characterization of Myocardial Infarction with Optical Coherence Tractography and Two-Photon Microscopy'. *Physiological Reports* 4(18): e12894. doi:10.14814/PHY2.12894.

Goffin, Jérôme M., Philippe Pittet, Gabor Csucs, Jost W. Lussi, Jean Jacques Meister, and Boris Hinz. 2006. 'Focal Adhesion Size Controls Tension-Dependent Recruitment of α-Smooth Muscle Actin to Stress Fibers'. *Journal of Cell Biology* 172(2): 259–68. doi:10.1083/JCB.200506179/VIDEO-3.

Goldfracht, Idit, Yael Efraim, Rami Shinnawi, Ekaterina Kovalev, Irit Huber, Amira Gepstein, Gil Arbel, et al. 2019. 'Engineered Heart Tissue Models from HiPSC-Derived Cardiomyocytes and Cardiac ECM for Disease Modeling and Drug Testing Applications'. *Acta Biomaterialia* 92: 145–59. doi:10.1016/j.actbio.2019.05.016.

Goldsmith, Edie C., Amy D. Bradshaw, Michael R. Zile, and Francis G. Spinale. 2014. 'Myocardial Fibroblast–Matrix Interactions and Potential Therapeutic Targets'. *Journal of Molecular and Cellular Cardiology* 70: 92–99. doi:10.1016/J.YJMCC.2014.01.008.

Goldsmith, Edie C., Adam Hoffman, Mary O. Morales, Jay D. Potts, Robert L. Price, Alex McFadden, Michael Rice, and Thomas K. Borg. 2004. 'Organization of Fibroblasts in the Heart'. *Developmental Dynamics* 230(4): 787–94. doi:10.1002/DVDY.20095.

González, Arantxa, Begoña López, Susana Ravassa, Gorka San José, Iñigo Latasa, Javed Butler, and Javier Díez. 2024. 'Myocardial Interstitial Fibrosis in Hypertensive Heart Disease: From Mechanisms to Clinical Management'. *Hypertension* 81(2): 218–28. doi:10.1161/HYPERTENSIONAHA.123.21708.

González, Arantxa, Susana Ravassa, Begoña López, María U. Moreno, Javier Beaumont, Gorka San José, Ramón Querejeta, Antoni Bayés-Genís, and Javier Díez. 2018. 'Myocardial Remodeling in Hypertension'. *Hypertension* 72(3): 549–58. doi:10.1161/HYPERTENSIONAHA.118.11125.

Granados-Riveron, Javier T., and J. David Brook. 2012. 'The Impact of Mechanical Forces in Heart Morphogenesis'. *Circulation: Cardiovascular Genetics* 5(1): 132–42. doi:10.1161/CIRCGENETICS.111.961086.

Grancharova, Tanya, Kaytlyn A. Gerbin, Alexander B. Rosenberg, Charles M. Roco, Joy E. Arakaki, Colette M. DeLizo, Stephanie Q. Dinh, et al. 2021. 'A Comprehensive Analysis of Gene Expression Changes in a High Replicate and Open-Source Dataset of Differentiating HiPSC-Derived Cardiomyocytes'. *Scientific Reports* 11(1). doi:10.1038/s41598-021-94732-1.

Grashoff, Carsten, Brenton D. Hoffman, Michael D. Brenner, Ruobo Zhou, Maddy Parsons, Michael T. Yang, Mark A. McLean, et al. 2010. 'Measuring Mechanical Tension across Vinculin Reveals Regulation of Focal Adhesion Dynamics'. *Nature 2010 466:7303* 466(7303): 263–66. doi:10.1038/nature09198.

Guo, Jingxuan, Daniel W. Simmons, Ghiska Ramahdita, Mary K. Munsell, Kasoorelope Oguntuyo, Brennan Kandalaft, Brandon Rios, et al. 2021. 'Elastomer-Grafted IPSC-Derived Micro Heart Muscles to Investigate Effects of Mechanical Loading on Physiology'. *ACS Biomaterials Science and Engineering* 7(7): 2973–89. doi:10.1021/ACSBIOMATERIALS.0C00318/SUPPL_FILE/AB0C00318_SI_005.AVI.

Guo, Yuxuan, Yangpo Cao, Blake D. Jardin, Isha Sethi, Qing Ma, Behzad Moghadaszadeh, Emily C. Troiano, et al. 2021. 'Sarcomeres Regulate Murine Cardiomyocyte Maturation through MRTF-SRF Signaling'. *Proceedings of the National Academy of Sciences of the United States of America* 118(2): e2008861118. doi:10.1073/PNAS.2008861118/SUPPL_FILE/PNAS.2008861118.SD01.XLSX.

Guo, Yuxuan, and William T. Pu. 2020. 'Cardiomyocyte Maturation'. *Circulation Research* 126(8): 1086–1106. doi:10.1161/CIRCRESAHA.119.315862.

Gut, Gabriele, Markus D. Herrmann, and Lucas Pelkmans. 2018. 'Multiplexed Protein Maps Link Subcellular Organization to Cellular States'. *Science* 361(6401). doi:10.1126/SCIENCE.AAR7042/SUPPL_FILE/AAR7042_TABLE_S4.CSV.

Guthold, M., W. Liu, E. A. Sparks, L. M. Jawerth, L. Peng, M. Falvo, R. Superfine, R. R. Hantgan, and S. T. Lord. 2007. 'A Comparison of the Mechanical and Structural Properties of Fibrin Fibers with Other Protein Fibers'. *Cell Biochemistry and Biophysics* 49(3): 165–81. doi:10.1007/S12013-007-9001-4/FIGURES/6.

Guyette, Jacques P., Jonathan M. Charest, Robert W. Mills, Bernhard J. Jank, Philipp T. Moser, Sarah E. Gilpin, Joshua R. Gershlak, et al. 2016. 'Bioengineering Human Myocardium on Native Extracellular Matrix'. *Circulation Research* 118(1): 56–72. doi:10.1161/CIRCRESAHA.115.306874.

Haack, Timm, and Salim Abdelilah-Seyfried. 2016. 'The Force within: Endocardial Development, Mechanotransduction and Signalling during Cardiac Morphogenesis'. *Development* 143(3): 373–86. doi:10.1242/DEV.131425.

Haas, Jan, Karen Frese, Barbara Peil, Wanda Kloos, Elham Kayvanpour, Britta Vogel, Farbod Sedaghat-Hamedani, et al. 2015. 'Atlas of the Clinical Genetics of Human Dilated Cardiomyopathy'. *European Heart Journal* 36(18): 1123–35. doi:10.1093/eurheartj/ehu402.

Hall, Caitlin, Katja Gehmlich, Chris Denning, and Davor Pavlovic. 2021. 'Complex Relationship Between Cardiac Fibroblasts and Cardiomyocytes in Health and Disease'. *Journal of the American Heart Association* 10(5): 1–15. doi:10.1161/JAHA.120.019338.

Han, Jingjia, Qingling Wu, Younan Xia, Mary B. Wagner, and Chunhui Xu. 2016. 'Cell Alignment Induced by Anisotropic Electrospun Fibrous Scaffolds Alone Has Limited Effect

on Cardiomyocyte Maturation'. *Stem Cell Research* 16(3): 740–50. doi:10.1016/j.scr.2016.04.014.

Hanna, Anis, and Nikolaos G. Frangogiannis. 2019. 'The Role of the TGF-β Superfamily in Myocardial Infarction'. *Frontiers in Cardiovascular Medicine* 6: 140. doi:10.3389/fcvm.2019.00140.

Hart, Cacie, Avra Kundu, Kowsik Kumar, Sreekanth J. Varma, Jayan Thomas, and Swaminathan Rajaraman. 2018. 'Rapid Nanofabrication of Nanostructured Interdigitated Electrodes (NIDES) for Long-Term in Vitro Analysis of Human Induced Pluripotent Stem Cell Differentiated Cardiomyocytes'. *Biosensors* 8(4). doi:10.3390/bios8040088.

Harvey, Pamela A., and Leslie A. Leinwand. 2011. 'Cellular Mechanisms of Cardiomyopathy'. *Journal of Cell Biology* 194(3): 355–65. doi:10.1083/jcb.201101100.

Hasenfuss, Gerd, Louis A Mulieri, Edward M Blanchard, Christian Holubarsch, Bruce J Leavitt, Frank Ittleman, and Norman R Alpert. 1990. *Energetics of Isometric Force Development in Control and Volume-Overload Human Myocardium Comparison With Animal Species*. http://ahajournals.org.

Hashimoto, Hisayuki, Eric N. Olson, and Rhonda Bassel-Duby. 2018. 'Therapeutic Approaches for Cardiac Regeneration and Repair'. *Nature Reviews Cardiology 2018 15:10* 15(10): 585–600. doi:10.1038/s41569-018-0036-6.

Hatani, Takeshi, Shunsuke Funakoshi, Thomas J. Deerinck, Eric A. Bushong, Takeshi Kimura, Hiroshi Takeshima, Mark H. Ellisman, Masahiko Hoshijima, and Yoshinori Yoshida. 2018. 'Nano-Structural Analysis of Engrafted Human Induced Pluripotent Stem Cell-Derived Cardiomyocytes in Mouse Hearts Using a Genetic-Probe APEX2'. *Biochemical and Biophysical Research Communications* 505(4): 1251–56. doi:10.1016/j.bbrc.2018.10.020.

Hawley, Megan H., Naif Almontashiri, Leslie G. Biesecker, Natalie Berger, Wendy K. Chung, John Garcia, Theresa A. Grebe, et al. 2020. 'An Assessment of the Role of Vinculin Loss of Function Variants in Inherited Cardiomyopathy'. *Human Mutation* 41(9): 1577–87. doi:10.1002/HUMU.24061.

Heineke, Joerg, and Jeffery D. Molkentin. 2006. 'Regulation of Cardiac Hypertrophy by Intracellular Signalling Pathways'. *Nature Reviews Molecular Cell Biology 2006 7:8* 7(8): 589–600. doi:10.1038/nrm1983.

Herron, Todd J., Andre Monteiro Da Rocha, Katherine F. Campbell, Daniela Ponce-Balbuena, B. Cicero Willis, Guadalupe Guerrero-Serna, Qinghua Liu, et al. 2016. 'Extracellular Matrix-Mediated Maturation of Human Pluripotent Stem Cell-Derived Cardiac Monolayer

Structure and Electrophysiological Function'. *Circulation: Arrhythmia and Electrophysiology* 9(4): e003638. doi:10.1161/CIRCEP.113.003638.

Herum, Kate M., Jonas Choppe, Aditya Kumar, Adam J. Engler, and Andrew D. McCulloch. 2017. 'Mechanical Regulation of Cardiac Fibroblast Pro-Fibrotic Phenotypes' ed. Andres J. Garcia. *Molecular Biology of the Cell*: mbc.E17-01-0014. doi:10.1091/mbc.E17-01-0014.

Hinson, John T., Anant Chopra, Navid Nafissi, William J. Polacheck, Craig C. Benson, Sandra Swist, Joshua Gorham, et al. 2015. 'Titin Mutations in IPS Cells Define Sarcomere Insufficiency as a Cause of Dilated Cardiomyopathy'. *Science* 349(6251): 982–86. doi:10.1126/science.aaa5458.

Hinz, Boris. 2006. 'Masters and Servants of the Force: The Role of Matrix Adhesions in Myofibroblast Force Perception and Transmission'. *European Journal of Cell Biology* 85(3–4): 175–81. doi:10.1016/j.ejcb.2005.09.004.

Ho, Carolyn Y., Sharlene M. Day, Euan A. Ashley, Michelle Michels, Alexandre C. Pereira, Daniel Jacoby, Allison L. Cirino, et al. 2018. 'Genotype and Lifetime Burden of Disease in Hypertrophic Cardiomyopathy Insights from the Sarcomeric Human Cardiomyopathy Registry (SHaRe)'. *Circulation* 138(14): 1387–98. doi:10.1161/CIRCULATIONAHA.117.033200.

Ho, Carolyn Y., Begoña López, Otavio R. Coelho-Filho, Neal K. Lakdawala, Allison L. Cirino, Petr Jarolim, Raymond Kwong, et al. 2010. 'Myocardial Fibrosis as an Early Manifestation of Hypertrophic Cardiomyopathy'. *New England Journal of Medicine* 363(6): 552–63. doi:10.1056/NEJMOA1002659/SUPPL_FILE/NEJMOA1002659_DISCLOSURES.PDF.

Hofbauer, Pablo, Stefan M. Jahnel, and Sasha Mendjan. 2021. 'In Vitro Models of the Human Heart'. *Development* 148(16). doi:10.1242/DEV.199672.

Holmes, Jeffrey W., Thomas K. Borg, and James W. Covell. 2005. 'Structure and Mechanics of Healing Myocardial Infarcts'. *Annual Review of Biomedical Engineering* 7(Volume 7, 2005): 223–53. doi:10.1146/ANNUREV.BIOENG.7.060804.100453/CITE/REFWORKS.

Hookway, Tracy A., Oriane B. Matthys, Federico N. Mendoza-Camacho, Sarah Rains, Jessica E. Sepulveda, David A. Joy, and Todd C. Mcdevitt. 2019. 'Phenotypic Variation between Stromal Cells Differentially Impacts Engineered Cardiac Tissue Function'. *Tissue Engineering - Part A* 25(9–10): 773–85. doi:10.1089/ten.tea.2018.0362.

Horikoshi, Yuichi, Yasheng Yan, Maia Terashvili, Clive Wells, Hisako Horikoshi, Satoshi Fujita, Zeljko J. Bosnjak, and Xiaowen Bai. 2019. 'Fatty Acid-Treated Induced Pluripotent Stem Cell-Derived Human Cardiomyocytes Exhibit Adult Cardiomyocyte-like Energy Metabolism Phenotypes'. *Cells* 8(9). doi:10.3390/cells8091095.

Houseman, B T, and M Mrksich. 2001. 22 Biomaterials *The Microenvironment of Immobilized Arg-Gly-Asp Peptides Is an Important Determinant of Cell Adhesion*.

Hove, Jay R., Reinhard W. Köster, Arian S. Forouhar, Gabriel Acevedo-Bolton, Scott E. Fraser, and Morteza Gharib. 2003. 'Intracardiac Fluid Forces Are an Essential Epigenetic Factor for Embryonic Cardiogenesis'. *Nature 2003 421:6919* 421(6919): 172–77. doi:10.1038/nature01282.

Huang, Chen Yu, Rebeca Peres Moreno Maia-Joca, Chin Siang Ong, Ijala Wilson, Deborah DiSilvestre, Gordon F. Tomaselli, and Daniel H. Reich. 2020. 'Enhancement of Human IPSC-Derived Cardiomyocyte Maturation by Chemical Conditioning in a 3D Environment'. *Journal of Molecular and Cellular Cardiology* 138: 1–11. doi:10.1016/j.yjmcc.2019.10.001.

Huebsch, Nathaniel, Berenice Charrez, Gabriel Neiman, Brian Siemons, Steven C. Boggess, Samuel Wall, Verena Charwat, et al. 2022. 'Metabolically Driven Maturation of Human-Induced-Pluripotent-Stem-Cell-Derived Cardiac Microtissues on Microfluidic Chips'. *Nature Biomedical Engineering 2022 6:4* 6(4): 372–88. doi:10.1038/s41551-022-00884-4.

Huebsch, Nathaniel, Peter Loskill, Nikhil Deveshwar, C. Ian Spencer, Luke M. Judge, Mohammad A. Mandegar, Cade B. Fox, et al. 2016. 'Miniaturized IPS-Cell-Derived Cardiac Muscles for Physiologically Relevant Drug Response Analyses'. *Scientific Reports* 6(1): 1–12. doi:10.1038/srep24726.

Huebsch, Nathaniel, Peter Loskill, Mohammad A. Mandegar, Natalie C. Marks, Alice S. Sheehan, Zhen Ma, Anurag Mathur, et al. 2015. 'Automated Video-Based Analysis of Contractility and Calcium Flux in Human-Induced Pluripotent Stem Cell-Derived Cardiomyocytes Cultured over Different Spatial Scales'. *Tissue Engineering - Part C: Methods* 21(5): 467–79. doi:10.1089/ten.tec.2014.0283.

Huethorst, Eline, Marie F.A. Cutiongco, Fraser A. Campbell, Anwer Saeed, Rachel Love, Paul M. Reynolds, Matthew J. Dalby, and Nikolaj Gadegaard. 2020. 'Customizable, Engineered Substrates for Rapid Screening of Cellular Cues'. *Biofabrication* 12(2). doi:10.1088/1758-5090/ab5d3f.

Ieda, Masaki, Takatoshi Tsuchihashi, Kathryn N. Ivey, Robert S. Ross, Ting Ting Hong, Robin M. Shaw, and Deepak Srivastava. 2009. 'Cardiac Fibroblasts Regulate Myocardial Proliferation through B1 Integrin Signaling'. *Developmental Cell* 16(2): 233–44. doi:10.1016/J.DEVCEL.2008.12.007.

Israeli-Rosenberg, Sharon, Ana Maria Manso, Hideshi Okada, and Robert S. Ross. 2014. 'Integrins and Integrin-Associated Proteins in the Cardiac Myocyte'. *Circulation Research* 114(3): 572–86. doi:10.1161/CIRCRESAHA.114.301275/-/DC1.

Jabbour, Richard J, Thomas J Owen, Pragati Pandey, Marina Reinsch, Brian Wang, Oisín King, Liam Steven Couch, et al. 2021. 'In Vivo Grafting of Large Engineered Heart Tissue Patches for Cardiac Repair'. doi:10.1172/jci.

Jackman, Christopher P., Aaron L. Carlson, and Nenad Bursac. 2016. 'Dynamic Culture Yields Engineered Myocardium with Near-Adult Functional Output'. *Biomaterials* 111: 66–79. doi:10.1016/j.biomaterials.2016.09.024.

Jacot, Jeffrey G., Jody C. Martin, and Darlene L. Hunt. 2010. 'Mechanobiology of Cardiomyocyte Development'. *Journal of Biomechanics* 43(1): 93–98. doi:10.1016/J.JBIOMECH.2009.09.014.

Jacot, Jeffrey G., Andrew D. McCulloch, and Jeffrey H. Omens. 2008. 'Substrate Stiffness Affects the Functional Maturation of Neonatal Rat Ventricular Myocytes'. *Biophysical Journal* 95(7): 3479–87. doi:10.1529/biophysj.107.124545.

Järveläinen, Hannu, Annele Sainio, Markku Koulu, Thomas N. Wight, and Risto Penttinen. 2009. 'Extracellular Matrix Molecules: Potential Targets in Pharmacotherapy'. *Pharmacological Reviews* 61(2): 198–223. doi:10.1124/PR.109.001289.

Jayne, Rachael K., M. Çağatay Karakan, Kehan Zhang, Noelle Pierce, Christos Michas, David J. Bishop, Christopher S. Chen, Kamil L. Ekinci, and Alice E. White. 2021. 'Direct Laser Writing for Cardiac Tissue Engineering: A Microfluidic Heart on a Chip with Integrated Transducers'. *Lab on a Chip* 21(9): 1724–37. doi:10.1039/d0lc01078b.

Jia, Jia, Robert C. Coyle, Dylan J. Richards, Christopher Lloyd Berry, Ryan Walker Barrs, Joshua Biggs, C. James Chou, Thomas C. Trusk, and Ying Mei. 2016. 'Development of Peptide-Functionalized Synthetic Hydrogel Microarrays for Stem Cell and Tissue Engineering Applications'. *Acta Biomaterialia* 45: 110–20. doi:10.1016/j.actbio.2016.09.006.

Jilberto, Javiera, Samuel J. DePalma, Jason Lo, Hiba Kobeissi, Lani Quach, Emma Lejeune, Brendon M. Baker, and David Nordsletten. 2023. 'A Data-Driven Computational Model for Engineered Cardiac Microtissues'. *Acta Biomaterialia*. doi:10.1016/J.ACTBIO.2023.10.025.

Jordan, Elizabeth, Laiken Peterson, Tomohiko Ai, Babken Asatryan, Lucas Bronicki, Emily Brown, Rudy Celeghin, et al. 2021. 'Evidence-Based Assessment of Genes in Dilated

Cardiomyopathy'. *Circulation* 144(1): 7–19. doi:10.1161/CIRCULATIONAHA.120.053033.

Jung, Gwanghyun, Giovanni Fajardo, Alexandre J.S. Ribeiro, Kristina Bezold Kooiker, Michael Coronado, Mingming Zhao, Dong Qing Hu, et al. 2016. 'Time-Dependent Evolution of Functional vs. Remodeling Signaling in Induced Pluripotent Stem Cell-Derived Cardiomyocytes and Induced Maturation with Biomechanical Stimulation'. *The FASEB Journal* 30(4): 1464–79. doi:10.1096/FJ.15-280982.

Kaiser, Nicholas J., Rajeev J. Kant, Alicia J. Minor, and Kareen L.K. Coulombe. 2019. 'Optimizing Blended Collagen-Fibrin Hydrogels for Cardiac Tissue Engineering with Human IPSC-Derived Cardiomyocytes'. *ACS Biomaterials Science and Engineering* 5(2): 887–99. doi:10.1021/acsbiomaterials.8b01112.

Kakkar, Rahul, and Richard T. Lee. 2010. 'Intramyocardial Fibroblast Myocyte Communication'. *Circulation Research* 106(1): 47–57. doi:10.1161/CIRCRESAHA.109.207456.

Kamakura, Tsukasa, Takeru Makiyama, Kenichi Sasaki, Yoshinori Yoshida, Yimin Wuriyanghai, Jiarong Chen, Tetsuhisa Hattori, et al. 2013. 'Ultrastructural Maturation of Human-Induced Pluripotent Stem Cell-Derived Cardiomyocytes in a Long-Term Culture'. *Circulation Journal* 77(5): 1307–14. doi:10.1253/CIRCJ.CJ-12-0987.

Kanchanawong, Pakorn, and David A. Calderwood. 2022. 'Organization, Dynamics and Mechanoregulation of Integrin-Mediated Cell–ECM Adhesions'. *Nature Reviews Molecular Cell Biology 2022 24:2* 24(2): 142–61. doi:10.1038/s41580-022-00531-5.

Kanisicak, Onur, Hadi Khalil, Malina J. Ivey, Jason Karch, Bryan D. Maliken, Robert N. Correll, Matthew J. Brody, et al. 2016. 'Genetic Lineage Tracing Defines Myofibroblast Origin and Function in the Injured Heart'. *Nature Communications* 7(1): 1–14. doi:10.1038/ncomms12260.

Kanzaki, Yumiko, Fumio Terasaki, Makoto Okabe, Shuichi Fujita, Takashi Katashima, Kaoru Otsuka, and Nobukazu Ishizaka. 2010. 'Three-Dimensional Architecture of Cardiomyocytes and Connective Tissue in Human Heart Revealed by Scanning Electron Microscopy'. *Circulation* 122(19): 1973–74. doi:10.1161/CIRCULATIONAHA.110.979815.

Karbassi, Elaheh, Aidan Fenix, Silvia Marchiano, Naoto Muraoka, Kenta Nakamura, Xiulan Yang, and Charles E. Murry. 2020. 'Cardiomyocyte Maturation: Advances in Knowledge and Implications for Regenerative Medicine'. *Nature Reviews Cardiology* 17(6): 341–59. doi:10.1038/s41569-019-0331-x.

Kaur, Kuljeet, Manuel Zarzoso, Daniela Ponce-Balbuena, Guadalupe Guerrero-Serna, Luqia Hou, Hassan Musa, and José Jalife. 2013. 'TGF-B1, Released by Myofibroblasts, Differentially Regulates Transcription and Function of Sodium and Potassium Channels in Adult Rat Ventricular Myocytes'. *PLOS ONE* 8(2): e55391. doi:10.1371/JOURNAL.PONE.0055391.

Kaushik, Gaurav, Alice Spenlehauer, Ayla O. Sessions, Adriana S. Trujillo, Alexander Fuhrmann, Zongming Fu, Vidya Venkatraman, et al. 2015. 'Vinculin Network-Mediated Cytoskeletal Remodeling Regulates Contractile Function in the Aging Heart'. *Science Translational Medicine* 7(292). doi:10.1126/SCITRANSLMED.AAA5843.

Kent, Robert N., Mohamed Said, Megan E. Busch, Ethan R. Poupard, Ariane Tsai, Jingyi Xia, Daniel L. Matera, et al. 2022. 'Physical and Soluble Cues Enhance Tendon Progenitor Cell Invasion into Injectable Synthetic Hydrogels'. *Advanced Functional Materials* 32(48): 2207556. doi:10.1002/ADFM.202207556.

Kerscher, Petra, Irene C. Turnbull, Alexander J. Hodge, Joonyul Kim, Dror Seliktar, Christopher J. Easley, Kevin D. Costa, and Elizabeth A. Lipke. 2016. 'Direct Hydrogel Encapsulation of Pluripotent Stem Cells Enables Ontomimetic Differentiation and Growth of Engineered Human Heart Tissues'. *Biomaterials* 83: 383–95. doi:10.1016/j.biomaterials.2015.12.011.

Khalil, Hadi, Onur Kanisicak, Vikram Prasad, Robert N. Correll, Xing Fu, Tobias Schips, Ronald J. Vagnozzi, et al. 2017. 'Fibroblast-Specific TGF-β–Smad2/3 Signaling Underlies Cardiac Fibrosis'. *The Journal of Clinical Investigation* 127(10): 3770–83. doi:10.1172/JCI94753.

Khan, Mahmood, Yanyi Xu, Serena Hua, Jed Johnson, Andriy Belevych, Paul M.L. Janssen, Sandor Gyorke, Jianjun Guan, and Mark G. Angelos. 2015. 'Evaluation of Changes in Morphology and Function of Human Induced Pluripotent Stem Cell Derived Cardiomyocytes (HiPSC-CMs) Cultured on an Aligned-Nanofiber Cardiac Patch'. *PLoS ONE* 10(5): 1–19. doi:10.1371/journal.pone.0126338.

Kharaziha, Mahshid, Mehdi Nikkhah, Su Ryon Shin, Nasim Annabi, Nafiseh Masoumi, Akhilesh K. Gaharwar, Gulden Camci-Unal, and Ali Khademhosseini. 2013. 'PGS:Gelatin Nanofibrous Scaffolds with Tunable Mechanical and Structural Properties for Engineering Cardiac Tissues'. *Biomaterials* 34(27): 6355–66. doi:10.1016/j.biomaterials.2013.04.045.

Kidokoro, Hinako, Sayuri Yonei-Tamura, Koji Tamura, Gary C. Schoenwolf, and Yukio Saijoh. 2018. 'The Heart Tube Forms and Elongates through Dynamic Cell Rearrangement Coordinated with Foregut Extension'. *Development (Cambridge)* 145(7). doi:10.1242/DEV.152488/VIDEO-7.

Kim, Sudong, Marina Uroz, Jennifer L. Bays, and Christopher S. Chen. 2021. 'Harnessing Mechanobiology for Tissue Engineering'. *Developmental Cell* 56(2): 180–91. doi:10.1016/j.devcel.2020.12.017.

Kit-Anan, Worrapong, Manuel M. Mazo, Brian X. Wang, Vincent Leonardo, Isaac J. Pence, Sahana Gopal, Amy Gelmi, et al. 2021. 'Multiplexing Physical Stimulation on Single Human Induced Pluripotent Stem Cell-Derived Cardiomyocytes for Phenotype Modulation'. *Biofabrication* 13(2). doi:10.1088/1758-5090/abce0a.

Knight, Walter E., Yingqiong Cao, Ying Hsi Lin, Congwu Chi, Betty Bai, Genevieve C. Sparagna, Yuanbiao Zhao, et al. 2021. 'Maturation of Pluripotent Stem Cell-Derived Cardiomyocytes Enables Modeling of Human Hypertrophic Cardiomyopathy'. *Stem Cell Reports* 16(3): 519–33. doi:10.1016/j.stemcr.2021.01.018.

Knöll, Ralph, Masahiko Hoshijima, and Kenneth Chien. 2003. 'Cardiac Mechanotransduction and Implications for Heart Disease'. *Journal of Molecular Medicine* 81(12): 750–56. doi:10.1007/S00109-003-0488-X/TABLES/1.

Kobayashi, Hideki, Shugo Tohyama, Hajime Ichimura, Noburo Ohashi, Shuji Chino, Yusuke Soma, Hidenori Tani, et al. 2024. 'Regeneration of Nonhuman Primate Hearts With Human Induced Pluripotent Stem Cell-Derived Cardiac Spheroids.' *Circulation*. doi:10.1161/CIRCULATIONAHA.123.064876.

Kobeissi, Hiba, Javiera Jilberto, M. Çağatay Karakan, Xining Gao, Samuel J. DePalma, Shoshana L. Das, Lani Quach, et al. 2023. 'MicroBundleCompute: Automated Segmentation, Tracking, and Analysis of Subdomain Deformation in Cardiac Microbundles'. *arXiv preprint arXiv:2308.04610*. https://arxiv.org/abs/2308.04610v1 (October 18, 2023).

Kocadal, Kumsal. 2018. 'İlaca Bağlı Kardiyovasküler Risk: Geri Çekilen İlaçların Retrospektif Değerlendirilmesi'. *Northern Clinics of Istanbul*. doi:10.14744/nci.2018.44977.

Kofron, Celinda M., Tae Yun Kim, Fabiola Munarin, Arvin H. Soepriatna, Rajeev J. Kant, Ulrike Mende, Bum Rak Choi, and Kareen L.K. Coulombe. 2021. 'A Predictive in Vitro Risk Assessment Platform for Pro-Arrhythmic Toxicity Using Human 3D Cardiac Microtissues'. *Scientific Reports* 11(1). doi:10.1038/s41598-021-89478-9.

Kolanowski, Tomasz Jan, Mathias Busek, Mario Schubert, Anna Dmitrieva, Björn Binnewerg, Jessie Pöche, Konstanze Fisher, et al. 2020. 'Enhanced Structural Maturation of Human Induced Pluripotent Stem Cell-Derived Cardiomyocytes under a Controlled Microenvironment in a Microfluidic System'. *Acta Biomaterialia* 102: 273–86. doi:10.1016/j.actbio.2019.11.044.

Koncz, István, Tamás Szél, Miklós Bitay, Elisabetta Cerbai, Kristian Jaeger, Ferenc Fülöp, Norbert Jost, et al. 2011. 'Electrophysiological Effects of Ivabradine in Dog and Human Cardiac Preparations: Potential Antiarrhythmic Actions'. *European Journal of Pharmacology* 668(3): 419–26. doi:10.1016/j.ejphar.2011.07.025.

Kong, Ping, Panagiota Christia, and Nikolaos G. Frangogiannis. 2014. 'The Pathogenesis of Cardiac Fibrosis'. *Cellular and Molecular Life Sciences* 71(4): 549–74. doi:10.1007/s00018-013-1349-6.

Kong, Ping, Panagiota Christia, Amit Saxena, Ya Su, and Nikolaos G. Frangogiannis. 2013. 'Lack of Specificity of Fibroblast-Specific Protein 1 in Cardiac Remodeling and Fibrosis'. *American Journal of Physiology - Heart and Circulatory Physiology* 305(9): 1363–72. doi:10.1152/AJPHEART.00395.2013/ASSET/IMAGES/LARGE/ZH40211309210006.JPEG.

Kroll, Katharina, Mamta Chabria, Ken Wang, Fabian Häusermann, Franz Schuler, and Liudmila Polonchuk. 2017. 'Electro-Mechanical Conditioning of Human IPSC-Derived Cardiomyocytes for Translational Research'. *Progress in Biophysics and Molecular Biology* 130: 212–22. doi:10.1016/j.pbiomolbio.2017.07.003.

Kujala, Ville J., Francesco Silvio Pasqualini, Josue A. Goss, Janna C. Nawroth, and Kevin Kit Parker. 2016. 'Laminar Ventricular Myocardium on a Microelectrode Array-Based Chip'. *Journal of Materials Chemistry B* 4(20): 3534–43. doi:10.1039/c6tb00324a.

Kumar, Aditya, Stephanie K. Thomas, Kirsten C. Wong, Valentina Lo Sardo, Daniel S. Cheah, Yang Hsun Hou, Jesse K. Placone, et al. 2019. 'Mechanical Activation of Noncoding-RNA-Mediated Regulation of Disease-Associated Phenotypes in Human Cardiomyocytes'. *Nature Biomedical Engineering* 3(2): 137–46. doi:10.1038/s41551-018-0344-5.

Kumar, Naresh, Divya Sridharan, Arunkumar Palaniappan, Julie A. Dougherty, Andras Czirok, Dona Greta Isai, Muhamad Mergaye, et al. 2020. 'Scalable Biomimetic Coaxial Aligned Nanofiber Cardiac Patch: A Potential Model for "Clinical Trials in a Dish"'. *Frontiers in Bioengineering and Biotechnology* 8. doi:10.3389/fbioe.2020.567842.

Laflamme, Michael A., and Charles E. Murry. 2005. 'Regenerating the Heart'. *Nature Biotechnology* 23(7): 845–56. doi:10.1038/nbt1117.

LaFramboise, W. A., D. Scalise, P. Stoodley, S. R. Graner, R. D. Guthrie, J. A. Magovern, and M. J. Becich. 2007. 'Cardiac Fibroblasts Influence Cardiomyocyte Phenotype in Vitro'. *American Journal of Physiology - Cell Physiology* 292(5): 1799–1808. doi:10.1152/AJPCELL.00166.2006/ASSET/IMAGES/LARGE/ZH00050752080007.JPEG.

de Lange, Willem J., Emily T. Farrell, Caroline R. Kreitzer, Derek R. Jacobs, Di Lang, Alexey V. Glukhov, and J. Carter Ralphe. 2021. 'Human IPSC-Engineered Cardiac Tissue Platform Faithfully Models Important Cardiac Physiology'. *American Journal of Physiology - Heart and Circulatory Physiology* 320(4): H1670–86. doi:10.1152/AJPHEART.00941.2020.

Lapp, Hendrik, Tobias Bruegmann, Daniela Malan, Stephanie Friedrichs, Carsten Kilgus, Alexandra Heidsieck, and Philipp Sasse. 2021. 'Author Correction: Frequency-Dependent Drug Screening Using Optogenetic Stimulation of Human IPSC-Derived Cardiomyocytes (Scientific Reports, (2017), 7, 1, (9629), 10.1038/S41598-017-09760-7)'. *Scientific Reports* 11(1). doi:10.1038/s41598-020-80763-7.

Lee, Jee Hoon, Stephanie I. Protze, Zachary Laksman, Peter H. Backx, and Gordon M. Keller. 2017. 'Human Pluripotent Stem Cell-Derived Atrial and Ventricular Cardiomyocytes Develop from Distinct Mesoderm Populations'. *Cell Stem Cell* 21(2): 179-194.e4. doi:10.1016/j.stem.2017.07.003.

Lee, Soah, Vahid Serpooshan, Xinming Tong, Sneha Venkatraman, Meelim Lee, Jaecheol Lee, Orlando Chirikian, et al. 2017. 'Contractile Force Generation by 3D HiPSC-Derived Cardiac Tissues Is Enhanced by Rapid Establishment of Cellular Interconnection in Matrix with Muscle-Mimicking Stiffness'. *Biomaterials* 131: 111–20. doi:10.1016/j.biomaterials.2017.03.039.

Legant, W. R., A. Pathak, M. T. Yang, V. S. Deshpande, R. M. McMeeking, and C. S. Chen. 2009. 'Microfabricated Tissue Gauges to Measure and Manipulate Forces from 3D Microtissues'. *Proceedings of the National Academy of Sciences* 106(25): 10097–102. doi:10.1073/pnas.0900174106.

Legerstee, Karin, Bart Geverts, Johan A. Slotman, and Adriaan B. Houtsmuller. 2019. 'Dynamics and Distribution of Paxillin, Vinculin, Zyxin and VASP Depend on Focal Adhesion Location and Orientation'. *Scientific Reports 2019 9:1* 9(1): 1–18. doi:10.1038/s41598-019-46905-2.

LeGrice, I J, B H Smaill, L Z Chai, S G Edgar, J B Gavin, and P J Hunter. 1995. 'Laminar Structure of the Heart: Ventricular Myocyte Arrangement and Connective Tissue Architecture in the Dog.' *The American journal of physiology* 269(2 Pt 2): H571-82. doi:10.1152/ajpheart.1995.269.2.H571.

Lelovas, Pavlos P, Nikolaos G Kostomitsopoulos, and Theodoros T Xanthos. 2014. *A Comparative Anatomic and Physiologic Overview of the Porcine Heart*.

Lemcke, Heiko, Anna Skorska, Cajetan Immanuel Lang, Lisa Johann, and Robert David. 2020. 'Quantitative Evaluation of the Sarcomere Network of Human HiPSC-Derived

Cardiomyocytes Using Single-Molecule Localization Microscopy'. *International Journal of Molecular Sciences* 21(8). doi:10.3390/ijms21082819.

Lemme, Marta, Ingke Braren, Maksymilian Prondzynski, Bülent Aksehirlioglu, Bärbel M. Ulmer, Mirja L. Schulze, Djemail Ismaili, et al. 2020. 'Chronic Intermittent Tachypacing by an Optogenetic Approach Induces Arrhythmia Vulnerability in Human Engineered Heart Tissue'. *Cardiovascular Research* 116(8): 1487–99. doi:10.1093/cvr/cvz245.

Leonard, Andrea, Alessandro Bertero, Joseph D. Powers, Kevin M. Beussman, Shiv Bhandari, Michael Regnier, Charles E. Murry, and Nathan J. Sniadecki. 2018. 'Afterload Promotes Maturation of Human Induced Pluripotent Stem Cell Derived Cardiomyocytes in Engineered Heart Tissues'. *Journal of Molecular and Cellular Cardiology* 118: 147–58. doi:10.1016/j.yjmcc.2018.03.016.

Li, Junjun, Itsunari Minami, Motoko Shiozaki, Leqian Yu, Shin Yajima, Shigeru Miyagawa, Yuji Shiba, et al. 2017. 'Human Pluripotent Stem Cell-Derived Cardiac Tissue-like Constructs for Repairing the Infarcted Myocardium'. *Stem Cell Reports* 9(5): 1546–59. doi:10.1016/j.stemcr.2017.09.007.

Li, Junjun, Itsunari Minami, Leqian Yu, Kiyotaka Tsuji, Minako Nakajima, Jing Qiao, Masato Suzuki, et al. 2016. 'Extracellular Recordings of Patterned Human Pluripotent Stem Cell-Derived Cardiomyocytes on Aligned Fibers'. *Stem Cells International* 2016. doi:10.1155/2016/2634013.

Li, Rui, Sien Lin, Meiling Zhu, Yingrui Deng, Xiaoyu Chen, Kongchang Wei, Jianbin Xu, Gang Li, and Liming Bian. 2019. 'Synthetic Presentation of Noncanonical Wnt5a Motif Promotes Mechanosensing-Dependent Differentiation of Stem Cells and Regeneration'. *Science Advances* 5(10): 3896–3912. doi:10.1126/sciadv.aaw3896.

Lian, Xiaojun, Cheston Hsiao, Gisela Wilson, Kexian Zhu, Laurie B. Hazeltine, Samira M. Azarin, Kunil K. Raval, et al. 2012. 'Robust Cardiomyocyte Differentiation from Human Pluripotent Stem Cells via Temporal Modulation of Canonical Wnt Signaling'. *Proceedings of the National Academy of Sciences of the United States of America* 109(27): E1848–57. doi:10.1073/pnas.1200250109.

Lin, Bin, Xianming Lin, Maxine Stachel, Elisha Wang, Yumei Luo, Joshua Lader, Xiaofang Sun, Mario Delmar, and Lei Bu. 2017. 'Culture in Glucose-Depleted Medium Supplemented with Fatty Acid and 3,3',5-Triiodo-L-Thyronine Facilitates Purification and Maturation of Human Pluripotent Stem Cell-Derived Cardiomyocytes'. *Frontiers in Endocrinology* 8(OCT). doi:10.3389/fendo.2017.00253.

Lin, Wen, Deqiang Li, Lan Cheng, Li Li, Feiyan Liu, Nicholas J. Hand, Jonathan A. Epstein, and Daniel J. Rader. 2018. 'Zinc Transporter Slc39a8 Is Essential for Cardiac Ventricular Compaction'. *The Journal of Clinical Investigation* 128(2): 826–33. doi:10.1172/JCI96993.

Lin, Yi Fan, Ian Swinburne, and Deborah Yelon. 2012. 'Multiple Influences of Blood Flow on Cardiomyocyte Hypertrophy in the Embryonic Zebrafish Heart'. *Developmental Biology* 362(2): 242–53. doi:10.1016/J.YDBIO.2011.12.005.

Lin, Zuwan, Jessica C Garbern, Ren Liu, Qiang Li, Estela Mancheño Juncosa, Hannah LT Elwell, Morgan Sokol, et al. 2023. *Tissue-Embedded Stretchable Nanoelectronics Reveal Endothelial Cell-Mediated Electrical Maturation of Human 3D Cardiac Microtissues*. https://www.science.org.

Lind, Johan U., Travis A. Busbee, Alexander D. Valentine, Francesco S. Pasqualini, Hongyan Yuan, Moran Yadid, Sung Jin Park, et al. 2017. 'Instrumented Cardiac Microphysiological Devices via Multimaterial Three-Dimensional Printing'. *Nature Materials* 16(3): 303–8. doi:10.1038/nmat4782.

Lippi, Melania, Mattia Chiesa, Ciro Ascione, Matteo Pedrazzini, Saima Mushtaq, Davide Rovina, Daniela Riggio, et al. 2022. 'Spectrum of Rare and Common Genetic Variants in Arrhythmogenic Cardiomyopathy Patients'. *Biomolecules* 12(8). doi:10.3390/biom12081043.

Little, C. D., and B. J. Rongish. 1995. 'The Extracellular Matrix during Heart Development'. *Experientia 1995 51:9* 51(9): 873–82. doi:10.1007/BF01921738.

Litviňuková, Monika, Carlos Talavera-López, Henrike Maatz, Daniel Reichart, Catherine L. Worth, Eric L. Lindberg, Masatoshi Kanda, et al. 2020. 'Cells of the Adult Human Heart'. *Nature 2020 588:7838* 588(7838): 466–72. doi:10.1038/s41586-020-2797-4.

Liu, Yen Wen, Billy Chen, Xiulan Yang, James A. Fugate, Faith A. Kalucki, Akiko Futakuchi-Tsuchida, Larry Couture, et al. 2018. 'Human Embryonic Stem Cell–Derived Cardiomyocytes Restore Function in Infarcted Hearts of Non-Human Primates'. *Nature Biotechnology 2018 36:7* 36(7): 597–605. doi:10.1038/nbt.4162.

Lockhart, Marie, Elaine Wirrig, Aimee Phelps, and Andy Wessels. 2011. 'Extracellular Matrix and Heart Development'. *Birth Defects Research Part A - Clinical and Molecular Teratology* 91(6): 535–50. doi:10.1002/bdra.20810.

Loiben, Alexander M., Wei Ming Chien, Clayton E. Friedman, Leslie S.L. Chao, Gerhard Weber, Alex Goldstein, Nathan J. Sniadecki, Charles E. Murry, and Kai Chun Yang. 2023. 'Cardiomyocyte Apoptosis Is Associated with Contractile Dysfunction in Stem Cell Model

of MYH7 E848G Hypertrophic Cardiomyopathy'. *International Journal of Molecular Sciences* 24(5): 4909. doi:10.3390/IJMS24054909/S1.

Lu, Bingchuan, Min Ye, Jingjing Xia, Zhenrui Zhang, Zhuo Xiong, and Ting Zhang. 2023. 'Electrical Stimulation Promotes the Vascularization and Functionalization of an Engineered Biomimetic Human Cardiac Tissue'. *Advanced Healthcare Materials*. doi:10.1002/adhm.202300607.

Luna, Jesus Isaac, Jesus Ciriza, Marcos E. Garcia-Ojeda, Marco Kong, Anthony Herren, Deborah K. Lieu, Ronald A. Li, et al. 2011. 'Multiscale Biomimetic Topography for the Alignment of Neonatal and Embryonic Stem Cell-Derived Heart Cells'. *Tissue Engineering - Part C: Methods* 17(5): 579–88. doi:10.1089/ten.tec.2010.0410.

Lundy, Scott D., Wei Zhong Zhu, Michael Regnier, and Michael A. Laflamme. 2013. 'Structural and Functional Maturation of Cardiomyocytes Derived from Human Pluripotent Stem Cells'. *Stem Cells and Development* 22(14): 1991–2002. doi:10.1089/scd.2012.0490.

Lutolf, M. P., and J. A. Hubbell. 2005. 'Synthetic Biomaterials as Instructive Extracellular Microenvironments for Morphogenesis in Tissue Engineering'. *Nature Biotechnology 2005 23:1* 23(1): 47–55. doi:10.1038/nbt1055.

Lv, Wenjian, Apoorva Babu, Michael P. Morley, Kiran Musunuru, and Marie Guerraty. 2024. 'Resource of Gene Expression Data From a Multiethnic Population Cohort of Induced Pluripotent Cell–Derived Cardiomyocytes'. *Circulation: Genomic and Precision Medicine*. doi:10.1161/circgen.123.004218.

Lyon, Robert C., Fabian Zanella, Jeffrey H. Omens, and Farah Sheikh. 2015. 'Mechanotransduction in Cardiac Hypertrophy and Failure'. *Circulation Research* 116(8): 1462–76. doi:10.1161/CIRCRESAHA.116.304937.

Ma, Xuanyi, Sukriti Dewan, Justin Liu, Min Tang, Kathleen L. Miller, Claire Yu, Natalie Lawrence, Andrew D. McCulloch, and Shaochen Chen. 2019. '3D Printed Micro-Scale Force Gauge Arrays to Improve Human Cardiac Tissue Maturation and Enable High Throughput Drug Testing'. *Acta Biomaterialia* 95: 319–27. doi:10.1016/j.actbio.2018.12.026.

Ma, Zhen, Nathaniel Huebsch, Sangmo Koo, Mohammad A. Mandegar, Brian Siemons, Steven Boggess, Bruce R. Conklin, Costas P. Grigoropoulos, and Kevin E. Healy. 2018. 'Contractile Deficits in Engineered Cardiac Microtissues as a Result of MYBPC3 Deficiency and Mechanical Overload'. *Nature Biomedical Engineering 2018 2:12* 2(12): 955–67. doi:10.1038/s41551-018-0280-4.

Ma, Zhen, Jason Wang, Peter Loskill, Nathaniel Huebsch, Sangmo Koo, Felicia L. Svedlund, Natalie C. Marks, et al. 2015. 'Self-Organizing Human Cardiac Microchambers Mediated by Geometric Confinement'. *Nature Communications* 6. doi:10.1038/ncomms8413.

MacKenna, Deidre A., Sara M. Vaplon, and Andrew D. McCulloch. 1997. 'Microstructural Model of Perimysial Collagen Fibers for Resting Myocardial Mechanics during Ventricular Filling'. *American Journal of Physiology - Heart and Circulatory Physiology* 273(3 42-3). doi:10.1152/ajpheart.1997.273.3.h1576.

Maddah, Mahnaz, Julia D. Heidmann, Mohammad A. Mandegar, Chase D. Walker, Sara Bolouki, Bruce R. Conklin, and Kevin E. Loewke. 2015. 'A Non-Invasive Platform for Functional Characterization of Stem-Cell-Derived Cardiomyocytes with Applications in Cardiotoxicity Testing'. *Stem Cell Reports* 4(4): 621–31. doi:10.1016/j.stemcr.2015.02.007.

Maesen, Bart, Sander Verheule, Stef Zeemering, Mark La Meir, Jan Nijs, Stijn Lumeij, Dennis H. Lau, et al. 2022. 'Endomysial Fibrosis, Rather than Overall Connective Tissue Content, Is the Main Determinant of Conduction Disturbances in Human Atrial Fibrillation'. *EP Europace* 24(6): 1015–24. doi:10.1093/EUROPACE/EUAC026.

Mahoney, Vanessa M., Valeria Mezzano, and Gregory E. Morley. 2016. 'A Review of the Literature on Cardiac Electrical Activity between Fibroblasts and Myocytes'. *Progress in Biophysics and Molecular Biology* 120(1–3): 128–33. doi:10.1016/J.PBIOMOLBIO.2015.12.006.

Majkut, Stephanie, Timon Idema, Joe Swift, Christine Krieger, Andrea Liu, and Dennis E. Discher. 2013. 'Heart-Specific Stiffening in Early Embryos Parallels Matrix and Myosin Expression to Optimize Beating'. *Current Biology* 23(23): 2434–39. doi:10.1016/J.CUB.2013.10.057.

Mandrycky, Christian J., Nisa P. Williams, Ivan Batalov, Danny El-Nachef, Bernadette S. de Bakker, Jennifer Davis, Deok Ho Kim, et al. 2020. 'Engineering Heart Morphogenesis'. *Trends in Biotechnology* 38(8): 835–45. doi:10.1016/J.TIBTECH.2020.01.006.

Mannhardt, Ingra, Umber Saleem, Diogo Mosqueira, Malte F. Loos, Bärbel M. Ulmer, Marc D. Lemoine, Camilla Larsson, et al. 2020. 'Comparison of 10 Control HPSC Lines for Drug Screening in an Engineered Heart Tissue Format'. *Stem Cell Reports* 15(4): 983–98. doi:10.1016/j.stemcr.2020.09.002.

Marijianowski, Monique M.H., Peter Teeling, Jessica Mann, and Anton E. Becker. 1995. 'Dilated Cardiomyopathy Is Associated with an Increase in the Type I/Type III Collagen Ratio: A Quantitative Assessment'. *Journal of the American College of Cardiology* 25(6): 1263–72. doi:10.1016/0735-1097(94)00557-7.

Marinho, Paulo A., Thanathom Chailangkarn, and Alysson R. Muotri. 2015. 'Systematic Optimization of Human Pluripotent Stem Cells Media Using Design of Experiments'. *Scientific Reports* 5. doi:10.1038/srep09834.

Maron, Barry J., and Martin S. Maron. 2013. 'Hypertrophic Cardiomyopathy'. *The Lancet* 381(9862): 242–55. doi:10.1016/S0140-6736(12)60397-3.

Marsano, Anna, Chiara Conficconi, Marta Lemme, Paola Occhetta, Emanuele Gaudiello, Emiliano Votta, Giulia Cerino, Alberto Redaelli, and Marco Rasponi. 2016. 'Beating Heart on a Chip: A Novel Microfluidic Platform to Generate Functional 3D Cardiac Microtissues'. *Lab on a Chip* 16(3): 599–610. doi:10.1039/c5lc01356a.

Martewicz, Sebastian, Camilla Luni, Elena Serena, Piero Pavan, Huei Sheng Vincent Chen, Alessandra Rampazzo, and Nicola Elvassore. 2019. 'Transcriptomic Characterization of a Human In Vitro Model of Arrhythmogenic Cardiomyopathy Under Topological and Mechanical Stimuli'. *Annals of Biomedical Engineering* 47(3): 852–65. doi:10.1007/s10439-018-02134-8.

Martin Gerdes, A, Scott E Kellerman, Jo Ann Moore, Karl E Muffly, Linda C Clark, Phyllis Y Reaves, Krystyna B Malec, Peter P McKeown, and Douglas D Schocken. 1992. *Structural Remodeling of Cardiac Myocytes in Patients With Ischemic Cardiomyopathy*. http://ahajournals.org.

Matera, Daniel L., William Y. Wang, Makenzee R. Smith, Ariella Shikanov, and Brendon M. Baker. 2019. 'Fiber Density Modulates Cell Spreading in 3D Interstitial Matrix Mimetics'. *ACS Biomaterials Science and Engineering* 5(6): 2965–75. doi:10.1021/acsbiomaterials.9b00141.

Matsumoto, Katsuhiko, Tomoki T. Mitani, Shuhei A. Horiguchi, Junichi Kaneshiro, Tatsuya C. Murakami, Tomoyuki Mano, Hiroshi Fujishima, et al. 2019. 'Advanced CUBIC Tissue Clearing for Whole-Organ Cell Profiling'. *Nature Protocols 2019 14:12* 14(12): 3506–37. doi:10.1038/s41596-019-0240-9.

McCain, Megan L., Hyungsuk Lee, Yvonne Aratyn-Schaus, André G. Kléber, and Kevin Kit Parker. 2012. 'Cooperative Coupling of Cell-Matrix and Cell-Cell Adhesions in Cardiac Muscle'. *Proceedings of the National Academy of Sciences of the United States of America* 109(25): 9881–86. doi:10.1073/pnas.1203007109.

Mccormick, Richard J, and D Paul Thomas. 1998. 'Collagen Crosslinking in the Heart: Relationship to Development and Function'. *Basic Appl. Myol* 8(2): 143–50.

McKenna, William J., and Daniel P. Judge. 2021. 'Epidemiology of the Inherited Cardiomyopathies'. *Nature Reviews Cardiology* 18(1): 22–36. doi:10.1038/s41569-020-0428-2.

McNally, Elizabeth M., David Y. Barefield, and Megan J. Puckelwartz. 2015. 'The Genetic Landscape of Cardiomyopathy and Its Role in Heart Failure'. *Cell Metabolism* 21(2): 174–82. doi:10.1016/j.cmet.2015.01.013.

Melby, Jake A., Willem J. De Lange, Jianhua Zhang, David S. Roberts, Stanford D. Mitchell, Trisha Tucholski, Gina Kim, et al. 2021. 'Functionally Integrated Top-Down Proteomics for Standardized Assessment of Human Induced Pluripotent Stem Cell-Derived Engineered Cardiac Tissues'. *Journal of Proteome Research* 20(2): 1424–33. doi:10.1021/ACS.JPROTEOME.0C00830/ASSET/IMAGES/LARGE/PR0C00830_0004.JPEG.

Merkel, Chelsea D., Yang Li, Qanber Raza, Donna B. Stolz, and Adam V. Kwiatkowski. 2019. 'Vinculin Anchors Contractile Actin to the Cardiomyocyte Adherens Junction'. *Molecular Biology of the Cell* 30(21): 2639–50. doi:10.1091/MBC.E19-04-0216.

Mihic, Anton, Jiao Li, Yasuo Miyagi, Mark Gagliardi, Shu Hong Li, Jean Zu, Richard D. Weisel, Gordon Keller, and Ren Ke Li. 2014. 'The Effect of Cyclic Stretch on Maturation and 3D Tissue Formation of Human Embryonic Stem Cell-Derived Cardiomyocytes'. *Biomaterials* 35(9): 2798–2808. doi:10.1016/j.biomaterials.2013.12.052.

Miki, Kenji, Kohei Deguchi, Misato Nakanishi-Koakutsu, Antonio Lucena-Cacace, Shigeru Kondo, Yuya Fujiwara, Takeshi Hatani, et al. 2021. 'ERRγ Enhances Cardiac Maturation with T-Tubule Formation in Human IPSC-Derived Cardiomyocytes'. *Nature Communications 2021 12:1* 12(1): 1–15. doi:10.1038/s41467-021-23816-3.

Milani-Nejad, Nima, and Paul M.L. Janssen. 2014. 'Small and Large Animal Models in Cardiac Contraction Research: Advantages and Disadvantages'. *Pharmacology and Therapeutics* 141(3): 235–49. doi:10.1016/j.pharmthera.2013.10.007.

Miller, Renee, Eric Kerfoot, Charlène Mauger, Tevfik F. Ismail, Alistair A. Young, and David A. Nordsletten. 2021. 'An Implementation of Patient-Specific Biventricular Mechanics Simulations With a Deep Learning and Computational Pipeline'. *Frontiers in Physiology* 12: 716597. doi:10.3389/FPHYS.2021.716597/BIBTEX.

Mittal, Ashok, Maria Pulina, Shuan Yu Hou, and Sophie Astrof. 2013. 'Fibronectin and Integrin Alpha 5 Play Requisite Roles in Cardiac Morphogenesis'. *Developmental Biology* 381(1): 73–82. doi:10.1016/j.ydbio.2013.06.010.

Mohammadzadeh, Saeed, and Emma Lejeune. 2023. 'SarcGraph: A Python Package for Analyzing the Contractile Behavior of Pluripotent Stem Cell-Derived Cardiomyocytes'. *Journal of Open Source Software* 8(85): 5322. doi:10.21105/JOSS.05322.

del Monte-Nieto, Gonzalo, Mirana Ramialison, Arne A.S. Adam, Bingruo Wu, Alla Aharonov, Gabriele D'uva, Lauren M. Bourke, et al. 2018. 'Control of Cardiac Jelly Dynamics by NOTCH1 and NRG1 Defines the Building Plan for Trabeculation'. *Nature 2018 557:7705* 557(7705): 439–45. doi:10.1038/s41586-018-0110-6.

Morrill, Erica E., Azamat N. Tulepbergenov, Christina J. Stender, Roshani Lamichhane, Raquel J. Brown, and Trevor J. Lujan. 2016. 'A Validated Software Application to Measure Fiber Organization in Soft Tissue'. *Biomechanics and Modeling in Mechanobiology* 15(6): 1467–78. doi:10.1007/s10237-016-0776-3.

Mosqueira, Diogo, Ingra Mannhardt, Jamie R. Bhagwan, Katarzyna Lis-Slimak, Puspita Katili, Elizabeth Scott, Mustafa Hassan, et al. 2018. 'CRISPR/Cas9 Editing in Human Pluripotent Stem Cell-Cardiomyocytes Highlights Arrhythmias, Hypocontractility, and Energy Depletion as Potential Therapeutic Targets for Hypertrophic Cardiomyopathy'. *European Heart Journal* 39(43): 3879–92. doi:10.1093/EURHEARTJ/EHY249.

Mulieri, Louis A, Gerd Hasenfuss, Bruce Leavitt, Paul D Allen, and N R Alpert. 1992. *Altered Myocardial Force-Frequency Relation in Human Heart Failure.* http://ahajournals.org.

Mummery, Christine L., Jianhua Zhang, Elizabeth S. Ng, David A. Elliott, Andrew G. Elefanty, and Timothy J. Kamp. 2012. 'Differentiation of Human Embryonic Stem Cells and Induced Pluripotent Stem Cells to Cardiomyocytes: A Methods Overview'. *Circulation Research* 111(3): 344–58. doi:10.1161/CIRCRESAHA.110.227512.

Murry, Charles E., and W. Robb MacLellan. 2020. 'Stem Cells and the Heart - The Road Ahead'. *Science* 367(6480): 854–55. doi:10.1126/science.aaz3650.

Nagueh, Sherif F., Gopi Shah, Yiming Wu, Guillermo Torre-Amione, Nicholas M.P. King, Sunshine Lahmers, Christian C. Witt, et al. 2004. 'Altered Titin Expression, Myocardial Stiffness, and Left Ventricular Function in Patients with Dilated Cardiomyopathy'. *Circulation* 110(2): 155–62. doi:10.1161/01.CIR.0000135591.37759.AF.

Nakamura, Michinari, and Junichi Sadoshima. 2018. 'Mechanisms of Physiological and Pathological Cardiac Hypertrophy'. *Nature Reviews Cardiology 2018 15:7* 15(7): 387–407. doi:10.1038/s41569-018-0007-y.

Neff, Lily S., and Amy D. Bradshaw. 2021. 'Cross Your Heart? Collagen Cross-Links in Cardiac Health and Disease'. *Cellular Signalling* 79: 109889. doi:10.1016/j.cellsig.2020.109889.

Neiman, Gabriel, María Agustina Scarafía, Alejandro La Greca, Natalia L. Santín Velazque, Ximena Garate, Ariel Waisman, Alan M. Möbbs, et al. 2019. 'Integrin Alpha-5 Subunit Is Critical for the Early Stages of Human Pluripotent Stem Cell Cardiac Differentiation'. *Scientific Reports* 9(1): 1–10. doi:10.1038/s41598-019-54352-2.

Ng, Ronald, X R Lorenzo Sewanan, X L Allison Brill, Paul Stankey, Xia Li, Yibing Qyang, Barbara E Ehrlich, and Stuart G Campbell. 2020. 'Contractile Work Directly Modulates Mitochondrial Protein Levels in Human Engineered Heart Tissues'. *Am J Physiol Heart Circ Physiol* 318: 1516–24. doi:10.1152/ajpheart.00055.2020.-Engineered.

Nielsen, Morten S., Chantal J.M. van Opbergen, Toon A.B. van Veen, and Mario Delmar. 2023. 'THE INTERCALATED DISC: A UNIQUE ORGANELLE FOR ELECTROMECHANICAL SYNCHRONY IN CARDIOMYOCYTES'. *Physiological Reviews* 103(3): 2271–2319. doi:10.1152/PHYSREV.00021.2022/ASSET/IMAGES/LARGE/PHYSREV.00021.2022_F011.JPEG.

Nijak, Aleksandra, Eline Simons, Bert Vandendriessche, Dieter Van de Sande, Erik Fransen, Ewa Sieliwończyk, Ilse Van Gucht, et al. 2022. 'Morpho-Functional Comparison of Differentiation Protocols to Create IPSC-Derived Cardiomyocytes'. *Biology Open* 11(2). doi:10.1242/bio.059016.

Nishiga, Masataka, Chun Liu, Lei S. Qi, and Joseph C. Wu. 2022. 'The Use of New CRISPR Tools in Cardiovascular Research and Medicine'. *Nature Reviews Cardiology* 19(8): 505–21. doi:10.1038/s41569-021-00669-3.

Noor, Nadav, Assaf Shapira, Reuven Edri, Idan Gal, Lior Wertheim, and Tal Dvir. 2019. '3D Printing of Personalized Thick and Perfusable Cardiac Patches and Hearts'. *Advanced Science* 6(11). doi:10.1002/advs.201900344.

Notari, Mario, Antoni Ventura-Rubio, Sylvia J. Bedford-Guaus, Ignasi Jorba, Lola Mulero, Daniel Navajas, Mercè Martí, and Ángel Raya. 2018. 'The Local Microenvironment Limits the Regenerative Potential of the Mouse Neonatal Heart'. *Science Advances* 4(5). doi:10.1126/SCIADV.AAO5553/SUPPL_FILE/AAO5553_SUPPLEMENTARYDATASET.XLS.

Olivetti, Giorgio, Elena Cigola, Roberta Maestri, Domenico Corradi, Costanza Lagrasta, Steven R Gambert, and Piero Anversa. 1996. 28 Journal of Molecular and Cellular Cardiology *Aging, Cardiac Hypertrophy and Ischemic Cardiomyopathy Do Not Affect the Proportion of Mononucleated and Multinucleated Myocytes in the Human Heart*.

Ottaviani, Daniele, Menno ter Huurne, David A. Elliott, Milena Bellin, and Christine L. Mummery. 2023. 'Maturing Differentiated Human Pluripotent Stem Cells in Vitro: Methods and Challenges'. *Development* 150(11). doi:10.1242/DEV.201103.

Padin-Iruega, M. Elena, Yu Misao, Michael E. Davis, Vincent F.M. Segers, Grazia Esposito, Tomotake Tokunou, Konrad Urbanek, et al. 2009. 'Cardiac Progenitor Cells and Biotinylated Insulin-like Growth Factor-1 Nanofibers Improve Endogenous and Exogenous Myocardial Regeneration after Infarction'. *Circulation* 120(10): 876–87. doi:10.1161/CIRCULATIONAHA.109.852285.

Pandey, Pragati, William Hawkes, Junquiang Hu, William Valentine Megone, Julien Gautrot, Narayana Anilkumar, Min Zhang, et al. 2018. 'Cardiomyocytes Sense Matrix Rigidity through a Combination of Muscle and Non-Muscle Myosin Contractions'. *Developmental Cell* 44(3): 326-336.e3. doi:10.1016/j.devcel.2017.12.024.

Pardo, J. V., J. D'Angelo Siliciano, and S. W. Craig. 1983a. 'A Vinculin-Containing Cortical Lattice in Skeletal Muscle: Transverse Lattice Elements ("costameres") Mark Sites of Attachment between Myofibrils and Sarcolemma.' *Proceedings of the National Academy of Sciences* 80(4): 1008–12. doi:10.1073/PNAS.80.4.1008.

Pardo, J. V., J. D'Angelo Siliciano, and S. W. Craig. 1983b. 'Vinculin Is a Component of an Extensive Network of Myofibril-Sarcolemma Attachment Regions in Cardiac Muscle Fibers.' *Journal of Cell Biology* 97(4): 1081–88. doi:10.1083/JCB.97.4.1081.

Parikh, Shan S., Daniel J. Blackwell, Nieves Gomez-Hurtado, Michael Frisk, Lili Wang, Kyungsoo Kim, Christen P. Dahl, et al. 2017. 'Thyroid and Glucocorticoid Hormones Promote Functional T-Tubule Development in Human-Induced Pluripotent Stem Cell-Derived Cardiomyocytes'. *Circulation Research* 121(12): 1323–30. doi:10.1161/CIRCRESAHA.117.311920.

Park, Shuin, Ngoc B. Nguyen, Arash Pezhouman, and Reza Ardehali. 2019. 'Cardiac Fibrosis: Potential Therapeutic Targets'. *Translational Research* 209: 121–37. doi:10.1016/J.TRSL.2019.03.001.

Parker, Kevin K., and Donald E. Ingber. 2007. 'Extracellular Matrix, Mechanotransduction and Structural Hierarchies in Heart Tissue Engineering'. *Philosophical Transactions of the Royal Society B: Biological Sciences* 362(1484): 1267–79. doi:10.1098/rstb.2007.2114.

Parsons, J. Thomas, Alan Rick Horwitz, and Martin A. Schwartz. 2010. 'Cell Adhesion: Integrating Cytoskeletal Dynamics and Cellular Tension'. *Nature Reviews Molecular Cell Biology 2010 11:9* 11(9): 633–43. doi:10.1038/nrm2957.

Pasqualini, Francesco Silvio, Sean Paul Sheehy, Ashutosh Agarwal, Yvonne Aratyn-Schaus, and Kevin Kit Parker. 2015. 'Structural Phenotyping of Stem Cell-Derived Cardiomyocytes'. *Stem Cell Reports* 4(3): 340–47. doi:10.1016/j.stemcr.2015.01.020.

Passer, Derek, Annebel van de Vrugt, Ayhan Atmanli, and Ibrahim J. Domian. 2016. 'Atypical Protein Kinase C-Dependent Polarized Cell Division Is Required for Myocardial Trabeculation'. *Cell Reports* 14(7): 1662–72. doi:10.1016/J.CELREP.2016.01.030.

Pathak, Manas, Sagartirtha Sarkar, Elangovan Vellaichamy, and Subha Sen. 2001. 'Role of Myocytes in Myocardial Collagen Production'. *Hypertension* 37(3): 833–40. doi:10.1161/01.HYP.37.3.833.

Pellman, Jason, Jing Zhang, and Farah Sheikh. 2016. 'Myocyte-Fibroblast Communication in Cardiac Fibrosis and Arrhythmias: Mechanisms and Model Systems'. *Journal of Molecular and Cellular Cardiology* 94: 22–31. doi:10.1016/J.YJMCC.2016.03.005.

Perestrelo, Ana Rubina, Ana Catarina Silva, Jorge Oliver-De La Cruz, Fabiana Martino, Vladimír Horváth, Guido Caluori, Ondřej Polanský, et al. 2021. 'Multiscale Analysis of Extracellular Matrix Remodeling in the Failing Heart'. *Circulation Research* 128(1): 24–38. doi:10.1161/CIRCRESAHA.120.317685.

Pesce, Maurizio, Georg N. Duda, Giancarlo Forte, Henrique Girao, Angel Raya, Pere Roca-Cusachs, Joost P. G. Sluijter, Carsten Tschöpe, and Sophie Van Linthout. 2022. 'Cardiac Fibroblasts and Mechanosensation in Heart Development, Health and Disease'. *Nature Reviews Cardiology 2022*: 1–16. doi:10.1038/s41569-022-00799-2.

Peters, Marijn C., Sofia Di Martino, Thomas Boelens, Jiabin Qin, Alain van Mil, Pieter A. Doevendans, Steven A.J. Chamuleau, Joost P.G. Sluijter, and Klaus Neef. 2022. 'Follistatin-like 1 Promotes Proliferation of Matured Human Hypoxic IPSC-Cardiomyocytes and Is Secreted by Cardiac Fibroblasts'. *Molecular Therapy - Methods and Clinical Development* 25: 3–16. doi:10.1016/j.omtm.2022.02.005.

Piccini, Ilaria, Jyoti Rao, Guiscard Seebohm, and Boris Greber. 2015. 'Human Pluripotent Stem Cell-Derived Cardiomyocytes: Genome-Wide Expression Profiling of Long-Term in Vitro Maturation in Comparison to Human Heart Tissue'. *Genomics Data* 4: 69–72. doi:10.1016/J.GDATA.2015.03.008.

Pioner, Josè Manuel, Alice W. Racca, Jordan M. Klaiman, Kai Chun Yang, Xuan Guan, Lil Pabon, Veronica Muskheli, et al. 2016. 'Isolation and Mechanical Measurements of Myofibrils from Human Induced Pluripotent Stem Cell-Derived Cardiomyocytes'. *Stem Cell Reports* 6(6): 885–96. doi:10.1016/j.stemcr.2016.04.006.

Pioner, Josè Manuel, Lorenzo Santini, Chiara Palandri, Daniele Martella, Flavia Lupi, Marianna Langione, Silvia Querceto, et al. 2019. 'Optical Investigation of Action Potential and Calcium Handling Maturation of HiPSC-Cardiomyocytes on Biomimetic Substrates'. *International Journal of Molecular Sciences* 20(15). doi:10.3390/ijms20153799.

Polonchuk, Liudmila, Mamta Chabria, Laura Badi, Jean Christophe Hoflack, Gemma Figtree, Michael J. Davies, and Carmine Gentile. 2017. 'Cardiac Spheroids as Promising in Vitro Models to Study the Human Heart Microenvironment'. *Scientific Reports* 7(1): 1–12. doi:10.1038/s41598-017-06385-8.

Pope, Adèle J., Gregory B. Sands, Bruce H. Smaill, and Ian J. LeGrice. 2008. 'Three-Dimensional Transmural Organization of Perimysial Collagen in the Heart'. *American Journal of Physiology - Heart and Circulatory Physiology* 295(3): 1243–52. doi:10.1152/AJPHEART.00484.2008/ASSET/IMAGES/LARGE/ZH40090884650008.JPEG.

Porter, George A., Jennifer R. Hom, David L. Hoffman, Rodrigo A. Quintanilla, Karen L.de Mesy Bentley, and Shey Shing Sheu. 2011. 'Bioenergetics, Mitochondria, and Cardiac Myocyte Differentiation'. *Progress in Pediatric Cardiology* 31(2): 75–81. doi:10.1016/j.ppedcard.2011.02.002.

Poveda, Ferran, Debora Gil, Enric Martí, Albert Andaluz, Manel Ballester, and Francesc Carreras. 2013. 'Helical Structure of the Cardiac Ventricular Anatomy Assessed by Diffusion Tensor Magnetic Resonance Imaging With Multiresolution Tractography'. *Revista Española de Cardiología (English Edition)* 66(10): 782–90. doi:10.1016/J.REC.2013.04.021.

Pretorius, Danielle, Asher M. Kahn-Krell, Xi Lou, Vladimir G. Fast, Joel L. Berry, Timothy J. Kamp, and Jianyi Zhang. 2021. 'Layer-By-Layer Fabrication of Large and Thick Human Cardiac Muscle Patch Constructs With Superior Electrophysiological Properties'. *Frontiers in Cell and Developmental Biology* 9. doi:10.3389/fcell.2021.670504.

Price, Andrew J., Anna Lena Cost, Hanna Ungewiß, Jens Waschke, Alexander R. Dunn, and Carsten Grashoff. 2018. 'Mechanical Loading of Desmosomes Depends on the Magnitude and Orientation of External Stress'. *Nature Communications* 9(1): 1–11. doi:10.1038/s41467-018-07523-0.

Priya, Rashmi, Srinivas Allanki, Alessandra Gentile, Shivani Mansingh, Veronica Uribe, Hans Martin Maischein, and Didier Y.R. Stainier. 2020. 'Tension Heterogeneity Directs Form and Fate to Pattern the Myocardial Wall'. *Nature 2020 588:7836* 588(7836): 130–34. doi:10.1038/s41586-020-2946-9.

Prondzynski, Maksymilian, Marc D Lemoine, Antonia TL Zech, András Horváth, Vittoria Di Mauro, Jussi T Koivumäki, Nico Kresin, et al. 2019. 'Disease Modeling of a Mutation in A-actinin 2 Guides Clinical Therapy in Hypertrophic Cardiomyopathy'. *EMBO Molecular Medicine* 11(12). doi:10.15252/EMMM.201911115/SUPPL_FILE/EMMM201911115-SUP-0007-SDATAEV.PDF.

Psaras, Yiangos, Francesca Margara, Marcelo Cicconet, Alexander J. Sparrow, Giuliana G. Repetti, Manuel Schmid, Violetta Steeples, et al. 2021. 'CalTrack: High-Throughput Automated Calcium Transient Analysis in Cardiomyocytes'. *Circulation Research* 129(2): 326–41. doi:10.1161/CIRCRESAHA.121.318868.

Pushp, Pallavi, Bijayalaxmi Sahoo, Frederico C. Ferreira, Joaquim M. Sampaio Cabral, Ana Fernandes-Platzgummer, and Mukesh K. Gupta. 2020. 'Functional Comparison of Beating Cardiomyocytes Differentiated from Umbilical Cord-Derived Mesenchymal/Stromal Stem Cells and Human Foreskin-Derived Induced Pluripotent Stem Cells'. *Journal of Biomedical Materials Research - Part A* 108(3): 496–514. doi:10.1002/jbm.a.36831.

van Putten, Sander, Yousef Shafieyan, and Boris Hinz. 2016. 'Mechanical Control of Cardiac Myofibroblasts'. *Journal of Molecular and Cellular Cardiology* 93: 133–42. doi:10.1016/j.yjmcc.2015.11.025.

Qu, Yusheng, Nicole Feric, Isabella Pallotta, Rishabh Singh, Rooz Sobbi, and Hugo M. Vargas. 2020. 'Inotropic Assessment in Engineered 3D Cardiac Tissues Using Human Induced Pluripotent Stem Cell-Derived Cardiomyocytes in the BiowireTM II Platform'. *Journal of Pharmacological and Toxicological Methods* 105. doi:10.1016/j.vascn.2020.106886.

Querdel, Eva, Marina Reinsch, Liesa Castro, Deniz Köse, Andrea Bähr, Svenja Reich, Birgit Geertz, et al. 2021. 'Human Engineered Heart Tissue Patches Remuscularize the Injured Heart in a Dose-Dependent Manner'. *Circulation* 143(20): 1991–2006. doi:10.1161/CIRCULATIONAHA.120.047904.

Quinn, T. Alexander, Patrizia Camelliti, Eva A. Rog-Zielinska, Urszula Siedlecka, Tommaso Poggioli, Eileen T. O'Toole, Thomas Knöpfel, and Peter Kohl. 2016. 'Electrotonic Coupling of Excitable and Nonexcitable Cells in the Heart Revealed by Optogenetics'. *Proceedings of the National Academy of Sciences* 113(51): 14852–57. doi:10.1073/PNAS.1611184114.

Ragazzini, Sara, Franca Scocozza, Giacomo Bernava, Ferdinando Auricchio, Gualtiero I. Colombo, Marianna Barbuto, Michele Conti, Maurizio Pesce, and Gloria Garoffolo. 2022. 'Mechanosensor YAP Cooperates with TGF-B1 Signaling to Promote Myofibroblast Activation and Matrix Stiffening in a 3D Model of Human Cardiac Fibrosis'. *Acta Biomaterialia* 152: 300–312. doi:10.1016/J.ACTBIO.2022.08.063.

Rai, Vikrant, Poonam Sharma, Swati Agrawal, and Devendra K. Agrawal. 2016. 'Relevance of Mouse Models of Cardiac Fibrosis and Hypertrophy in Cardiac Research'. *Molecular and Cellular Biochemistry 2016 424:1* 424(1): 123–45. doi:10.1007/S11010-016-2849-0.

Rainer, Peter P., Scarlett Hao, Davy Vanhoutte, Dong Ik Lee, Norimichi Koitabashi, Jeffery D. Molkentin, and David A. Kass. 2014. 'Cardiomyocyte-Specific Transforming Growth Factor β Suppression Blocks Neutrophil Infiltration, Augments Multiple Cytoprotective Cascades, and Reduces Early Mortality after Myocardial Infarction'. *Circulation Research* 114(8): 1246–57. doi:10.1161/CIRCRESAHA.114.302653.

Ramachandran, Abhinay, Carissa E. Livingston, Alexia Vite, Elise A. Corbin, Alexander I. Bennett, Kevin T. Turner, Benjamin W. Lee, et al. 2023. 'Biomechanical Impact of Pathogenic MYBPC3 Truncation Variant Revealed by Dynamically Tuning In Vitro Afterload'. *Journal of Cardiovascular Translational Research*: 1–14. doi:10.1007/S12265-022-10348-4/FIGURES/6.

Rampazzo, Alessandra, Martina Calore, Jolanda van Hengel, and Frans van Roy. 2014. 'Intercalated Discs and Arrhythmogenic Cardiomyopathy'. *Circulation: Cardiovascular Genetics* 7(6): 930–40. doi:10.1161/CIRCGENETICS.114.000645.

Del Re, Dominic P. 2022. 'Hippo-Yap Signaling in Cardiac and Fibrotic Remodeling'. *Current Opinion in Physiology* 26: 100492. doi:10.1016/J.COPHYS.2022.100492.

Reichardt, Isabella M., Kalen Z. Robeson, Michael Regnier, and Jennifer Davis. 2021. 'Controlling Cardiac Fibrosis through Fibroblast State Space Modulation'. *Cellular Signalling* 79: 109888. doi:10.1016/J.CELLSIG.2020.109888.

Ribeiro, Alexandre J. S., Yen-Sin Ang, Ji-Dong Fu, Renee N. Rivas, Tamer M. A. Mohamed, Gadryn C. Higgs, Deepak Srivastava, and Beth L. Pruitt. 2015. 'Contractility of Single Cardiomyocytes Differentiated from Pluripotent Stem Cells Depends on Physiological Shape and Substrate Stiffness'. *Proceedings of the National Academy of Sciences* 112(41): 12705–10. doi:10.1073/pnas.1508073112.

Ribeiro, Alexandre J.S., Olivier Schwab, Mohammad A. Mandegar, Yen Sin Ang, Bruce R. Conklin, Deepak Srivastava, and Beth L. Pruitt. 2017. 'Multi-Imaging Method to Assay the Contractile Mechanical Output of Micropatterned Human IPSC-Derived Cardiac Myocytes'. *Circulation Research* 120(10): 1572–83. doi:10.1161/CIRCRESAHA.116.310363.

Ribeiro, Marcelo C., Leon G. Tertoolen, Juan A. Guadix, Milena Bellin, Georgios Kosmidis, Cristina D'Aniello, Jantine Monshouwer-Kloots, et al. 2015. 'Functional Maturation of Human Pluripotent Stem Cell Derived Cardiomyocytes Invitro - Correlation between

Contraction Force Andelectrophysiology'. *Biomaterials* 51: 138–50. doi:10.1016/j.biomaterials.2015.01.067.

Richards, Dylan J., Yang Li, Charles M. Kerr, Jenny Yao, Gyda C. Beeson, Robert C. Coyle, Xun Chen, et al. 2020. 'Human Cardiac Organoids for the Modelling of Myocardial Infarction and Drug Cardiotoxicity'. *Nature Biomedical Engineering 2020 4:4* 4(4): 446–62. doi:10.1038/s41551-020-0539-4.

Richardson, William J., and Jeffrey W. Holmes. 2016. 'Emergence of Collagen Orientation Heterogeneity in Healing Infarcts and an Agent-Based Model'. *Biophysical Journal* 110(10): 2266–77. doi:10.1016/J.BPJ.2016.04.014.

Rienks, Marieke, Anna-Pia Papageorgiou, Nikolaos G Frangogiannis, and Stephane Heymans. 2014. 'Myocardial Extracellular Matrix: An Ever-Changing and Diverse Entity.' *Circulation research* 114(5): 872–88. doi:10.1161/CIRCRESAHA.114.302533.

Da Rocha, André Monteiro, Katherine Campbell, Sergey Mironov, Jiang Jiang, Lakshmi Mundada, Guadalupe Guerrero-Serna, José Jalife, and Todd J. Herron. 2017. 'HiPSC-CM Monolayer Maturation State Determines Drug Responsiveness in High Throughput Pro-Arrhythmia Screen'. *Scientific Reports* 7(1). doi:10.1038/s41598-017-13590-y.

Roest, Alison Schroer Vander, Chao Liu, Makenna M. Morck, Kristina Bezold Kooiker, Gwanghyun Jung, Dan Song, Aminah Dawood, et al. 2021. 'Hypertrophic Cardiomyopathy β-Cardiac Myosin Mutation (P710R) Leads to Hypercontractility by Disrupting Super Relaxed State'. *Proceedings of the National Academy of Sciences of the United States of America* 118(24): e2025030118. doi:10.1073/PNAS.2025030118/SUPPL_FILE/PNAS.2025030118.SM02.AVI.

Rogers, Aaron J., Vladimir G. Fast, and Palaniappan Sethu. 2016. 'Biomimetic Cardiac Tissue Model Enables the Adaption of Human Induced Pluripotent Stem Cell Cardiomyocytes to Physiological Hemodynamic Loads'. *Analytical Chemistry* 88(19): 9862–68. doi:10.1021/acs.analchem.6b03105.

Ronaldson-Bouchard, Kacey, Stephen P. Ma, Keith Yeager, Timothy Chen, Lou Jin Song, Dario Sirabella, Kumi Morikawa, et al. 2018. 'Advanced Maturation of Human Cardiac Tissue Grown from Pluripotent Stem Cells'. *Nature* 556(7700): 239–43. doi:10.1038/s41586-018-0016-3.

Rouhani, Foad, Natsuhiko Kumasaka, Miguel Cardoso de Brito, Allan Bradley, Ludovic Vallier, and Daniel Gaffney. 2014. 'Genetic Background Drives Transcriptional Variation in Human Induced Pluripotent Stem Cells'. *PLoS Genetics* 10(6). doi:10.1371/journal.pgen.1004432.

Ruan, Jia Ling, Nathaniel L. Tulloch, Maria V. Razumova, Mark Saiget, Veronica Muskheli, Lil Pabon, Hans Reinecke, Michael Regnier, and Charles E. Murry. 2016. 'Mechanical Stress Conditioning and Electrical Stimulation Promote Contractility and Force Maturation of Induced Pluripotent Stem Cell-Derived Human Cardiac Tissue'. *Circulation* 134(20): 1557–67. doi:10.1161/CIRCULATIONAHA.114.014998.

Ruan, Jia Ling, Nathaniel L. Tulloch, Mark Saiget, Sharon L. Paige, Maria V. Razumova, Michael Regnier, Kelvin Chan Tung, et al. 2015. 'Mechanical Stress Promotes Maturation of Human Myocardium from Pluripotent Stem Cell-Derived Progenitors'. *Stem Cells* 33(7): 2148–57. doi:10.1002/stem.2036.

Rubart, Michael, Wen Tao, Xiao Long Lu, Simon J. Conway, Sean P. Reuter, Shien Fong Lin, and Mark H. Soonpaa. 2018. 'Electrical Coupling between Ventricular Myocytes and Myofibroblasts in the Infarcted Mouse Heart'. *Cardiovascular Research* 114(3): 389–400. doi:10.1093/CVR/CVX163.

Rupert, Cassady E., Tae Yun Kim, Bum Rak Choi, and Kareen L.K. Coulombe. 2020. 'Human Cardiac Fibroblast Number and Activation State Modulate Electromechanical Function of HiPSC-Cardiomyocytes in Engineered Myocardium'. *Stem Cells International* 2020. doi:10.1155/2020/9363809.

Ruwhof, Cindy, Annemieke E.T. Van Wamel, Janneke M. Egas, and Arnoud Van Der Laarse. 2000. 'Cyclic Stretch Induces the Release of Growth Promoting Factors from Cultured Neonatal Cardiomyocytes and Cardiac Fibroblasts'. *Molecular and Cellular Biochemistry* 208(1–2): 89–98. doi:10.1023/A:1007046105745/METRICS.

Sala, Luca, Berend J. Van Meer, Leon G.J. Tertoolen, Jeroen Bakkers, Milena Bellin, Richard P. Davis, Chris Denning, et al. 2018. 'Musclemotion: A Versatile Open Software Tool to Quantify Cardiomyocyte and Cardiac Muscle Contraction in Vitro and in Vivo'. *Circulation Research* 122(3): e5–16. doi:10.1161/CIRCRESAHA.117.312067/-/DC1.

Samarel, Allen M. 2005. 'Costameres, Focal Adhesions, and Cardiomyocyte Mechanotransduction'. *American Journal of Physiology - Heart and Circulatory Physiology* 289(6 58-6): 2291–2301. doi:10.1152/AJPHEART.00749.2005/ASSET/IMAGES/LARGE/ZH40120563640003.JPEG.

Sarker, Muzaddid, Hyunna T. Lee, Lin Mei, Andrey Krokhotin, Santiago Espinosa de los Reyes, Laura Yen, Lindsey M. Costantini, et al. 2019. 'Cardiomyopathy Mutations in Metavinculin Disrupt Regulation of Vinculin-Induced F-Actin Assemblies'. *Journal of Molecular Biology* 431(8): 1604–18. doi:10.1016/J.JMB.2019.02.024.

Saucerman, Jeffrey J., Philip M. Tan, Kyle S. Buchholz, Andrew D. McCulloch, and Jeffrey H. Omens. 2019. 'Mechanical Regulation of Gene Expression in Cardiac Myocytes and Fibroblasts'. *Nature Reviews Cardiology* 16(6): 361–78. doi:10.1038/s41569-019-0155-8.

Schimmel, Katharina, Kenzo Ichimura, Sushma Reddy, Francois Haddad, and Edda Spiekerkoetter. 2022. 'Cardiac Fibrosis in the Pressure Overloaded Left and Right Ventricle as a Therapeutic Target'. *Frontiers in Cardiovascular Medicine* 9: 886553. doi:10.3389/FCVM.2022.886553/BIBTEX.

Schmitt, Matthew S., Jonathan Colen, Stefano Sala, John Devany, Shailaja Seetharaman, Alexia Caillier, Margaret L. Gardel, Patrick W. Oakes, and Vincenzo Vitelli. 2024. 'Machine Learning Interpretable Models of Cell Mechanics from Protein Images'. *Cell* 187(2): 481-494.e24. doi:10.1016/j.cell.2023.11.041.

Schnabel, Lauren V., Christian M. Abratte, John C. Schimenti, Teresa L. Southard, and Lisa A. Fortier. 2012. 'Genetic Background Affects Induced Pluripotent Stem Cell Generation'. *Stem Cell Research and Therapy* 3(4). doi:10.1186/scrt121.

Schroer, Alison K., and W. David Merryman. 2015. 'Mechanobiology of Myofibroblast Adhesion in Fibrotic Cardiac Disease'. *Journal of Cell Science* 128(10): 1865–75. doi:10.1242/jcs.162891.

Schultheiss, Heinz Peter, De Lisa Fairweather, Alida L.P. Caforio, Felicitas Escher, Ray E. Hershberger, Steven E. Lipshultz, Peter P. Liu, et al. 2019. 'Dilated Cardiomyopathy'. *Nature Reviews Disease Primers 2019 5:1* 5(1): 1–19. doi:10.1038/s41572-019-0084-1.

Schulze, Mirja L., Marc D. Lemoine, Alexander W. Fischer, Katharina Scherschel, Robert David, Kristoffer Riecken, Arne Hansen, Thomas Eschenhagen, and Bärbel M. Ulmer. 2019. 'Dissecting HiPSC-CM Pacemaker Function in a Cardiac Organoid Model'. *Biomaterials* 206: 133–45. doi:10.1016/j.biomaterials.2019.03.023.

Schwan, Jonas, Andrea T. Kwaczala, Thomas J. Ryan, Oscar Bartulos, Yongming Ren, Lorenzo R. Sewanan, Aaron H. Morris, et al. 2016. 'Anisotropic Engineered Heart Tissue Made from Laser-Cut Decellularized Myocardium'. *Scientific Reports* 6. doi:10.1038/srep32068.

Sengupta, Partho P., A. Jamil Tajik, Krishnaswamy Chandrasekaran, and Bijoy K. Khandheria. 2008. 'Twist Mechanics of the Left Ventricle: Principles and Application'. *JACC: Cardiovascular Imaging* 1(3): 366–76. doi:10.1016/J.JCMG.2008.02.006.

Sengupta, Swarnali, Katheryn E. Rothenberg, Hanjun Li, Brenton D. Hoffman, and Nenad Bursac. 2019. 'Altering Integrin Engagement Regulates Membrane Localization of Kir2.1 Channels'. *Journal of cell science* 132(17). doi:10.1242/jcs.225383.

Shadrin, Ilya Y., Brian W. Allen, Ying Qian, Christopher P. Jackman, Aaron L. Carlson, Mark E. Juhas, and Nenad Bursac. 2017. 'Cardiopatch Platform Enables Maturation and Scale-up of Human Pluripotent Stem Cell-Derived Engineered Heart Tissues'. *Nature Communications* 8(1). doi:10.1038/s41467-017-01946-x.

Shakp, Will W., David G. Simpson, Thomas K. Borg, Allen M. Samarel, and Louis Terracio. 1997. 'Mechanical Forces Regulate Focal Adhesion and Costamere Assembly in Cardiac Myocytes'. *American Journal of Physiology - Heart and Circulatory Physiology* 273(2 42-2). doi:10.1152/AJPHEART.1997.273.2.H546.

Sharma, Arun, Christopher N. Toepfer, Manuel Schmid, Amanda C. Garfinkel, and Christine E. Seidman. 2018. 'Differentiation and Contractile Analysis of GFP-Sarcomere Reporter HiPSC-Cardiomyocytes'. *Current Protocols in Human Genetics* 96(1): 21.12.1-21.12.12. doi:10.1002/cphg.53.

Sharma, Arun, Christopher N. Toepfer, Tarsha Ward, Lauren Wasson, Radhika Agarwal, David A. Conner, Johnny H. Hu, and Christine E. Seidman. 2018. 'CRISPR/Cas9-Mediated Fluorescent Tagging of Endogenous Proteins in Human Pluripotent Stem Cells'. *Current Protocols in Human Genetics* 96(1): 21.11.1-21.11.20. doi:10.1002/cphg.52.

Sheehy, Sean P., Anna Grosberg, Pu Qin, David J. Behm, John P. Ferrier, Mackenzie A. Eagleson, Alexander P. Nesmith, et al. 2017. 'Toward Improved Myocardial Maturity in an Organ-on-Chip Platform with Immature Cardiac Myocytes'. *Experimental Biology and Medicine* 242(17): 1643–56. doi:10.1177/1535370217701006.

Shen, Shi, Lorenzo R. Sewanan, Stephanie Shao, Saiti S. Halder, Paul Stankey, Xia Li, and Stuart G. Campbell. 2022. 'Physiological Calcium Combined with Electrical Pacing Accelerates Maturation of Human Engineered Heart Tissue'. *Stem Cell Reports* 17(9): 2037–49. doi:10.1016/J.STEMCR.2022.07.006.

Shi, Huaiyu, Chenyan Wang, Bruce Z. Gao, James H. Henderson, and Zhen Ma. 2022. 'Cooperation between Myofibril Growth and Costamere Maturation in Human Cardiomyocytes'. *Frontiers in Bioengineering and Biotechnology* 10: 1049523. doi:10.3389/FBIOE.2022.1049523/BIBTEX.

Shi, Huaiyu, Xiangjun Wu, Shiyang Sun, Chenyan Wang, Zacharias Vangelatos, Ariel Ash-Shakoor, Costas P. Grigoropoulos, et al. 2022. 'Profiling the Responsiveness of Focal Adhesions of Human Cardiomyocytes to Extracellular Dynamic Nano-Topography'. *Bioactive Materials* 10: 367–77. doi:10.1016/J.BIOACTMAT.2021.08.028.

Shiba, Yuji, Toshihito Gomibuchi, Tatsuichiro Seto, Yuko Wada, Hajime Ichimura, Yuki Tanaka, Tatsuki Ogasawara, et al. 2016. 'Allogeneic Transplantation of IPS Cell-Derived

Cardiomyocytes Regenerates Primate Hearts'. *Nature 2016 538:7625* 538(7625): 388–91. doi:10.1038/nature19815.

Shinde, Arti V., and Nikolaos G. Frangogiannis. 2014. 'Fibroblasts in Myocardial Infarction: A Role in Inflammation and Repair'. *Journal of Molecular and Cellular Cardiology* 70: 74–82. doi:10.1016/j.yjmcc.2013.11.015.

Shinnawi, Rami, Irit Huber, Leonid Maizels, Naim Shaheen, Amira Gepstein, Gil Arbel, Anke J. Tijsen, and Lior Gepstein. 2015. 'Monitoring Human-Induced Pluripotent Stem Cell-Derived Cardiomyocytes with Genetically Encoded Calcium and Voltage Fluorescent Reporters'. *Stem Cell Reports* 5(4): 582–96. doi:10.1016/j.stemcr.2015.08.009.

Shroff, Sanaya N., Shoshana L. Das, Hua an Tseng, Jad Noueihed, Fernando Fernandez, John A. White, Christopher S. Chen, and Xue Han. 2020. 'Voltage Imaging of Cardiac Cells and Tissue Using the Genetically Encoded Voltage Sensor Archon1'. *iScience* 23(4). doi:10.1016/j.isci.2020.100974.

Silva, Ana Catarina, Cassilda Pereira, Ana Catarina R.G. Fonseca, Perpétua Pinto-do-Ó, and Diana S. Nascimento. 2021. 'Bearing My Heart: The Role of Extracellular Matrix on Cardiac Development, Homeostasis, and Injury Response'. *Frontiers in Cell and Developmental Biology* 8: 621644. doi:10.3389/FCELL.2020.621644/BIBTEX.

Simmons, Daniel W., Ganesh Malayath, David R. Schuftan, Jingxuan Guo, Kasoorelope Oguntuyo, Ghiska Ramahdita, Yuwen Sun, et al. 2024. 'Engineered Tissue Geometry and Plakophilin-2 Regulate Electrophysiology of Human IPSC-Derived Cardiomyocytes'. *APL Bioengineering* 8(1): 16118. doi:10.1063/5.0160677/3270283.

Simpson, D. G., M. L. Decker, W. A. Clark, and R. S. Decker. 1993. 'Contractile Activity and Cell-Cell Contact Regulate Myofibrillar Organization in Cultured Cardiac Myocytes.' *Journal of Cell Biology* 123(2): 323–36. doi:10.1083/JCB.123.2.323.

Smith, Alec S.T., Eunpyo Choi, Kevin Gray, Jesse Macadangdang, Eun Hyun Ahn, Elisa C. Clark, Michael A. Laflamme, et al. 2020. 'NanoMEA: A Tool for High-Throughput, Electrophysiological Phenotyping of Patterned Excitable Cells'. *Nano Letters* 20(3): 1561–70. doi:10.1021/acs.nanolett.9b04152.

Smith, Lucas R., Sangkyun Cho, and Dennis E. Discher. 2018. 'Stem Cell Differentiation Is Regulated by Extracellular Matrix Mechanics'. *Physiology* 33(1): 16–25. doi:10.1152/PHYSIOL.00026.2017/ASSET/IMAGES/LARGE/PHY0011804110004.JPEG.

Soepriatna, Arvin H., Allison Navarrete-Welton, Tae Yun Kim, Mark C. Daley, Peter Bronk, Celinda M. Kofron, Ulrike Mende, Kareen L.K. Coulombe, and Bum Rak Choi. 2023. 'Action Potential Metrics and Automated Data Analysis Pipeline for Cardiotoxicity Testing

Using Optically Mapped HiPSC-Derived 3D Cardiac Microtissues'. *PLoS ONE* 18(2 February). doi:10.1371/journal.pone.0280406.

Souders, Colby A., Stephanie L.K. Bowers, and Troy A. Baudino. 2009. 'Cardiac Fibroblast'. *Circulation Research* 105(12): 1164–76. doi:10.1161/CIRCRESAHA.109.209809.

Sparrow, John C., and Frieder Schöck. 2009. 'The Initial Steps of Myofibril Assembly: Integrins Pave the Way'. *Nature Reviews Molecular Cell Biology 2009 10:4* 10(4): 293–98. doi:10.1038/nrm2634.

Spinale, Francis G., Nikolaos G. Frangogiannis, Boris Hinz, Jeffrey W. Holmes, Zamaneh Kassiri, and Merry L. Lindsey. 2016. 'Crossing into the Next Frontier of Cardiac Extracellular Matrix Research'. *Circulation Research* 119(10): 1040–45. doi:10.1161/CIRCRESAHA.116.309916.

Squire, John M. 1997. *Architecture and Function in the Muscle Sarcomere*.

Stein, Jeroen M., Ulgu Arslan, Marnix Franken, Jessica C. de Greef, Sian E. Harding, Neda Mohammadi, Valeria V. Orlova, et al. 2022. 'Software Tool for Automatic Quantification of Sarcomere Length and Organization in Fixed and Live 2D and 3D Muscle Cell Cultures In Vitro'. *Current Protocols* 2(7). doi:10.1002/cpz1.462.

Strimaityte, Dovile, Chengyi Tu, Apuleyo Yanez, Ilanit Itzhaki, Haodi Wu, Joseph C. Wu, and Huaxiao Yang. 2022. 'Contractility and Calcium Transient Maturation in the Human IPSC-Derived Cardiac Microfibers'. *ACS Applied Materials and Interfaces* 14(31): 35376–88. doi:10.1021/ACSAMI.2C07326/ASSET/IMAGES/LARGE/AM2C07326_0008.JPEG.

Struijk, P. C., V. J. Mathews, T. Loupas, P. A. Stewart, E. B. Clark, E. A.P. Steegers, and J. W. Wladimiroff. 2008. 'Blood Pressure Estimation in the Human Fetal Descending Aorta'. *Ultrasound in Obstetrics and Gynecology* 32(5): 673–81. doi:10.1002/UOG.6137.

Stüdemann, Tim, Judith Rössinger, Christoph Manthey, Birgit Geertz, Rajiven Srikantharajah, Constantin Von Bibra, Aya Shibamiya, et al. 2022. 'Contractile Force of Transplanted Cardiomyocytes Actively Supports Heart Function after Injury'. *Circulation* 146(15): 1159–69. doi:10.1161/CIRCULATIONAHA.122.060124.

Sun, Shiyang, Huaiyu Shi, Sarah Moore, Chenyan Wang, Ariel Ash-Shakoor, Patrick T. Mather, James H. Henderson, and Zhen Ma. 2020. 'Progressive Myofibril Reorganization of Human Cardiomyocytes on a Dynamic Nanotopographic Substrate'. *ACS Applied Materials and Interfaces* 12(19): 21450–62. doi:10.1021/acsami.0c03464.

Sun, Y, Fazzi G.E., Meybrunn M., Blinston G.E., Daemen M.J.A.P., and Martinez-Maldonado M. 2000. 'Infarct Scar: A Dynamic Tissue'. *Cardiovascular Research* 46(2): 250–56. doi:10.1016/S0008-6363(00)00032-8.

Sutcliffe, Matthew D., Philip M. Tan, Antonio Fernandez-Perez, Young Jae Nam, Nikhil V. Munshi, and Jeffrey J. Saucerman. 2018. 'High Content Analysis Identifies Unique Morphological Features of Reprogrammed Cardiomyocytes'. *Scientific Reports* 8(1). doi:10.1038/s41598-018-19539-z.

Takada, Takuma, Daisuke Sasaki, Katsuhisa Matsuura, Koichiro Miura, Satoru Sakamoto, Hiroshi Goto, Takashi Ohya, et al. 2022. 'Aligned Human Induced Pluripotent Stem Cell-Derived Cardiac Tissue Improves Contractile Properties through Promoting Unidirectional and Synchronous Cardiomyocyte Contraction'. *Biomaterials* 281. doi:10.1016/j.biomaterials.2021.121351.

Takahashi, Kazutoshi, Koji Tanabe, Mari Ohnuki, Megumi Narita, Tomoko Ichisaka, Kiichiro Tomoda, and Shinya Yamanaka. 2007. 'Induction of Pluripotent Stem Cells from Adult Human Fibroblasts by Defined Factors'. *Cell* 131(5): 861–72. doi:10.1016/j.cell.2007.11.019.

Takeda, Norifumi, Ichiro Manabe, Yuichi Uchino, Kosei Eguchi, Sahohime Matsumoto, Satoshi Nishimura, Takayuki Shindo, et al. 2010. 'Cardiac Fibroblasts Are Essential for the Adaptive Response of the Murine Heart to Pressure Overload'. *The Journal of Clinical Investigation* 120(1): 254–65. doi:10.1172/JCI40295.

Tallquist, Michelle D., and Jeffery D. Molkentin. 2017. 'Redefining the Identity of Cardiac Fibroblasts'. *Nature Reviews Cardiology* 14(8): 484–91. doi:10.1038/nrcardio.2017.57.

Talman, Virpi, and Heikki Ruskoaho. 2016. 'Cardiac Fibrosis in Myocardial Infarction—from Repair and Remodeling to Regeneration'. *Cell and Tissue Research* 365(3): 563. doi:10.1007/S00441-016-2431-9.

Tamargo, Manuel Alejandro, Trevor Ray Nash, Sharon Fleischer, Youngbin Kim, Olaia Fernandez Vila, Keith Yeager, Max Summers, et al. 2021. 'MilliPillar: A Platform for the Generation and Real-Time Assessment of Human Engineered Cardiac Tissues'. *ACS Biomaterials Science and Engineering* 7(11): 5215–29. doi:10.1021/acsbiomaterials.1c01006.

Taneja, Nilay, Abigail C. Neininger, and Dylan T. Burnette. 2020. 'Coupling to Substrate Adhesions Drives the Maturation of Muscle Stress Fibers into Myofibrils within Cardiomyocytes'. *Molecular Biology of the Cell* 31(12): 1273–88. doi:10.1091/MBC.E19-11-0652.

Tang, Yadong, Li Liu, Junjun Li, Leqian Yu, Li Wang, Jian Shi, and Yong Chen. 2016. 'Induction and Differentiation of Human Induced Pluripotent Stem Cells into Functional Cardiomyocytes on a Compartmented Monolayer of Gelatin Nanofibers'. *Nanoscale* 8(30): 14530–40. doi:10.1039/c6nr04545f.

Tani, Hidenori, Eiji Kobayashi, Shinomi Yagi, Keisuke Tanaka, Kotaro Kameda-Haga, Shinsuke Shibata, Nobuko Moritoki, et al. 2023. 'Heart-Derived Collagen Promotes Maturation of Engineered Heart Tissue'. *Biomaterials* 299. doi:10.1016/j.biomaterials.2023.122174.

Tao, Arnold, Andrew S. LaCroix, T. Curtis Shoyer, Vidya Venkatraman, Karen L. Xu, Bradley Feiger, and Brenton D. Hoffman. 2023. 'Identifying Constitutive and Context-Specific Molecular-Tension-Sensitive Protein Recruitment within Focal Adhesions'. *Developmental Cell* 58(6): 522-534.e7. doi:10.1016/J.DEVCEL.2023.02.015.

Teekakirikul, Polakit, Robert F. Padera, J. G. Seidman, and Christine E. Seidman. 2012. 'Hypertrophic Cardiomyopathy: Translating Cellular Cross Talk into Therapeutics'. *Journal of Cell Biology* 199(3): 417–21. doi:10.1083/jcb.201207033.

Tenreiro, Miguel F., Ana F. Louro, Paula M. Alves, and Margarida Serra. 2021. 'Next Generation of Heart Regenerative Therapies: Progress and Promise of Cardiac Tissue Engineering'. *npj Regenerative Medicine 2021 6:1* 6(1): 1–17. doi:10.1038/s41536-021-00140-4.

Thavandiran, Nimalan, Nicole Dubois, Alexander Mikryukov, Stéphane Massé, Bogdan Beca, Craig A. Simmons, Vikram S. Deshpande, et al. 2013. 'Design and Formulation of Functional Pluripotent Stem Cell-Derived Cardiac Microtissues'. *Proceedings of the National Academy of Sciences of the United States of America* 110(49): E4698–4707. doi:10.1073/PNAS.1311120110/SUPPL_FILE/SM14.AVI.

Thomas, Dilip, Suji Choi, Christina Alamana, Kevin Kit Parker, and Joseph C. Wu. 2022. 'Cellular and Engineered Organoids for Cardiovascular Models'. *Circulation Research* 130(12): 1780–1802. doi:10.1161/CIRCRESAHA.122.320305.

Thompson, Susan A., Craig R. Copeland, Daniel H. Reich, and Leslie Tung. 2011. 'Mechanical Coupling between Myofibroblasts and Cardiomyocytes Slows Electric Conduction in Fibrotic Cell Monolayers'. *Circulation* 123(19): 2083–93. doi:10.1161/CIRCULATIONAHA.110.015057.

Tiburcy, Malte, James E. Hudson, Paul Balfanz, Susanne Schlick, Tim Meyer, Mei Ling Chang Liao, Elif Levent, et al. 2017. 'Defined Engineered Human Myocardium with Advanced Maturation for Applications in Heart Failure Modeling and Repair'. *Circulation* 135(19): 1832–47. doi:10.1161/CIRCULATIONAHA.116.024145/-/DC1.

Toepfer, Christopher N., Amanda C. Garfinkel, Gabriela Venturini, Hiroko Wakimoto, Giuliana Repetti, Lorenzo Alamo, Arun Sharma, et al. 2020. 'Myosin Sequestration Regulates Sarcomere Function, Cardiomyocyte Energetics, and Metabolism, Informing the Pathogenesis of Hypertrophic Cardiomyopathy'. *Circulation*: 828–42. doi:10.1161/CIRCULATIONAHA.119.042339.

Toepfer, Christopher N., Arun Sharma, Marcelo Cicconet, Amanda C. Garfinkel, Michael Mücke, Meraj Neyazi, Jon A.L. Willcox, et al. 2019. 'SarcTrack'. *Circulation research* 124(8): 1172–83. doi:10.1161/CIRCRESAHA.118.314505.

Tohyama, Shugo, Jun Fujita, Takako Hishiki, Tomomi Matsuura, Fumiyuki Hattori, Rei Ohno, Hideaki Kanazawa, et al. 2016. 'Glutamine Oxidation Is Indispensable for Survival of Human Pluripotent Stem Cells'. *Cell Metabolism* 23(4): 663–74. doi:10.1016/j.cmet.2016.03.001.

Tohyama, Shugo, Fumiyuki Hattori, Motoaki Sano, Takako Hishiki, Yoshiko Nagahata, Tomomi Matsuura, Hisayuki Hashimoto, et al. 2013. 'Distinct Metabolic Flow Enables Large-Scale Purification of Mouse and Human Pluripotent Stem Cell-Derived Cardiomyocytes'. *Cell Stem Cell* 12(1): 127–37. doi:10.1016/j.stem.2012.09.013.

Toischer, Karl, Adam G. Rokita, Bernhard Unsöld, Wuqiang Zhu, Georgios Kararigas, Samuel Sossalla, Sean P. Reuter, et al. 2010. 'Differential Cardiac Remodeling in Preload Versus Afterload'. *Circulation* 122(10): 993–1003. doi:10.1161/CIRCULATIONAHA.110.943431.

Trappmann, Britta, Julien E. Gautrot, John T. Connelly, Daniel G.T. Strange, Yuan Li, Michelle L. Oyen, Martien A. Cohen Stuart, et al. 2012. 'Extracellular-Matrix Tethering Regulates Stem-Cell Fate'. *Nature Materials* 11(7): 642–49. doi:10.1038/nmat3339.

Travers, Joshua G., Fadia A. Kamal, Jeffrey Robbins, Katherine E. Yutzey, and Burns C. Blaxall. 2016. 'Cardiac Fibrosis: The Fibroblast Awakens'. *Circulation Research* 118(6): 1021–40. doi:10.1161/CIRCRESAHA.115.306565.

Tsan, Yao Chang, Samuel J. DePalma, Yan Ting Zhao, Adela Capilnasiu, Yu Wei Wu, Brynn Elder, Isabella Panse, et al. 2021. 'Physiologic Biomechanics Enhance Reproducible Contractile Development in a Stem Cell Derived Cardiac Muscle Platform'. *Nature Communications 2021 12:1* 12(1): 1–16. doi:10.1038/s41467-021-26496-1.

Tsao, Connie W., Aaron W. Aday, Zaid I. Almarzooq, Cheryl A.M. Anderson, Pankaj Arora, Christy L. Avery, Carissa M. Baker-Smith, et al. 2023. 'Heart Disease and Stroke Statistics-2023 Update: A Report From the American Heart Association'. *Circulation* 147(8): E93–621. doi:10.1161/CIR.0000000000001123.

Tsui, Jonathan H., Andrea Leonard, Nathan D. Camp, Joseph T. Long, Zeid Y. Nawas, Rakchanok Chavanachat, Alec S.T. Smith, et al. 2021. 'Tunable Electroconductive Decellularized Extracellular Matrix Hydrogels for Engineering Human Cardiac Microphysiological Systems'. *Biomaterials* 272. doi:10.1016/j.biomaterials.2021.120764.

Tzahor, Eldad, and Stefanie Dimmeler. 2022. 'A Coalition to Heal-the Impact of the Cardiac Microenvironment'. *Science* 377(6610). doi:10.1126/SCIENCE.ABM4443/ASSET/B6DDD854-256D-429C-99CE-FD049E1736E6/ASSETS/IMAGES/LARGE/SCIENCE.ABM4443-F4.JPG.

Ulmer, Bärbel M., Andrea Stoehr, Mirja L. Schulze, Sajni Patel, Marjan Gucek, Ingra Mannhardt, Sandra Funcke, et al. 2018. 'Contractile Work Contributes to Maturation of Energy Metabolism in HiPSC-Derived Cardiomyocytes'. *Stem Cell Reports* 10(3): 834–47. doi:10.1016/j.stemcr.2018.01.039.

Uosaki, Hideki, Patrick Cahan, Dong I. Lee, Songnan Wang, Matthew Miyamoto, Laviel Fernandez, David A. Kass, and Chulan Kwon. 2015. 'Transcriptional Landscape of Cardiomyocyte Maturation'. *Cell Reports* 13(8): 1705–16. doi:10.1016/j.celrep.2015.10.032.

Uscategui Calderon, Maria, Brittany A. Gonzalez, and Katherine E. Yutzey. 2023. 'Cardiomyocyte-Fibroblast Crosstalk in the Postnatal Heart'. *Frontiers in Cell and Developmental Biology* 11: 1163331. doi:10.3389/FCELL.2023.1163331/BIBTEX.

Vannozzi, Lorenzo, Immihan Ceren Yasa, Hakan Ceylan, Arianna Menciassi, Leonardo Ricotti, and Metin Sitti. 2018. 'Self-Folded Hydrogel Tubes for Implantable Muscular Tissue Scaffolds'. *Macromolecular Bioscience* 18(4). doi:10.1002/mabi.201700377.

Varga, Zoltán V., Peter Ferdinandy, Lucas Liaudet, and Pál Pacher. 2015. 'Drug-Induced Mitochondrial Dysfunction and Cardiotoxicity'. *American Journal of Physiology - Heart and Circulatory Physiology* 309(9): H1453–67. doi:10.1152/ajpheart.00554.2015.

Vasquez, Carolina, Poornima Mohandas, Karen L. Louie, Najate Benamer, Ashwini C. Bapat, and Gregory E. Morley. 2010. 'Enhanced Fibroblast–Myocyte Interactions in Response to Cardiac Injury'. *Circulation Research* 107(8): 1011–20. doi:10.1161/CIRCRESAHA.110.227421.

Van Der Velden, J, L J Klein, M Van Der Bijl, M A J M Huybregts, W Stooker, J Witkop, L Eijsman, et al. 1999. 42 Cardiovascular Research *Isometric Tension Development and Its Calcium Sensitivity in Skinned Myocyte-Sized Preparations from Different Regions of the Human Heart*. www.elsevier.com/locate/cardioreswww.elsevier.nl/locate/cardiores.

Virani, Salim S., Alvaro Alonso, Emelia J. Benjamin, Marcio S. Bittencourt, Clifton W. Callaway, April P. Carson, Alanna M. Chamberlain, et al. 2020. 'Heart Disease and Stroke Statistics—2020 Update: A Report From the American Heart Association'. *Circulation* 141(9): e139–596. doi:10.1161/CIR.0000000000000757.

Vreeker, Arnold, Leonie van Stuijvenberg, Thomas J. Hund, Peter J. Mohler, Peter G. J. Nikkels, and Toon A. B. van Veen. 2014. 'Assembly of the Cardiac Intercalated Disk during Pre- and Postnatal Development of the Human Heart' ed. Marie Jose Goumans. *PLoS ONE* 9(4): e94722. doi:10.1371/journal.pone.0094722.

Walsh, Roddy, Joost A. Offerhaus, Rafik Tadros, and Connie R. Bezzina. 2021. 'Minor Hypertrophic Cardiomyopathy Genes, Major Insights into the Genetics of Cardiomyopathies'. *Nature Reviews Cardiology 2021 19:3* 19(3): 151–67. doi:10.1038/s41569-021-00608-2.

Wang, Erika Yan, Naimeh Rafatian, Yimu Zhao, Angela Lee, Benjamin Fook, Lun Lai, Rick Xingze Lu, et al. 2019. 'Biowire Model of Interstitial and Focal Cardiac Fibrosis'. *ACS Central Science* 5(7): 1146–58. doi:10.1021/acscentsci.9b00052.

Wang, Huan, Mark W. Tibbitt, Stephen J. Langer, Leslie A. Leinwand, and Kristi S. Anseth. 2013. 'Hydrogels Preserve Native Phenotypes of Valvular Fibroblasts through an Elasticity-Regulated PI3K/AKT Pathway'. *Proceedings of the National Academy of Sciences of the United States of America* 110(48): 19336–41. doi:10.1073/PNAS.1306369110/SUPPL_FILE/SM04.AVI.

Wang, Jun, Shijie Liu, Todd Heallen, and James F. Martin. 2018. 'The Hippo Pathway in the Heart: Pivotal Roles in Development, Disease, and Regeneration'. *Nature Reviews Cardiology* 15(11): 672–84. doi:10.1038/s41569-018-0063-3.

Wang, Yijie, Qihao Li, Bo Tao, Marina Angelini, Sivakumar Ramadoss, Baiming Sun, Ping Wang, et al. 2023. 'Fibroblasts in Heart Scar Tissue Directly Regulate Cardiac Excitability and Arrhythmogenesis'. *Science* 381(6665): 1480–87. doi:10.1126/SCIENCE.ADH9925/SUPPL_FILE/SCIENCE.ADH9925_MOVIE_S1.ZIP.

Wanjare, Maureen, Luqia Hou, Karina H. Nakayama, Joseph J. Kim, Nicholas P. Mezak, Oscar J. Abilez, Evangeline Tzatzalos, Joseph C. Wu, and Ngan F. Huang. 2017. 'Anisotropic Microfibrous Scaffolds Enhance the Organization and Function of Cardiomyocytes Derived from Induced Pluripotent Stem Cells'. *Biomaterials Science* 5(8): 1567–78. doi:10.1039/c7bm00323d.

Weber, K T. 2000. 'Fibrosis and Hypertensive Heart Disease'. *Current opinion in cardiology* 15(4): 264–72. doi:10.1097/01.hjh.0000388491.35836.d2.

Weber, Karl T. 1989. ‘Cardiac Interstitium in Health and Disease: The Fibrillar Collagen Network’. *Journal of the American College of Cardiology* 13(7): 1637–52. doi:10.1016/0735-1097(89)90360-4.

Weber, Karl T., Yao Sun, Syamal K. Bhattacharya, Robert A. Ahokas, and Ivan C. Gerling. 2012. ‘Myofibroblast-Mediated Mechanisms of Pathological Remodelling of the Heart’. *Nature Reviews Cardiology 2012 10:1* 10(1): 15–26. doi:10.1038/nrcardio.2012.158.

Weber, Karl T., Yao Sun, Suresh C. Tyagi, and Jack P.M. Cleutjens. 1994. ‘Collagen Network of the Myocardium: Function, Structural Remodeling and Regulatory Mechanisms’. *Journal of Molecular and Cellular Cardiology* 26(3): 279–92. doi:10.1006/jmcc.1994.1036.

Wheelwright, Matthew, Zaw Win, Jennifer L. Mikkila, Kamilah Y. Amen, Patrick W. Alford, and Joseph M. Metzger. 2018. ‘Investigation of Human IPSC-Derived Cardiac Myocyte Functional Maturation by Single Cell Traction Force Microscopy’. *PLoS ONE* 13(4). doi:10.1371/journal.pone.0194909.

Wiegerinck, Rob F., Anca Cojoc, Carlo M. Zeidenweber, Guoliang Ding, Ming Shen, Ronald W. Joyner, Janet D. Fernandez, et al. 2009. ‘Force Frequency Relationship of the Human Ventricle Increases During Early Postnatal Development’. *Pediatric Research 2009 65:4* 65(4): 414–19. doi:10.1203/pdr.0b013e318199093c.

Williams, C., K. P. Quinn, I. Georgakoudi, and L. D. Black. 2014. ‘Young Developmental Age Cardiac Extracellular Matrix Promotes the Expansion of Neonatal Cardiomyocytes in Vitro’. *Acta Biomaterialia* 10(1): 194–204. doi:10.1016/j.actbio.2013.08.037.

Williams, Corin, and Lauren D. Black. 2015. ‘The Role of Extracellular Matrix in Cardiac Development’. In *Biomaterials for Cardiac Regeneration*, Springer International Publishing, 1–35. doi:10.1007/978-3-319-10972-5_1.

Wipff, Pierre Jean, Daniel B. Rifkin, Jean Jacques Meister, and Boris Hinz. 2007. ‘Myofibroblast Contraction Activates Latent TGF-B1 from the Extracellular Matrix’. *Journal of Cell Biology* 179(6): 1311–23. doi:10.1083/JCB.200704042/VIDEO-6.

Wouters, Olivier J., Martin McKee, and Jeroen Luyten. 2020. ‘Estimated Research and Development Investment Needed to Bring a New Medicine to Market, 2009-2018’. *JAMA* 323(9): 844–53. doi:10.1001/jama.2020.1166.

Xu, Cong, Li Wang, Yue Yu, Fangchao Yin, Xiaoqing Zhang, Lei Jiang, and Jianhua Qin. 2017. ‘Bioinspired Onion Epithelium-like Structure Promotes the Maturation of Cardiomyocytes Derived from Human Pluripotent Stem Cells’. *Biomaterials Science* 5(9): 1810–19. doi:10.1039/c7bm00132k.

Xu, Weiming, Hélène Baribault, and Eileen D. Adamson. 1998. 'Vinculin Knockout Results in Heart and Brain Defects during Embryonic Development'. *Development* 125(2): 327–37. doi:10.1242/DEV.125.2.327.

Yadid, Moran, Johan U. Lind, Herdeline Ann M. Ardoña, Sean P. Sheehy, Lauren E. Dickinson, Feyisayo Eweje, Maartje M.C. Bastings, et al. 2020. 'Endothelial Extracellular Vesicles Contain Protective Proteins and Rescue Ischemia-Reperfusion Injury in a Human Heart-on-Chip'. *Science Translational Medicine* 12(565): 8005. doi:10.1126/scitranslmed.aax8005.

Yamada, Shintaro, Toshiyuki Ko, Satoshi Hatsuse, Seitaro Nomura, Bo Zhang, Zhehao Dai, Shunsuke Inoue, et al. 2022. 'Spatiotemporal Transcriptome Analysis Reveals Critical Roles for Mechano-Sensing Genes at the Border Zone in Remodeling after Myocardial Infarction'. *Nature Cardiovascular Research 2022 1:11* 1(11): 1072–83. doi:10.1038/s44161-022-00140-7.

Yang, Bai, Cecillia Lui, Enoch Yeung, Hiroshi Matsushita, Anjana Jeyaram, Isaree Pitaktong, Takahiro Inoue, et al. 2019. 'A Net Mold-Based Method of Biomaterial-Free Three-Dimensional Cardiac Tissue Creation'. *Tissue Engineering - Part C: Methods* 25(4): 243–52. doi:10.1089/ten.tec.2019.0003.

Yang, Hongbin, Will Stebbeds, Jo Francis, Amy Pointon, Olga Obrezanova, Kylie A. Beattie, Peter Clements, et al. 2022. 'Deriving Waveform Parameters from Calcium Transients in Human IPSC-Derived Cardiomyocytes to Predict Cardiac Activity with Machine Learning'. *Stem Cell Reports* 17(3): 556–68. doi:10.1016/j.stemcr.2022.01.009.

Yang, Lanti, Kees O. Van Der Werf, Bart F.J.M. Koopman, Vinod Subramaniam, Martin L. Bennink, Pieter J. Dijkstra, and Jan Feijen. 2007. 'Micromechanical Bending of Single Collagen Fibrils Using Atomic Force Microscopy'. *Journal of Biomedical Materials Research Part A* 82A(1): 160–68. doi:10.1002/JBM.A.31127.

Yang, Xiulan, Lil Pabon, and Charles E. Murry. 2014. 'Engineering Adolescence: Maturation of Human Pluripotent Stem Cell-Derived Cardiomyocytes'. *Circulation Research* 114(3): 511–23. doi:10.1161/CIRCRESAHA.114.300558.

Yang, Xiulan, Marita L. Rodriguez, Andrea Leonard, Lihua Sun, Karin A. Fischer, Yuliang Wang, Julia Ritterhoff, et al. 2019. 'Fatty Acids Enhance the Maturation of Cardiomyocytes Derived from Human Pluripotent Stem Cells'. *Stem Cell Reports* 13(4): 657–68. doi:10.1016/j.stemcr.2019.08.013.

Yang, Xiulan, Marita Rodriguez, Lil Pabon, Karin A. Fischer, Hans Reinecke, Michael Regnier, Nathan J. Sniadecki, Hannele Ruohola-Baker, and Charles E. Murry. 2014. 'Tri-Iodo-l-Thyronine Promotes the Maturation of Human Cardiomyocytes-Derived from Induced

Pluripotent Stem Cells'. *Journal of Molecular and Cellular Cardiology* 72: 296–304. doi:10.1016/j.yjmcc.2014.04.005.

Yoshida, Shohei, Shigeru Miyagawa, Satsuki Fukushima, Takuji Kawamura, Noriyuki Kashiyama, Fumiya Ohashi, Toshihiko Toyofuku, Koichi Toda, and Yoshiki Sawa. 2018. 'Maturation of Human Induced Pluripotent Stem Cell-Derived Cardiomyocytes by Soluble Factors from Human Mesenchymal Stem Cells'. *Molecular Therapy* 26(11): 2681–95. doi:10.1016/j.ymthe.2018.08.012.

Yoshikane, Hideki, Masaaki Honda, Yasutoshi Goto, Shigefumi Morioka, Katsutoshi Moriyama, and Akira Ooshima. 1992. 'COLLAGEN IN DILATED CARDIOMYOPATHY : Scanning Electron Microscopic and Immunohistochemical Observations'. *JAPANESE CIRCULATION JOURNAL* 56(9): 899–910. doi:10.1253/JCJ.56.899.

Young, Jennifer L., and Adam J. Engler. 2011. 'Hydrogels with Time-Dependent Material Properties Enhance Cardiomyocyte Differentiation in Vitro'. *Biomaterials* 32(4): 1002–9. doi:10.1016/j.biomaterials.2010.10.020.

Young, Jennifer L., Kyle Kretchmer, Matthew G. Ondeck, Alexander C. Zambon, and Adam J. Engler. 2014. 'Mechanosensitive Kinases Regulate Stiffness-Induced Cardiomyocyte Maturation'. *Scientific Reports* 4: 1–11. doi:10.1038/srep06425.

Yu, Jiashing, An-Rei Lee, Wei-Han Lin, Che-Wei Lin, Yuan-Kun Wu, and Wei-Bor Tsai. 2014. 'Electrospun PLGA Fibers Incorporated with Functionalized Biomolecules for Cardiac Tissue Engineering'. *Tissue Engineering Part A* 20(13–14): 1896–1907. doi:10.1089/ten.tea.2013.0008.

Zemljic-Harpf, Alice E., Joel C. Miller, Scott A. Henderson, Adam T. Wright, Ana Maria Manso, Laila Elsherif, Nancy D. Dalton, et al. 2007. 'Cardiac-Myocyte-Specific Excision of the Vinculin Gene Disrupts Cellular Junctions, Causing Sudden Death or Dilated Cardiomyopathy'. *Molecular and Cellular Biology* 27(21): 7522–37. doi:10.1128/MCB.00728-07/ASSET/F072FB18-87CF-4D7B-BBA5-30CDA28F083C/ASSETS/GRAPHIC/ZMB0210770790008.JPEG.

Zhang, Hao, Lei Tian, Mengcheng Shen, Chengyi Tu, Haodi Wu, Mingxia Gu, David T. Paik, and Joseph C. Wu. 2019. 'Generation of Quiescent Cardiac Fibroblasts From Human Induced Pluripotent Stem Cells for In Vitro Modeling of Cardiac Fibrosis'. *Circulation Research* 125(5): 552–66. doi:10.1161/CIRCRESAHA.119.315491.

Zhang, Jianhua, Zachery R. Gregorich, Ran Tao, Gina C. Kim, Pratik A. Lalit, Juliana L. Carvalho, Yogananda Markandeya, et al. 2022. 'Cardiac Differentiation of Human

Pluripotent Stem Cells Using Defined Extracellular Matrix Proteins Reveals Essential Role of Fibronectin'. *eLife* 11. doi:10.7554/ELIFE.69028.

Zhang, Jianyi, Wuqiang Zhu, Milica Radisic, and Gordana Vunjak-Novakovic. 2018. 'Can We Engineer a Human Cardiac Patch for Therapy?' *Circulation Research* 123(2): 244–65. doi:10.1161/CIRCRESAHA.118.311213.

Zhang, Joe Z., Vittavat Termglinchan, Ning Yi Shao, Ilanit Itzhaki, Chun Liu, Ning Ma, Lei Tian, et al. 2019. 'A Human IPSC Double-Reporter System Enables Purification of Cardiac Lineage Subpopulations with Distinct Function and Drug Response Profiles'. *Cell Stem Cell* 24(5): 802-811.e5. doi:10.1016/j.stem.2019.02.015.

Zhang, Kehan, Paige E. Cloonan, Subramanian Sundaram, Feng Liu, Shoshana L. Das, Jourdan K. Ewoldt, Jennifer L. Bays, et al. 2021. 'Plakophilin-2 Truncating Variants Impair Cardiac Contractility by Disrupting Sarcomere Stability and Organization'. *Science Advances* 7(42): 3995–4010. doi:10.1126/SCIADV.ABH3995/SUPPL_FILE/SCIADV.ABH3995_MOVIES_S1_TO_S12.ZIP.

Zhang, Qiangzhe, Junjie Jiang, Pengcheng Han, Qi Yuan, Jing Zhang, Xiaoqian Zhang, Yanyan Xu, et al. 2010. 'Direct Differentiation of Atrial and Ventricular Myocytes from Human Embryonic Stem Cells by Alternating Retinoid Signals'. *Cell Research 2011 21:4* 21(4): 579–87. doi:10.1038/cr.2010.163.

Zhang, Yu Shrike, Andrea Arneri, Simone Bersini, Su Ryon Shin, Kai Zhu, Zahra Goli-Malekabadi, Julio Aleman, et al. 2016. 'Bioprinting 3D Microfibrous Scaffolds for Engineering Endothelialized Myocardium and Heart-on-a-Chip'. *Biomaterials* 110: 45–59. doi:10.1016/j.biomaterials.2016.09.003.

Zhao, Bill, Kehan Zhang, Christopher S. Chen, and Emma Lejeune. 2021. 'Sarc-Graph: Automated Segmentation, Tracking, and Analysis of Sarcomeres in HiPSCderived Cardiomyocytes'. *PLoS Computational Biology* 17(10). doi:10.1371/journal.pcbi.1009443.

Zhao, Yimu, Naimeh Rafatian, Nicole T. Feric, Brian J. Cox, Roozbeh Aschar-Sobbi, Erika Yan Wang, Praful Aggarwal, et al. 2019. 'A Platform for Generation of Chamber-Specific Cardiac Tissues and Disease Modeling'. *Cell* 176(4): 913-927.e18. doi:10.1016/j.cell.2018.11.042.

Zuppinger, C., M. Eppenberger-Eberhardt, and H. M. Eppenberger. 2000. 'N-Cadherin: Structure, Function and Importance in the Formation of New Intercalated Disc-like Cell Contacts in Cardiomyocytes'. *Heart Failure Reviews* 5(3): 251–57. doi:10.1023/A:1009809520194.